



National Library  
of Canada

Acquisitions and  
Bibliographic Services Branch

395 Wellington Street  
Ottawa, Ontario  
K1A 0N4

Bibliothèque nationale  
du Canada

Direction des acquisitions et  
des services bibliographiques

395, rue Wellington  
Ottawa (Ontario)  
K1A 0N4

*Your file* *Votre référence*

*Our file* *Notre référence*

## NOTICE

## AVIS

The quality of this microform is heavily dependent upon the quality of the original thesis submitted for microfilming. Every effort has been made to ensure the highest quality of reproduction possible.

La qualité de cette microforme dépend grandement de la qualité de la thèse soumise au microfilmage. Nous avons tout fait pour assurer une qualité supérieure de reproduction.

If pages are missing, contact the university which granted the degree.

S'il manque des pages, veuillez communiquer avec l'université qui a conféré le grade.

Some pages may have indistinct print especially if the original pages were typed with a poor typewriter ribbon or if the university sent us an inferior photocopy.

La qualité d'impression de certaines pages peut laisser à désirer, surtout si les pages originales ont été dactylographiées à l'aide d'un ruban usé ou si l'université nous a fait parvenir une photocopie de qualité inférieure.

Reproduction in full or in part of this microform is governed by the Canadian Copyright Act, R.S.C. 1970, c. C-30, and subsequent amendments.

La reproduction, même partielle, de cette microforme est soumise à la Loi canadienne sur le droit d'auteur, SRC 1970, c. C-30, et ses amendements subséquents.

Canada

UNIVERSITY OF ALBERTA

Experimental Studies of Stimulated Brillouin Scattering  
from KrF Laser-Produced Plasma

by

Masayuki Fujita



A thesis

submitted to the Faculty of Graduate Studies and Research  
in partial fulfillment of the requirements for the degree of  
Doctor of Philosophy

DEPARTMENT OF ELECTRICAL ENGINEERING

EDMONTON, ALBERTA

Fall 1992



National Library  
of Canada

Acquisitions and  
Bibliographic Services Branch

395 Wellington Street  
Ottawa, Ontario  
K1A 0N4

Bibliothèque nationale  
du Canada

Direction des acquisitions et  
des services bibliographiques

395, rue Wellington  
Ottawa (Ontario)  
K1A 0N4

*Your file* *Votre référence*

*Our file* *Notre référence*

**The author has granted an irrevocable non-exclusive licence allowing the National Library of Canada to reproduce, loan, distribute or sell copies of his/her thesis by any means and in any form or format, making this thesis available to interested persons.**

**L'auteur a accordé une licence irrévocable et non exclusive permettant à la Bibliothèque nationale du Canada de reproduire, prêter, distribuer ou vendre des copies de sa thèse de quelque manière et sous quelque forme que ce soit pour mettre des exemplaires de cette thèse à la disposition des personnes intéressées.**

**The author retains ownership of the copyright in his/her thesis. Neither the thesis nor substantial extracts from it may be printed or otherwise reproduced without his/her permission.**

**L'auteur conserve la propriété du droit d'auteur qui protège sa thèse. Ni la thèse ni des extraits substantiels de celle-ci ne doivent être imprimés ou autrement reproduits sans son autorisation.**

ISBN 0-315-77368-5

**Canada**

UNIVERSITY OF ALBERTA

RELEASE FORM

NAME OF AUTHOR : Masayuki Fujita

TITLE OF THESIS : Experimental Studies of Stimulated Brillouin  
Scattering from KrF Laser-Produced Plasma

DEGREE : Doctor of Philosophy

YEAR THIS DEGREE GRANTED Fall 1992

Permission is hereby granted to the University of Alberta Library to reproduce single copies of this thesis and to lend or sell such copies for private, scholarly or scientific purposes only.

The author reserves all other publication and other rights in association with the copyright in the thesis, and except as hereinbefore provided neither the thesis nor any substantial portion thereof may be printed or otherwise reproduced in any material form whatever without the author's prior written permission.



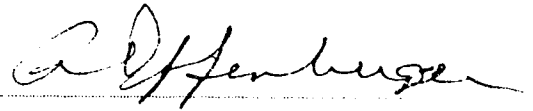
---

Permanent address :  
325 Yahata-machi  
Kumamoto, Kumamoto  
861-41, JAPAN

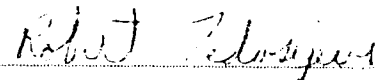
Dated June 30 1992

UNIVERSITY OF ALBERTA  
FACULTY OF GRADUATE STUDIES AND RESEARCH

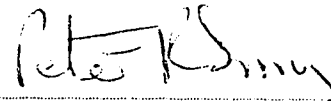
The undersigned certify that they have read, and recommend to the Faculty of Graduate Studies and Research, for acceptance, a thesis entitled Experimental Studies of Stimulated Brillouin Scattering from KrF Laser-Produced Plasma submitted by Masayuki Fujita in partial fulfillment of the requirements for the degree of Doctor of Philosophy.



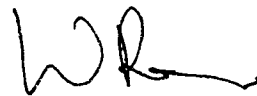
Dr. A. A. Offenberger



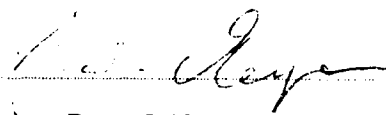
Dr. R. Fedosejevs



Dr. P. Smy



Dr. W. Rozmus



Dr. J. Meyer

Date June 18, 1992

## Abstract

A comprehensive study of stimulated Brillouin scattering (SBS) in nanosecond KrF laser-produced plasma at intensity  $I_L \approx 10^{14} \text{W/cm}^2$  has been performed. Measurements of reflectivity and time-resolved backscattered spectra were done for CH, Al, and Au targets at various angles of incidence  $\theta$ . The measured backscatter reflectivity ranged from 0.1% to 1.0% for Al and C plasma, with higher reflectivity being observed for larger  $\theta$ . Au plasma showed significantly lower reflectivity ( $\approx 0.005\%$ ). The time-resolved spectra of backscattered light were found to be correlated with laser intensity and pulse shape. Numerical codes developed to model the SBS process in homogeneous and inhomogeneous plasmas dominated by strong inverse bremsstrahlung absorption predicted an optimum density for SBS amplification. Two-dimensional hydrodynamic simulations predicted locally planar density and spherical pressure profiles as a consequence of the large mass ablation rate and localized plasma heating. Models for SBS in inhomogeneous plasma and non-uniform laser irradiation were proposed and used to explain the experimental data. Analytically and experimentally, we find evidence for the convective nature of the SBS instability. Supplementary experiments using thin foil targets showed strong temporal and spatial modulation in transmitted light. It was found that the laser beam non-uniformity was not smoothed out by the plasma but remained throughout the laser pulse.

## Acknowledgement

I would like to thank my supervisor, Dr.Allan Offenberger, for his permission to conduct research in his laboratory and for his inspiring guidance and advice. I am especially grateful to Dr.Offenberger for his encouragement and generous support of my activity during this work.

I am thankful to Dr.Fedosejevs for helping me in the completion of this thesis as well as his support for my experimental activities. I am also thankful to Dr.Capjack and Dr.Rozmus for the many useful discussions and their assistance in numerical and theoretical aspects of this study.

I wish to express my thanks to Dr.Tikhonchuk for his comprehensive advice during his visit to the University of Alberta. I also wish to express my thanks to Dr.Nishihara for his valuable advice.

I am thankful to all the members of the Plasma Group at the University of Alberta for illuminating discussions.

This research would not have been possible without the outstanding talents of the machine shop personnel and the excellent technical assistant of Mr.Blair Harwood and Mr.Alois Haromy.

The financial support from the Rotary International Foundation, the University of Alberta, and the Killam Trust as well as my supervisor during the past five years is gratefully acknowledged.

Finally, my wife, Anna, and my new-born son, Hidenori, gave the much needed love, patience, understanding and adorable enlightenment and disturbance to help me through my studies.

## Table of Contents

Chapter	Page
1. Introduction	1
1.1. Motivation	1
1.2. Early Work in Stimulated Brillouin Scattering	2
1.3. Objective of This Work	7
Bibliography	9
2. Theory	13
2.1. Coupling of Three Waves	13
2.2. Instability Threshold Criteria, Growth Rate and Region of Applicability	15
2.3. Ion Acoustic Wave Damping	18
2.4. Spectral Feature of Scattered Light	21
2.5. Noise Source of Scattered Light	22
2.6. Double Stimulated Brillouin Scattering (DSBS)	23
2.7. Density Fluctuation Related to SBS Reflectivity	24
Bibliography	26
3. Numerical Investigation of SBS	28
3.1. Outline of Differencing Scheme	28
3.1.1. Scheme 1 : Predictor-Corrector Method	29
3.1.2. Scheme 2 : Time-Splitting Method	30
3.2. Numerical Solutions in Finite Homogeneous Plasma	31
3.2.1. Comparison with Theoretical Predictions (Steady State)	31
3.2.2. Dependence of Reflectivity on Electron Density	34
3.2.3. Temporal Response of SBS Growth	36
3.3. Numerical Solutions in Finite Inhomogeneous Plasma	38



3.4. Summary	41
Bibliography	42
4. Hydrodynamic Simulation (CASTOR) Results	43
4.1. Outline of Simulation Code CASTOR	43
4.2. Laser Focal Spot and Density Scale Length	45
4.3. Temporal Evolution of Plasma	48
4.4. Temperature	51
4.5. Plasma flow	54
4.6. Phase Mismatch	56
4.7. Summary	59
Bibliography	60
5. Experimental Methods	61
5.1. Characteristics of KrF Laser at the University of Alberta	61
5.1.1. Outline of the KrF Laser System	61
5.1.2. Temporal and Spatial Characteristics	64
5.2. Targets	70
5.3. Diagnostics	72
5.3.1. Experimental Setup	72
5.3.2. Reflectivity	73
5.3.3. Backscatter Spectra	74
5.3.4. X-ray Measurement	75
Bibliography	76
6. Experimental Results	78
6.1. X-ray Image	78
6.2. Electron Temperature	81
6.3. Reflectivity	83

6.3.1. Backscatter Reflectivity	83
6.3.2. Specular Reflectivity	86
6.4. Spectral Shift	88
6.4.1. Time-Resolved Spectra	88
6.4.2. Spectral Shift at Peak Backscattering	96
6.4.3. Temporal Features of Spectrum : $d\lambda/dt$	99
6.5. Summary	101
Bibliography	102
7. Data Analysis I (Homogeneous Plasma)	103
7.1. Typical Plasma Conditions	103
7.1.1 Al and C Plasma	103
7.1.2 Au plasma	106
7.2. Instability Threshold and Gain	108
7.2.1. Infinite Homogeneous Plasma	108
7.2.2. Finite Homogeneous Plasma	110
7.2.3. Comparison between Theory and Experiment (Threshold and Gain)	110
7.3. Spectral Shift	112
7.4. Reflectivity	114
7.4.1. Dependence on Plasma Length	115
7.4.2. Dependence on Electron Density	117
7.4.3. Density Fluctuation Level	119
7.4.4. Noise Source of Scattered Light	121
7.5. Hotspot Effects	124
7.6. Double stimulated Brillouin scattering (DSBS)	132
7.7. Summary	134
Bibliography	136

8. Data Analysis II (Inhomogeneous Plasma)	137
8.1. Threshold and Gain (Inhomogeneous Plasma)	137
8.1.1. Phase Mismatch Condition	138
8.2. Spectral Shift	141
8.2.1. Effects of Expanding Inhomogeneous Plasma on Spectral Shift	141
8.2.2. Linewidth	142
8.2.3. Temporal Evolution of Spectral Shift	144
8.3. SBS Reflectivity from Inhomogeneous Plasma	151
8.3.1. Spatial Profile of SBS Gain	151
8.3.2. Coherent Model	153
8.3.3. Incoherent Model	161
8.3.4. Incoherent Model Results I : Constant $\kappa'$	165
8.3.5. Incoherent Model Results II : $\kappa'(L_n)$	170
8.3.6. Comparison among SBS Models and Experimental Data	173
8.4. Summary	179
Bibliography	180
9. Conclusions	181
Appendix 1. Derivation of Steady State Convective SBS Model for Finite Homogeneous Plasma	185
Appendix 2. Formulae to Convert Focal Length	189
Appendix 3. Formulae for Plasma Parameters in Practical Units	192
Appendix 4. Target Burnthrough Experiment	197
A4.1. Experimental Setup	197
A4.2. Experimental Results	198
A4.3. Discussion	206

A4.4. Possibility of Filamentation	207
A4.5. Summary	212
Bibliography	213
Vita	214

## List of Tables

Table	Page
4.1. Laser beam parameters for CASTOR .....	44
4.2. Density scale length $L_n$ and focal spot size $r_{90x}$ .....	48
4.3. Scale length $L_n$ , $L_v$ and focal spot size $r_{90x}$ and $r_{50x}$ .....	54
5.1. Model of focal spot energy fluence distribution .....	68
7.1. Estimated plasma conditions .....	104
7.2. Ionization potential for C, Al, and Au .....	107
7.3. Threshold intensity $I_{th}$ and growth rate $\gamma_0$ at $10^{14} \text{W/cm}^2$ .....	109
7.4. Damping rates $\gamma_s$ , $\gamma_{ib}$ , and parameter $\Gamma$ at $10^{14} \text{W/cm}^2$ .....	109
7.5. Comparison between theoretical predictions and experimental data with three component intensity distribution .....	111
7.6. Characteristics of focal spot .....	128

## List of Figures

Figure	Page
2.1. Ion acoustic damping in Al plasma	20
3.1. Simulation results in finite homogeneous plasma	32
3.2. Comparison between simulation results and analytical predictions in finite homogeneous plasma	33
3.3. Dependence of SBS reflectivity on electron density	35
3.4. Temporal evolution of SBS growth	35
3.5. SBS reflectivity with temporally varying pump pulse	37
3.6. Temporal evolution of SBS reflectivity in an inhomogeneous plasma	39
3.7. Spatial profiles of waves in homogeneous plasma and inhomogeneous plasma	40
4.1. Contour plots of laser flux and $\log(n_e/n_c)$	46
4.2. Temporal evolution of $n_e/n_c$ and $L_n$	47
4.3. Three-dimensional plots of electron density at early time in the laser pulse	49
4.4. Three-dimensional plots of $\log(n_e/0.01n_c)$	50
4.5. Contour plots of laser flux, $T_e$ , and $\log(n_e/n_c)$	52
4.6. Maximum electron temperature as a function of time	53
4.7. Plasma flow velocity vectors overlapped on contour plots of plasma pressure $\log(n_e T_e)$	55
4.8. Temporal evolution of velocity scale length $L_v$	56
4.9. Spatial profiles of $n_e/n_c$ , $T_e$ , $M$ , $\gamma_0$ , scale lengths ( $L_n$ , $L_v$ , and $L_T$ ), and phase mismatch $\kappa'$ (CASTOR predictions)	58
5.1. Schematic diagram of KrF laser system	62
5.2. Measured laser pulse shape and modeled Gaussian pulse	65

5.3.	Image of focal spot	66
5.4.	Histogram of focal spot energy fluence distribution	68
5.5.	Image of streaked focal spot	69
5.6.	Schematic diagram of experimental setup	72
6.1.	X-ray images of C, Al, and Au plasma	79
6.2.	X-ray intensities transmitted through Al filters	82
6.3.	Backscatter energy reflectivity for Al target	84
6.4.	Backscatter energy reflectivity for C target	85
6.5.	Backscatter energy reflectivity (C, Al, Au) at $45^\circ$	86
6.6.	Specular energy reflectivity for Al target	87
6.7.	An example of steady spectral shift	89
6.8.	An example of temporary varying spectral shift	89
6.9.	Intensity plots of incident and backscattered light and spectral shift as a function of time	90
6.10.	Intensity plots of incident and backscattered light (shifted and un-shifted components)	92
6.11.	Examples of time-resolved spectrum for Al targets	93
6.12.	Examples of time-resolved spectrum for Au targets	95
6.13.	Spectral shift measured at peak backscattering (C, Al)	97
6.14.	Spectral shift at $45^\circ$ (C, Al, and Au)	98
6.15.	Temporal change of spectral shift $d\lambda/dt$	100
7.1.	SBS reflectivity dependence on electron density	104
7.2.	Dependence of $\Gamma$ , $\gamma_s$ , $\gamma_{ib}$ , $\gamma_0$ and temperature on laser intensity	109
7.3.	Spectral shift as a function of the Mach number	113
7.4.	Frequency dependent part of the SBS growth rate $\gamma_k$	114
7.5.	SBS reflectivity for various plasma lengths	116

7.6.	SBS reflectivity for various electron densities	118
7.7.	Model of focal spot for hotspot analysis	125
7.8.	Two-level-intensity focal spot model	127
7.9.	Three-level-intensity focal spot model	129
7.10.	Details of three-level-intensity focal spot model	130
7.11.	Schematics of interacting wavevectors of DSBS	132
8.1.	Profiles of phase mismatch rate and SBS gain for inhomogeneous plasma	139
8.2.	CASTOR predictions of SBS red shift	145
8.3.	Comparison of dynamics of red shift between simulation and experimental data	146
8.4.	Measured red shift $\Delta\lambda(t)$ with relative scaling $I_L(t)^{0.22}$	148
8.5.	Measured red shift $\Delta\lambda(t)$ with relative scaling $I_L(t)^{1.0}$	149
8.6.	Spatial profiles of $\gamma_0$ for inhomogeneous plasma	152
8.7.	An example of SBS simulation results (coherent model)	155
8.8.	Coherent model calculations of SBS reflectivity	156
8.9.	Spatial profiles of SBS growth (coherent model)	158
8.10.	Relationship between SBS growth and $\gamma_0$ (coherent model)	159
8.11.	Effects of maximum density (coherent model)	160
8.12.	Incoherent model calculation procedure	163
8.13.	Incoherent model calculations of SBS reflectivity with constant $L_{coh}$	166
8.14.	Dependence of reflectivity on $L_{coh}$ and $L_n$	167
8.15.	Relationship between SBS growth and $\gamma_0$ (incoherent model)	168
8.16.	Effects of maximum density (incoherent model)	169
8.17.	Incoherent model calculations of SBS reflectivity with space dependent $L_{coh}$	171



8.18. Spatial profiles of $L_{coh}$ and SBS growth	172
8.19. Comparison among three SBS model calculations	175
8.20. Fitting of coherent model to the experimental data	177
8.21. Fitting of incoherent model to the experimental data	178
A4.1. Streaked image of original laser light	200
A4.2. Streaked image of transmitted light (CHCl target, 386mJ)	201
A4.3. Streaked image of transmitted light (CHCl target, 820mJ)	202
A4.4. Streaked image of transmitted light (Al 3 $\mu$ m target)	203
A4.5. Streaked image of transmitted light (Al 9 $\mu$ m target)	204
A4.6. Streaked image of transmitted light (Al 9 $\mu$ m target) showing partial burnthrough	205
A4.7. Intensity threshold of filamentations and relationship between perturbation wavenumber and growth length	209

## I. Introduction

### 1.1. Motivation

One of the critical issues in laser-driven fusion<sup>1)</sup> is the problem of laser-beam propagation and absorption in plasmas. A variety of parametric instabilities<sup>2)</sup> which can modify laser energy coupling and transport properties may occur in under-critical density plasmas, where electron density  $n_e < n_c$  ( $n_c = m_e \omega_0^2 / (4\pi e^2)$  is the critical density,  $m_e$  is electron mass,  $\omega_0$  is laser frequency,  $e$  is electron charge). Stimulated Brillouin scattering (SBS) is one such instability, which occurs when intense laser light interacts with ion acoustic waves in plasmas<sup>3)</sup>. SBS may severely reduce the absorption efficiency in plasmas by reflecting the incident light before it is absorbed<sup>4-6)</sup>.

A large quantity of literature is available on theoretical treatments of SBS<sup>2-4,7-36)</sup> and experimental results of (mainly long wavelength  $10\mu\text{m}$  or  $1\mu\text{m}$ ) laser-produced plasmas<sup>5,6,37-69)</sup>. Experimentally observed SBS-levels have, however, remained substantially below predictions of simple theoretical models of Brillouin scattering. The growth and saturation, characteristics of SBS, especially in the nonlinear regime<sup>4,19,25,34-36)</sup> are extremely complex and are not completely understood.

In recent laser fusion research<sup>68)</sup>, shorter wavelength lasers ( $\lambda < 1\mu\text{m}$ ) have attracted a great deal of attention because of increased energy absorption<sup>70)</sup>, reduced hot electron generation and target preheat and increased ablation rates and pressure. The KrF laser, especially, has become one of the primary candidates for a fusion driver, because of its potential for scaling to high energy at high

electrical efficiency.

Under these circumstances, studies of SBS in KrF laser-produced plasmas are required because of : a) the general lack of quantitative agreement between theoretical predictions and experiments for longer wavelength lasers, b) limited experimental results in short wavelength laser-produced plasmas, c) the importance to basic nonlinear plasma physics, and d) the importance to laser-driven inertial confinement fusion.

### 1.2. Early Work in Stimulated Brillouin Scattering

Early theoretical work by Nishikawa<sup>2)</sup> provided a general picture of electron and ion wave instabilities as a parametric process of coupled oscillators. He derived the threshold and growth rates for homogeneous infinite plasma. Rosenbluth<sup>7,8)</sup> extended the treatment for inhomogeneous plasma by solving the WKB coupled mode equations for the electromagnetic and electrostatic waves. Pesme et al.<sup>9)</sup> modeled the excitation of parametric instabilities in finite plasma, where wave damping and inhomogeneity effects were taken into account. Drake et al.<sup>3)</sup>, using the plasma fluid equations, derived a general dispersion relation for electron and ion wave. Analytical work by Forslund et al.<sup>4)</sup> extensively investigated stimulated Brillouin and Raman scattering in both kinetic and fluid limits and also numerically studied the instabilities. Cohen et al.<sup>12)</sup> treated the problem with a Green's function formulation. These basic theoretical works and early experimental data were reviewed by Offenberger.<sup>50)</sup>

More recently, double stimulated Brillouin scattering (DSBS) has been proposed by Zozulya et al.<sup>20,30)</sup>. This mechanism leads to

increased backward reflection without any assumption about the fixed spontaneous level of density fluctuation, which corresponds to an absolute instability for oblique incidence of radiation on a plasma layer.

A wide variety of SBS experiments have been carried out on targets ranging in  $Z$  from hydrogen gas to solid gold, in laser wavelength from 10 to  $0.25\mu\text{m}$ , and laser intensity from  $10^{10}$  to  $10^{16}$   $\text{W}/\text{cm}^2$ . Since SBS occurs in the underdense region ( $n_e < n_c$ , where  $n_e$  and  $n_c$  are electron density and critical density), gas targets or pre-formed low density targets were preferentially used in experiments rather than solid targets<sup>37-39,42,45,46,48</sup>). For solid targets, the pre-formed plasmas were generated by a prepulse preceding the main pulse<sup>40,44,51</sup>) or by an independent beam which is directed anti-parallel<sup>63</sup>) or perpendicular<sup>60</sup>) to the main beam. By adjusting the time interval between the two beams or the energy level of the preceding beam, one could control the plasma parameters. Foam targets or thin foils were also used to make underdense plasmas<sup>62,69</sup>). Tilting the solid target from the laser axis was another technique to control the plasma<sup>40,58,65</sup>), which was equivalent to changing the plasma scale length and density (changing the turning point of the laser).

Experimental investigations of the SBS process usually involve the measurement of reflectivity as a function of laser intensity, because the motivation of experiments is to determine absorption loss relevant to laser fusion. Experiments on gas or pre-formed targets for  $\text{CO}_2$  and glass lasers<sup>57</sup>) showed backscatter SBS reflectivities of 0.2% to 98% for focused laser intensities of  $10^{10}$  to  $10^{16}$   $\text{W}/\text{cm}^2$ . Experiments on solid and foam targets for  $1\mu\text{m}$ <sup>66</sup>),  $0.53\mu\text{m}$ <sup>58,65</sup>),  $0.35\mu\text{m}$ <sup>62</sup>),  $0.25\mu\text{m}$ <sup>68</sup>)

lasers also showed SBS reflectivities of 0.2 to 20 % for the intensities of  $10^{12}$  to  $10^{16}$  W/cm<sup>2</sup>. A wide variety of plasma conditions, as well as different laser pulse characteristics, have thus yielded a wide range of SBS reflectivities.

Various kinds of spectra have been observed experimentally. The spectral features vary markedly depending on laser wavelength and intensity, target material and geometry, and laser angle of incidence and direction of scattering. In CO<sub>2</sub> laser experiments on magnetically confined low density plasma (R.Fedosejevs et al.<sup>49)</sup>, good agreement was found between the experimental spectrum and the theoretical profile calculated using the frequency dependent growth rate<sup>37)</sup>. An interesting spectrum with two peaks separated from the nominal ion acoustic frequency by the bounce frequency of the oscillating trapped ions was observed by J.Handke et al.<sup>56)</sup>. In the experiment done by G.R.Mitchel<sup>52)</sup>, solid targets were obliquely irradiated by high intensity CO<sub>2</sub> laser radiation. It was observed that the SBS spectra for backscatter and near specular directions showed different frequency shifts. In glass laser experiments, broader SBS spectra were observed under higher intensity irradiance by R.E.Turner<sup>44)</sup>, suggesting strong pump wave dominated SBS. An interesting comparison was presented by D.W.Phillion<sup>41)</sup>, in which red-shifted spectra were observed for spherical targets (glass microballoons), whereas blue-shifted spectra were observed for plane disk targets. The balance of the Doppler shift due to plasma expansion and that due to ion waves seems to depend on target geometry. In the 0.53 $\mu$ m laser experiment performed by W.C.Mead et al.<sup>58)</sup>, target tilt angle and material dependence of the backscattered spectra were demonstrated. Tilting targets resulted in

reduced Doppler blue-shift, and low Z targets showed a blue-shifted plateau in the spectrum, whereas high Z targets showed mainly a single broad red-shifted peak. A comparison of SBS spectra for solid and underdense foam targets irradiated by  $0.35\mu\text{m}$  laser was presented by K.A.Tanaka et al.<sup>62)</sup>. Differences in spectra were explained by the existence of a critical surface and different densities in the interaction region.

Since the amplitude of the Thomson scattered light from a plasma is proportional to the square of the density fluctuations, it can be used to investigate ion fluctuations caused by SBS. Several researchers have performed experiments by this technique with ruby laser ( $\lambda=0.694\mu\text{m}$ ) as a probe beam<sup>53-55,64,67,71)</sup>. These investigations, however, have been limited to  $\text{CO}_2$  laser experiments because the wavelength of the probe beam must be much shorter than that of the main beam (to minimize absorption and refraction). Good correlation between the density fluctuation and the SBS reflectivity, which showed saturation at higher intensity, was demonstrated. Similar trends have been observed in most experiments.

When experiments are done on solid targets in which the laser or plasma parameters vary rapidly, resulting in a time-dependent mode structure for the SBS, time-resolved measurements are required to give us better information. Time-resolved backscatter and Thomson scattering measurements of SBS and ion density fluctuations driven by SBS were made in experiments using a  $10\mu\text{m}$  laser by J.Handke et al.<sup>56)</sup>, C.J.Walsh et al.<sup>53)</sup>, C.R.Giles et al.<sup>54)</sup>, J.E.Bernard et al.<sup>64)</sup>, and H.A.Baldis<sup>57)</sup>;  $1\mu\text{m}$  laser by D.R.Gray et al.<sup>43)</sup> and R.E.Turner et al.<sup>47)</sup>;  $0.53\mu\text{m}$  laser by G.P.Banfi<sup>65)</sup>, and  $0.53\mu\text{m}$  and  $0.26\mu\text{m}$  lasers by

C.Labaune et al.<sup>63)</sup>. In one CO<sub>2</sub> laser experiment<sup>57)</sup>, several quite distinct lines of the red-shifted component were observed at higher laser intensity, each appearing later in time as the shift increased. In a glass laser experiment<sup>43)</sup>, on the other hand, a short burst of blue shifted light was observed occurring very early in the incident pulse, followed by a long, red-shifted component which generally lasted throughout the incident pulse. The two components were observed to occur at different times. In the 0.53 $\mu$ m laser experiment<sup>65)</sup>, spiking behavior in time and wavelength were observed at low intensity and reflectivity. In the 0.26 $\mu$ m laser experiment<sup>63)</sup>, a red shift increasing in time (which is a Doppler shift related to the target motion) was observed for a thin foil target. This is due to a strong specular reflection from the critical surface; SBS backscatter was relatively too weak to be detected. For a pre-formed target, a red shift constant in time related to pure Brillouin backscattering was observed. In this case a pre-formed plasma was generated by a beam directed anti-parallel to the main beam.

When the experimental conditions do not permit analytical calculations, numerical simulation becomes a powerful tool to investigate the phenomena; a numerical code is used to solve the basic coupling equations (with or without accounting for laser propagation and hydrodynamics). The plasma scale length dependence of SBS reflectivity (quantitatively applicable to the convective instability) has been widely studied. Lower than expected levels of reflection in experiments have been explained by a variety of saturating mechanisms such as light wave damping<sup>72,73)</sup>, anisotropy<sup>74)</sup>, plasma density<sup>73)</sup>, and harmonic generation<sup>75)</sup>. It may be that many of these mechanisms occur

simultaneously. Absolute instabilities have also been studied in the form of the time history of the scattered light. J.A.Heikkinen et al.<sup>75)</sup> investigated the absolute instability in the presence of second harmonic generation. K.Baumgärtel et al.<sup>18)</sup>, and C.J.Randall et al.<sup>29)</sup> investigated the absolute instability taking into account reflected light from the critical density layer or density steepening in underdense plasma. The intensity dependence of reflectivity was studied by M.S.Sodha et al.<sup>22)</sup>, who showed that temporal non-uniformity of the pump wave leads to an optimum value of intensity at which the growth rate is maximum. SBS in inhomogeneous flowing plasma was studied by R.L.Berger<sup>27)</sup>, who presented thresholds in practical units and angular dependence of the wavelength shift for ease of comparison with experimental results. Another approach involved a fluid code simulation to which simple equations or scalings of SBS models were adapted. Intensity and wavelength scaling of SBS were investigated by K.Estabrook et al.<sup>76)</sup>, using the LASNEX fluid code, which showed lower SBS levels are expected for shorter wavelength lasers.

In summary, experimental results are many and varied, being highly dependent on laser/target conditions. Solid target experiments generally suffer from strong gradients in plasma parameters that make detailed quantitative comparison with theory more difficult. As a consequence, quantitative agreement between theory and experiment has generally been more satisfactory for gas target experiments.

### **1.3. Objective of This Work**

Although a wide variety of theoretical and numerical predictions and experimental results have been accumulated, general quantitative



agreement between theory and experiment is still lacking. This quantitative understanding of SBS is necessary for engineering application (e.g. laser fusion). Unfortunately, for short wavelength lasers which are the primary candidates for a fusion driver, very few experimental results exist.

One of the goals of this study is to establish a good SBS database for KrF laser-produced plasmas, including backscattered spectra and reflectivity, time-dependent characteristics, and evidence for the nature of the instability (absolute or convective). Numerical and analytical modeling has been also pursued to enable comparison with the experimental data. These results should contribute to an increased understanding of nonlinear laser/plasma physics and the significance of SBS in using the short wavelength KrF laser as an ICF driver.

Chapter 2 summarizes theoretical results used to analyze the experimental data. Details of numerical modeling of SBS are described in chapter 3. Results for homogeneous plasma are presented here. Results of two-dimensional hydrodynamic simulations, which characterize our laser/plasma conditions, are provided in chapter 4. These numerical results are used to guide interpretation of experimental data. Experimental methods are described in chapter 5. Characteristics of the KrF laser facility are reviewed here. The experimental results, which include measurements of x-ray images, electron temperature, and reflectivity and time-resolved spectrum of backscattered light, are presented in chapter 6. Detailed discussions of experimental results are presented in chapter 7 and 8. Chapter 7 contains analytical modeling of SBS for homogeneous plasma, whereas chapter 8 presents analytical and numerical modeling for inhomogeneous

plasma. Chapter 9 provides a conclusion for this work and suggestions for follow-up studies.

### Bibliography

- 1) C.H.Stickly, Phys.Today, 50, (May 1978).
- 2) K.Nishikawa, Jpn.Phys.Soc., 24, 916, 1154 (1968).  
K.Mima and K.Nishikawa, in *Handbook of Plasma Physics*, edited by A.A.Galeev and R.N.Sudan (North Holland Publishing Company, 1984), vol.2, p.452.
- 3) J.F.Drake, P.K.Kaw, Y.C.Lee, G.Schmidt, C.S.Liu, and M.N.Rosenbluth, Phys.Fluids, 17, 778 (1974).
- 4) D.W.Forslund, J.M.Kindel, and E.L.Lindman, Phys.Fluids, 18, 1002 (1975).  
D.W.Forslund, J.M.Kindel, and E.L.Lindman, Phys.Fluids, 18, 1017 (1975).
- 5) L.M.Goldman, J.Sources, and M.J.Lubin, Phys.Rev.Lett., 31, 1184 (1973).
- 6) C.Yamanaka, T.Yamanaka, T.Sasaki, J.Mizui, and H.B.Kang, Phys.Rev.Lett., 32, 1038 (1974).
- 7) M.N.Rosenbluth, Phys.Rev.Lett., 29, 565 (1972).
- 8) M.N.Rosenbluth, R.B.White, and C.S.Liu, Phys.Rev.Lett., 31, 1190 (1973).
- 9) D.Pesme, G.Laval, and R.Pellat, Phys.Rev.Lett., 31, 203 (1973).
- 10) D.R.Nicholson and A.L.Kauffman, Phys.Rev.Lett., 33, 1207 (1974).
- 11) D.F.DuBois, D.W.Forslund, and E.A.Williams, Phys.Rev.Lett., 33, 1013 (1974).
- 12) B.I.Cohen and C.E.Max, Phys.Fluids, 22, 1115 (1979).
- 13) W.L.Kruer, Phys.Fluids, 23, 1273 (1980).
- 14) T.Speziale, J.F.McGrath, and R.L.Berger, Phys.Fluids, 23, 1275 (1980).
- 15) C.J.Randall, J.R.Albritton, and J.J.Thomson, Phys.Fluids, 24, 1474 (1981).

- 16) G.R.Mitchel, T.W.Johnston, and B.Grek, Phys.Fluids, 25, 186(1982).
- 17) T.W.Johnston, G.R.Mitchel, and B.Grek, Phys.Fluids, 25, 179(1982).
- 18) K.Baumgärtel and K.Sauer, Phys.Rev.A, 26, 3031 (1982).
- 19) V.P.Silin and V.T.Tikhonchuk, Sov.Phys.JETP, 56, 765 (1982).
- 20) A.A.Zozulya, V.P.Silin, and V.T.Tikhonchuk, JETP Lett., 38, 52 (1983).
- 21) A.Ramani and C.E.Max, Phys.Fluids, 26, 1079 (1983).
- 22) M.S.Sodha, K.Ramamurthy, P.K.Malhorta, and R.P.Sharma, Phys.Rev.A, 23, 1098 (1983).
- 23) C.Montes, Phys.Rev.Lett., 50, 1129 (1983).
- 24) R.L.Berger, Phys.Rev.Lett., 51, 1554 (1983).
- 25) W.Rozmus, Y.Al-Shiraida, and A.A.Offenberger, Phys.Fluids, 27, 589 (1984).
- 26) G.R.Mitchel, T.W.Johnston, and H.Pepin, Phys.Fluids, 27, 1527 (1984).
- 27) R.L.Berger, Phys.Fluids, 27, 1796 (1984).
- 28) T.Speziale, Phys.Fluids, 27, 2583 (1984).
- 29) C.J.Randall and J.R.Albritton, Phys.Rev.Lett., 52, 1887 (1984).
- 30) A.A.Zozulya, V.P.Silin, and V.T.Tikhonchuk, Sov.Phys.JETP, 59, 756 (1984).
- 31) O.P.Zaskal'ko, A.A.Zozulya, Yu.I.Kyzylasov, N.B.Panaitoi, V.P.Silin, V.T.Tikhonchuk, and I.L.Fabelinskii, Sov.Phys.JETP, 60, 906 (1984).
- 32) V.P.Silin, V.T.Tikhonchuk, and M.V.Chegotov, Sov.J.Plasma Phys., 12, 204 (1986).
- 33) M.V.Chegotov, V.P.Silin, V.T.Tikhonchuk, and A.A.Zozulya, Plasma Phys.& Controlled Fusion, 28, 413 (1986).
- 34) W.Rozmus, R.P.Sharma, J.C.Samson, and W.Tighe, Phys.Fluids, 30, 2181 (1987).
- 35) H.A.Rose, D.F.DuBois, and B.Bezzerides, Phys.Rev.Lett., 58, 2547 (1987).
- 36) K.Baumgärtel and K.Sauer, "*Topics on Nonlinear Wave-Plasma Interaction*". (Birkhäuser Verlag, 1987).
- 37) A.A.Offenberger, M.R.Cervenak, A.M.Yam, and A.W.Pasternak J.Appl.Phys., 47, 1451 (1976).
- 38) J.J.Turechek and F.F.Chen, Phys.Rev.Lett., 36, 720 (1976).

- 39) R. Massey, K. Berggren, and Z. A. Pietrzyk, *Phys. Rev. Lett.*, **36**, 963 (1976).
- 40) B. H. Ripin, F. C. Young, J. A. Stamper, C. M. Armstrong, R. Decoste, E. A. McLean, and S. E. Bodner, *Phys. Rev. Lett.*, **39**, 611 (1977).
- 41) D. W. Phillion, W. L. Kruer, and V. C. Rupert, *Phys. Rev. Lett.*, **39**, 1529 (1977).
- 42) Z. A. Pietrzyk and T. N. Carlstrom, *Appl. Phys. Lett.*, **35**, 681 (1979).
- 43) D. R. Gray, J. Murdoch, S. M. L. Sim, A. J. Cole, R. G. Evans, and W. T. Toner, *Plasma Phys.*, **22**, 967 (1980).
- 44) R. E. Turner and L. M. Goldman, *Phys. Rev. Lett.*, **44**, 400 (1980).
- 45) F. G. Mayer, G. E. Busch, C. M. Kinzer, and K. G. Estabrook, *Phys. Rev. Lett.*, **44**, 1498 (1980).
- 46) A. A. Offenberger and A. Ng, *Phys. Rev. Lett.*, **45**, 1189 (1980).
- 47) R. E. Turner and L. M. Goldman, *Phys. Fluids*, **24**, 184 (1981).
- 48) J. Handke, S. A. H. Rizvi, and B. Kronast, *Appl. Phys.*, **25**, 109 (1981).
- 49) R. Fedosejevs, W. Tighe, D. C. D. McKen, and A. A. Offenberger, *Opt. Comm.*, **40**, 35 (1981).
- 50) A. A. Offenberger, *Mod. Plasma Phys.*, 437(1981).
- 51) R. Decoste, P. Lavigne, G. R. Mitchel, and J. C. Kieffer, *J. Appl. Phys.*, **53**, 3505(1982).
- 52) G. R. Mitchel, B. Grek, T. W. Johnston, H. Pepin, P. Church, P. Lavigne, F. Martin, and R. Decoste, *Phys. Rev. Lett.*, **48**, 1472 (1982).
- 53) C. J. Walsh and H. A. Baldis, *Phys. Rev. Lett.*, **48**, 1483 (1982).
- 54) R. Giles and A. A. Offenberger, *Phys. Rev. Lett.*, **50**, 421 (1983).
- 55) C. E. Clayton, C. Joshi, and F. F. Chen, *Phys. Rev. Lett.*, **51**, 1656 (1983).
- 56) J. Handke, S. A. H. Rizvi, and B. Kronast, *Phys. Rev. Lett.*, **51**, 1660 (1983).
- 57) H. A. Baldis, *Plasma Phys.*, **25**, 1297(1983).
- 58) W. C. Mead, E. M. Campbell, K. G. Estabrook, R. E. Turner, W. L. Kruer, P. H. Y. Lee, B. Pruett, V. C. Rupert, K. G. Tirsell, G. L. Stradling, F. Ze, C. E. Max, M. D. Rosen, and B. F. Lasinski, *Phys. Fluids*, **26**, 2316(1983).
- 59) H. A. Baldis and C. J. Walsh, *Phys. Fluids*, **26**, 3426 (1983).
- 60) C. J. Walsh, D. M. Villeneuve, and H. A. Baldis, *Phys. Rev. Lett.*, **53**, 1445 (1984).
- 61) T. Speziale, *Phys. Fluids*, **27**, 2583(1984).

- 62) K.A. Tanaka, B. Boswell, R.S. Craxton, L.M. Goldman, F. Guglielmi, W. Seka, R.W. Short, and J.M. Sources, *Phys. Fluids*, **28**, 2910 (1985).
- 63) C. Labaune, E. Fabre, A. Michard, and F. Briand, *Phys. Rev. A*, **32**, 577 (1985).
- 64) J.E. Bernard and J. Meyer, *Phys. Rev. Lett.*, **55**, 79 (1985).
- 65) G.P. Banfi, *Z. Phys. B. - Condensed Matter*, **62**, 51 (1985).
- 66) J.H. Gardner, M.J. Herbst, F.C. Young, J.A. Stamper, S.P. Obenschain, C.K. Manka, K.J. Kearney, J. Grun, D. Duston, and P.G. Burkhalter, *Phys. Fluids*, **29**, 1305 (1986).
- 67) J.E. Bernard and J. Meyer, *Phys. Fluids*, **29**, 2313 (1986).
- 68) A.A. Offenberger, P.D. Gupta, R. Popil, and Y.Y. Tsui, *Laser & Particle Beams*, **4**, 329 (1986).  
A.A. Offenberger, J. Santiago, M. Fujita, R. Fedosejevs, and W. Rozmus, *Laser & Particle Beams*, **8**, 153 (1990).
- 69) H. Figueroa, C. Joshi, and C.E. Clayton, *Phys. Fluids*, **30**, 586 (1987).
- 70) P. Mora, *Phys. Fluids*, **25**, 1051 (1982).
- 71) J. Meyer and J.E. Bernard, *Phys. Fluids*, **28**, 2618 (1985).
- 72) T. Speziale, *Phys. Fluids*, **25**, 389 (1982).
- 73) J.A. Heikkinen, S.J. Karttunen, and R.R.E. Salomaa, *Phys. Fluids*, **27**, 707 (1984).
- 74) T. Speziale, R.L. Berger, *Phys. Rev. Lett.*, **46**, 33 (1981).
- 75) J.A. Heikkinen, S.J. Karttunen, and R.R.E. Salomaa, *Phys. Lett. A*, **101**, 217 (1984).
- 76) K. Estabrook, J. Harte, E.M. Campbell, F. Ze, D.W. Phillion, M.D. Rosen, and J.T. Larsen, *Phys. Rev. Lett.*, **46**, 724 (1981).

## II. Theory

In this chapter, theoretical descriptions of stimulated Brillouin scattering are reviewed and summarized with emphasis on those aspects relevant to the interpretation of experimental results. Analytical equations are presented that are important for giving physical insight to the SBS process (threshold, growth rate, etc.). Since, in general, the coupled equations cannot be solved analytically, it is necessary to use numerical methods, these will be discussed in the following chapter. Collisional and Landau damping of the ion wave are both important and thus are discussed here. Source of noise from which instability can grow are also briefly reviewed here.

### 2.1. Coupling of Three Waves

Stimulated Brillouin scattering is a three-wave interaction process through which a high-intensity electromagnetic (pump) wave can decay into an ion acoustic wave and another (scattered) electromagnetic wave. The ion acoustic wave characterizes a density perturbation ( $\delta n/n$ ) in the plasma. A resonant interaction occurs for waves satisfying

$$\omega_0 = \omega_1 + \omega_s \quad (2.1)$$

$$\underline{k}_0 = \underline{k}_1 + \underline{k}_s \quad (2.2)$$

where subscripts 0, 1, s refer to the pump, scattered and sound (ion acoustic) waves, respectively;  $\omega$  is the angular frequency and  $\underline{k}$  is the wave number vector. Each wave satisfies dispersion relations

$$\omega_{0,1}^2 = \omega_{pe}^2 + k_{0,1}^2 c^2 \quad (2.3)$$

$$\omega_s^2 = k_s^2 c_s^2 \quad (2.4)$$

where  $\omega_{pe}$  ( $= (4\pi n_e e^2/m)^{1/2}$ ) is the electron plasma frequency and  $c_s$  ( $= [(ZT_e + 3T_i)/M_i]^{1/2}$ ) is the sound velocity.

The coupling of these three waves is described by second order (space and time) partial differential equations which can be derived from Maxwell and fluid equations. This set of equations includes nonlinearity of the coupling of the linearly excited waves and pump waves<sup>1,2)</sup>.

$$\left( \frac{\partial^2}{\partial t^2} + 2\gamma_{A0} \frac{\partial}{\partial t} + \omega_{pe}^2 - c^2 \frac{\partial^2}{\partial x^2} \right) \mathbf{A}_0 = -\omega_{pe}^2 \frac{n_e}{N_0} \frac{\mathbf{A}_1^*}{2} \quad (2.5a)$$

$$\left( \frac{\partial^2}{\partial t^2} + 2\gamma_{A1} \frac{\partial}{\partial t} + \omega_{pe}^2 - c^2 \frac{\partial^2}{\partial x^2} \right) \mathbf{A}_1 = -\omega_{pe}^2 \frac{n_e}{N_0} \frac{\mathbf{A}_0^*}{2} \quad (2.5b)$$

$$\left( \frac{\partial^2}{\partial t^2} + 2\gamma_p \frac{\partial}{\partial t} - \gamma v_e^2 \frac{\partial^2}{\partial x^2} \right) n_e + \omega_{pe}^2 (n_e - n_i) = \frac{e^2 N_0}{2 m_e^2 c^2} \frac{\partial^2}{\partial x^2} \mathbf{A}_0 \cdot \mathbf{A}_1^* \quad (2.5c)$$

$$\frac{\partial^2 n_i}{\partial t^2} - 3v_1^2 \frac{\partial^2 n_i}{\partial x^2} + \omega_{pi}^2 (n_i - n_e) = 0 \quad (2.5d)$$

where  $\omega_{pi}$  ( $= (4\pi n_i Z^2 e^2/M_i)^{1/2}$ ) is ion plasma frequency;  $\gamma_A$  and  $\gamma_p$  are the damping rates of light and sound waves (phenomenologically introduced);  $\gamma$  is the ratio of specific heats for electrons;  $m_e$  and  $M_i$  are electron and ion mass;  $v_e$  ( $= (T_e/m_e)^{1/2}$ ) and  $v_i$  ( $= (T_i/M_i)^{1/2}$ ) are thermal velocities of electrons and ions,  $v_0$  ( $= eE_0/m\omega_0$ ) is the oscillating velocity of an electron in the electric field of the pump wave; and  $\mathbf{A}_0$  and  $\mathbf{A}_1$  are vector potentials of pump and scattered EM waves ( $\mathbf{A} = A \cdot \exp(i\omega t - ikx)$ ,  $A = -cE/\omega$ , or  $c \cdot \mathbf{E} = -\partial/\partial t \cdot \mathbf{A}$ .  $\mathbf{E}$  is the wave electric field). The electron density  $N_e$  is given as  $N_e = N_0 + n_e$ , where  $n_e$  is the local perturbed density.

This set of coupled equations can be reduced to a set of

first-order equations for the approximation of slow amplitude variation:

$$\left( \frac{\partial}{\partial t} + v_g \frac{\partial}{\partial x} + \gamma_{ib} + \frac{1}{2} \frac{v_g}{k_0} \frac{\partial k_0}{\partial x} \right) a_0 = - \frac{1}{4} \frac{\omega_{pe}^2}{\omega_0^2} \cdot a_1 \cdot n \quad (2.6a)$$

$$\left( \frac{\partial}{\partial t} - v_g \frac{\partial}{\partial x} + \gamma_{ib} + \frac{1}{2} \frac{v_g}{k_1} \frac{\partial k_1}{\partial x} \right) a_1 = \frac{1}{4} \frac{\omega_{pe}^2}{\omega_1^2} \cdot n^* \cdot a_0 \quad (2.6b)$$

$$\left( \frac{\partial}{\partial t} + c_s \frac{\partial}{\partial x} + \gamma_s + \frac{1}{2} \frac{c_s}{k_s} \frac{\partial k_s}{\partial x} \right) n = \frac{1}{4} Z \frac{m_e}{M_1} \frac{k_s^2 v_0^2}{\omega_s^2} \cdot a_1^* \cdot a_0 \quad (2.6c)$$

Here,  $v_g (= c \cdot (1 - n_e/n_c)^{1/2})$  and  $c_s$  are the group velocities of light and sound in the plasma,  $\gamma_{ib}$  and  $\gamma_s$  are the inverse bremsstrahlung absorption rate and ion acoustic wave damping rate, respectively.  $a_0 = A_0(x,t)/A_0(0,0)$ ,  $a_1 = A_1(x,t)/A_0(0,0)$ , and  $n = n_i/N_0$  is the density fluctuation. It is assumed that  $\omega_0 \approx \omega_1$ ,  $k_0 \approx k_1$ .

## 2.2. Instability Threshold Criteria, Growth Rate and Region of Applicability

It is helpful to briefly summarize analytical results for laser intensity threshold and growth rate for the SBS instability in various plasma conditions.

For laser intensity  $I_0$ , the associated field strength  $E_0$  is given by

$$\frac{E_0^2}{8\pi} c = I_0 \quad (\text{CGS units}) \quad (2.7)$$

for linearly polarized wave and the oscillating velocity of an electron in the pump field  $E_0$  is given by

$$\begin{aligned} v_0 &= \frac{eE_0}{m\omega_0} \propto \lambda_0 I_0^{1/2} \\ &= 25.6 (I \lambda^2)^{1/2} \quad (\text{cm/s}) \end{aligned} \quad (2.8)$$

where  $I$  is in  $\text{W/cm}^2$ ,  $\lambda$  in  $\mu\text{m}$ . The intensity threshold for the



instability is usually described in terms of  $v_0$  ( which removes the dependence on wavelength ) rather than  $I_0$  itself.

Assuming time dependence of the form  $e^{i\omega t}$ , solution of eqs.2.6 gives a threshold condition (for  $Im\omega=0$ ),

$$\gamma_0^2 > \gamma_s \cdot \gamma_{1b} \quad (2.9)$$

which reflects a balance between growth rate  $\gamma_0$ , which is specified later, and damping  $\gamma_s$  and  $\gamma_{1b}$ .

a) For infinite homogeneous plasma, eq.2.9 for absolute instability reduces to an equivalent threshold of<sup>1)</sup>

$$\frac{v_0^2}{v_e^2} > 4 \frac{\gamma_s}{\omega_s} \frac{\nu_{ei}}{\omega_0} \quad (2.10)$$

with growth rate given by

$$\gamma_0 = \frac{1}{2} \frac{v_0}{c} \left( \frac{\omega_0}{\omega_s} \right)^{1/2} \omega_{pi} \left( 1 - \frac{n_e}{n_c} \right)^{1/2} \quad (2.11)$$

where,  $\nu_{ei}$  ( =  $4 (2\pi)^{1/2} e^4 Z n_e \ln\Lambda / 3 m_e^{1/2} T_e^{3/2}$  ) is the electron-ion collision frequency.

b) For inhomogeneous plasma, convective instability is predicted, if conditions<sup>3)</sup>

$$2 \gamma_0 > \left( \frac{\gamma_{1b}}{v_g} + \frac{\gamma_s}{c_s} \right) \cdot (v_g c_s)^{1/2} \quad (2.12)$$

and

$$G = \frac{2\pi\gamma_0^2}{|\kappa'| |v_g c_s|} > 1 \quad (2.13)$$

are satisfied. In this situation, the gain is limited to  $e^G$ .  $\kappa'$  is the space derivative of wavenumber mismatch  $\underline{\kappa}$  ( =  $\underline{k}_0 - \underline{k}_1 - \underline{k}_s$  ) where  $\underline{k}_{0,1,s}$  is determined by the local dispersion relation in the

inhomogeneous plasma. For a linear phase mismatch in space ( $\kappa = \kappa'x$ ), from eqs. (2.3) and (2.4),  $\kappa'$  is given by<sup>3)</sup>

$$\kappa' = k_0 \cdot \left( \frac{\frac{2}{L_v} - \frac{1}{L_T}}{1 - M} + \frac{n_e}{n_c} \cdot \left( 1 - \frac{n_e}{n_c} \right)^{-1} \cdot \frac{1}{L_n} \right) \quad (2.14)$$

for  $k_s \approx 2k_0$ , where  $M$  is the Mach number, and  $L_v$ ,  $L_T$ , and  $L_n$  are scale length of velocity, temperature and electron density, defined as  $L_v = [(dv/dx)/c_s]^{-1}$ ,  $L_T = [(dT/dx)/T]^{-1}$ , and  $L_n = [(dn/dx)/n]^{-1}$ . If both wave damping and plasma inhomogeneity are allowed in a finite length plasma, the effective growth rate can be shown to be<sup>4)</sup>

$$\gamma_{1h} = \left[ \frac{2\gamma_0}{(v_g c_s)^{1/2}} \left( 1 - \frac{1}{\pi^{1/2} \lambda^{2/3}} \right) - \left( \frac{\gamma_{1b}}{v_g} + \frac{\gamma_s}{c_s} \right) \right] \cdot \left( \frac{v_g c_s}{v_g + c_s} \right) \quad (2.15)$$

where  $\lambda = \gamma_0^2 / |\kappa' v_g c_s|$ . The effects of plasma inhomogeneity will be discussed in detail in chapters 4 and 8, since the phase mismatch is a dominant factor in determining the SBS level.

c) For finite homogeneous plasma, both absolute and convective instability can occur. In the case of weak damping, the criteria are given by<sup>5)</sup>

$$\begin{aligned} \frac{\gamma_0 L}{(v_g c_s)^{1/2}} &> \pi/2 && ; \text{ absolute} \\ &< \pi/2 && ; \text{ convective} \end{aligned} \quad (2.16)$$

Here,  $L$  is set by the finite length, which is determined by plasma inhomogeneity or by the plasma size. In the case of strong damping, (i.e.,  $\frac{\gamma_s}{\gamma_0} (v_g/c_s)^{1/2} \gg 1$ ), only convective instability is expected and the spatial gain in length  $L$  is<sup>1)</sup>

$$G_L = \frac{2 \gamma_0^2 L}{\gamma_s v_g} \quad (2.17)$$

or equivalently<sup>6)</sup>

$$G_L = \frac{1}{4} \frac{\omega_p^2}{\omega_0^2} \frac{v_0^2}{v_e^2} \frac{\omega_s}{2\gamma_s} k_0 L \quad (2.18)$$

Even in inhomogeneous plasma, this criterion is applicable if damping dominates inhomogeneity<sup>5)</sup>

$$\frac{\gamma_s}{|\kappa'| c_s} > L \quad (2.19)$$

If pump wave absorption  $\gamma_{1b}$  is strong (and hence limits the gain length) and one can neglect pump depletion, eq.(2.15) can be rewritten as ( see appendix.1 )

$$G_L = \frac{\gamma_0^2}{\gamma_s} \frac{1}{\gamma_{1b}} ( 1 - \exp(-2\gamma_{1b} L/v_g) ) \quad (2.20)$$

These results will be used to analyze the experimental data; specifically, in considering the threshold and the absolute or convective nature of the instability.

### 2.3. Ion Acoustic Wave Damping

Proper estimation of ion wave damping is very important, since most of the gain and threshold calculations involve ion wave damping rate  $\gamma_s$ , as seen in the previous section. In this section, we review the effects of collisionality of plasma on the ion wave damping.

#### a) Collisional Damping

The effect of ion-ion collisions on the damping of ion acoustic waves has been studied by several authors<sup>7-10)</sup>. If  $k_s \lambda_{11} \ll 1$  ( $\lambda_{11}$  is the ion-ion collisional mean free path), or  $\bar{\lambda}_s \gg \lambda_{11}$  ( $\bar{\lambda}_s$  is the

wavelength of ion acoustic wave divided by  $2\pi$ ), a plasma model in the strongly collisional limit is applicable, for which an analytical expression of damping was obtained by Kuckes<sup>7)</sup>.  $\lambda_{11}$  is given by  $\lambda_{11} = v_i \cdot \tau_{11}$ , where  $\tau_{11}$  is the ion-ion collision time defined by Braginskii<sup>11)</sup>.

$$\tau_{11} = 4 \pi e^4 Z^4 n_i \ln \Lambda / 3 M_i^{1/2} T_i^{3/2} \quad (2.21)$$

A complication emerges when the plasma is moderately collisional, i.e.  $k_s \lambda_{11} \approx 1$ . In this regime, no analytical solution exists. Randall solved the linearized Fokker-Planck equation numerically and tabulated the results<sup>12)</sup>. Subsequently Casanova proposed an empirical expression for the damping rate<sup>13)</sup>.

#### b) Collisionless Damping (Landau Damping)

In the weakly collisional case,  $k_s \lambda_{11} \gg 1$ . Even without significant energy dissipation by collisions, the ion wave can be damped by transferring energy to particles (electron and ion)<sup>14,15)</sup>. By solving the collisionless Boltzmann equation (Vlasov equation), the ion Landau Damping is calculated to be

$$\frac{\gamma_s}{\omega_s} = \left( \frac{\pi}{8} \right)^{1/2} \left( \left( \frac{Zm}{M} \right)^{1/2} + \frac{ZT_e}{T_i} \frac{k_s c_s}{k_s v_i} \exp\left( - \frac{ZT_e}{2T_i} - \frac{3}{2} \right) \right) \quad (2.22)$$

Here the first ( $= \omega_{pe} / \omega_{pi}$ ) and the second terms on the right hand side correspond to interactions between ion wave and electrons and ion wave and ions, respectively. When the phase velocity of the ion wave  $v_\phi = \omega_s / k_s$  satisfies  $v_\phi \approx v_i$ , strong ion Landau damping occurs. It is noted that the second term in eq.2.22 is not applicable for the collisional plasma, since the wavelength of the sound wave is longer than the ion-ion collision mean free path. The first term in eq.2.22,

however, holds for the collisional plasma.

Figure 2.1 shows a comparison between Landau damping (eq.2.22) and semi-collisional damping (Casanova formula<sup>13</sup>) for Al plasma. The Landau damping was calculated by eq.2.22 with assumption of  $ZT_e/T_i = 11$  for comparison purposes (the formulae is not valid for the collisional plasma). The semi-collisional damping (includes both collisionless and collisional damping) as a function of temperature  $T$  ( $= T_e = T_i$ ) was calculated for  $n_e = 1.8 \times 10^{21} \text{ cm}^{-3}$  ( $0.1 \cdot n_c$  for KrF laser). For these parameters,  $k_s \lambda_{s11} \approx 0.3$  at  $T = 500 \text{ eV}$ . To achieve  $k_s \lambda_{s11} \gg 1$  (collisionless regime) at this temperature,  $n_e / n_c = 0.001$  ( $n_e \approx 2 \times 10^{19} \text{ cm}^{-3}$ ) would be required for KrF laser-produced plasma.

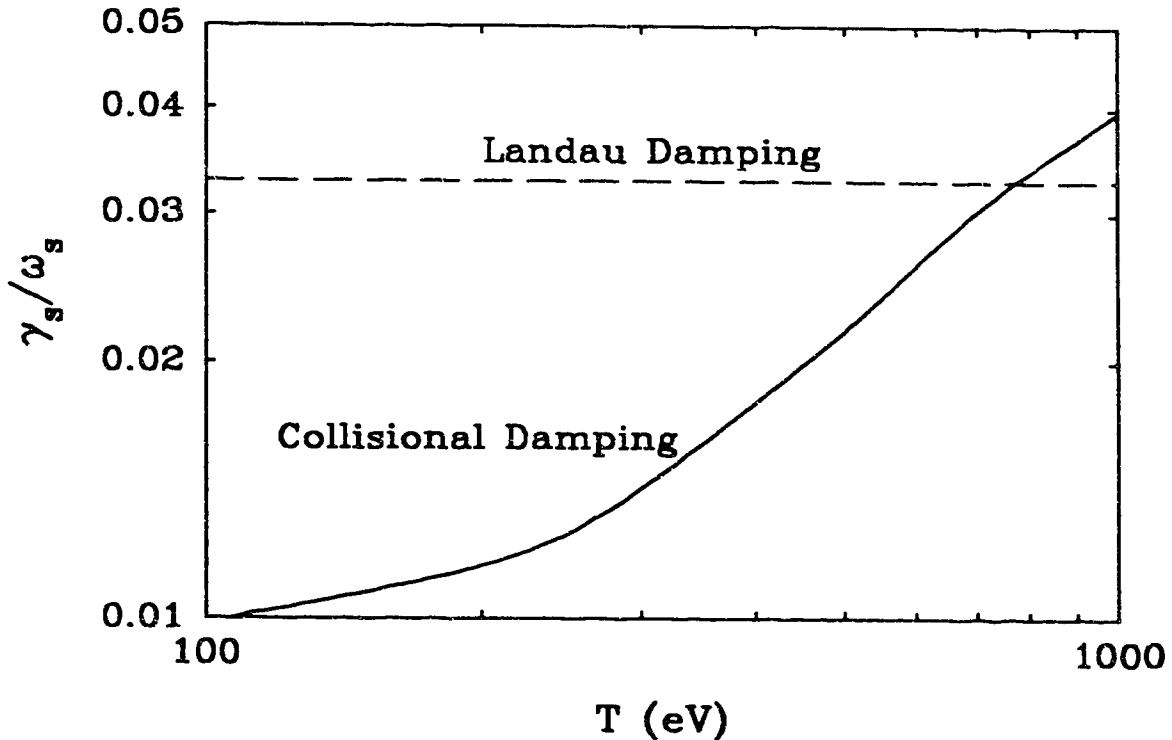


Fig.2.1. Ion acoustic wave damping in Al plasma.  $ZT_e/T_i = 11$ ,  $T = T_e = T_i$  were assumed. The dashed line shows level of Landau damping. The solid line shows dependence of semi-collisional damping on temperature at  $n_e = 1.8 \times 10^{21} \text{ cm}^{-3}$  ( $0.1 \cdot n_c$ ).

## 2.4. Spectral Feature of Scattered Light

SBS results in backscattered light slightly shifted to the red ( $\omega_1 = \omega_0 - \omega_s$ ). The frequency and spectral shift,  $\Delta\omega$  and  $\Delta\lambda$  are given by

$$\frac{\Delta\omega}{\omega_0} = \frac{\omega_s}{\omega_0} = \frac{\Delta\lambda}{\lambda_0} = 2 \frac{c_s}{c} \left( 1 - \frac{n_e}{n_c} \right)^{1/2} \quad (2.23)$$

for stationary plasma. For flowing plasma, however, one must include the Doppler effect to interpret experimental data<sup>16)</sup>.

$$\frac{\Delta\lambda}{\lambda} = 2 \frac{c_s}{c} \left( 1 - \frac{n_e}{n_c} \right)^{1/2} (1 - M \cos\theta) \quad (2.24)$$

where  $M$  is the Mach number, and  $\theta$  is an angle between incident laser and plasma flow.

Offenberger et al. calculated the frequency dependent growth rate from random phase theory<sup>17)</sup> which reduces to

$$\gamma_k = - \frac{(2\pi)^3 r_0^2 n_0 I_0 \times \Gamma_\beta(x)}{\Gamma_i k_0^3 \pi^{1/2}} \quad (2.25)$$

$$x = \sqrt{\frac{1}{2}} \frac{1}{v_i} \frac{\omega_s}{k_s} \quad (2.26)$$

where  $r_0$  is the classical electron radius,  $\Gamma_\beta$  is a function of  $x$  and is shown in reference 17. Equation (2.25) can be used to calculate the spectral shape of backscattered light, if the ion acoustic damping is given by Landau damping.

If the plasma is not steady and inhomogeneous, the backscattered light will show a time varying spectral shift and its spectral width will be broadened by plasma inhomogeneity. From eq.(2.26), the spectral shift dependence on inhomogeneity or temporal variation of temperature, density, and Mach number can be easily derived, giving

$$\Delta \left( \frac{\delta\lambda}{\lambda_0} \right) = \frac{c_s}{c} \left( 1 - \frac{n_e}{n_c} \right)^{1/2} \left( \frac{\Delta T}{T} - \frac{\Delta n_e / n_c}{(1 - n_e / n_c)} (1 - M \cos\theta) - 2 \Delta M \cos\theta \right) \quad (2.27)$$

Here,  $T = T_e = T_i$ ,  $k_s \lambda_D \ll 1$  was assumed.  $\delta\lambda$  is equivalent to  $\Delta\lambda$  in eq. (2.26).  $\Delta$  can be replaced by  $\Delta/\Delta x$  or  $\Delta/\Delta t$ . For example,  $\Delta T/\Delta x \equiv \partial T/\partial x$  or  $\approx T/L_T$ , where  $1/L_T \equiv (\partial T/\partial x) / T$ .

## 2.5. Noise Source of Scattered Light

SBS growth from initial background noise has been investigated by several authors<sup>18-20)</sup>. There are a number of possible noise sources which can seed the spatial or temporal growth of SBS. These are briefly considered below.

### a) Thomson Scattering<sup>21)</sup>

When an electromagnetic wave is incident on a free charged particle, the particle will be accelerated and emit radiation. The scattered power per unit solid angle ( $\Omega$ ) by a single electron is given by

$$\frac{dP_{is}}{d\Omega} = r_e^2 \sin^2 \phi I_0 \quad (2.28)$$

where  $r_e$  is the electron radius,  $I_0$  is the incident light wave intensity,  $\phi$  is the angle between the direction of the scattered wave and electric field vector of the incident wave. If particle correlations can be ignored, the total scattered power can be calculated as an incoherent sum of the radiation from single particles.

### b) Bremsstrahlung<sup>22)</sup>

Spontaneous emission of light by bremsstrahlung can be amplified by SBS. The bremsstrahlung power density  $W_{BR}$  is given by

$$W_{BR} = 5 \times 10^{-48} \frac{Z^2 n_e n_i}{T_e^{1/2}} \exp(-h\nu/kT) d\nu d\Omega \quad (2.29)$$

where  $W_{BR}$  is in  $W/cm^3$ ,  $n_e$  and  $n_i$  are in  $cm^{-3}$ ,  $T$  is in eV.

### c) Blackbody Radiation<sup>23)</sup>

If the plasma is optically thick enough, it is reasonable to assume that thermal emission from the plasma approaches the blackbody radiation limit. The blackbody radiation flux per unit solid angle and unit frequency interval is given by

$$\frac{dI_{BB}}{d\Omega d\nu} = \frac{h \nu^3}{c^2} \frac{1}{\exp(h\nu/kT) - 1} \quad (2.30)$$

#### d) Reflection from Critical Surface

SBS growth from nonabsorbed light returning from the plasma critical surface was studied by Randall et al.<sup>20,24)</sup> and Baumgärtel et al.<sup>25)</sup>. Since the reflected light has almost the same frequency as the pump wave, it is likely to enhance or initiate SBS.

### 2.6. Double Stimulated Brillouin Scattering (DSBS)

Double stimulated Brillouin scattering is an interesting theoretical idea proposed by Zozulya et al.<sup>26)</sup> (see section 7.6). This mechanism leads to increased backward reflection without any assumption about the fixed spontaneous level of fluctuation, which corresponds to an absolute instability for oblique incidence of radiation on a plasma layer. DSBS theory predicts a wavelength shift<sup>27)</sup>

$$\frac{\Delta\lambda}{\lambda} = 2 \frac{c_s}{c} \left( 1 - \frac{n_e}{n_c} \right)^{1/2} \sin\theta \quad (2.31)$$

The threshold for instability in the limit of strong absorption (applicable to KrF laser plasma interaction) for inhomogeneous plasma is given by

$$\frac{I_{th} \lambda_0^2}{10^{16} T} = 2 \frac{\gamma_s}{\omega_s} \frac{\lambda_0}{L} \tau_0^{1.6} (\cos\theta)^{4.4} \quad (2.32)$$

where  $T = T_e + 3T_i / Z$ ,  $\tau_0 (= \nu_{ei} (n_e) L_n / c)$  is the optical depth,  $I_{th}$  is



in  $W/cm^2$ ,  $\lambda_0$  in  $\mu m$ ,  $T$  in keV and  $\theta$  = angle of incidence.

## 2.7. Density Fluctuation Related to SBS Reflectivity

For steady state homogeneous plasma of length  $L$ , reflectivity is given by<sup>29)</sup>

$$R = \tanh^2 \left( \frac{\omega_{pe} L}{4 k_0 c^2} \frac{\delta n}{n} \right) \quad (2.33)$$

which for small exponent reduces to

$$\approx \left( \frac{\pi}{2} \right)^2 \left( \frac{\delta n}{n} \right)^2 \left( \frac{n_e}{n_c} \right)^2 \left( \frac{L}{\lambda} \right)^2 \left( 1 - \frac{n_e}{n_c} \right)^{-2} \quad (2.34)$$

By measuring the reflectivity, one can therefore estimate the scale length  $L$  of the gain region, if  $\delta n/n$  is known.

More generally, Drake et al.<sup>28)</sup> have shown the ion fluctuation level  $\delta n/n$  is related to the ponderomotive force.

$$\frac{\delta n}{n} = \frac{-k_s^2}{8 \pi n_e m_e \omega^2} \frac{\chi_e \chi_i}{1 + \chi_e + \chi_i} E_0 \cdot E_1 \quad (2.35)$$

where  $\chi_e$  and  $\chi_i$  are the electron and ion susceptibilities. This expression can be reduced to

$$\frac{\delta n}{n} = \frac{1}{2} \frac{v_0^2}{v_e^2} \left( \frac{\omega_s}{2\gamma_s} \right) R^{1/2} \quad (2.36)$$

for uniform conditions appropriate to heavy damping of the ion waves. Again, by measuring  $R$  experimentally, one can estimate  $\delta n/n$ . Note these expressions do not include damping of the backscattered light.

From eqs. (2.6), at threshold, the minimum reflectivity  $R_{\min}$  can be related to the background noise fluctuation by (see appendix 2)

$$R_{\min}^{1/2} = \frac{1}{8} \frac{\omega_p^2}{\gamma_{ib} \omega_0} \left( \frac{\delta n}{n} \right)_{ini} \quad (2.37)$$

and the steady state solution of reflectivity in finite plasma can be

shown to be

$$R^{1/2} = \frac{1}{4} \frac{\omega_p^2}{\omega_0} \frac{\gamma_s}{\gamma_0^2} \left( \frac{\delta n}{n} \right)_{ini} \cdot \left[ \exp \left( \frac{\gamma_0^2}{2\gamma_{1b} \gamma_s} \left( 1 - \exp \left( - \frac{2\gamma_{1b}}{v_g} L \right) \right) \right) - 1 \right] \quad (2.38)$$

, if one can ignore pump depletion.

The density fluctuation can be limited by particle trapping in a potential well. The water bag model proposed by Dawson et al<sup>29)</sup> gives the trapping limit

$$\frac{\delta n}{n} \approx \frac{1}{2} \left[ \left( 1 + \frac{3T_i}{2T_e} \right)^{1/2} - 2 \left( \frac{T_i}{2T_e} \right)^{1/2} \right]^2 \quad (2.39)$$

Whether ion heating is expected to be significant or not may be inferred from the formula<sup>30)</sup>

$$n_i v_i T_i = IR\omega_s / \omega_0 \quad (2.40)$$

which is derived from energy balance.

In summary, the nature of the instability is strongly dependent on pump intensity, pump frequency, target Z, wave damping, and plasma conditions (hydrodynamic variables, inhomogeneity, velocity distribution). Varying the pump frequency can change the interaction from weakly to strongly ponderomotive driven, for a fixed high intensity. Thus it is necessary to use different theoretical treatments for different experiments.

In this study, the KrF laser parameters establish SBS conditions of high plasma density, strong electromagnetic wave absorption, weak ponderomotive effects, inhomogeneity of plasma flow velocity and density etc. This profoundly affects the nature of the instability.

Bibliography

- 1) D.W.Forslund, J.M.Kindel, and E.L.Lindman, Phys.Fluids, **18**, 1002 (1975).
- 2) A.A.Offenberger, Mod. Plasma Phys., 437 (1981).
- 3) M.N.Rosenbluth, Phys.Rev.Lett., **29**, 565 (1972).  
C.S.Liu, M.N.Rosenbluth, and R.B.White, Phys.Fluids, **17**, 1211 (1974).
- 4) D.F.DuBois, D W.Forslund, and E.A.Williams, Phys. Rev. Lett., **33**, 1013 (1974).
- 5) D.Pesme, G.Laval, and R.Pellat, Phys.Rev.Lett., **31**, 203 (1973).
- 6) B. I. Cohen and C.E.Max, Phys.Fluids, **22**, 1115 (1979).
- 7) A.F.Kuckes, Phys.Fluids, **7**, 511 (1964).
- 8) R.M.Kursslund and C.S.Shen, Phys.Fluids, **9**, 177 (1966).
- 9) T.Huang, L.Chen, and A.Hasegawa , Phys.Fluids, **17**, 1744 (1974).
- 10) M.Ono and R.M.Kulsrud, Phys.Fluids, **18**, 1287 (1975).
- 11) S. I. Brasinskii, in *Review of Plasma Physics*, edited by M.A.Leontovich (Consultants Bureau, New York, 1965), vol.1, p.205.
- 12) C.J.Randall, Phys.Fluids, **25**, 2231(1982).
- 13) M.Casanova, Laser and Particle Beams, **7**, 165(1989).
- 14) V.D.Shafranov, in *Review of Plasma Physics* edited by M.A.Leontovich (Consultants Bureau, New York, 1965), vol.1, p.1.
- 15) F.F.Chen, in *Introduction to Plasma Physics and Controlled Fusion* (Plenum, NewYork).
- 16) G.R.Mitchel, T.W.Johnston, and B.Grek, Phys.Fluids, **25**, 186 (1982).
- 17) A. A. Offenberger, M.R.Cervenak, A.M.Yam, and A.W.Pasternak, J.Appl.Phys., **47**, 1451(1976).
- 18) C.Oberman and G.Auer, Phys.Fluids, **17**, 1980 (1974).
- 19) R.L.Berger, E.A.Williams, and A.Simon, Phys.Fluids, **B1**, 414(1989).
- 20) C.J.Randall, J.R.Albritton, and J.J.Thomson, Phys.Fluids, **24**, 1474 (1981).
- 21) I.H.Hutchinson, in *Principles of Plasma Diagnostics* (Cambridge Univ. Press) p.239.
- 22) J.D.Jackson, in *Classical Electrodynamics* (John Wiley & Sons), p.701.

- 23) A. Yariv, in *Quantum Electronics* (John Wiley & Sons), p.99.
- 24) C. J. Randall and J. R. Albritton, *Phys. Rev. Lett.*, **52**, 1887 (1984).
- 25) K. Baumgärtel and K. Sauer, *Phys. Rev. A*, **26**, 3031 (1982).
- 26) A. A. Zozulya, V. P. Silin, and V. T. Tikhonchuk, *JETP Lett.*, **38**, 52 (1983). A. A. Zozulya, V. P. Silin, and V. T. Tikhonchuk, *Sov. Phys. JETP*, **59**, 756 (1984).
- 27) M. V. Chegotov, V. P. Silin, V. T. Tikhonchuk, and A. A. Zozulya, *Plasma Phys. & Controlled Fusion*, **28**, 413(1986).
- 28) J. F. Drake, P. K. Kaw, Y. C. Lee, G. Schmidt, C. S. Liu, and M. N. Rosenbluth, *Phys. Fluids*, **17**, 778(1974).
- 29) J. W. Dawson et al., "*Dynamics of Ionized Gas*", **47**, (John Wiley & Sons, 1971). 30) W. L. Kruer, *Phys. Fluids*, **23**, 1273(1980).

### III. Numerical Investigation of SBS

In order to simulate the complicated nonlinear SBS process in temporally and spatially varying plasma, computer calculation codes were developed as part of this study. With plasma parameters obtained from hydrodynamic codes (MEDUSA, CASTOR), the coupling equations [eqs. (2.6)] have been solved numerically. To check the performance of the simulation codes and study basic properties of SBS, calculations were first done for finite uniform steady plasma. The calculated results agreed very well with analytical solutions in steady state. Advanced codes were subsequently developed to calculate SBS in non-uniform plasma. General properties of SBS growth were examined for typical plasma parameters expected in our experimental conditions. These SBS modeling results will be compared with experimental data in chapters 7 and 8.

#### 3.1. Outline of Differencing Scheme

The equations to be solved are<sup>1)</sup>

$$\left( \frac{\partial}{\partial t} + v_g \frac{\partial}{\partial x} + \gamma_{ib} + K_0 \right) a_0 = - A \cdot a_1 \cdot n \quad (3.1a)$$

$$\left( \frac{\partial}{\partial t} - v_g \frac{\partial}{\partial x} + \gamma_{ib} + K_1 \right) a_1 = A \cdot n^* \cdot a_0 \quad (3.1b)$$

$$\left( \frac{\partial}{\partial t} + c_s \frac{\partial}{\partial x} + \gamma_s + K_s \right) n = B \cdot a_1^* \cdot a_0 \quad (3.1c)$$

$$A = \frac{1}{4} \frac{\omega_{pe}^2}{\omega_0}, \quad B = \frac{1}{4} \frac{m_e}{M_i} \frac{k_s^2 v_0^2}{\omega_s} \quad (3.1d)$$

$$K_i = \frac{1}{2} \frac{v_g}{k_i} \frac{\partial k_i}{\partial x}, \quad (i = 0, 1) \quad K_s = \frac{1}{2} \frac{c_s}{k_s} \frac{\partial k_s}{\partial x} \quad (3.1e)$$

In solving eqs. (3.1) numerically, eq. (3.1c) was modified to

include a noise source term:

$$\left( \frac{\partial}{\partial t} + c_s \frac{\partial}{\partial x} + \gamma_s + K_s \right) n = B \cdot a_1^* \cdot a_0 + \gamma_s N_n \quad (3.2)$$

Here, the second term on the right hand side was phenomenologically added to provide a variable thermal density fluctuation level  $N_n$  (with damping  $\gamma_s$ ). If one assumes a noise source of scattered light instead of density fluctuation, this source term should be added to eq.(3.1b) as  $\gamma_{1b} N_1$ . Equations (3.1) and (3.2) were solved with boundary conditions

$$a_0(0, t) = \sqrt{I(t)} \quad (3.3a)$$

$$a_1(L, t) = 0 \quad (3.3b)$$

$$a_2(0, t) = a_2(L, t) = N_n \quad (3.3c)$$

where  $I(t)$  is the given pump intensity normalized by peak intensity (either step function or gaussian pulse),  $L$  is the length of plasma. Reflectivity is given by  $[ a_1(0, t) / a_0(0, t) ]^2$ . The pump radiation is assumed to be a KrF laser ( $\lambda=0.248\mu\text{m}$ ) throughout this thesis, unless otherwise noted. Two calculation schemes were tested here.

### 3.1.1. Scheme 1 : Predictor-Corrector Method

The first calculation scheme used was the predictor-corrector method<sup>2)</sup> in which prediction of the following time step was calculated by an explicit method from the previous step

$$a_1^{n+1} = a_1^n + \Delta t \cdot F(a_1^n) \quad (3.4)$$

where  $a_1^n$  is  $( a_0, a_1, n )$  at the  $n$ -th time step,  $\Delta t$  is the time increment and  $F(a_1^n)$  is a function of  $a_1^n$ . The predictors were corrected by using an Euler corrector method

$$a_1^{n+1} = a_1^n + \frac{\Delta t}{2} [ F(a_1^{n+1}) + F(a_1^n) ] \quad (3.5)$$

and iterated. The initial value of the ion density fluctuation can be

an arbitrary parameter. Each mesh size  $\Delta x$  is kept constant over the plasma.  $\Delta t$  is defined as  $\Delta x/v_g$ . The advantage of this scheme was that it was fairly straightforward to derive a differential scheme. The major drawback was choosing a differential scheme for the second convective term ( $v_g \partial/\partial x$ ). This is, especially, the case for inhomogeneous plasma, where the group velocity of the light wave  $v_g$  is non-uniform and the basic differencing scheme (e.g. LAX-Wendroff) becomes inaccurate and unstable. Since this method gives reasonable results in uniform plasma, however, it is useful for simulating incoherent SBS in inhomogeneous plasma (which can be approximated by linearly adding many small uniform plasmas).

### 3.1.2. Scheme 2 : Time-Splitting Method

The second calculation scheme used was the time-splitting method<sup>2)</sup>. The equation was separated into two sub-equations (one with the  $\partial/\partial x$  term and another one without the  $\partial/\partial x$  term). Each sub-equation was calculated sequentially for the time increment  $\Delta t$ . For example, eq. (3.1a) can be separated into

$$\left( \frac{\partial}{\partial t} + \gamma_{1b} + K_0 \right) a_0 = - A \cdot a_1 \cdot n \quad (3.6a)$$

$$\left( \frac{\partial}{\partial t} + v_g \frac{\partial}{\partial x} \right) a_0 = 0 \quad (3.6b)$$

During the time  $\Delta t$ , eq. (3.6a) was first calculated for  $\Delta t/2$ , then eq. (3.6b) was calculated for  $\Delta t$ , and finally eq. (3.6a) was calculated for  $\Delta t/2$  again.  $\Delta x$  was kept constant for each mesh.  $\Delta t$  was defined as  $\alpha \cdot \Delta x/v_g$  at first ( $\alpha$  is constant, typically  $\approx 0.5$ ) and then, depending on convergence of calculation, adjusted during the calculation.

The advantage of this method is that one can choose an optimum

scheme for each equation. For solving eq.(3.6a), the time-step controlled 4th-order Runge-Kutta method<sup>2)</sup> was used. For eq.(3.6b), a differential scheme was not used, but rather the calculation was based on a physical picture of wave propagation.<sup>3)</sup> To calculate  $a_{1j}^{n+1}$  at the  $j$ -th mesh, first  $a_1^n(x)$  is interpolated between mesh  $j-1$  ( $x=0$ ) and  $j$  ( $x=\Delta x$ ) as a function of space  $x$  by using a cubic spline function. Then  $a_{1j}^{n+1}(x=\Delta x)$  is given by  $a_1^n(x=\Delta x - \Delta t \cdot v_g)$ . In order to calculate the coefficients of the cubic spline function in eq.(3.6b),  $a_1'$  ( $=\partial a_1/\partial x$ ) was solved simultaneously in both eqs.(3.6a) and (3.6b).

### 3.2. Numerical Solutions in Finite Homogeneous Plasma

#### 3.2.1. Comparison with Theoretical Predictions (Steady State)

In order to check performance of the simulation codes, several calculations were done in finite homogeneous plasma and the results were compared with analytical solutions.

An analytical solution of  $a_n(x, \omega)$  in finite plasma without damping was given by Forslund et al.<sup>1)</sup>

$$c_0(x) = c_1(x) = c(0) \operatorname{sech}(x / L_1) \quad (3.7a)$$

$$c_p(x) = c_0^2(0) \tanh(x / L_1) \quad (3.7b)$$

where  $L_1 = (v_g / c_s)^{1/2} / \gamma_0$ . Here  $c_0(x) = a_0(x, \omega)$ ,  $c_1(x) = (k_1 / k_0)^{1/2} \cdot a_1 \cong a_1(x, \omega)$ ,  $c_p(x) = (c_s / v_g)^{1/2} \cdot (A / B)^{1/2} \cdot n(x, \omega)$ , and  $c(0) = 1.0$  in our case (eqs.3.1). Figure 3.1 shows simulation results of the temporal evolution of reflectivity (a) and spatial profiles of each wave along with analytical solutions (b). Parameters used in these calculations were  $L = 30\mu\text{m}$ ,  $v_g / c_s = 1800$ ,  $A/B = 2.8 \times 10^6$ ,  $N_n = 10^{-4}$ ,  $\gamma_{1b} = \gamma_s = 0$ . In fig.3.1 (a), the reflectivity does not quite reach 100%, however, there is only a small discrepancy between analytical and



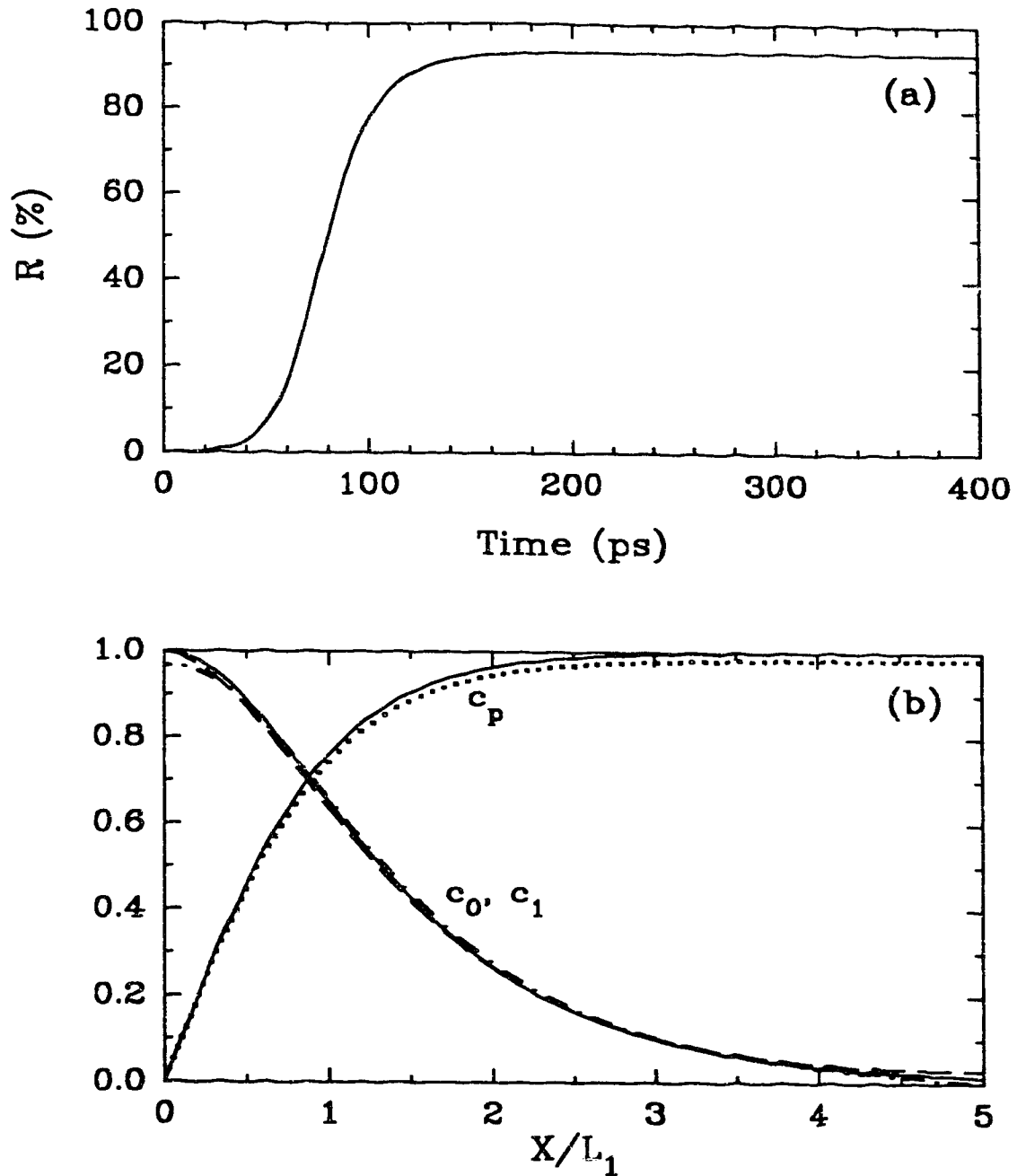


Fig.3.1. Simulation results in finite homogeneous plasma without damping; (a) temporal evolution of reflectivity, and (b) spatial profiles of each wave at  $t=400$ ps [  $c_0$ : pump (the dashed line),  $c_1$ : scattered wave (the dash-dot line),  $c_p$ : density fluctuation (dotted line) ]. The solid lines are analytical solutions in steady state for  $c_0$  ( $c_1$ ) and  $c_p$ .

numerical results as seen in fig.3.1 (b). Reflectivity  $R < 1$  is a consequence of the finite time of calculation  $t_{\max}$  and finite size of mesh  $\Delta x$  at the boundary. At time  $t = 400\text{ps}$ ,  $a_1(0,t)$  reaches 0.967. The value of  $a_1(0,t)$  would be closer to unity if one reduced  $\Delta x$  and increased  $t_{\max}$  significantly by extending the computational time. These results, however, are satisfactory for our purposes.

Figure 3.2 shows a comparison between simulation results and analytical predictions of reflectivity (eq.2.38) in finite homogeneous plasma (with  $L = 100\mu\text{m}$  and  $400\mu\text{m}$ ) and infinite plasma with damping.

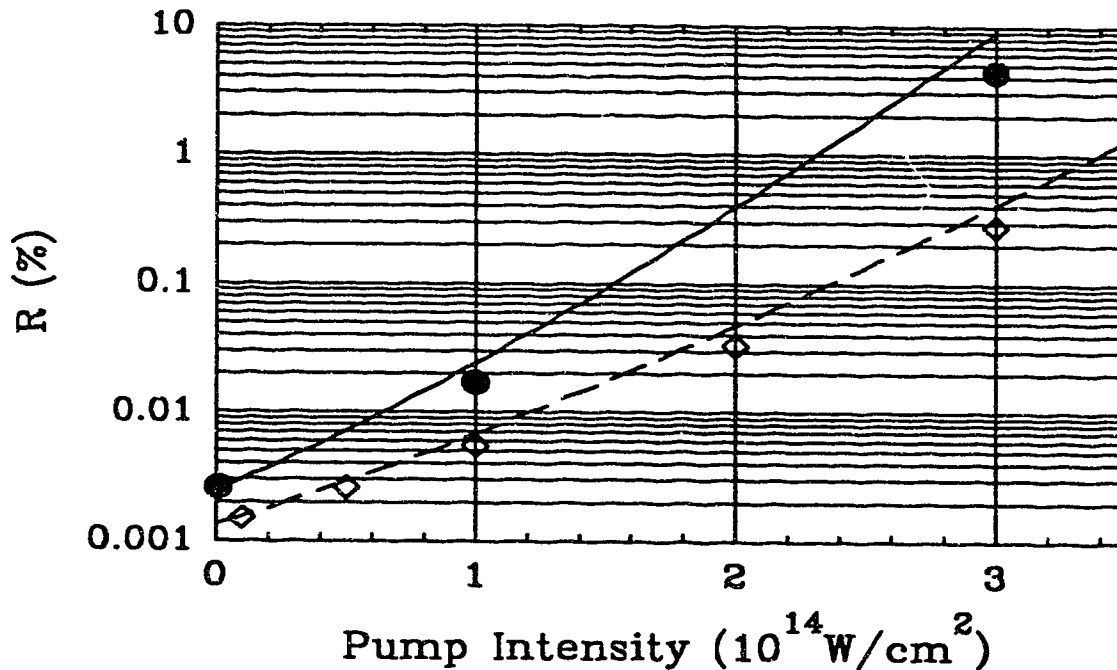


Fig.3.2. Comparison between simulation results and analytical predictions for homogeneous plasma with damping. The solid and dashed lines are calculated from eq.2.38 for infinite plasma and finite plasma with  $L = 100\mu\text{m}$ , respectively. The solid circles and open diamonds are simulation results for finite plasma with  $L = 400\mu\text{m}$ , and  $100\mu\text{m}$ , respectively.

Parameters used here were  $n_e/n_c=0.1$ ,  $N_n = 10^{-4}$ ,  $\gamma_0 = 8.5 \times 10^{11} \cdot I_{14}^{1/2}$  (1/s),  $\gamma_{1b} = 2 \times 10^{12}$  (1/s),  $\gamma_s = 2 \times 10^{11}$  (1/s).  $I_{14}$  is the pump intensity normalized to  $10^{14} \text{W/cm}^2$  which was kept constant at the boundary during calculation. The reflectivity R was taken after a time long enough for SBS to be saturated in the simulation. These simulation results show slightly lower reflectivity than analytical predictions, especially at higher reflectivity, because of finite  $t_{\text{max}}$  and  $\Delta x$  as mentioned in 3.2.1. and also because the pump depletion is ignored in eq.2.38. Thus for low reflectivity (< a few %), eq.2.38 can be used to analyze SBS, whereas for higher reflectivity numerical calculation is necessary, since pump depletion becomes important.

### 3.2.2. Dependence of Reflectivity on Electron Density

By using the simulation code mentioned above, the dependence of SBS growth on electron density and pump intensity was studied for Al plasma. In order to model density effects, the plasma temperature T ( $= T_e = T_i$ ) was kept constant for each intensity and density. Plasma parameters assumed here are  $T = 500 \text{eV}$ ,  $Z = 11$ ,  $L = 100 \mu\text{m}$ ,  $N_n = 10^{-3}$ ,  $\gamma_s$  was given by the Casanova formula for collisional damping and  $\gamma_{1b}$  was given by<sup>4)</sup>

$$2\gamma_{1b} \text{ (1/s)} = 9.2494 \times 10^3 Z n_e^2 \text{ (cm}^{-3}) \ln \Lambda T_e^{-3/2} \text{ (eV)} \omega_0^{-2} \text{ (1/s)} \quad (3.8)$$

The factor 2 was introduced in the left hand side, since the value given by the right hand side of eq.(3.8) is the energy damping rate.

Figure 3.3 shows the dependence of SBS reflectivity on electron density at different pump intensity. The results show that the optimum density for maximum reflectivity in this case ranges from

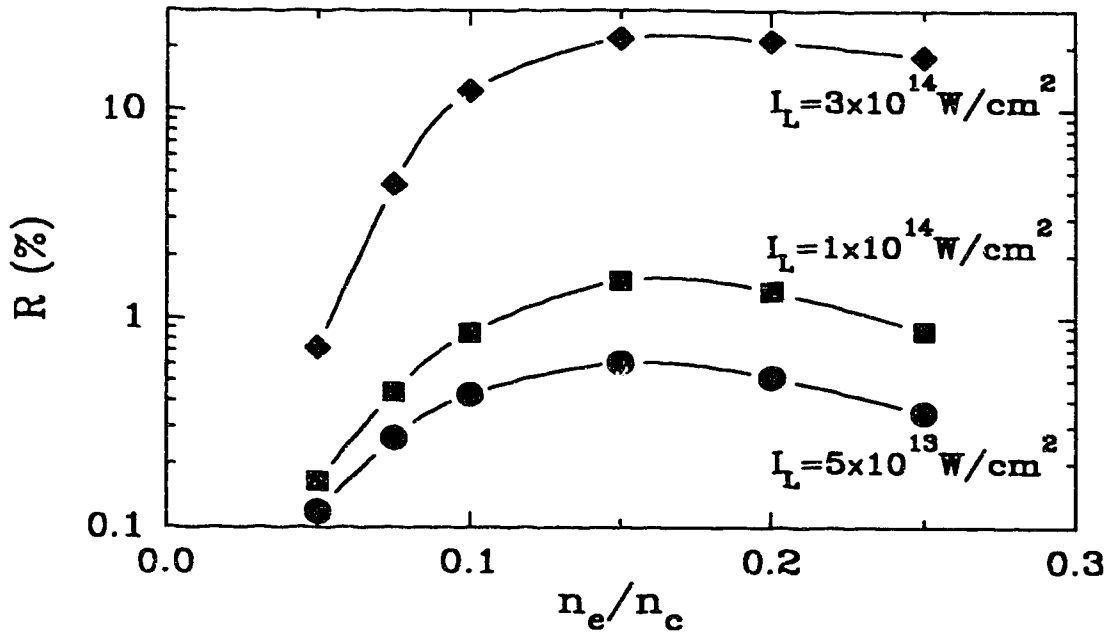


Fig. 3.3. Dependence of SBS reflectivity on electron density for  $I = 5 \times 10^{13} \text{ W/cm}^2$  (solid circles),  $1 \times 10^{14} \text{ W/cm}^2$  (solid squares), and  $3 \times 10^{14} \text{ W/cm}^2$  (solid diamonds).

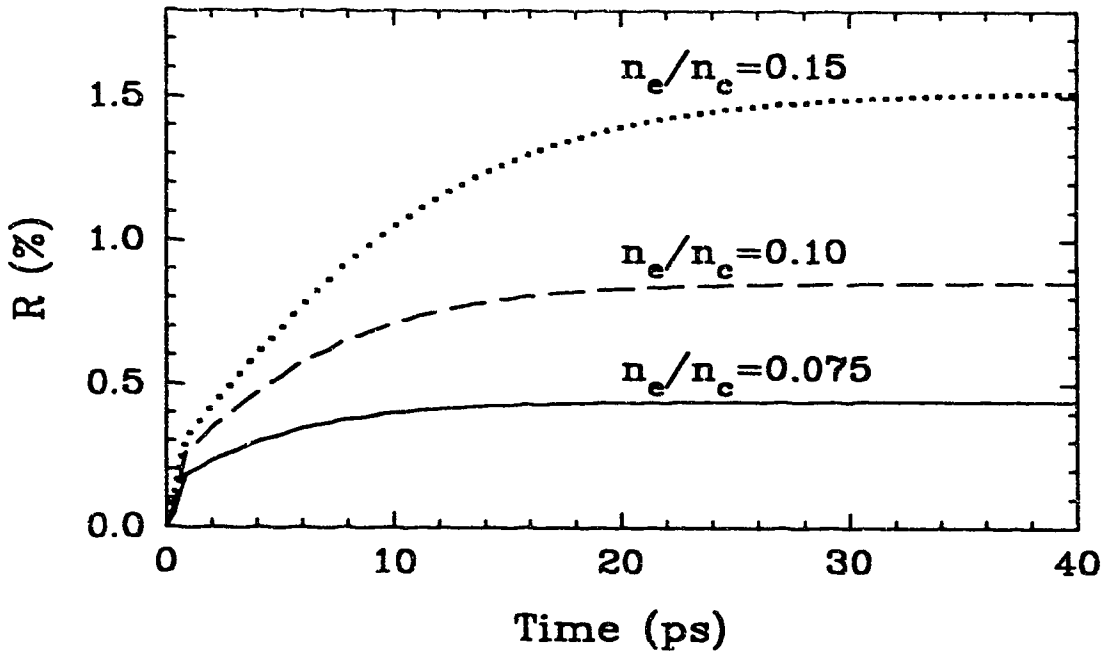


Fig. 3.4. Temporal evolution of SBS growth at  $I = 1 \times 10^{14} \text{ W/cm}^2$  for  $n_e/n_c = 0.075$  (solid curve), 0.10 (dashed curve), 0.15 (dotted curve).

$n_e/n_c = 0.1$  to  $0.2$ , depending on pump intensity. The existence of an optimum density is a direct consequence of competition between growth and damping of the waves. On the one hand, the SBS growth rate  $\gamma_0$  scales as  $n_e^{1/2}$ , and therefore growth is enhanced at higher density. At the same time, inverse bremsstrahlung absorption of the pump wave ( scaling as  $n_e^2$  ) increases with higher density. Several factors can change the details of this figure; e.g., temperature, plasma length, etc.. If one allows for higher temperature at higher laser intensity, the optimum density will shift to higher density, since  $\gamma_{ib}$  scales as  $T_e^{-3/2}$ . For shorter plasma length, the optimum density will be higher, since growth at lower density requires longer gain length.

### 3.2.3. Temporal Response of SBS Growth

The temporal evolution of SBS was numerically examined to estimate the time scale of SBS growth in the experiments. Figure 3.4 shows the temporal behavior for constant pump pulse. Calculations were made for the same simulation parameters used in section 3.2.2. (  $I = 10^{14}$  W/cm<sup>2</sup>,  $n_e/n_c = 0.075, 0.10, \text{ and } 0.15$  ). The reflectivity reached steady state in a time of 30ps. For typical plasma parameters expected in the experiments ( $T=500\text{eV}$ ,  $Z=11$ ,  $\gamma_0 \approx 8 \times 10^{11}$ ,  $\gamma_s \approx 3 \times 10^{11}$ ,  $\gamma_{ib} \approx 10^{12}$ ), the time scale of SBS growth was estimated to be 20-30ps. If the duration of the pump pulse is  $\gg 30\text{ps}$  and the plasma is stationary, it is reasonable to assume that SBS reaches steady state for any given time during the laser pulse.

Numerical experiments were also done for temporally modulated pump pulses to follow the dynamic response of SBS. A temporally varying pump pulse was injected into homogeneous Al plasma (  $L=100\mu\text{m}$ ,

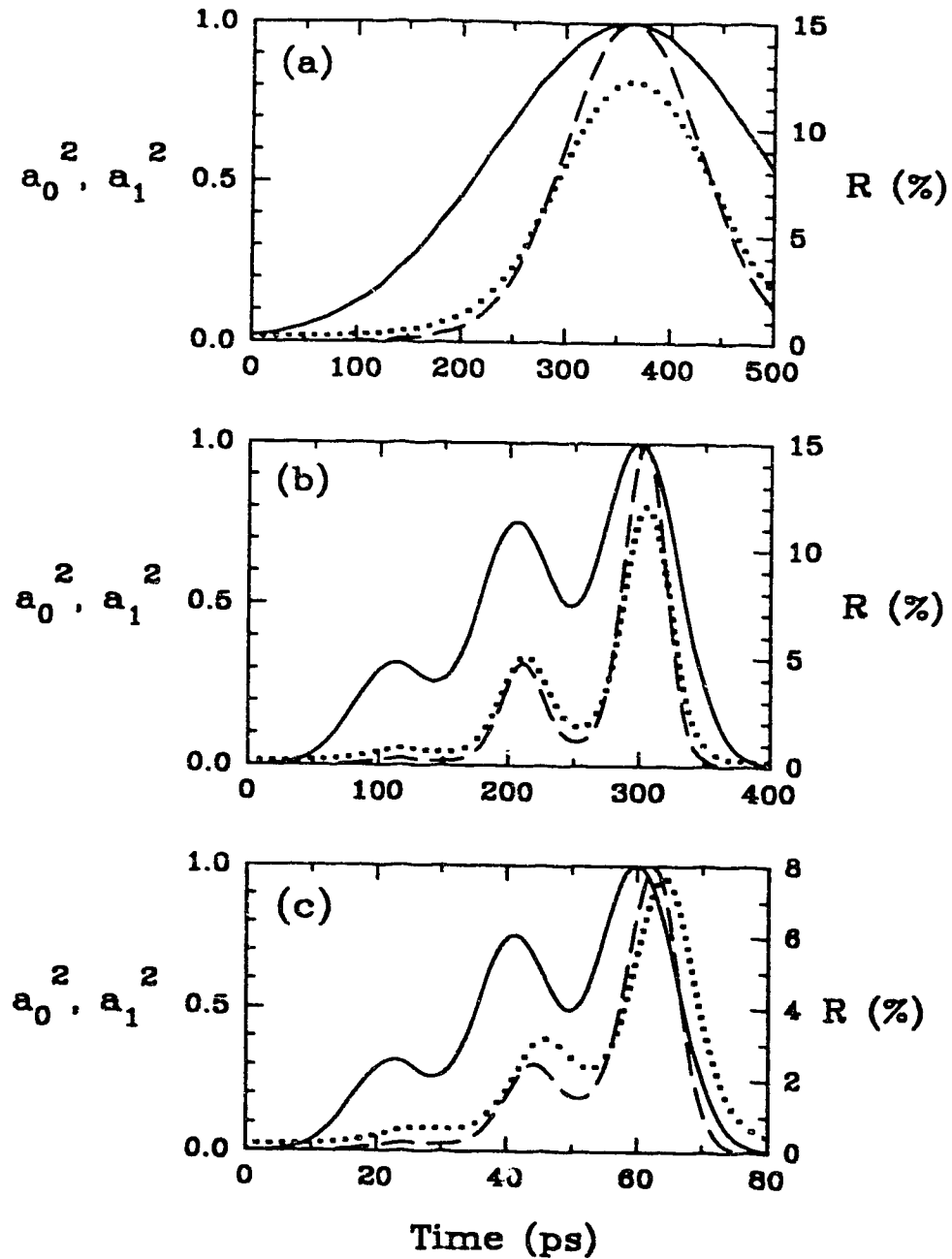


Fig. 3.5. SBS reflectivity with temporally varying pump pulse. Pump intensity  $a_0^2$  (solid lines), backscattered intensity  $a_1^2$  (dashed lines), and reflectivity  $R (=a_0^2/a_1^2)$  (dotted lines) are plotted as a function of time for various pump pulses; (a) Gaussian pulse with FWHM 300ps, (b) modulated Gaussian pulse with global FWHM 300ps and 100ps modulation, (c) modulated Gaussian pulse with global FWHM 60ps and 20ps modulation.  $a_1^2$  is normalized to its peak value.

$n_e/n_c=0.1$ ,  $T=500\text{eV}$ ,  $Z=11$ ,  $N_n=10^{-3}$ ) and SBS reflectivity was calculated. Figure 3.5 (a) shows SBS growth for a Gaussian pump pulse ( peak intensity =  $3\times 10^{14}\text{W/cm}^2$ , 300ps FWHM ). The backscattered intensity showed a FWHM of 150ps, 2 times narrower than the pump pulse. The calculated peak reflectivity was 12% which was the same as that calculated for constant pump (section 3.2.2.). At one-third of the peak intensity ( $=1\times 10^{14}\text{W/cm}^2$ ), the reflectivity is 0.79% which is almost the same as the value calculated with constant pump (0.85%). Figure 3.5 (b) shows the SBS reflectivity for modulated Gaussian pulse (peak I =  $3\times 10^{14}\text{W/cm}^2$ , global FWHM = 300ps, modulation period = 100ps). Again the peak reflectivity was calculated to be 12%. At the first peak where the pump intensity is  $9\times 10^{13}\text{W/cm}^2$ , the reflectivity is 0.78%, consistent with results of fig.3.5 (a). Even with strong modulation ( $\approx 50\%$ ) with a time scale of 50ps, the SBS reaches a steady state value corresponding to the instant intensity throughout the pulse. In fig. 3.5 (c), the time scale of the modulated Gaussian pump pulse was reduced 5 times. In this case, the calculated reflectivity was 8% at the peak and 0.6% at the first peak. SBS did not reach steady state on this fast time scale. Since the typical time scale of the laser pulse in our experiment is 800ps (FWHM), we expect SBS responds quickly enough to the incident laser intensity to achieve steady state.

### 3.3. Numerical Solutions in Finite Inhomogeneous Plasma

To simulate SBS in an inhomogeneous plasma, special attention was paid to the group velocity ( $v_g$ ) of the EM waves, which is now a function of space, since the electron density changes spatially. As

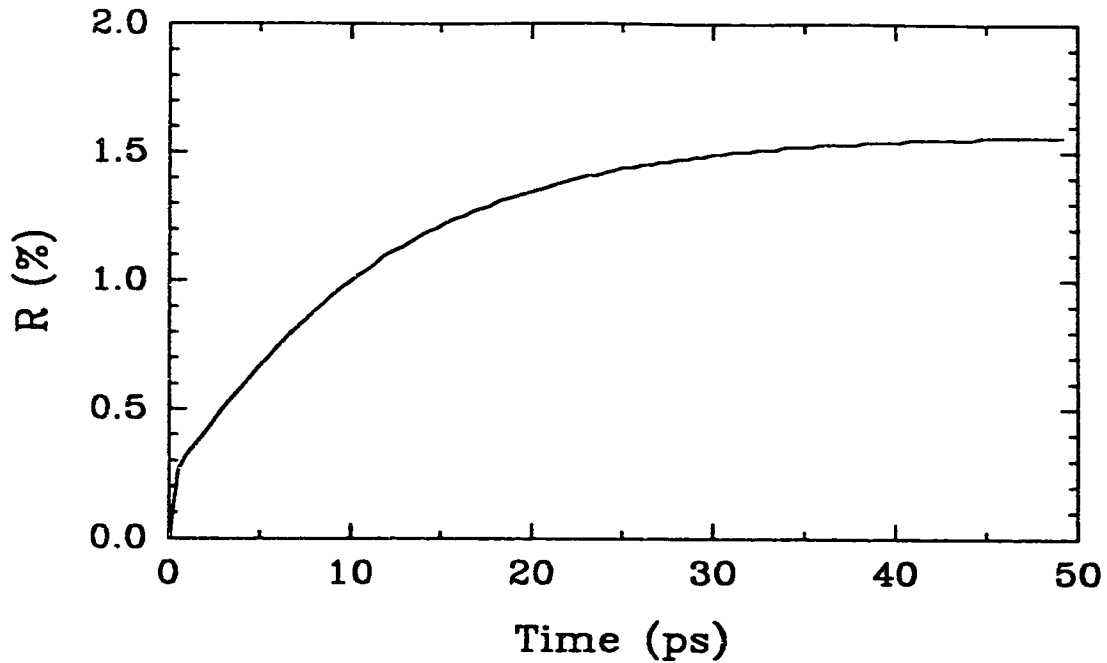


Fig.3.6. Temporal evolution of SBS reflectivity in an inhomogeneous plasma.

described in section 3.1.2., the time-splitting method was employed to solve the coupled equations. For simplicity, phase mismatch  $\kappa'$  was ignored and only inhomogeneity of electron density was taken into account. The density profile was assumed to be of the form  $n_e/n_c = n_{\text{max}} \cdot \exp(-x/L_n)$ , where  $L_n$  is a density scale length. The temperature  $T(x)$  was assumed to be constant (isothermal expansion). Plasma flow effects were ignored in these calculations, but will be considered in chapter 8. These assumptions are expected to give an upper limit for SBS reflectivity. Figure 3.6 shows simulation results for the temporal evolution of SBS reflectivity. The parameters used here are  $T=500\text{eV}$ ,  $Z=11$  (Al plasma),  $n_e/n_c = 0.5\exp(-x/30\mu\text{m})$ ,  $I=1 \times 10^{14}\text{W/cm}^2$ ,  $N_n=10^{-3}$ ,  $L=90\mu\text{m}$  ( $= 3 \cdot L_n$ ); identical conditions to those used in



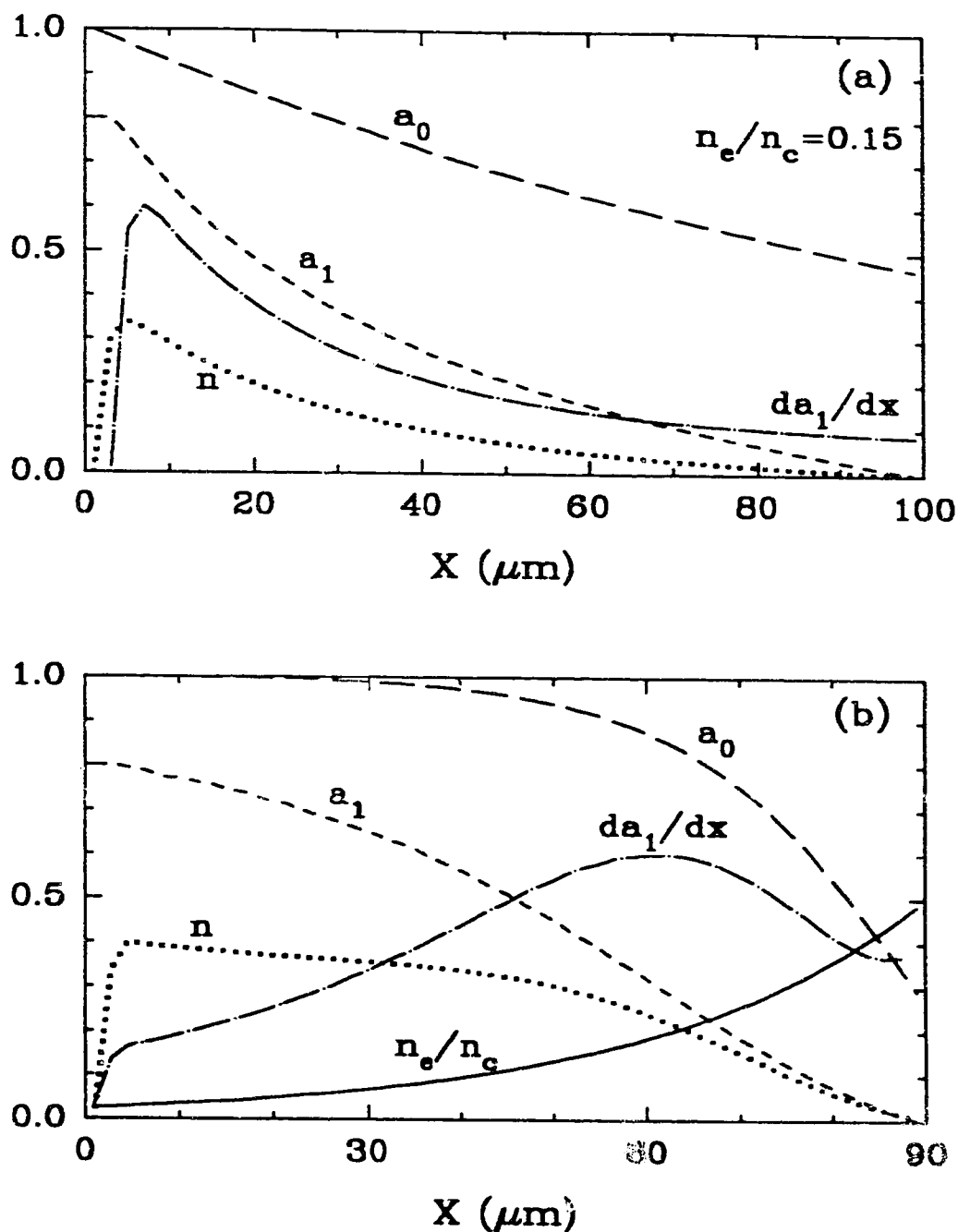


Fig. 3.7. Spatial profiles of waves in (a) homogeneous plasma and (b) inhomogeneous plasma. The spatial derivative of the scattered wave  $da_1/dx$  is also plotted (dash-dot line) to show the region of amplification. Peak values are normalized differently for each wave for a better view.

fig.3.5 (a) except for density and plasma length. The pump intensity was kept constant. The time to reach steady state is about 40-50ps which is similar to that obtained for homogeneous plasma. Figure 3.7 shows a comparison of spatial profiles of each wave in (a) homogeneous and (b) inhomogeneous plasma;  $a_0$ : pump wave amplitude (long dashed line),  $a_1$ : scattered wave amplitude (short dashed line),  $n$ : density fluctuation (dotted line). The spatial derivative of  $a_1$ ,  $da_1/dx$ , is also plotted (dash-dot line) to show the region of SBS amplification. In the case of fig.3.7 (a), the calculations were made for the same simulation parameters used in section 3.2.2. ( $I = 1 \times 10^{14} \text{ W/cm}^2$ ,  $n_e/n_c = 0.15$ , peak reflectivity = 1.52% ). Figure 3.6 (b) corresponds to parameters at 50ps in fig.3.5 (reflectivity = 1.56% ); the density profile is shown as a solid line. In the homogeneous case, the scattered wave is amplified mostly in the region where the pump intensity is strong. In the inhomogeneous case, however, the scattered wave is amplified mostly around  $n_e/n_c = 0.18$  ( $x = 60 \mu\text{m}$ ), since the growth rate  $\gamma_0(x)$  ( $\propto a_0(x) \cdot \sqrt{n_e(x)}$ ) is the highest at  $n_e/n_c = 0.22$  ( $x = 64 \mu\text{m}$ ). Note the peaks of amplification and  $\gamma_0$  do not match because of the convective effect; the amplification peaks downstream (for backscattering,  $x \rightarrow 0$ ) of the peak of  $\gamma_0$ .

### 3.4. Summary

Simulation codes for solving the SBS coupling equations have been developed. Calculations were made with parameters appropriate to our experiments. The simulation results showed clearly that pump absorption due to inverse bremsstrahlung is important and SBS amplification has an optimum density as a consequence of competition

between parametric wave growth and damping. More calculation results for inhomogeneous plasma will be presented and compared with the experimental data in chapter 8.

#### Bibliography

- 1) D.W.Forslund, J.M.Kindel, and E.L.Lindman, Phys. Fluids, **18**, 1002 (1975).
- 2) W.H.Press et al., "*Numerical Recipes*", (Cambridge University Press 1989).
- 3) K.Nishihara, private communication.
- 4) T.W.Johnston and J.M.Dawson, Phys. Fluids, **16**, 722 (1973).

#### IV. Hydrodynamic Simulation (CASTOR) Results

In this chapter, characteristics of the KrF laser-produced plasma are studied using a two-dimensional hydrodynamic simulation code CASTOR. Plasma scale lengths (density and velocity) are compared with the size of focal spot. Plasma refraction of the laser beam is important for small focus irradiation and causes two major effects: 1) plasma size larger than the focal spot, 2) large scale density variations. Two-dimensional profiles of density, temperature, and flow velocity are presented which help to clarify features of plasma created by tightly focused short wavelength laser radiation. The simulation results are used to calculate phase mismatch for SBS interaction and to interpret the experimental results in the following chapters.

##### **4.1. Outline of Simulation Code CASTOR**

In this section, an outline of the two-dimensional cylindrically symmetric Eulerian-plasma hydrodynamic code CASTOR<sup>1)</sup> is summarized. The laser routine in CASTOR accounts for laser absorption, refraction, diffraction, and ponderomotive force. The heat flux is taken to be a limited free-streaming with flux limiter  $f=0.08$ . Typically the simulation uses a non-uniform  $50 \times 75$  grid to represent a spatial region of  $200 \mu\text{m}$  radially (R direction) by  $400 \mu\text{m}$  axially (Z direction). The radial mesh spacing  $\Delta R$  was  $1.0 \mu\text{m}$  at  $R=0$  and was increased geometrically by a factor of 1.05. The axial mesh spacing  $\Delta Z$  was  $0.25 \mu\text{m}$  at  $Z=380 \mu\text{m}$  (initial target surface) and was also increased geometrically. This relatively small spacing enables us to study the density region near  $n_c$ .

in detail. The initial condition of electron density  $n_e$  for Al target was set in the following way. In the vacuum zone ( $Z < 375\mu\text{m}$ ),  $n_e$  was held constant at  $7.78 \times 10^{17} \text{cm}^{-3}$ , then exponentially increased to  $7.78 \times 10^{22} \text{cm}^{-3}$  over the region  $375\mu\text{m} < Z < 380\mu\text{m}$ . In the solid region ( $Z > 380\mu\text{m}$ ),  $n_e$  was held constant at  $7.78 \times 10^{22} \text{cm}^{-3}$ . The initial condition of temperature ( $T_e$  and  $T_i$ ) and average charge state  $\bar{Z}$  was taken to be 0.0258eV and 1.3 in all space. The laser beam profile was assumed cylindrically symmetric and given by

$$I(r, t) = \frac{P(t)}{\pi\sigma^2} \exp\left(-\frac{r^2}{\sigma^2}\right) \quad (4.1)$$

$$P(t) = P_{\max} \exp\left\{-\frac{1}{2} \left(\frac{t - t_{\max}}{\tau}\right)^2\right\} \quad (4.2)$$

where  $\sigma = 1.20 \cdot r_{50\%}$ ,  $r_{50\%}$  is 50% energy radius,  $\tau = (0.6/\sqrt{2})t_{\text{FWHM}}$ ,  $t_{\text{FWHM}}$  is full width at half maximum laser pulse duration,  $P_{\max} = E_L / (\tau\sqrt{2\pi})$ ,  $E_L$  is total laser energy. Following these formulae, 90% energy radius is given by  $r_{90\%} = 1.83 \cdot r_{50\%}$ .

Simulations of Al targets were performed for three conditions of focused incident laser beam. Table 4.1. summarizes parameters for these cases. The focal spot size (90% energy radius) was changed from  $28\mu\text{m}$  (large focus, LF) to  $17\mu\text{m}$  (small focus, SF) to study the relationship between the lateral effects resulting from laser

Table 4.1. Laser beam parameters for CASTOR.

Case	Energy (J)	Peak intensity (W/cm <sup>2</sup> )	Focal spot radius ( $\mu\text{m}$ )	
			90% energy	50% energy
LF1	1.0	$3 \times 10^{13}$	28	15
SF1	1.0	$8 \times 10^{13}$	17	9
SFS	0.5	$4 \times 10^{13}$	17	9

refraction and the focal spot size. In addition, the laser energy was varied from 1J to 0.5J. In all cases, the laser pulse peaked at 2.2ns ( $t_{\max} = 2.2\text{ns}$ ), and  $t_{\text{FWHM}} = 1.6\text{ns}$ , giving 50% intensity at 1.4ns. Some data analysis was done on laser axis ( $R=0$ ) where the laser intensity was higher and hence SBS was most likely to occur.

#### 4.2. Laser Focal Spot and Density Scale Length

Figure 4.1 shows contour plots of the laser flux ( (a)-(c) ) and electron density  $\log_{10}(n_e/n_c)$  ( (d)-(f) ) for simulation conditions listed in table 4.1. (a) and (d), (b) and (e), and (c) and (f) correspond to the cases LF1, SF1 and SF5, respectively. These snapshots were taken at  $t = 1.5\text{ns}$  (0.7ns before the laser peak where the laser intensity is about half of the peak value). The laser flux is normalized to the peak value. The laser beam propagates in the positive Z direction (from bottom to top in the figures). Since critical density for the  $0.25\mu\text{m}$  laser wavelength is  $1.8 \times 10^{22} \text{ cm}^{-3}$  which is about one-fourth of the solid density of aluminum, the critical surface (plotted in thick solid line) occurs inside the initial target surface and moves toward the target. The tightly focused laser beam virtually digs a deep hole into the target. The radius of the hole is about the size of the 10% intensity contour of the laser beam. As expected, the aspect ratio  $d/R$  of the hole depth ( $d$ ) and radius ( $R$ ) for the small focus (SF1 and SF5) cases is larger than that for the large focus (LF1). It is also noted that the underdense plasma ( $n_e < 0.1n_c$ ) was created over a wide region - about  $80\mu\text{m}$  and  $50\mu\text{m}$  in radius for LF and SF case, which is larger than the focal spot (90% energy radius). This is due to plasma refraction of the laser beam.

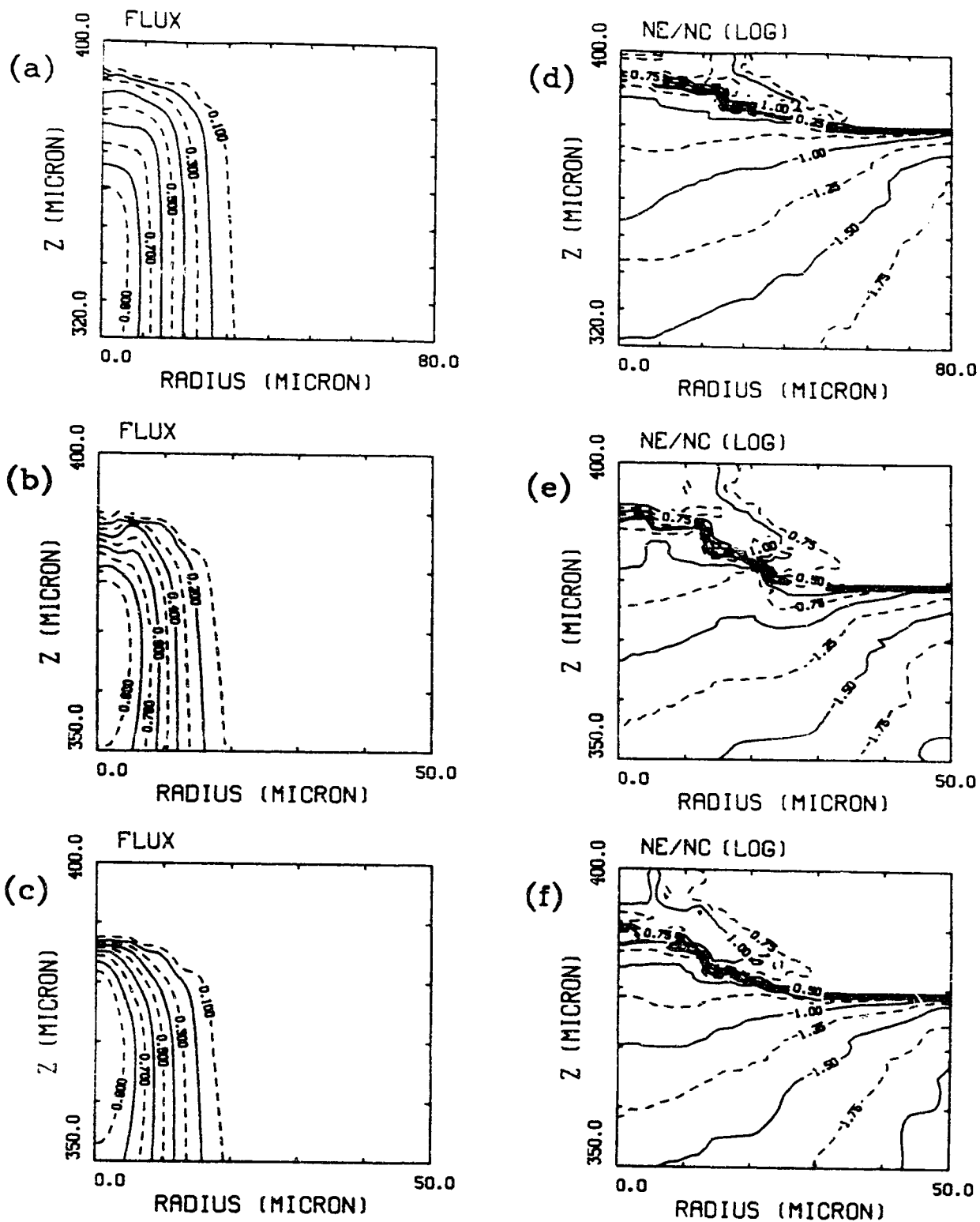


Fig.4.1. Contour plots of laser flux ( (a)-(c) ) and  $\log_{10}(n_e/n_c)$  ( (d)-(f) ) at  $t=1.5\text{ns}$ . (a) and (d), (b) and (e), and (c) and (f) correspond to cases LF1, SF1 and SF5.

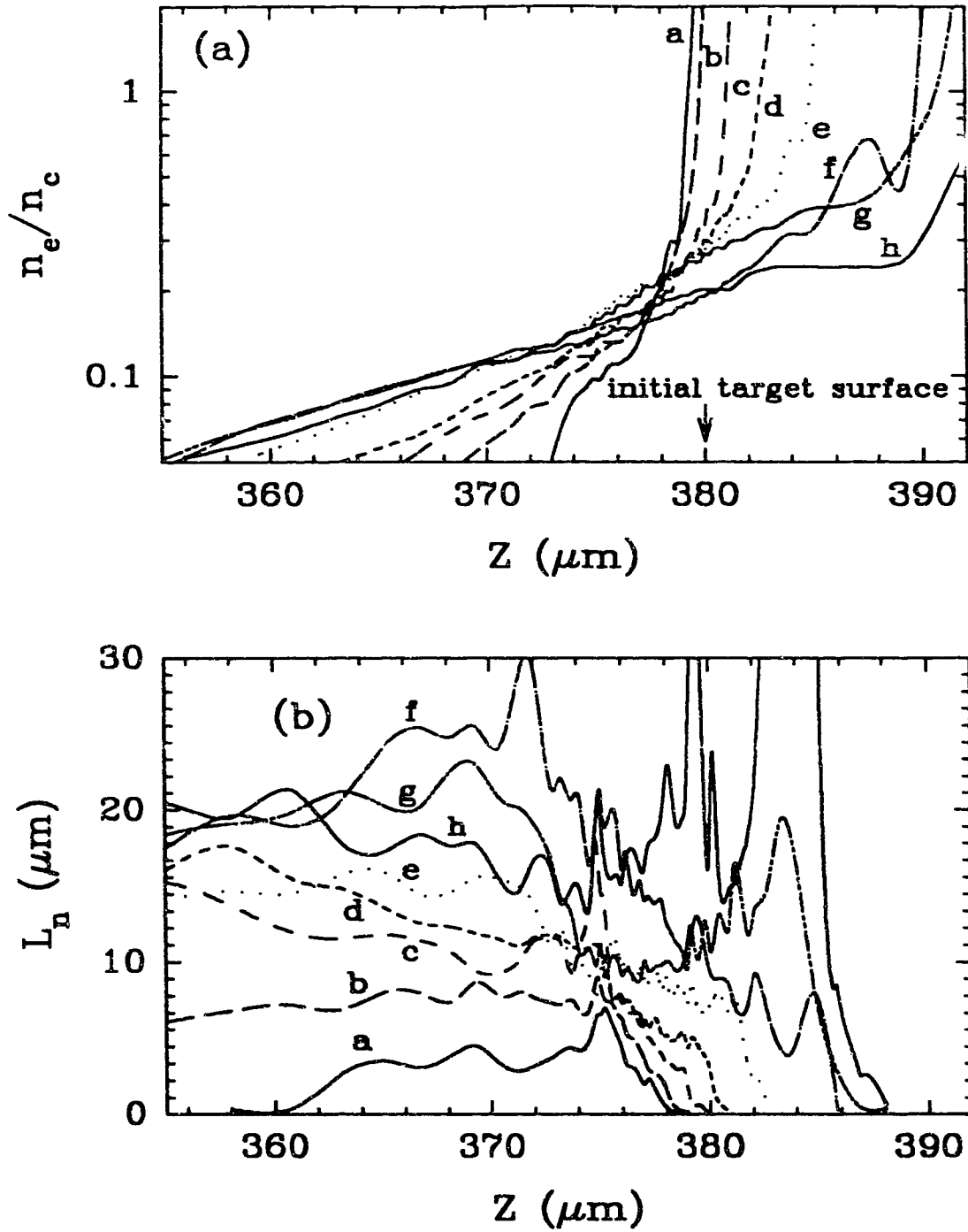


Fig. 4.2. Temporal evolution of  $n_e/n_c$  and  $L_n$  at  $R = 0$  for case SF1.  $t = 0.1\text{ns}$  (a),  $0.2\text{ns}$  (b),  $0.5\text{ns}$  (c),  $0.75\text{ns}$  (d),  $1.0\text{ns}$  (e),  $1.3\text{ns}$  (f),  $1.5\text{ns}$  (g), and  $1.8\text{ns}$  (h).



Figure 4.2 shows the temporal evolution of electron density  $n_e/n_c$  (a) and density scale length  $L_n$  (defined as  $[(dn_e/dx)/n_e]^{-1}$ ) (b) on laser axis (at  $R=0$ ) for the simulation case SF1. The symbols a-h denote time  $t = 0.1\text{ns}$  (a),  $0.2\text{ns}$  (b),  $0.5\text{ns}$  (c),  $0.75\text{ns}$  (d),  $1.0\text{ns}$  (e),  $1.3\text{ns}$  (f),  $1.5\text{ns}$  (g), and  $1.8\text{ns}$  (h), respectively. The density scale length is steady for  $t > 1.0\text{ns}$  as expected for spherical plasma expansion with small focus (i.e., focal spot smaller than  $c_s \tau$ ). This is true for all three simulation cases. Table 4.2. summarizes density scale length and focal spot size for each case. The results show that for large focus,  $L_n$  is slightly larger than  $r_{50\%}$ , whereas  $L_n$  is comparable to  $r_{90\%}$  for small focus. The effect of laser beam refraction is significant for smaller focus.

Table 4.2. Density scale length  $L_n$  and focal spot size  $r_{90\%}$ .

Case	$L_n$ ( $\mu\text{m}$ )	$r_{90\%}$ ( $\mu\text{m}$ )	$r_{50\%}$ ( $\mu\text{m}$ )
LF1	20	28	15
SF1	18	17	9
SF5	15	17	9

#### 4.3. Temporal Evolution of Plasma

Figure 4.3 shows three-dimensional plots of electron density for case SF1 at early time during the laser pulse ( $t < 60\text{ps}$ ). The vertical axis is in units of  $10^{22}\text{cm}^{-3}$  and the upper edge corresponds to the critical density. The time at which each snapshot is taken is indicated in the figure. The laser is incident on the front centre of each box. At  $t=32\text{ps}$  (a), a smooth spherical plasma is created by a Gaussian focused laser beam with density peaking on-axis ( $R=0$ ). At

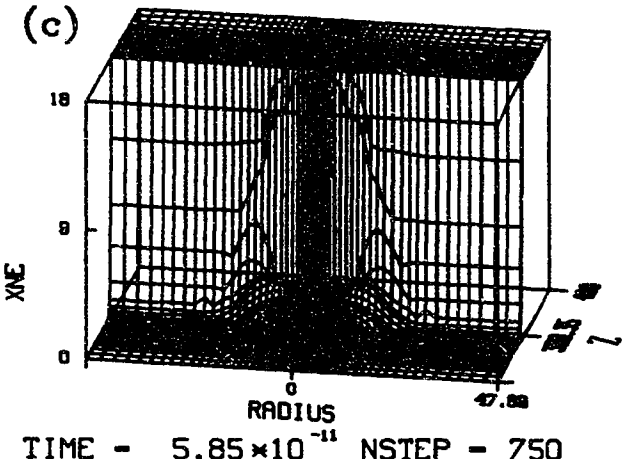
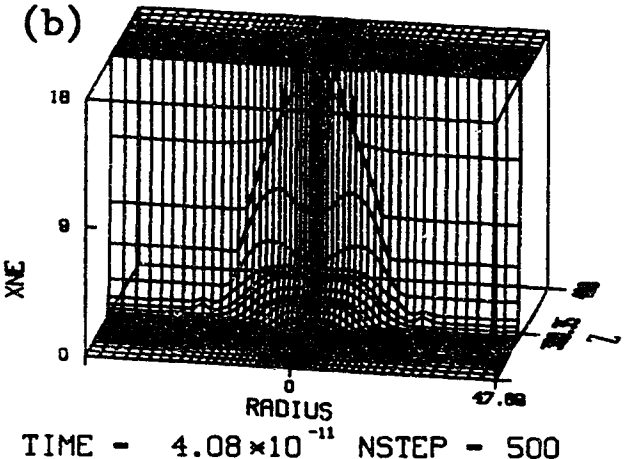
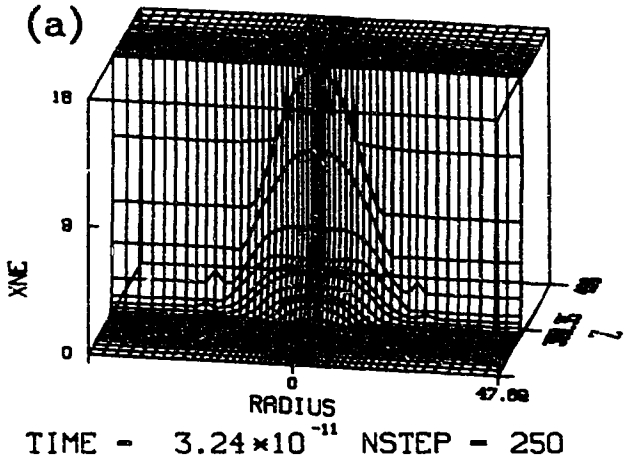


Fig.4.3. Three-dimensional plots of electron density for case SF1 at early time in the laser pulse. The upper edge corresponds to  $n_c$ .

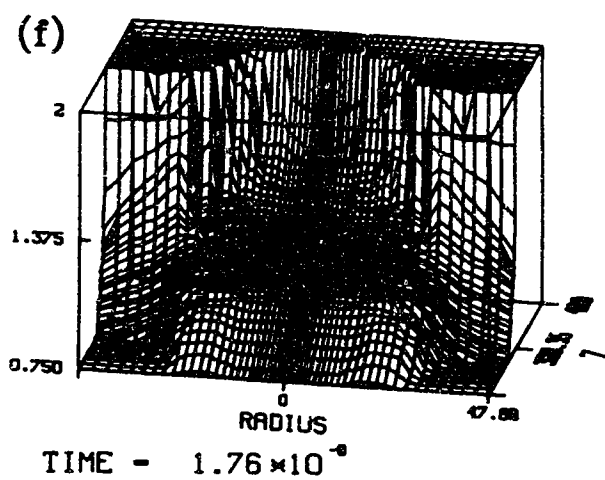
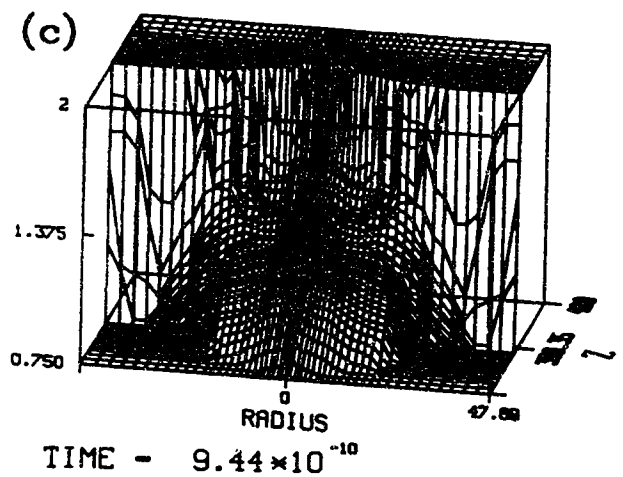
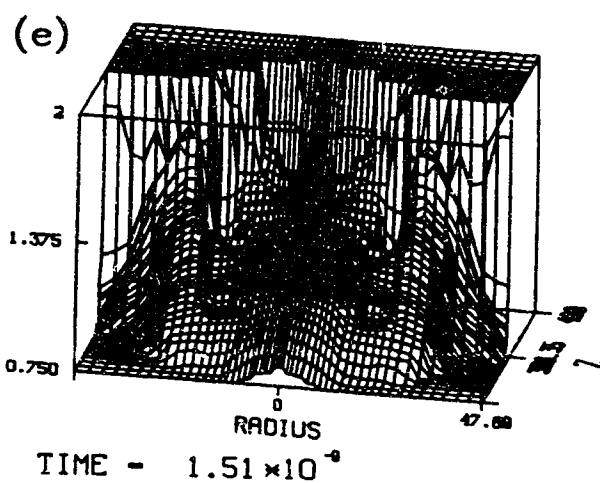
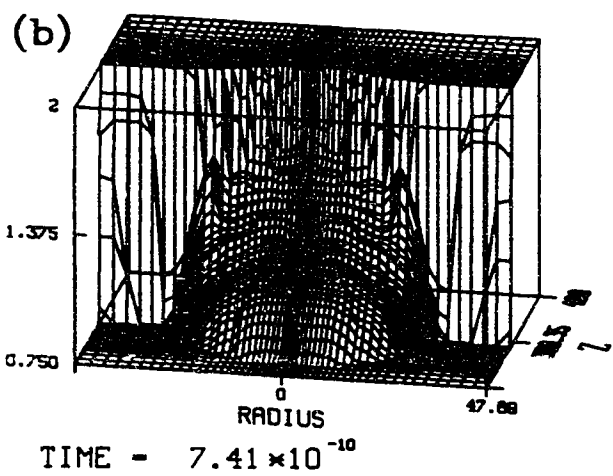
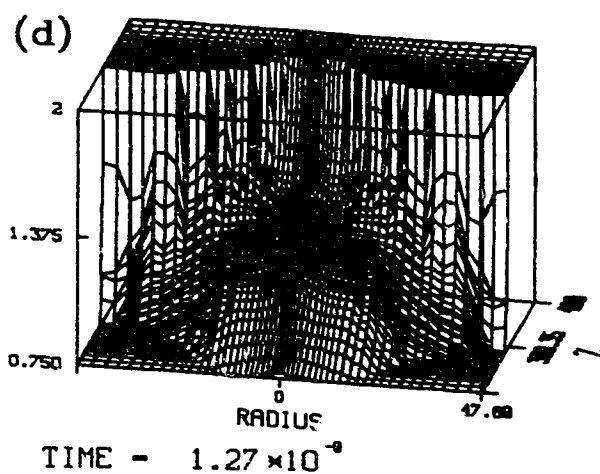
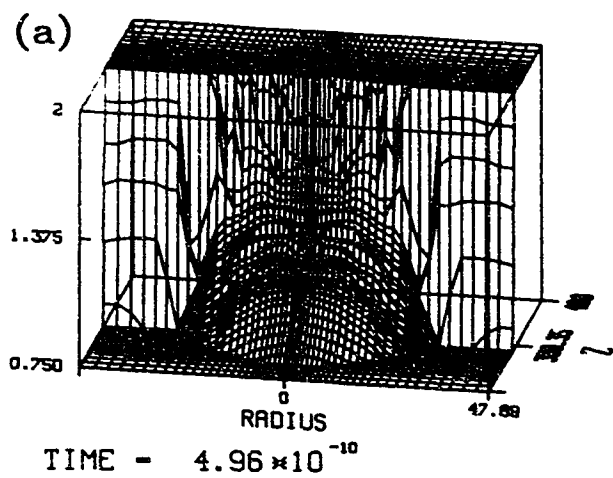


Fig. 4.4. Three-dimensional plots of  $\log_{10}(n_e/0.01n_c)$  for case SF1. The upper edge corresponds to  $n_c$ .

$t=41\text{ps}$  (b), the laser beam is refracted by the already-created plasma, resulting in more plasma ablation off-axis ( $R \approx 10\mu\text{m}$ ). Finally, at  $t=59\text{ps}$  (c), the density peaks off-axis ( $R \approx 20\mu\text{m}$ ) and another density peak appears on-axis ( $R=0$ ), the latter created by laser beam refraction from the off-axis density peak. These results show that large scale ( $\approx$  focal spot radius) density variations can be created by laser beam refraction even with spatially smooth gaussian beams. The time scale of such variations is as small as 20ps.

Figure 4.4 shows three-dimensional plots of  $\log_{10}(n_e/0.01n_c)$  at various times for case SF1. Note values 2 and 1 on the vertical axis correspond to  $n_c$  and  $0.1n_c$ . The time of each snapshot is indicated in the figure. From  $t=0.5\text{ns}$  to  $1.0\text{ns}$  ( (a)-(c) ), plasma expansion is almost spherical and the laser has ablated a shallow layer of the target. One can see 'rattling' density variations overlapped on the spherical plasma. From  $t=1.0\text{ns}$  to  $1.5\text{ns}$  ( (c)-(e) ), the laser has dug a deep hole in the target and plasma created at the edge of the hole ( $R \approx 25\mu\text{m}$ ) starts to expand. At  $t=1.5\text{ns}$  (e), plasma expansion from the bottom and the edge of the hole is comparable. At  $t=1.8\text{ns}$  (f), both plasmas merge together, resulting in large scale locally planar plasma. These results show that a tightly focused short wavelength laser beam can create a locally planar plasma, and the scale of the plasma can be larger than the focal spot due to the refraction.

#### 4.4. Temperature

Figure 4.5 shows contour plots of laser flux ( (a) and (d) ), electron temperature ( (b) and (e) ), and  $\log_{10}(n_e/n_c)$  ( (c) and (f) ) for case SF1 at  $1.8\text{ns}$  ( (a)-(c) ) and SF5 at  $2.0\text{ns}$  ( (d)-(f) ). As

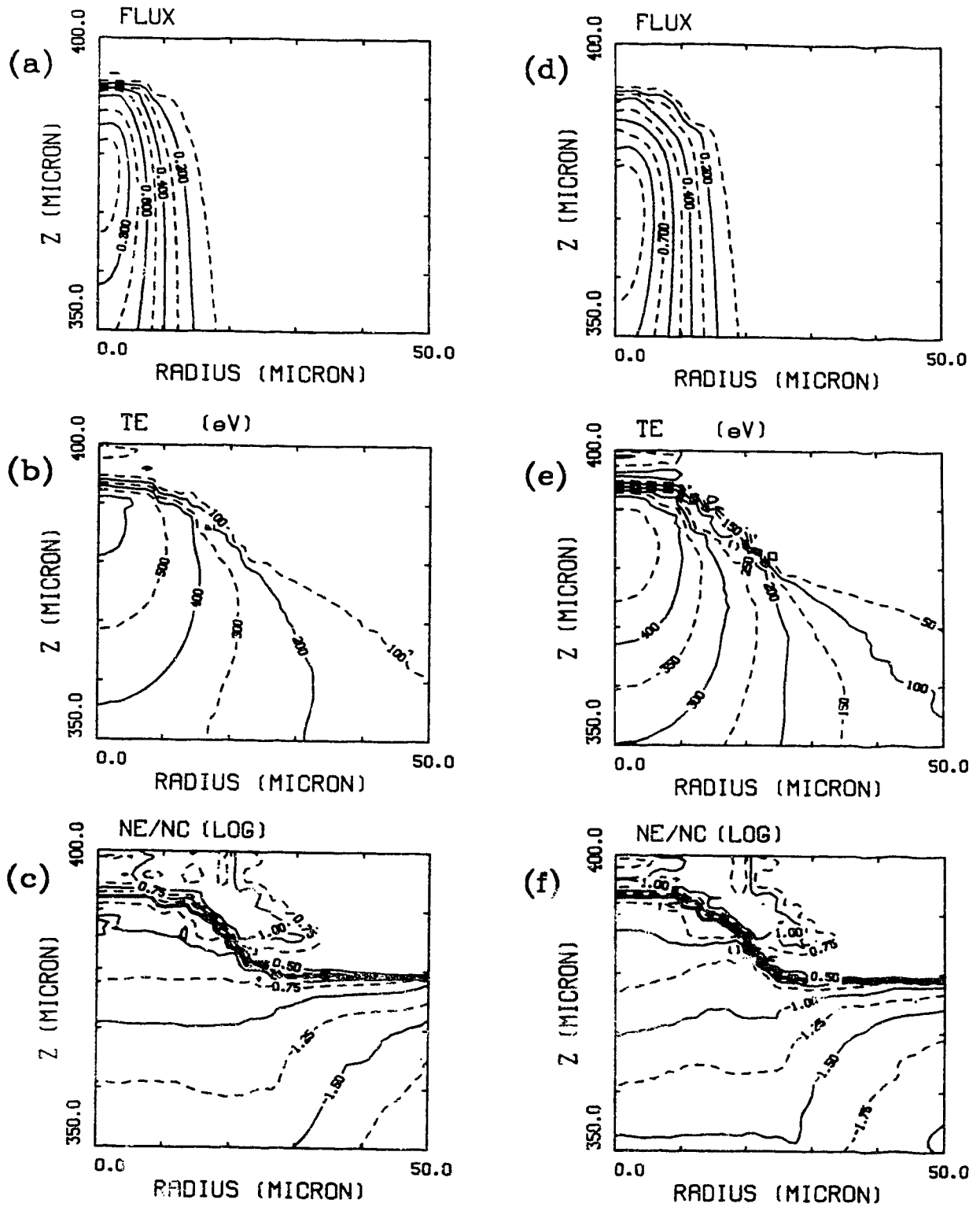


Fig. 4.5. Contour plots of laser flux, electron temperature, and  $\log_{10}(n_e/n_c)$  for case SF1 at 1.8ns ( (a)-(c) ) and SF5 at 2.0ns ( (d)-(f) ).

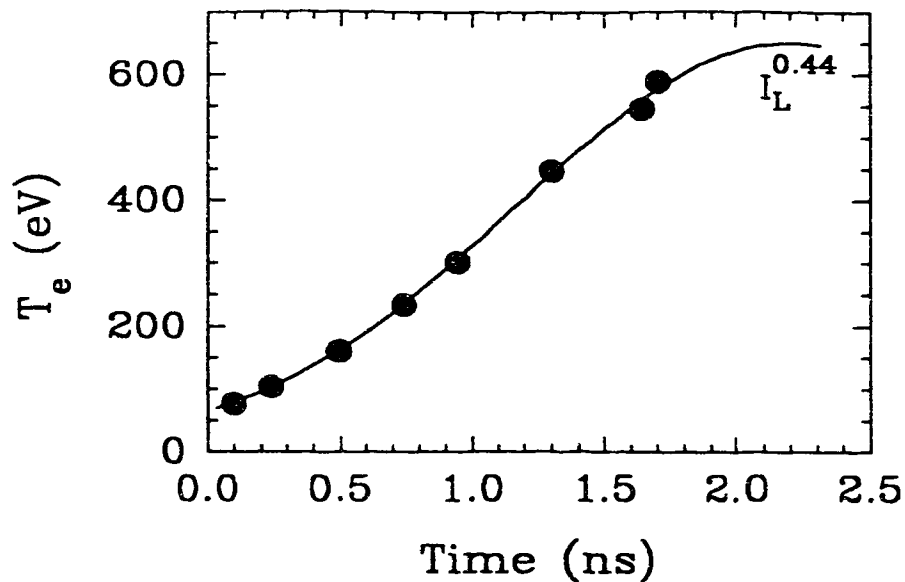


Fig.4.6. Maximum electron temperature as a function of time at  $R=0$  in case SF1 (solid circles). The solid curve shows relative scaling on laser intensity  $I_L^{0.44}$ .

discussed in the previous section, the density contour shows locally planar plasma structure whose scale is about two times larger than the focal spot radius (10% intensity radius). The electron temperature contour, however, shows that plasma heating is localized to the region where laser flux is strong. This is related to the short electron-ion mean free path  $\lambda_{e1}$  which is about  $0.2\text{-}1\mu\text{m}$  in our case. Moreover, x-ray pinhole pictures support this local heating along the laser axis (see section 6.1). It is also noted in passing that  $\nabla T_e \times \nabla n_e$  may cause the formation of strong magnetic fields.

Figure 4.6 shows the maximum electron temperature on axis ( $R=0$ ) as a function of time (solid circles) for case SF1. The solid curve shows the analytical scaling of temperature with intensity expected from the self-regulating model<sup>2)</sup> for spherical steady plasma. The

simulation data agree well with this scaling ( $I_L^{0.44}$ ). This scaling suggests a temperature of 650eV near the peak of the laser pulse which agrees well with the experimentally measured  $T_e \approx 600\text{eV}$  (see section 6.2). Note the simulation data plotted is the maximum temperature but the bulk of the plasma should be cooler than that.

#### 4.5. Plasma flow

Figure 4.7 shows plasma flow velocity vectors overlapped on contour plots of plasma pressure  $\log_{10}(p_e)$  ( $p_e = n_e \cdot T_e$ ) for case SF1 at 1.8ns (a) and SF5 at 2.0ns (b). The pressure  $p_e$  is normalized to the minimum value. Although the density contour showed planar plasma, the plasma pressure profile is spherical. Since plasma flow is driven by  $\nabla p$ , the direction of flow vectors indicates that the expansion is spherical. This novel condition is the consequence of planar plasma created around the hole dug out by the laser and localized plasma heating around the laser axis.

From the velocity data on axis ( $R=0$ ), a velocity scale length  $L_v$  (defined as  $[(dv/dx)/c_s]^{-1}$ , where  $c_s$  is sound speed) was calculated. Figure 4.8 shows the temporal evolution of velocity scale length  $L_v$  on laser axis for case SF1. The symbols a-h denote time  $t = 0.1\text{ns}$  (a),  $0.2\text{ns}$  (b),  $0.5\text{ns}$  (c),  $0.75\text{ns}$  (d),  $1.0\text{ns}$  (e),  $1.3\text{ns}$  (f),  $1.5\text{ns}$  (g), and

Table 4.3. Scale length  $L_n$ ,  $L_v$  and focal spot size  $r_{90\%}$  and  $r_{50\%}$

Case	$L_n$ ( $\mu\text{m}$ )	$L_v$ ( $\mu\text{m}$ )	$r_{90\%}$ ( $\mu\text{m}$ )	$r_{50\%}$ ( $\mu\text{m}$ )
LF1	20	50	28	15
SF1	18	30	17	9
SF5	15	25	17	9

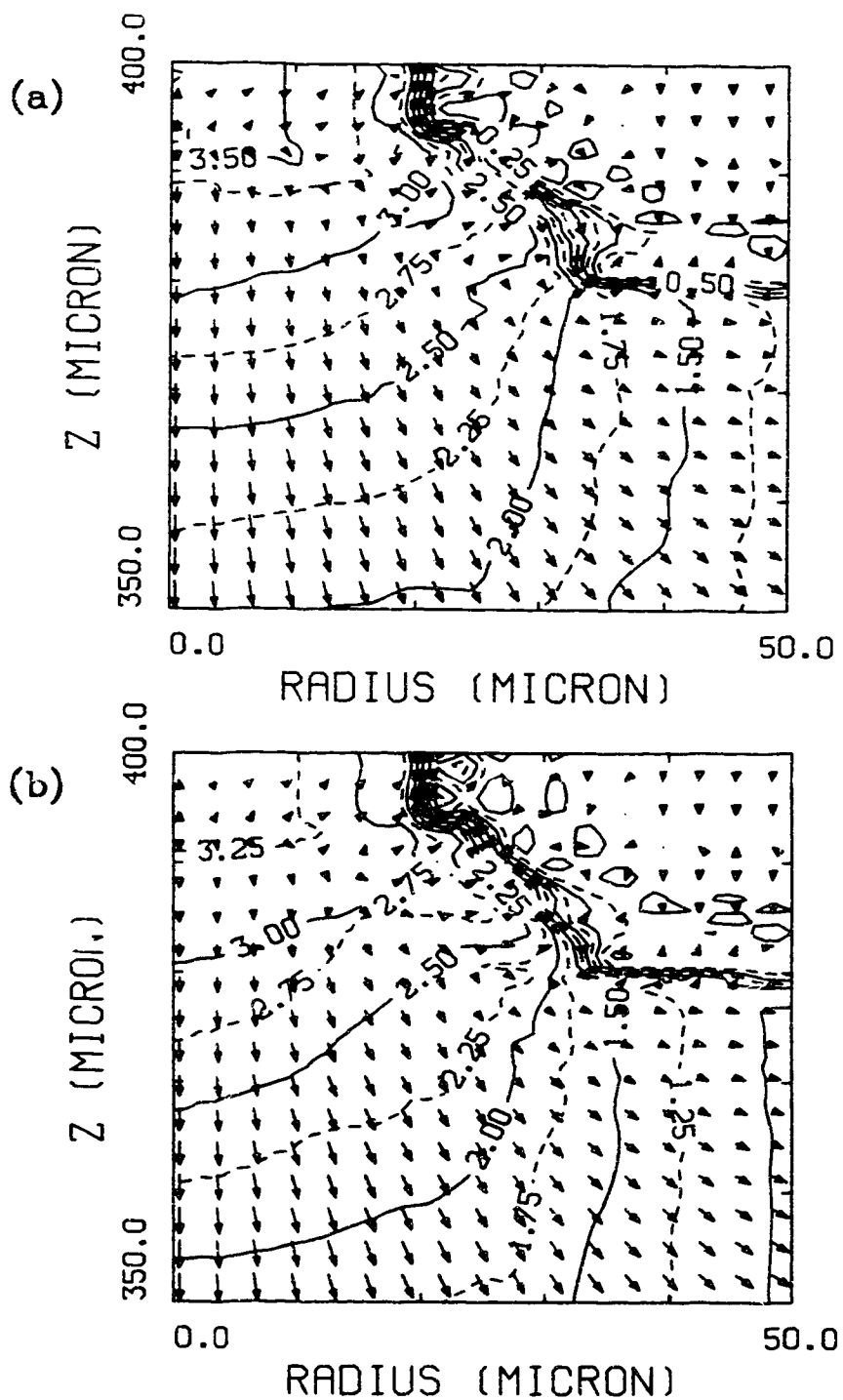


Fig.4.7. Plasma flow velocity vectors overlapped on contour plots of plasma pressure  $\log_{10}(n_e \cdot T_e)$  for case SF1 at 1.8ns (a) and SF5 at 2.0ns (b).



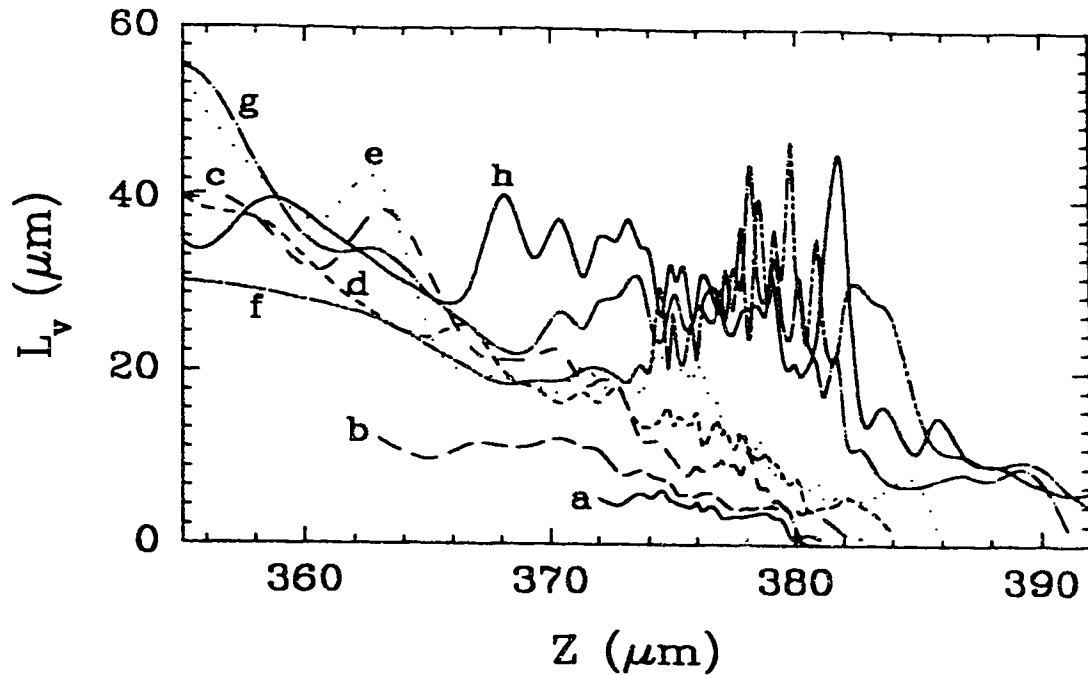


Fig.4.8. Temporal evolution of velocity scale length  $L_v$  at  $R=0$  for case SF1.  $t = 0.1\text{ns}$  (a),  $0.2\text{ns}$  (b),  $0.5\text{ns}$  (c),  $0.75\text{ns}$  (d),  $1.0\text{ns}$  (e),  $1.3\text{ns}$  (f),  $1.5\text{ns}$  (g), and  $1.8\text{ns}$  (h).

$1.8\text{ns}$  (h), respectively. The velocity scale length is steady for  $t > 1.0\text{ns}$ , consistent with the density scale length results. Again, this is true for all three simulation cases. Table 4.3. summarizes density scale length, velocity scale length and focal spot size for each case.  $L_v$  is about twice as large as  $L_n$ .

#### 4.6. Phase Mismatch

For SBS in an inhomogeneous plasma, phase mismatch among three waves is an important factor in restricting the SBS growth<sup>3)</sup>. Here, we estimate the phase mismatch in our plasma from the CASTOR data. Assuming matching conditions of SBS, eq.(2.1) and (2.2), are satisfied at  $x=0$ , the wave number mismatch  $\kappa(x)$  is defined as

$$\kappa(x) = k_0(x) + k_1(x) - k_s(x) \quad (4.3)$$

with condition  $\kappa(0) = 0$ . Assuming  $\kappa(x)$  changes linearly in space, that is  $\kappa(x) = \kappa'x$ , the phase mismatch rate  $\kappa'$  is given by

$$\kappa'(x) = \frac{\partial}{\partial x} k_0 + \frac{\partial}{\partial x} k_1 - \frac{\partial}{\partial x} k_s \quad (4.4)$$

From the dispersion equations (2.3) and (2.4), eq.(4.4) is reduced to<sup>4)</sup>

$$\kappa' = k_0 \cdot \left[ \frac{\frac{2}{L_v} - \frac{1}{L_T}}{1 - M} + \frac{n_e}{n_c} \cdot \left( 1 - \frac{n_e}{n_c} \right)^{-1} \cdot \frac{1}{L_n} \right] \quad (4.5)$$

for  $k_s \approx 2k_0$ , where  $M$  is the Mach number, and  $L_v$ ,  $L_T$ , and  $L_n$  are scale length of velocity, temperature and electron density, defined as

$$L_v = [(dv/dx)/c_s]^{-1} \quad (4.6a)$$

$$L_T = [(dT/dx)/T]^{-1} \quad (4.6b)$$

$$L_n = [(dn/dx)/n]^{-1} \quad (4.6c)$$

where  $c_s$  is sound speed. Using this phase mismatch rate  $\kappa'$ , the SBS gain in an inhomogeneous plasma is given by<sup>3)</sup>

$$G_{lh} = \frac{2\pi\gamma_0^2}{|v_g v_s \kappa'|} \quad (4.7)$$

where  $v_g$  and  $v_s$  are group velocities of EM wave and ion wave. In a flowing plasma  $v_s = c_s - v_p$ , where  $v_p$  is the plasma flow velocity. From eq.(4.5), the denominator of eq.(4.7) is given by

$$|v_g v_s \kappa'| = c_s \omega_0 \left[ 2 \left( 1 - \frac{n_e}{n_c} \right) \frac{1}{L_v} - \frac{n_e}{n_c} \frac{1}{L_n} (1-M) \right] \quad (4.8)$$

Figure 4.9 shows the CASTOR prediction of plasma profile (a), scale length (b) and phase mismatch  $\kappa'$  and denominator of eq.(4.7) (c). These data are plotted for case SF5 at 2.0ns and R=0. In fig.4.9 (a), the electron temperature  $T_e$  and the homogeneous growth rate  $\gamma_0$  are normalized to 500eV and  $1 \times 10^{12}$  1/s. From the profile shown in (a), the scale lengths of velocity, temperature and density were calculated

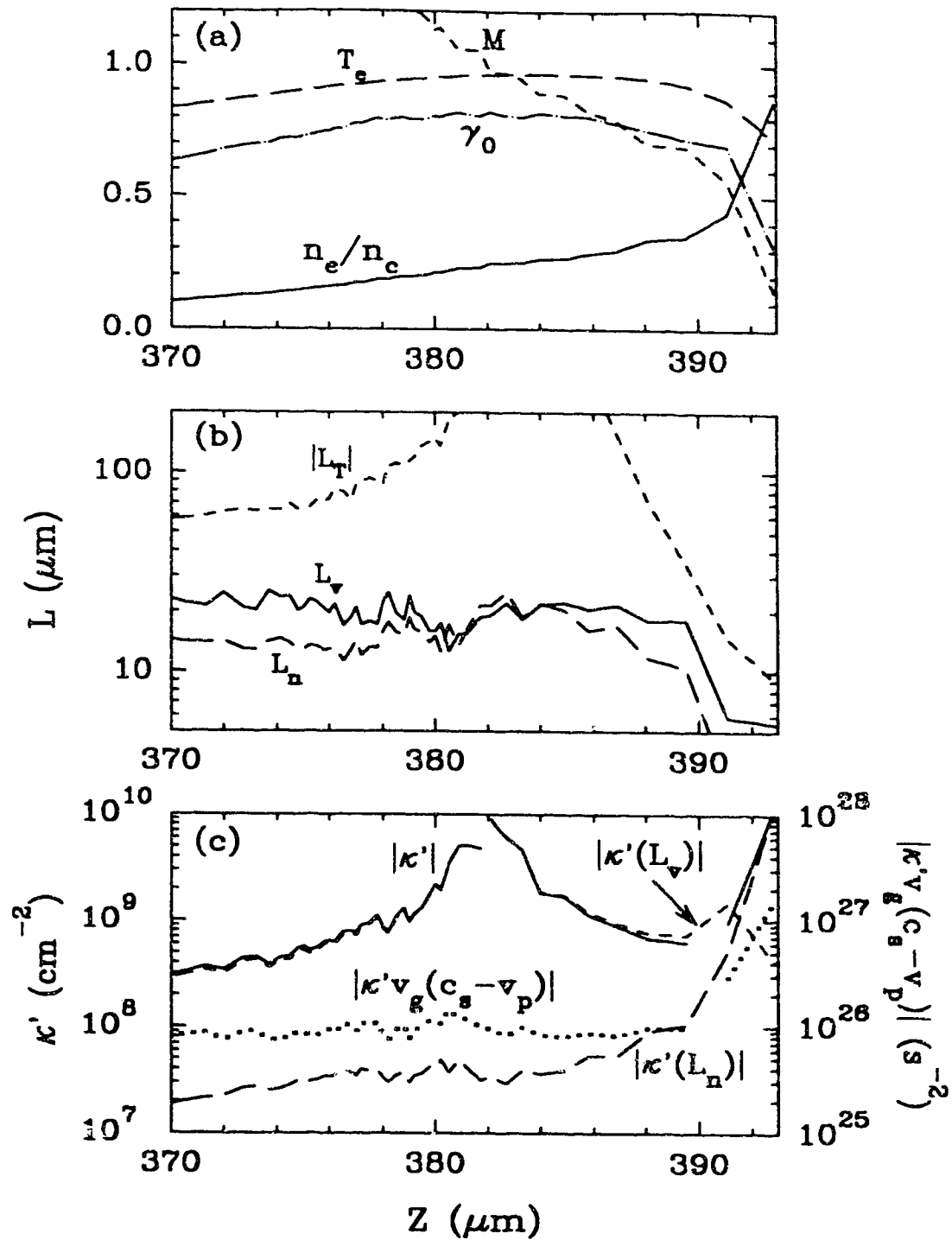


Fig.4.9. CASTOR predictions at  $R=0$  for case SF5 at 2.0ns. Spatial profile of  $n_e/n_c$ ,  $T_e$ ,  $M$ ,  $\gamma_0$  (a), scale lengths (b), and phase mismatch (c).

and are shown in (b).  $L_v$  ( $\approx 25\mu\text{m}$ ) is slightly larger than  $L_n$  ( $\approx 15\mu\text{m}$ ), whereas  $L_T$  ( $>60\mu\text{m}$ ) is much larger than  $L_n$ . Therefore, in eq.(4.5), it is reasonable to ignore  $L_T$ . Using data shown in (a) and (b),  $\kappa'$  was calculated. Since eq.(4.5) has a singular point at  $M=1$ , the solid line in (c) is discontinued at  $Z \approx 382\mu\text{m}$  where  $M=1$ . The denominator in eq.(4.7), however, is smooth at  $M=1$ . It is noted that since in our typical plasma,  $L_v$  and  $L_n$  have an opposite signs in eq.(4.5),  $\kappa'$  vanishes at some point. Assuming  $L_v = -\alpha \cdot L_n$ , where  $\alpha$  is a constant, eq.(4.5) can be solved for the density at which  $\kappa'=0$ , giving condition

$$\frac{n_e}{n_c} = \frac{2}{(1-M)\alpha} \cdot \left( 1 - \frac{n_e}{n_c} \right) \quad (4.9)$$

or

$$\frac{n_e}{n_c} = 2 / \{ (1-M)\alpha + 2 \} \quad (4.10)$$

when  $L_T$  is ignored. For example,  $\kappa'=0$  at  $n_e/n_c=0.77$  for  $\alpha=2$ ,  $M=0.7$ . In fig.4.9 (c), such a point exists at  $Z \approx 390\mu\text{m}$  hence the solid line ( $|\kappa'|$ ) and the dotted line ( $|\kappa' v_g (c_s - v_p)|$ ) are discontinued in the log scale. Contributions from  $L_v$  and  $L_n$  to  $\kappa'$  are also plotted in fig.4.9 (c). In the region we are interested ( $0.3 < n_e/n_c < 0.5$ ),  $\kappa'$  is approximately  $10^9 \text{cm}^{-2}$  and the denominator  $|\kappa' v_g (c_s - v_p)|$  is about  $10^{26} \text{s}^{-2}$ . Note these calculations and the location of the singular points are rough estimates, since the simulation data do not have enough resolution at  $Z > 385\mu\text{m}$  (mesh spacing  $\Delta Z$  is large).

#### 4.7. Summary

The two-dimensional hydrodynamic simulation code CASTOR predicts that: 1) a plasma larger than the focal spot is created by plasma

refraction of the laser radiation, 2) the refraction effect is more significant for smaller focus, 3) even a spatially smooth gaussian beam can produce large scale density variations, 4) a tightly-focused short wavelength laser beam tends to 'dig' a hole on the target surface, resulting in locally planar plasma, 5) plasma heating is localized due to the short  $\lambda_{ei}$ , 6) as a consequence of the planar plasma and local heating, plasma expansion becomes spherical and steady at early time in the laser pulse, 7) the density scale length is comparable to the 90% energy radius in the case of small focus and the velocity scale length is about twice as large as the density scale length, and 8) plasma inhomogeneity is important for SBS and the phase mismatch rate is estimated to be  $10^9 \text{cm}^{-2}$ .

#### Bibliography

- 1) J.P.Christiansen and N.K.Winsor, Comp.Phys.Comm., **17**, 397 (1979).  
R.Rankin, R.Marchand, and C.E.Capjack, Phys.Fluids, **31**, 2327 (1988).
- 2) P.Mora, Phys.Fluids, **25**, 1051 (1982).  
F.Dahmani and T.Kerdja, Phys.Fluids, **B3**, 1232 (1991).
- 3) M.N.Rosenbluth, Phys.Rev.Lett., **29**, 565(1972).
- 4) C.S.Liu, M.N.Rosenbluth, and R.B.White, Phys.Fluids, **17**, 1211 (1974).

## V. Experimental Methods

In this chapter, characteristics of the laser system and an outline of the SBS experiments are described. Temporal behavior of the laser pulse and spatial features of the laser focal spot were monitored every shot. Details of the focal spot were measured separately by using high resolution optics to characterize the temporal and spatial intensity distribution in the spot. These results provided basic information for interpreting the experimental results. The SBS experiments were performed with the 0.248 $\mu\text{m}$  wavelength KrF laser. Various kinds of materials, with atomic number ranges from 6 (carbon) to 79 (gold) were used as solid targets. The targets were oriented at various angles from 0° to 60° with respect to the laser axis. A wide variety of instrumentation was used in the experiments to measure SBS features and to monitor background plasma conditions. X-ray and UV emissions from the plasma were used as principal diagnostics. The apparatus and its implementation are discussed in this chapter.

### **5.1. Characteristics of the KrF Laser at the University of Alberta**

#### **5.1.1. Outline of the KrF Laser System**

The KrF laser used in this study is a multi-module, pulse compressed laser system, consisting of four major components. These are: 1) injection locked front-end laser system<sup>1)</sup>, 2) KrF discharge pumped pre-amplifiers, 3) electron beam pumped power amplifier<sup>2)</sup>, and 4) optical compressor utilizing stimulated backward Brillouin scattering (SBS) in SF<sub>6</sub><sup>3)</sup>. A schematic diagram of this system is

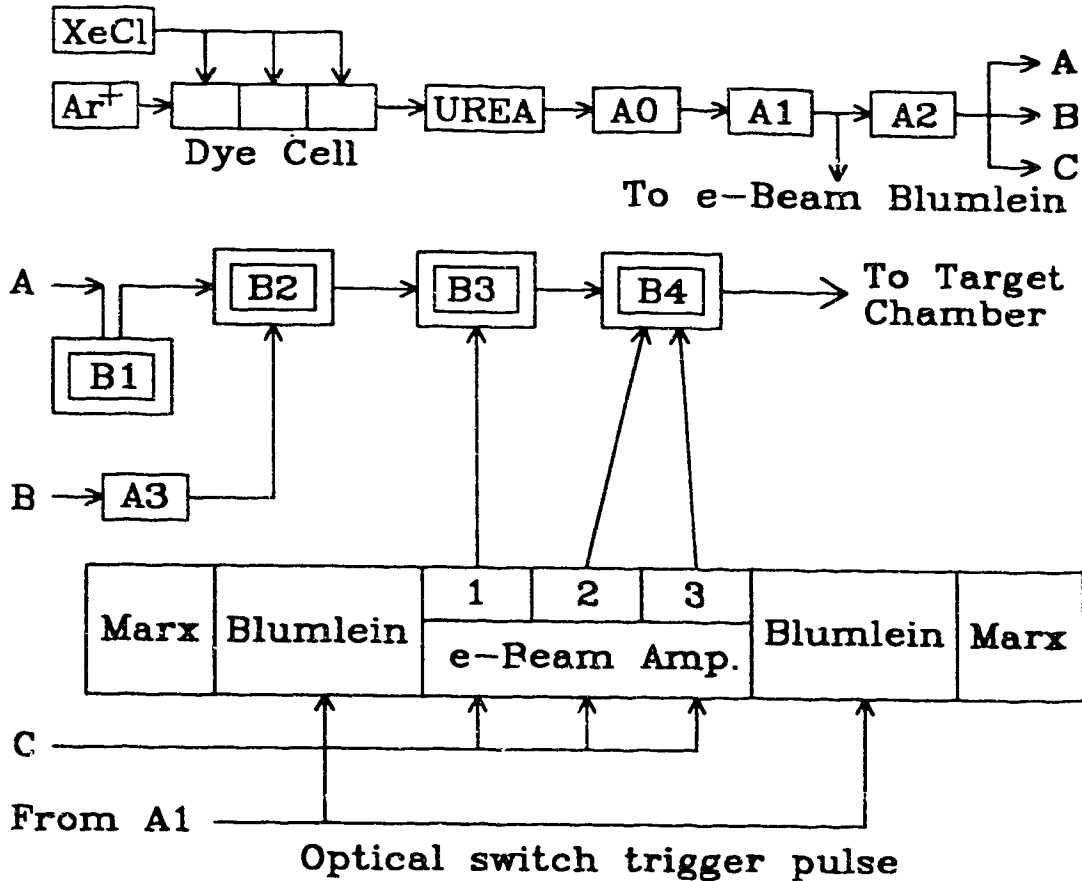


Fig.5.1. Schematic diagram of KrF laser system at University of Alberta

shown in fig.5.1.

The injection locking laser system utilizes the output of a cw Argon ion laser ( $\lambda=0.4965\mu\text{m}$ ) which is amplified in three dye laser pumped amplifier stages, and then frequency-doubled in a UREA crystal to give a narrowband  $0.25\mu\text{m}$  light source for injecting into the KrF discharge front-end. The Argon ion laser is operated in the  $\text{TEM}_{00}$  single frequency mode to provide a narrow linewidth source. The dye (Coumarin 500) amplifier stages are pumped by a XeCl pulsed laser (7ns

duration). The output from UREA crystal (pulse width of 3.5ns) is split into two beams and then stacked to provide a 6.5ns pulse.

The narrowband output ( $\approx 100\text{MHz}$ ) is amplified in A0 before injecting into A1, which has an unstable resonator cavity, and utilizes UV-preionized discharge pumping. A portion of the A1 oscillator (25ns duration) output is used to laser trigger the e-beam pumped amplifier. The output of amplifier A2 is split into three beams. The first beam is focused into  $\text{SF}_6$  Brillouin cell B1 and the phase conjugated Stokes output provides the seed pulse for amplification in the following Brillouin cells. The second one is amplified by A3 to pump the Brillouin cell B2. The third one is split into three beamlets which are optically delayed and angle encoded to extract the e-beam pumped KrF amplifier (60ns pulse duration).

The electron beam pumped amplifier consists of two pulsed power modules (Marx banks and Blumlein pulse forming lines) which generate electron beams to pump the laser cell from opposite sides. The composite beam from A2 extracts the high energy amplifier by using a 3 beam triple pass technique. One of the three amplified beamlets is used to pump Brillouin cell B3 and the other two beamlets are used to pump Brillouin cell B4.

The optical compressor system thus consists of 4 stages of  $\text{SF}_6$  gas cells: one SBS generator (B1) and 3 SBS amplifiers (B2, B3, B4). The Stokes pulse (short duration, low energy) and counter-propagating pump pulse (long duration, high energy) pass through the cell at the same time. Stimulated Brillouin scattering in the  $\text{SF}_6$  gas transfers energy from the pump pulse to the Stokes pulse, resulting in power amplification and reduction in pulse duration of the Stokes pulse.



Power amplification of  $\approx 40$  with energy conversion efficiencies of  $\approx 20\%$  can be achieved in practice. The final output of cell B4 is transported to the target chamber for the laser-plasma interaction experiments.

This high energy KrF laser system can provide 248nm wavelength radiation in pulses of 1-2ns with energy of 1J. The 4cm  $\times$  6cm laser beam was focused with an 18cm aspheric doublet quartz lens producing a spot size of 20 $\mu$ m (90% energy contour) and the intensity at the focus is typically  $\approx 10^{14}$  W/cm<sup>2</sup>. The system is controlled by a computer (IBM PC-AT). A trigger pulse is sent from the computer and energy and pulse timing data at each amplifier stage are measured on every shot. For e-beam operation, the pressure of gas cells and vacuum diodes as well as charging voltage of Marx banks are monitored in real time. These data are collected by a CAMAC based integrated data acquisition system and displayed on a video screen.

### 5.1.2. Temporal and Spatial Characteristics

Figure 5.2 shows multiple plots of typical laser pulse shapes measured by a streak camera (temporal resolution  $\Delta t = 200$ ps for 10ns streak time and camera slit width of 30 $\mu$ m). The thick solid line is a modelled double Gaussian pulse which is given by

$$I(t) = I_{\max} \exp \left[ - \left( \frac{t - t_{\max}}{1.2 \cdot t_{\text{HWHM}}} \right)^2 \right] \quad (5.1)$$

$$t_{\text{HWHM}} = 0.8\text{ns} \quad (t \leq t_{\max})$$

$$1.6\text{ns} \quad (t > t_{\max})$$

where HWHM is half width at half maximum. The FWHM (full width at half maximum) of the laser pulse is 2.4ns and  $t_{\max}$  is 2.2ns in this

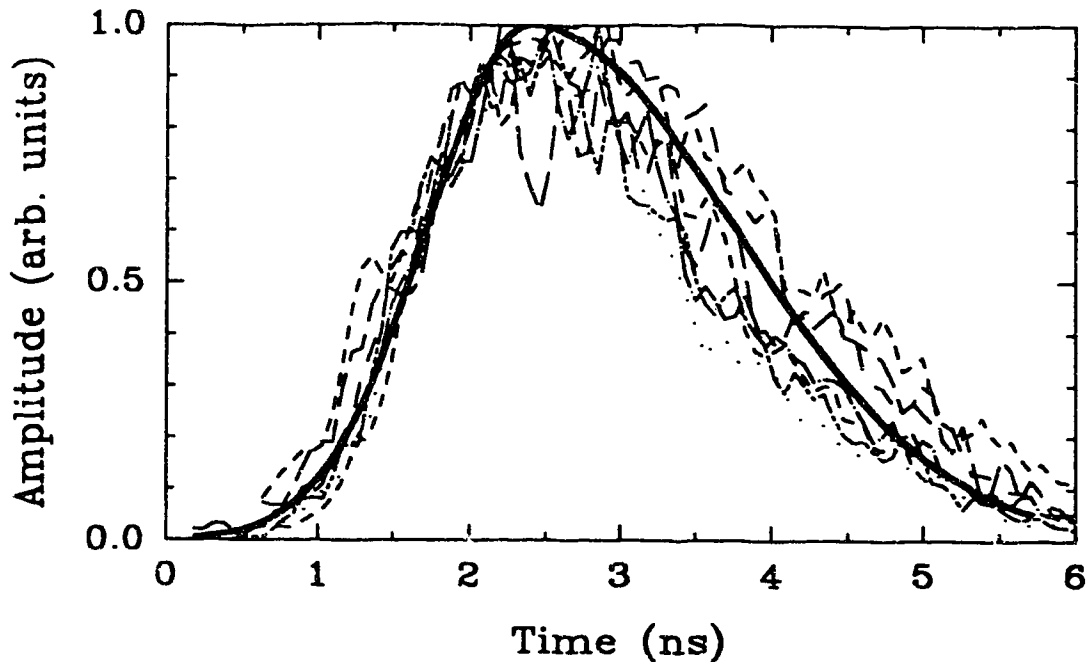


Fig.5.2. Multiple plots of measured laser pulse shapes (dashed and dotted lines) and modelled double Gaussian pulse (thick solid line) .

case. The measured pulse shape has a slight temporal modulation; typically 100-200ps in time and 10-20% in amplitude. Overall, it is a fairly smooth pulse in time.

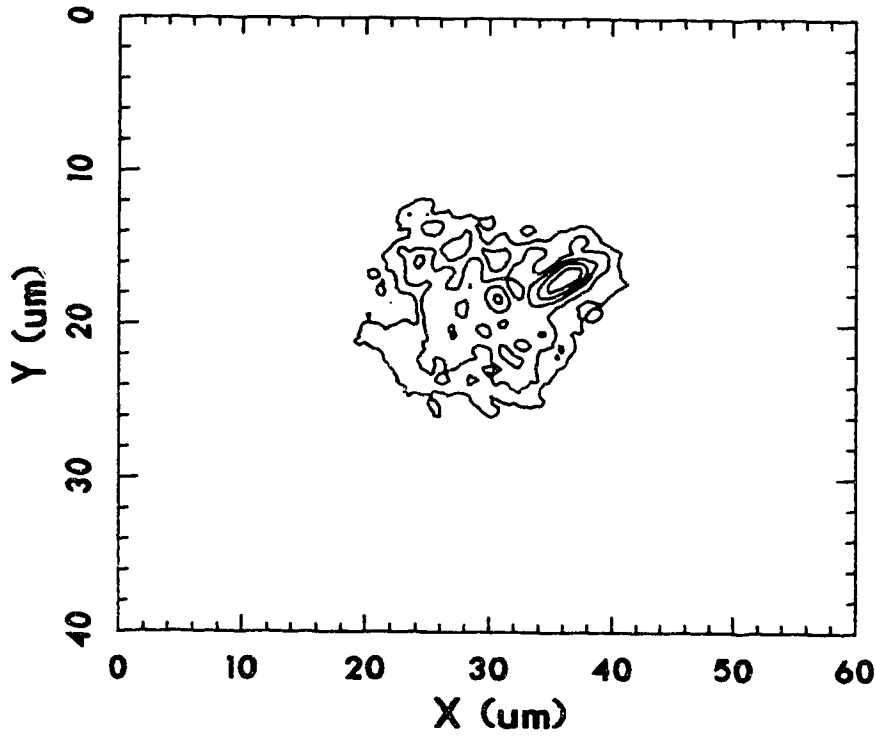
Pre-pulse level was measured separately by a pair of photodiodes, one for the main pulse (with high attenuation) and the other for the prepulse (with much less attenuation). The photodiode response time was about 0.5ns. The power level of the prepulse which begins 7ns prior to the main pulse was measured to be  $3 \times 10^{-5}$  relative to the main pulse. The amount of energy contained in the prepulse was estimated to be  $8 \times 10^{-5}$  relative to the main pulse.

Figure 5.3 shows the spatial profile of a typical focal spot energy distribution for the case of amplified pulse with output energy

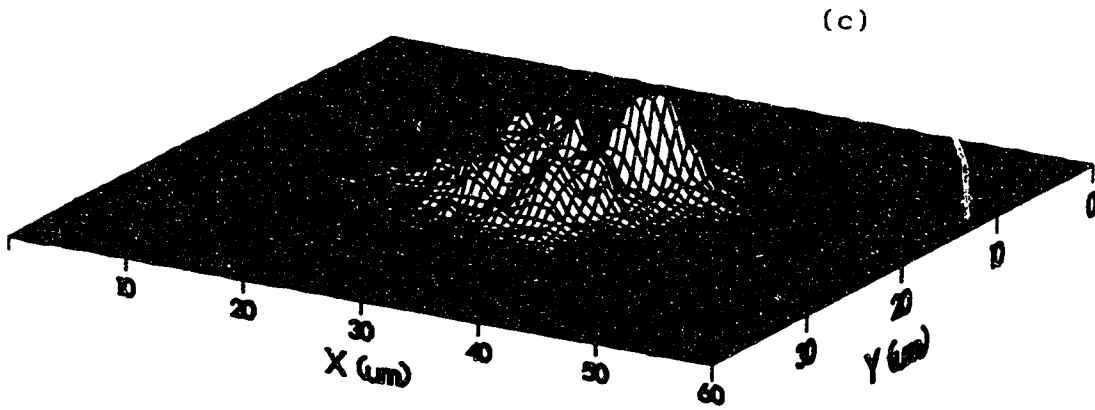


(a)

Fig.5.3. Image of focal spot (a), its contour (b), and 3D intensity map (c). Laser energy was 750mJ.



(b)



(c)

of 750mJ. The image of the focal spot was magnified by a UV-microscope objective lens and relayed to the streak camera which was operated in focus mode (time-integrated). The streak camera has a dynamic range of  $10^2$ . The magnification M was  $\approx 50$ , and the spatial resolution of the optical system was better than  $2\mu\text{m}$ . The time-integrated image shows several intense spots whose scale is smaller than  $\approx 5\mu\text{m}$ . Figure 5.4 shows the energy distribution 'histogram' of the spot; each pixel in the image was sorted in order of amplitude and the amplitude is plotted in descending order from the left to the right. The number of pixels represents total area and is normalized to 100. Four sets of data are plotted in various solid, dashed, dotted curves. The horizontal long-dashed line shows the average energy fluence which is defined below. If the focal spots were perfectly uniform, it would be a flat level line. The thick solid line is our model of focal spot energy fluence distribution which is described later. The peak amplitude and total area were normalized to 100. 90% and 50% of energy was contained in areas of  $330\mu\text{m}^2$  (equivalent to  $20\mu\text{m}$  diameter spot) and  $86\mu\text{m}^2$  (equivalent to  $10.5\mu\text{m}$  diameter spot).

We define the average energy fluence  $\Phi$  as

$$\Phi_{\text{av}} = E_{\text{total}} / \text{Area}_{90\% \text{ energy}} \quad (5.2)$$

where  $E_{\text{total}}$  is the total laser energy and  $\text{Area}_{90\% \text{ energy}}$  is the area which contains 90% of the total energy. The dashed line in fig.5.4 shows the average fluence of the measured energy profile. The peak fluence is about four times higher than the average fluence. We have modelled our non-uniform focal spot with three levels of fluence. Table 5.1 shows parameters of the focal spot model. Fluence is

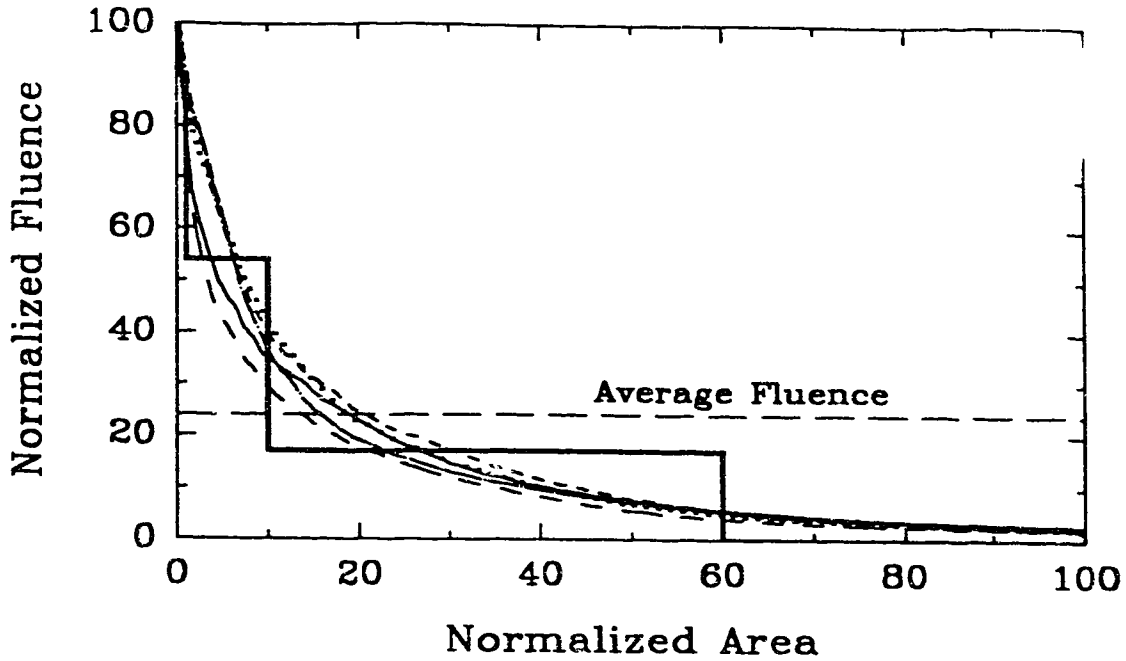


Fig.5.4. 'Histogram' of focal spot energy fluence distribution. The long-dashed line shows average fluence. The thick solid line shows our model of the fluence distribution.

Table 5.1. Model of focal spot energy fluence distribution

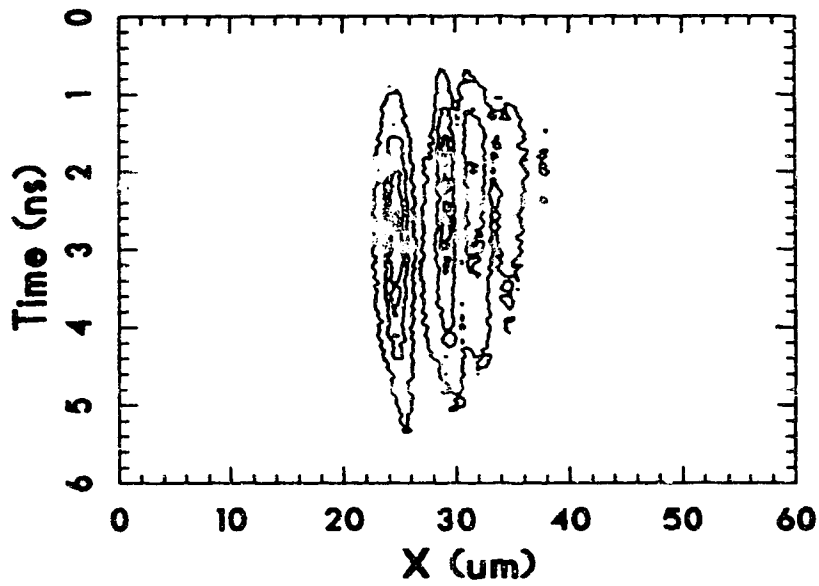
Area No.	Fluence	Area (%)	Energy contained
1	90 (3.8)	1	0.06
2	54 (2.3)	9	0.34
3	17 (0.7)	50	0.60
Average	24 (1.0)	100	1.00

normalized to its peak value of 100 and the numbers in the brackets are fluence relative to the average fluence. The area is also normalized to a total area of 100. The total contained energy is normalized to unity. This distribution is shown in the thick solid line in fig.5.4. Although the focal spot has an intense hotspot (area 1) whose fluence

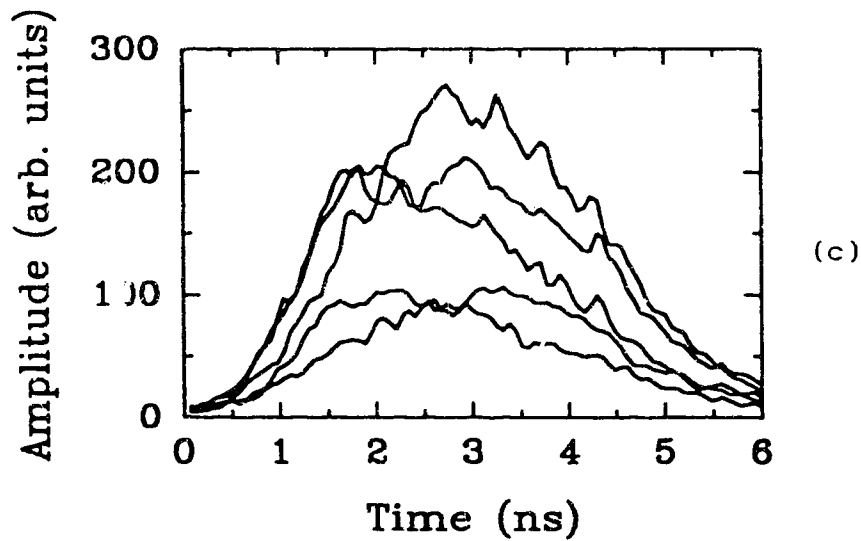


(a)

Fig.5.5. Image of streaked focal spot (a), its contour (b), and temporal shape of each bright stripe in the image (c).



(b)



(c)

is four times higher than the average fluence, the energy contained in the hotspot is only 6% of the total. The medium fluence area (area 2) has two times higher fluence than the average. Its area is about 10% of the total and contains 30% of the total energy. We expect this area plays an important role in the nonlinear evolution of SBS at high intensity. Most of the energy is contained in area 3, and its fluence level is almost the same as the average fluence. Since it contains 60% of the total energy, we expect this region dominates the interaction process.

It is important to measure the temporal behavior of the hotspot. To determine whether the hotspot is temporally changing or not, we streaked the image of the focal spot. A slice of the focal spot (width  $\approx 3\mu\text{m}$ ) was streaked in time. Figure 5.5 shows a typical streaked image of the focal spot: (a) streaked image, (b) its contour map, and (c) temporal shape of each bright stripe in the image which corresponds to the hotspot and its vicinity. The results show that each part of the focal spot has a similar temporal shape. Even the intense hotspot showed a smooth temporal shape similar to the overall (space-integrated) pulse shape (see fig.5.2). Consequently, the intensity variations in the focused beam are primarily due to spatial variation in energy distribution.

## 5.2. Targets

Three kinds of target material were used to investigate SBS in the KrF laser-produced-plasma. Mainly aluminum (Al, atomic weight  $A=27$ ) was used as a target. The surface of the aluminum target was polished by a micro-lathe giving a mirror-like-surface. Additionally, as a low

Z target, Carbon (C, A=12) ( both pure carbon slab and plastic plate (polystyrene,  $C_8H_8$ ) ) and, as a high Z target, gold (Au, A=197) were used. Both carbon and gold targets were prepared by pasting commercially available foils on a plate. The thickness of the pure carbon and pure gold foils were 125 $\mu$ m and 25 $\mu$ m, respectively. These foils were thick enough not to burn through during the laser pulse. Target Z is important in determining plasma collisionality, i.e., electron-ion and ion-ion collisions (see section 2.3). This is especially so in KrF laser-produced plasma where the critical density is about one-fourth of solid density and the collisional mean free path is much shorter than typical plasma scale lengths.

The targets were oriented at various angles (  $0^\circ$ ,  $22.5^\circ$ ,  $45^\circ$ , and  $60^\circ$  ) with respect to the incident laser beam. If the plasma expansion is planar, the angle of incidence is expected to change the conditions of laser-plasma interactions. In the first place, the incident beam propagates through plasma with longer density scale length at an oblique angle. Secondly, the laser light is specularly reflected at lower density. The density of the turning point  $n_t$  is given by<sup>4)</sup>

$$n_t = n_c \cdot \cos^2 \theta \quad (5.3)$$

where  $n_c$  is the critical density,  $\theta$  is angle of incidence. The variation of these two parameters may affect the net Brillouin backscatter reflectivity. Furthermore, experimentally measured SBS spectra are doppler-shifted (see eq.(2.24) ) due to the plasma flow hence  $\theta$  is important in interpretation of the experimental data. On the other hand, if the expansion becomes spherical, the influence of  $\theta$  may not be as important.



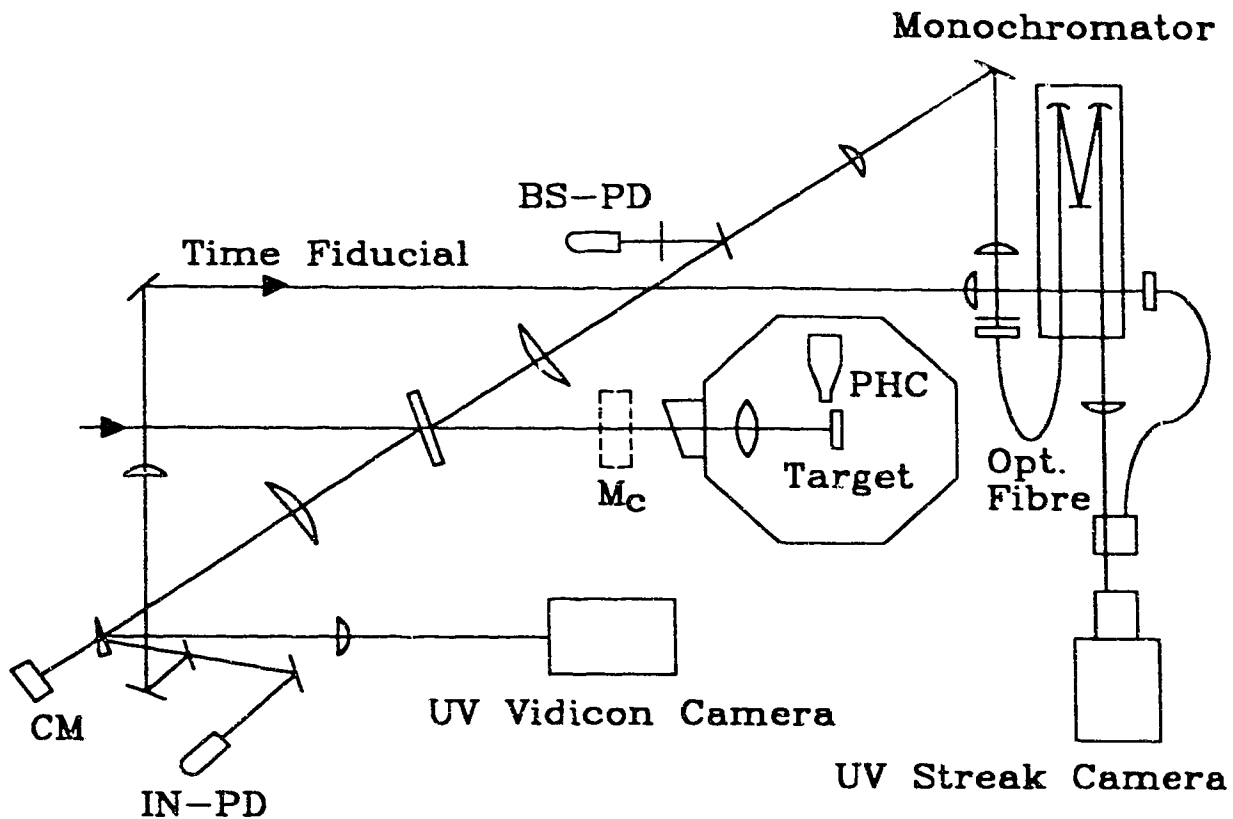


Fig.5.6. Schematic diagram of experimental setup

### 5.3. Diagnostics

#### 5.3.1. Experimental Setup

Figure 5.6 shows a schematic diagram of the experimental setup. CM, PD and PHC represent pyroelectric calorimeter, photodiode and pinhole camera. The 4cm x 6cm laser beam was focused with an 18cm aspheric doublet quartz lens onto targets mounted in a vacuum chamber of 80cm diameter. In this experiment, the laser focus was kept constant for all measurements. Variation of laser intensity was obtained by changing the laser energy. Part of the incoming laser beam was split into a calorimeter (energy monitor), a photodiode (pulse monitor), a UV vidicon camera (equivalent focal spot monitor) and a

streak camera (time fiducial). Inside the target chamber, an x-ray image of the laser-produced plasma was taken by using a pinhole camera which viewed targets at nearly  $90^\circ$  from target normal. A PIN diode was used to monitor the level of x-ray emission. Three channels of an absorber/scintillator/photomultiplier array were used to measure the x-ray spectrum for electron temperature estimation. The backscattered light collected by the focusing lens was directed to a photodiode and to a monochromator through an optical fibre. The frequency dispersed light was measured by a streak camera to obtain time-resolved spectra. The calorimeter and the photomultiplier signals were collected and processed by CAMAC automatically.

### 5.3.2. Reflectivity

Backscatter reflectivity was measured by a pair of photodiodes (one for the incident, the other for the backscattered light; HAMAMATSU biplanar phototube R1193U and R1328U). The ratio of the two photodiode signals was used to calculate the total energy reflectivity. The relative sensitivity of the photodiodes was calibrated every day. By placing a high reflectivity mirror in the beam (see  $M_c$  in fig.5.6), the same amount of energy was introduced to both IN-PD and BS-PD. This calibration was done with a front-end laser pulse energy of  $\approx 50\text{mJ}$ . Reflectivity of the mirror  $M_c$  and transmission from  $M_c$  to the target were calibrated and taken into account in calculating the SBS reflectivity. For full energy pulse with e-beam amplification, calibrated attenuation filters (Oriel/Optics for Research Inc., fused silica metallic (inconel alloy coated) neutral density filters) were used to adjust the signal level. For normal incidence, only the

wavelength-shifted component fraction, which was calculated from measured spectra, was taken as backscatter reflectivity.

Specularly reflected light was also measured for several angles of incidence for Al target. The specular reflection was collected by  $f/2$  optics (for normal incidence, the focussing lens was used). The specular energy reflectivity was measured by a calorimeter for oblique incidence. For normal incidence, the signal at the laser wavelength was assumed to be principally specular reflection and calculated from the measured backscatter reflectivity and spectra. This assumption was verified from time-resolved spectral measurements; the shifted component of backscattered light showed a fast and delayed rise of pulse and had a pulse peak around the peak of incident laser pulse, whereas the un-shifted component showed a slow rise similar to the incident pulse and disappeared quickly as plasma was created.

### 5.3.3. Backscatter Spectra

Time-resolved backscatter spectra were obtained using a monochromator-slit camera combination. The backscattered light was introduced into the monochromator (Perkin-Elmer,  $f \approx 580\text{mm}$ ) through an optical fibre ( $\approx 30\text{cm}$ ; General Fiber Optics Inc., soft plastic-clad silica fibre, core diameter  $600\mu\text{m}$ , transmission 75%/m for  $240\text{nm}$ , index of refraction 1.40). A quartz diffuser was placed before the fibre to enhance the stability of alignment. The other end of the fibre was placed close to the entrance slit of the monochromator for maximum efficiency. The monochromator resolution, determined by the grating (blaze angle and wavelength are  $20^\circ$  and  $2370\text{\AA}$ ), was  $0.01\text{\AA}$  at  $2480\text{\AA}$ , which is given by  $\Delta\lambda/\lambda = 1/(Nm)$  where  $N$  is total number of grooves per

mm (= 2880 lines/mm) and  $m$  is the length of the grating (= 84mm). Although the spectral resolution of the grating was 0.01Å, the instrument width was measured to be 0.2Å due to the finite slit width  $\Delta s$  ( $\approx 30\mu\text{m}$  then  $\Delta s = 2f\Delta\theta$ , where  $f$  is the focal length of collimating mirror,  $\Delta\theta = d\cos\theta \cdot \Delta\lambda$ ,  $d=1/N$ ,  $\theta \approx 25^\circ$  for 2480Å ) and imaging optics. The image of the exit of the monochromator was magnified ( $M \approx 3$ ) and relayed to the streak camera (HAMAMATSU C979 temporal disperser with SIT camera C1000). The streak camera was controlled by a CP/M computer (HAMAMATSU C2280) and the digitized image (480x512 pixels) was stored in a floppy disk every shot. A time fiducial was introduced through an optical fibre to the streak camera without frequency dispersion. The laser wavelength  $\lambda_0$  position was calibrated every few shots by the same method used to calibrate the photodiodes. The temporal resolution was determined by the slit installed in the streak camera; for most data, it was 200ps and for the low reflectivity data (Au target), it was reduced to 300ps to improve signal level. The stored image data were transferred later to an IBM-PC computer and then to the university main frame computer for analysis.

#### 5.3.4. X-ray Measurement

X-ray images of the plasma were measured by a pinhole camera. Double pinholes ( $12.5\mu\text{m}^\phi$  and  $27.5\mu\text{m}^\phi$ ) made of Ni disks (40 $\mu\text{m}$  thickness) were used so that the magnification of the image was self-calibrated. The cut-off energy (defined as 1/e transmission) of the pinhole disk was 20keV. Images were recorded on KODAK DEF film. For light shields, two layers of B-10 foil (aluminum coated plastic film) were placed before the film. Typical x-ray transmission of two B-10 foils

was 10% at 700eV, 40% at 1keV and 80% at 2keV.

X-ray intensity was measured by cross calibrated filtered scintillator photomultiplier detectors to estimate electron temperature. Foils of different thickness of aluminum (15 $\mu$ m, 25 $\mu$ m and 50 $\mu$ m) were used as filters to transmit different energies of the x-ray emission spectrum. The cut-off energy of the thinnest foil was  $\approx$  4.5keV. X-rays were converted to visible light in a NE102A plastic scintillator which is linked to a photomultiplier through an optical fibre. The response of the scintillators for x-ray energy  $>$  1keV is known to be linear<sup>5)</sup>. The detectors were positioned at angles of between 20° and 40° with respect to target normal. Over this range of angles, the angular distribution of x-ray radiation ( $h\nu \geq 1\text{keV}$ ) was assumed to be isotropic<sup>6)</sup>. The relative photomultiplier signal as a function of aluminum foil thickness was fitted to theoretical calculations. The theoretical predictions of x-ray emission including line radiation were constructed from a CR (collisional-radiative) model<sup>6)</sup> and tabulated.

#### Bibliography

- 1) X. X. Shan, R. Fedosejevs, B. Harwood, C. Yamanaka, D. C. Thompson, and A. A. Offenberger, IEEE J. Quantum Electron., **26**, 169 (1990).
- 2) D. C. Thompson, R. Fedosejevs, A. A. Offenberger, J. P. Santiago, and H. R. Manjunath, IEEE J. Quantum Electron., **25**, 2161 (1989).
- 3) R. Fedosejevs and A. A. Offenberger, IEEE J. Quantum Electron., **21**, 1558 (1985).
- 4) W. L. Kruer, 'The Physics of Laser Plasma Interaction', (Addison-Wesley, 1988).

- 5) A. J. Meyerott, P. C. Fischer, and D. T. Roething, *Rev. Sci. Instrum.*, **35**, 669 (1964).
- 6) P. D. Gupta, R. Popil, R. Fedosejevs, A. A. Offenberger, D. Salzmann, and C. E. Capjack, *Appl. Phys. Lett.*, **48**, 103 (1986).
- 7) D. Salzmann and A. Krumbein, *J. Appl. Phys.*, **49**, 3229 (1978).

## VI. Experimental Results

In this chapter, the experimental results will be summarized. X-ray images ( $h\nu \geq 1\text{keV}$ ) taken by a pinhole camera showed the dependence of plasma expansion and heating on angle of incidence  $\theta$  and target materials. From the x-ray emission measurements, electron temperatures for aluminum (Al) and carbon (C) plasmas were estimated to be  $600 \pm 150\text{eV}$  at  $I_L = 1.5 \times 10^{14}\text{W/cm}^2$  and  $500 \pm 100\text{eV}$  at  $1.1 \times 10^{14}\text{W/cm}^2$ , respectively. Backscatter reflectivity was measured to be 0.1 - 1.0% for both Al and C plasma in the intensity range from  $3 \times 10^{13}$  to  $2 \times 10^{14}\text{W/cm}^2$ . Gold (Au) plasma showed significantly lower reflectivity ( $\approx 0.005\%$ ). The reflectivity depended on laser intensity and angle of incidence. Specular reflectivity was measured to be 0.01-0.1% for Al plasma at several angles of incidence. Spectrally resolved backscattered light always showed a red shift, typically 120.Å. The amount of shift at peak backscattering increased slightly with increasing laser intensity. No strong dependence on the angle of incidence was observed. Time-resolved spectra revealed the dynamics of the spectral shift; in particular, temporal behavior of the spectral shift depended on laser intensity. No significant difference between pure carbon and plastic ( $\text{C}_8\text{H}_8$ ) target was observed in the above measurement.

### 6.1. X-ray Images

X-ray images of plasma emission ( $h\nu \geq 1\text{keV}$ ) were taken using a pinhole camera with a spatial resolution of  $12\mu\text{m}$ . Figure 6.1 shows several observed x-ray images for Al targets at  $0^\circ$ ,  $22.5^\circ$ ,  $45^\circ$ ,  $60^\circ$  (

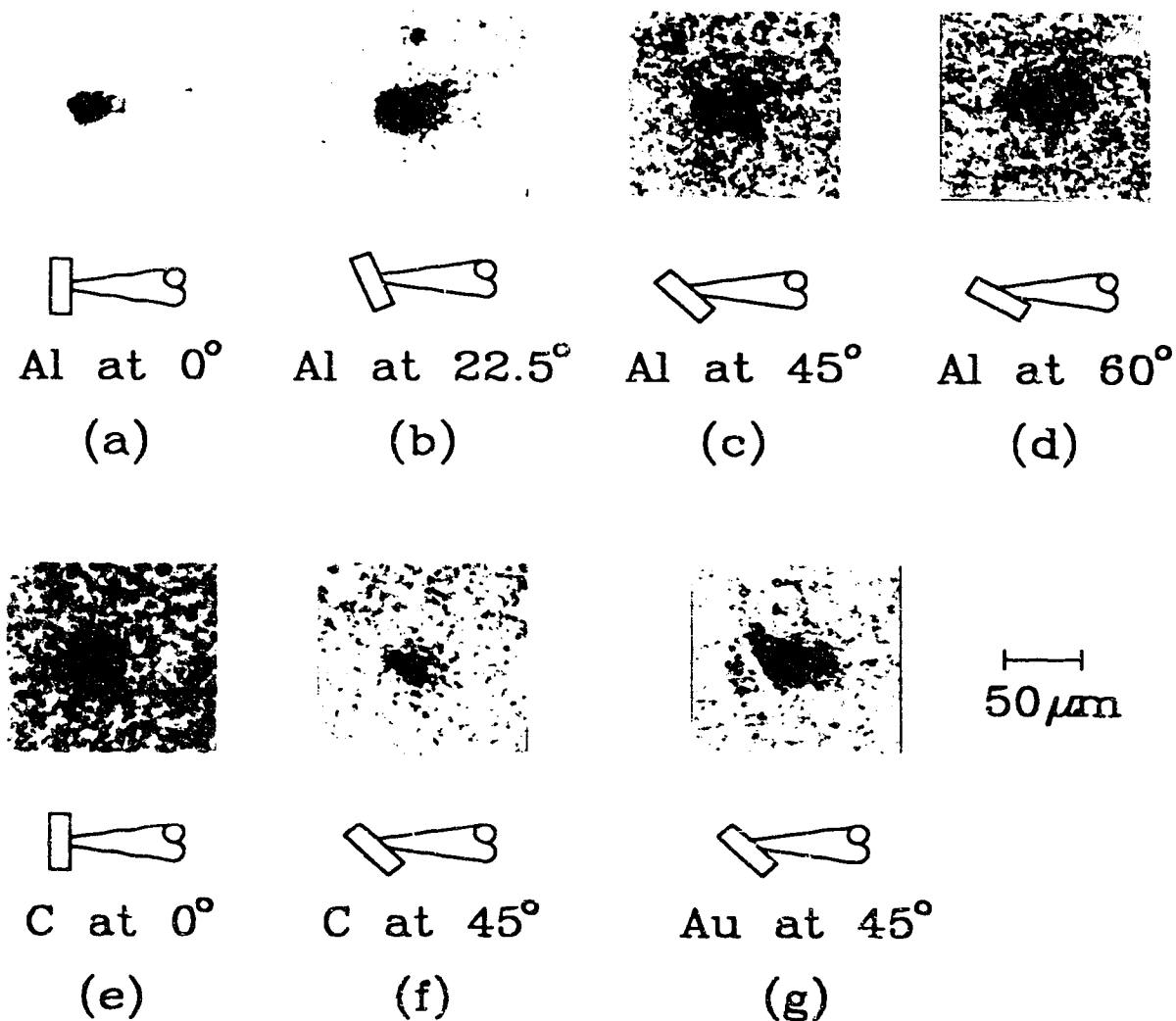


Fig.6.1. X-ray images for Al (a)-(d), C (e)-(f), and Au (g) plasmas at various angles of incidence. Scale of  $50\mu\text{m}$  is also shown. Spatial resolution was  $12\mu\text{m}$  except for (e) with  $27\mu\text{m}$  resolution.

(a)-(d) ), C targets at  $0^\circ$ ,  $45^\circ$  ( (e), (f) ), and Au target at  $45^\circ$  (g). Laser energies for each shot were 808mJ (a), 731mJ (b), 678mJ (c), 723mJ (d), 877mJ (e), 880mJ(f), and 824mJ (g). The spatial scale of the pictures is also shown. Only (e) was taken with a reduced resolution of  $27\mu\text{m}$  because of poor X-ray emission from C plasma.



For  $0.25\mu\text{m}$  illumination, the total x-ray conversion efficiencies for C, Al and Au targets were reported to be 5%, 14%, and 51% at a laser intensity of  $5 \times 10^{12} \text{W/cm}^2$  <sup>1)</sup>. For an Al target, the x-ray conversion efficiency for  $h\nu \geq 1\text{keV}$  was measured to be 0.35% <sup>2)</sup> at a laser intensity of  $3.5 \times 10^{13} \text{W/cm}^2$  and the x-ray intensity scales as  $I_L^{2.4}$ .

As seen in fig.6.1, Au plasma showed the strongest emission among the target materials used here. It is also interesting to note that although the lateral spread of the x-ray emission region is about  $20\mu\text{m}$ , the axial emitting region extends  $50\mu\text{m}$  along the laser axis, despite slow plasma expansion due to the heavy atomic mass. C plasmas showed weak nearly spherical emission of x-rays as expected for low Z plasma. The sequence of pictures (a)-(d) for Al targets indicates the dependence of plasma expansion and heating on angle of incidence  $\theta$ . The weak x-ray emission region (coronal plasma) shows the lateral plasma size ( $\approx 30\text{-}50\mu\text{m}$ , along target surface) increases with increasing  $\theta$  and the shape of the plasma is more planar for larger  $\theta$ . Since our focal spot size ( $\approx 20\mu\text{m}$ ) is much less than  $c_s \tau$  ( $\approx 100\mu\text{m}$ ), it is expected that the plasma scale length is decided by the focal size as discussed in chapter 4. The focal size for oblique incidence is effectively  $1/\cos\theta$  times larger than that for normal incidence. The strong emission region (saturated in the pictures; hot and dense plasma) shows the lateral plasma size exceeds the axial size (in target normal) as the angle changes from  $0^\circ$  to  $60^\circ$ , suggesting strong heating occurs along the laser axis in a size comparable to the focal spot. A jet-like structure at target normal is also seen in all pictures. These features were observed in the hydrodynamic simulation results.

## 6.2. Electron Temperature

X-ray emission measured by cross calibrated filtered scintillator photomultiplier detectors was used to estimate electron temperature. The determination was made by fitting the experimentally observed relative x-ray signals for various filters to those calculated using a collisional-radiative (CR) model<sup>3)</sup>. Figure 6.2 shows the measured and calculated x-ray intensity as a function of aluminum filter thickness, relative to the 50 $\mu\text{m}$ -thick filter intensity, for various electron temperatures of Al (a) and C plasma (b). The ion density was assumed to be  $3.6 \times 10^{20} \text{ cm}^{-3}$  for both cases, since relative emission depends only weakly on density over range of  $10^{20}$  to  $10^{21} \text{ cm}^{-3}$ . Solid circles show the experimentally observed ratio of the transmitted x-ray intensity at a laser intensity of  $1.5 \pm 0.4 \times 10^{14} \text{ W/cm}^2$  for Al target (a), and  $1.1 \pm 0.2 \times 10^{14} \text{ W/cm}^2$  for C target (b). Each data point is an average of at least 19 individual measurements. The vertical error bars are the standard deviation in data. The horizontal error bar ( $\pm 1 \mu\text{m}$ ) is due to the uncertainty in actual foil thickness. There was no systematic difference among data taken at different angles of incidence; the data points shown are average for all angles of incidence. This is not surprising because of the following reasons. Firstly, we expect heating mainly occurs along the laser axis as seen in the simulation results (chapter 4) and the x-ray pictures. Secondly, dependence of the  $T_e$  on plasma scale length  $L$  is not strong ( $T_e$  scales as  $L^{2/9}$ ), if one assumes a self-regulating model<sup>4)</sup>. From comparison of experimental data and theoretical calculation, the electron temperatures of the Al and C plasmas were estimated to be  $600 \pm 150 \text{ eV}$  and  $500 \pm 100 \text{ eV}$ , respectively. These values are consistent with theoretical

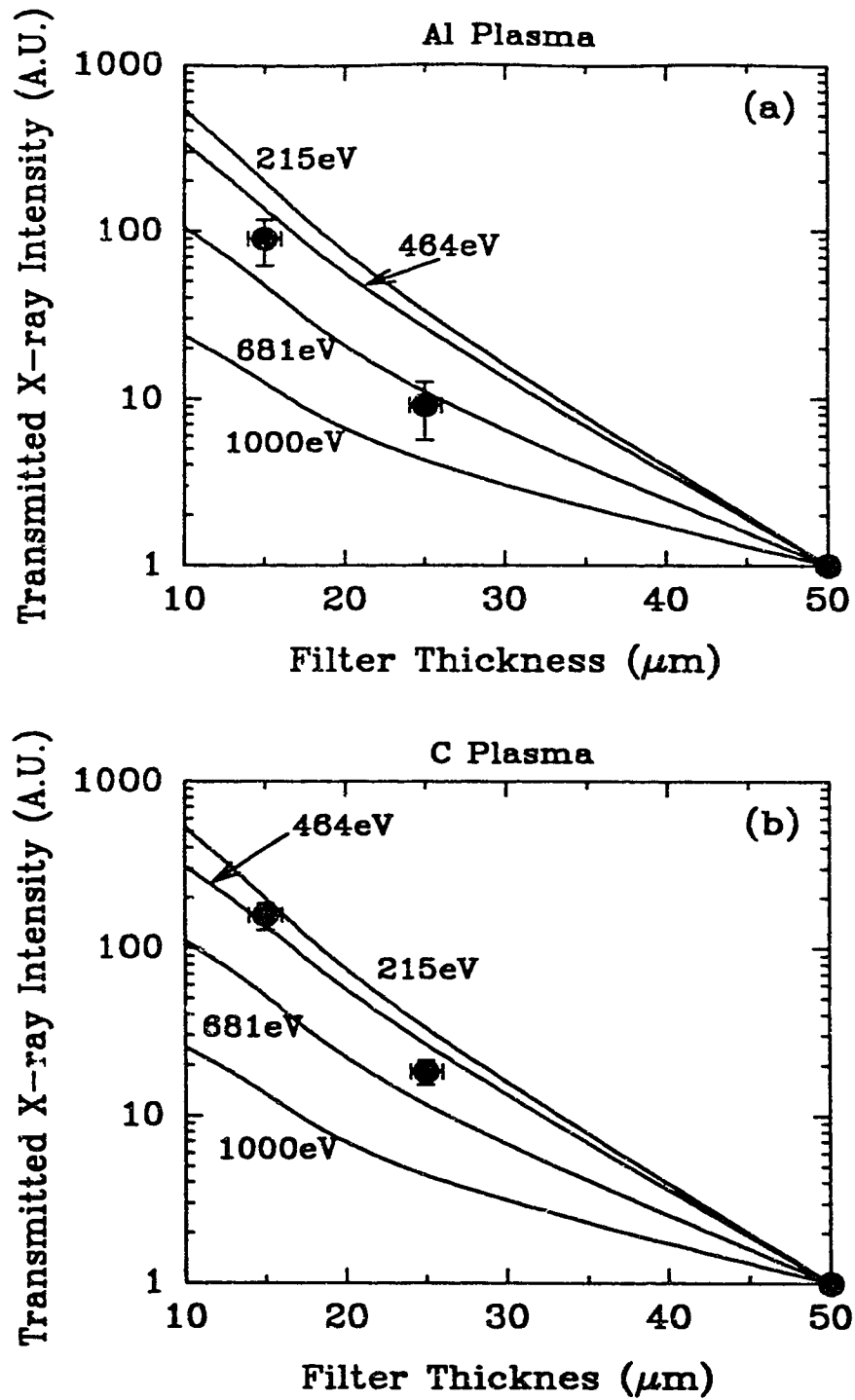


Fig.6.2. X-ray intensities transmitted through Al filters (normalized to 50 $\mu\text{m}$  filter) computed on the basis of the CR model for Al plasma (a) and C plasma (b). Solid circles represent the experimentally observed data.

predictions of the self-regulating model and the 2-dimensional hydrodynamic simulation results.

### 6.3. Reflectivity

#### 6.3.1. SBS Backscatter Reflectivity

In figs 6.3 to 6.5, backscatter energy reflectivity as a function of average laser intensity is summarized for various targets and angles of incidence. Each data point is an average of at least 5 and typically 10 individual measurements. The error bars are the standard error in data. The geometrical effect at oblique incidence ( $1/\cos\theta$ ) has not been included in the intensity calculation. It is noted that variation in individual measurements was as much as one order of magnitude at the same intensity level, especially near threshold. The data at normal incidence was processed to exclude specular reflection.

Backscatter reflectivity data for Al targets was obtained at angles of incidence of  $0^\circ$ ,  $22.5^\circ$ ,  $45^\circ$ , and  $60^\circ$ . Figure 6.3 shows the measured reflectivity as a function of average laser intensity for Al targets. There is an additional data point of  $R = 0.13\%$  for  $I_L = 3.5 \times 10^{14} \text{ W/cm}^2$  at  $\theta = 0^\circ$ , not shown in the figure. At  $0^\circ$ , the reflectivity was almost constant ( $\approx 0.15\%$ ) over the intensity range from  $3 \times 10^{13}$  to  $4 \times 10^{14} \text{ W/cm}^2$ . At  $22.5^\circ$  and  $45^\circ$ , however, the reflectivity increased with increasing laser intensity with values up to 1% on average. The highest reflectivity observed was 3.5% at  $45^\circ$ . In general, for  $\theta = 60^\circ$  and  $45^\circ$  and higher intensity, the reflectivity decreased with increasing intensity.

Figure 6.4 shows backscatter reflectivity for carbon targets at angles of incidence of  $0^\circ$  and  $45^\circ$ . There was no systematic difference

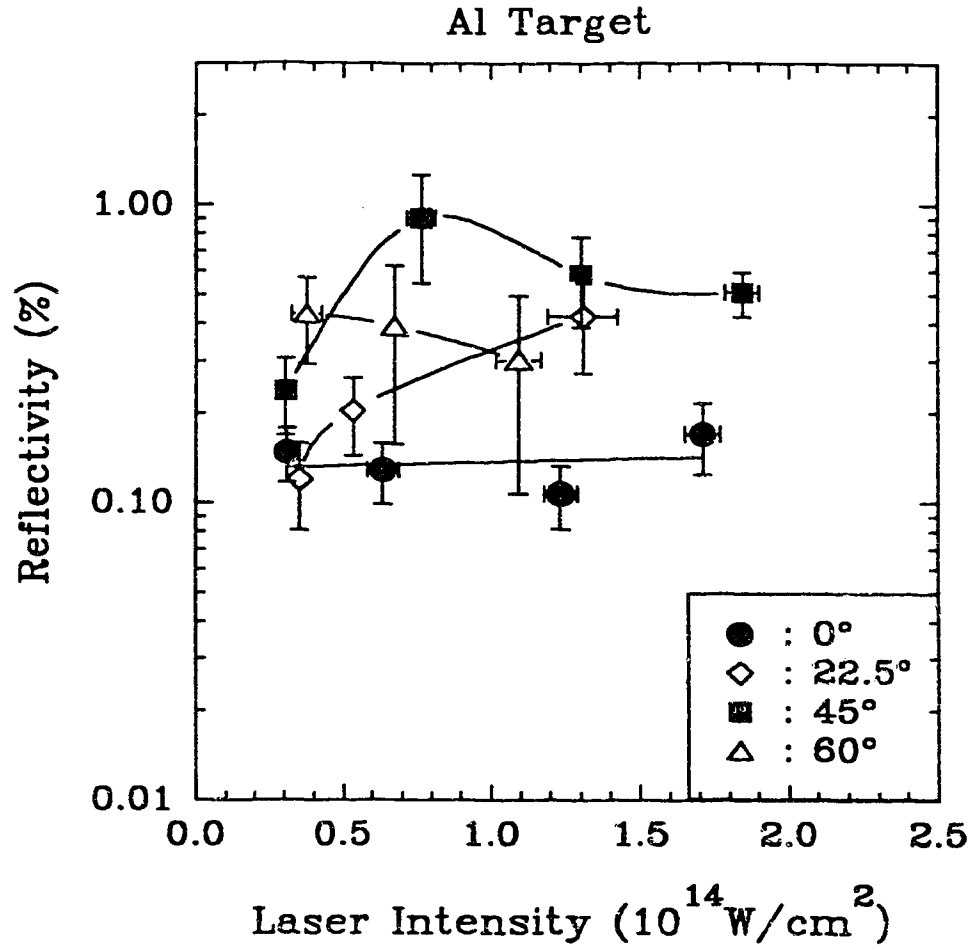


Fig.6.3. Backscatter energy reflectivity for Al targets as a function of average laser intensity.

in measured reflectivity between C and CH target. The data points are therefore the averages of both C and CH targets. Similar features to those observed for Al targets were observed. The highest reflectivity observed was 2.7% at  $45^\circ$ . For both Al and C target, the reflectivity increased with increasing angle of incidence (except for the highest intensities), suggesting convective amplification in a longer interaction length in planar plasma.

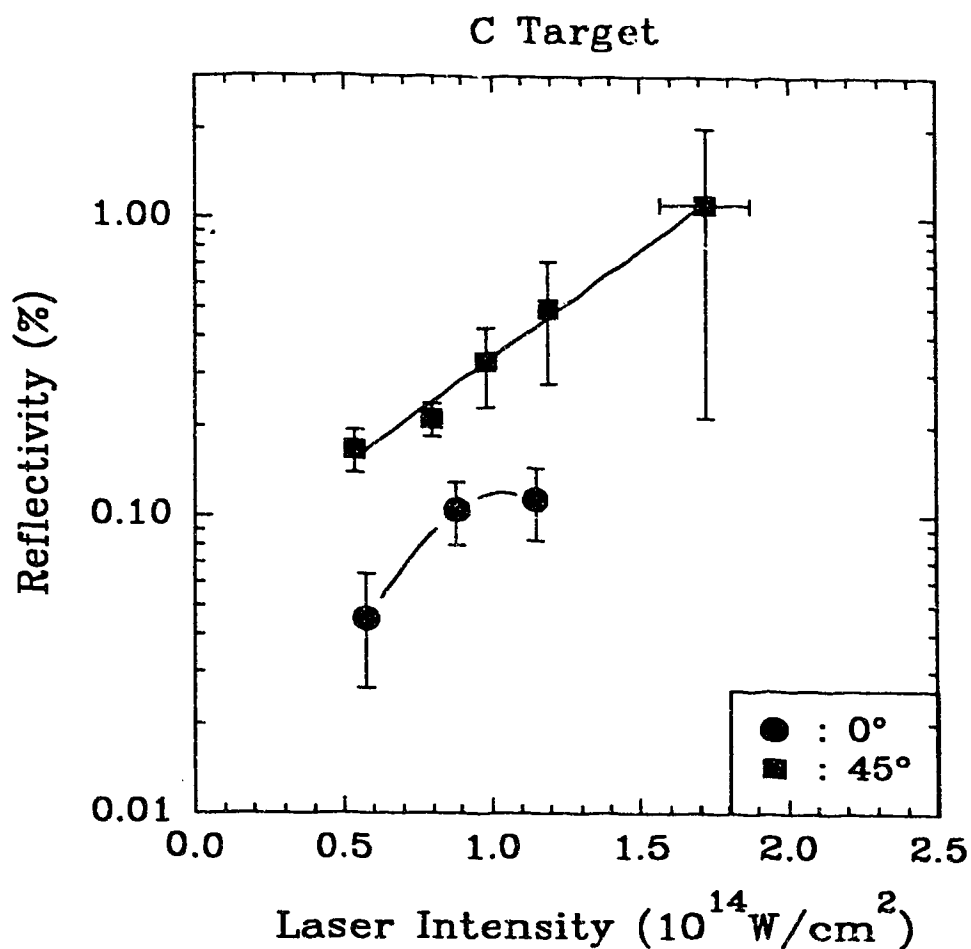


Fig.6.4. Backscatter energy reflectivity for C targets as a function of average laser intensity.

Figure 6.5 summarizes backscatter reflectivity for C, Al, and Au targets at  $45^\circ$ . The measured reflectivity was roughly comparable for C and Al, while the Au target showed significantly lower reflectivity, as expected for the strongly collisional high Z target.

From figs.6.3, 6.4, and 6.5, it is interesting to estimate the (nearly saturated) convective gain coefficient  $G$  for SBS amplification from

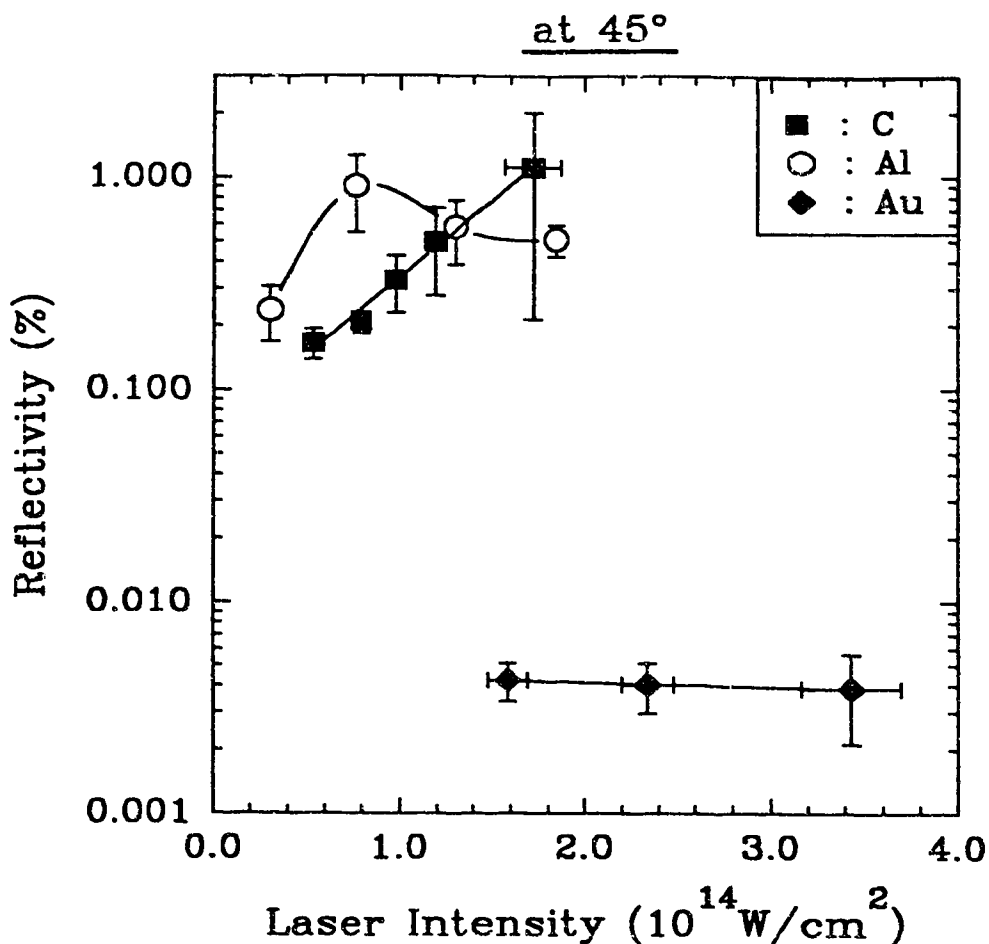


Fig.6.5. Backscatter energy reflectivity for C, Al and Au targets at 45° as a function of average laser intensity

$$I_{\text{SBS}} = I_{\text{N}} \exp( G I_{14} ) \quad (6.1)$$

where  $I_{14}$  is intensity in units of  $10^{14} \text{ W/cm}^2$ . For Al at 22.5° and 45°,  $G$  is calculated to be 1.0 and 3.2, respectively. For C at 45°,  $G$  is 1.1. Details of analysis will be presented in chapter 7.

### 6.3.2. Specular Reflectivity

Specular reflectivity was measured for Al targets at 0°, 22.5°,

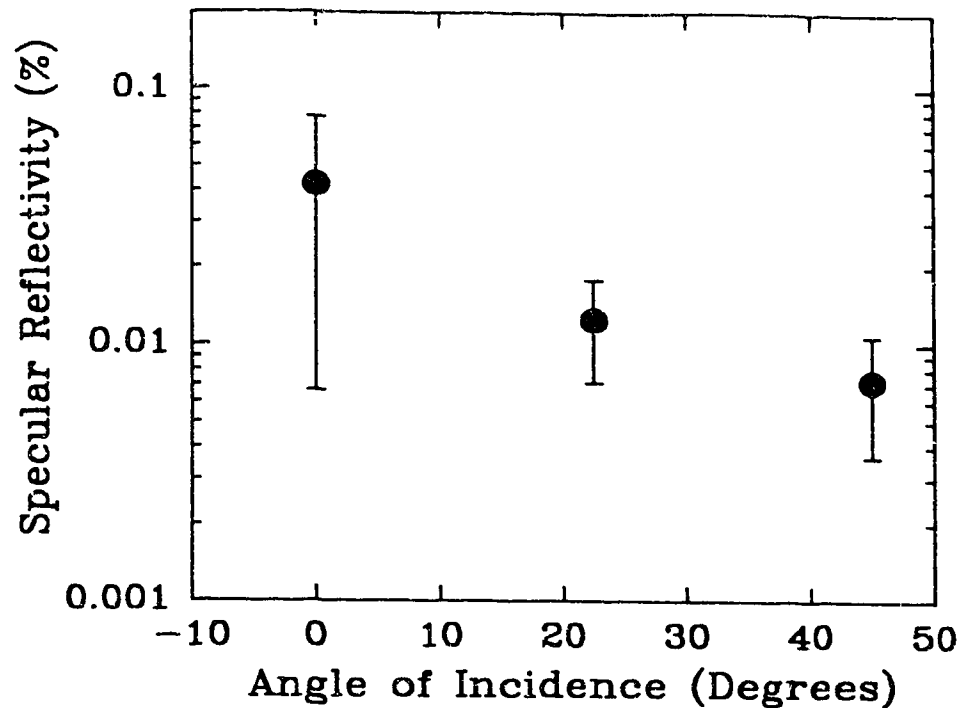


Fig.6.6. Specular energy reflectivity for Al target as a function of angle of incidence.

and  $45^\circ$ . Figure 6.6 shows specular reflectivity as a function of angle of incidence at a laser intensity of  $1 \pm 0.5 \times 10^{14} \text{ W/cm}^2$ . The measured specular reflectivity was approximately one order magnitude lower than the SBS backscatter reflectivity, with lower reflectivity at larger angle. The reduction with increasing  $\theta$  is a consequence of strong absorption and possibly refraction in the expanding plasma. For KrF laser-produced plasma, inverse bremsstrahlung absorption is so strong that specular reflection from the critical surface (or turning point for oblique incidence) exists only in the rising part of the laser pulse where the plasma scale length is still shorter than the



absorption length. This was observed in the time-resolved spectrum for Al target at  $0^\circ$  (see next section). Once the plasma is created, specular reflection for the oblique incidence would be less because of longer interaction length in the planar plasma. As seen in the simulation results in chapter 4, the plasma changes from spherical to locally planar early in the laser pulse. Moreover, the large scale density variations seen in the simulation results could cause complicated refraction of the laser beam, resulting in less collimated reflection toward the collection optics, especially for oblique incidence. Thus time-integrated specular reflection is expected to be less for the oblique incidence.

#### 6.4. Spectral Shift

##### 6.4.1. Time-Resolved Spectra

Time-resolved spectra of the backscattered light were measured by using a combination of monochromator and streak camera with respective resolutions of  $\Delta\lambda=0.2\text{\AA}$  and  $\Delta t=200\text{ps}$ . Both steady and temporally varying red shift and also both temporally smooth and pulsating backscattered light were observed. There was no systematic difference in behavior for different targets ( Al, CH, and C ) or angles of incidence. Figures 6.7 and 6.8 show examples of steady and temporally varying spectra. The SBS spectrum shown in fig.6.7 was for an Al target at  $22.5^\circ$  with  $I_L=4\times 10^{13}\text{W/cm}^2$ . The corresponding backscatter reflectivity for this shot was 0.35%. The spectrum shown in fig.6.8 was for an Al target at  $45^\circ$  with  $I_L=1.3\times 10^{14}\text{W/cm}^2$  for which the reflectivity was 0.13%.

Figure 6.9 shows intensity plots of incident (solid line) and

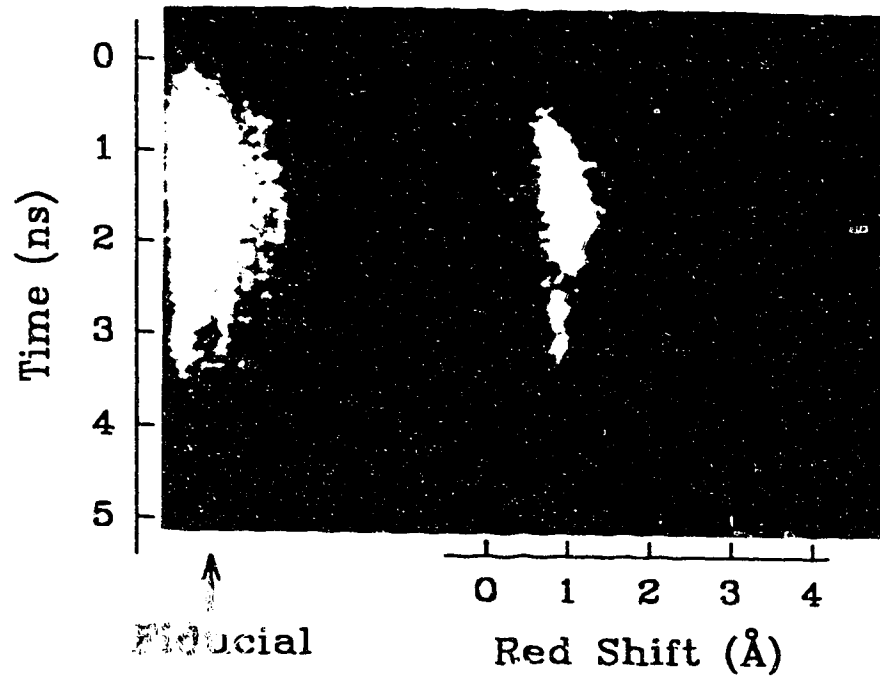


Fig.6.7. An example of steady spectral shift

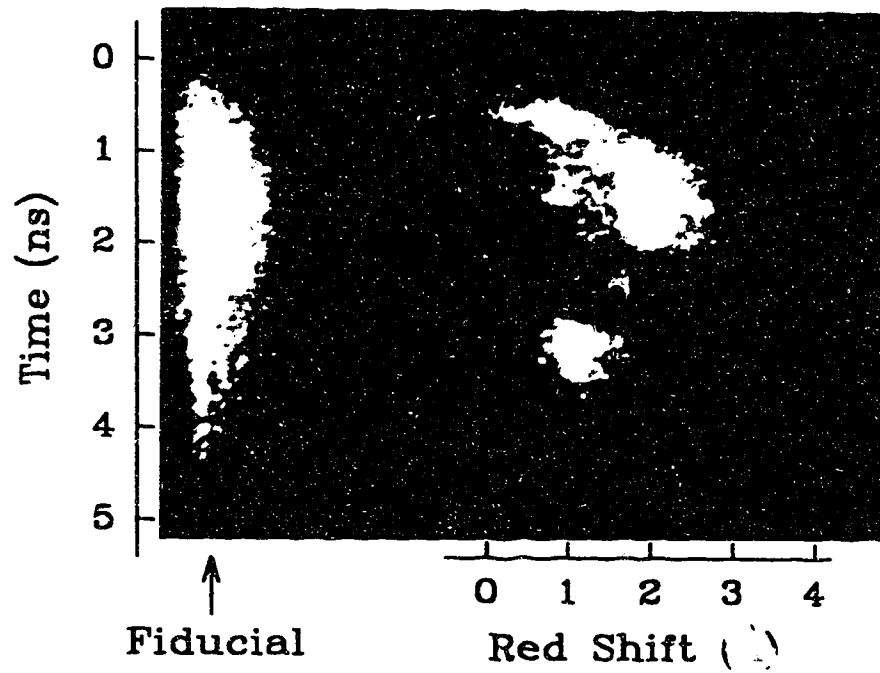


Fig.6.8. An example of temporally varying spectral shift

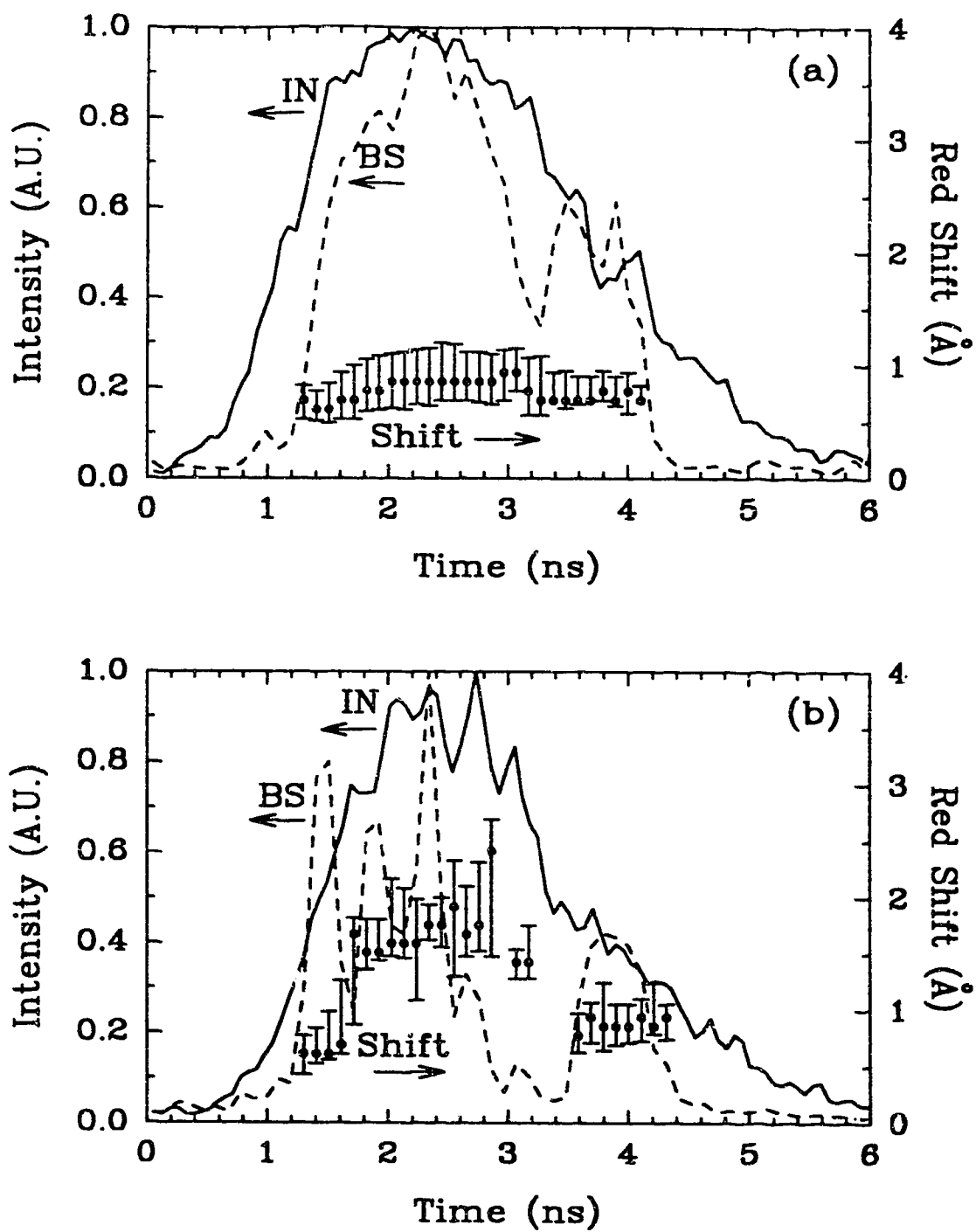


Fig.6.9. Intensity plots of incident (solid line) and backscattered light (dashed line) and spectral shift (solid circles) as a function of time derived from fig.6.8.

spectrally integrated backscattered light (dashed line) along with spectral shift as a function of time in order to compare the time behavior among them. Solid circles and vertical bars represent the mean peak (taken to correspond to the intensity) and FWHM of the spectral shift. Figures 6.9 (a) and (b) correspond to the data shown in fig.6.7 and fig.6.8, respectively. The width of the spectrum was typically  $0.5\text{\AA}$ , larger than the instrument width of  $0.2\text{\AA}$ . The rate for the dynamic spectral red shift in fig.6.8 was typically  $1\text{\AA}/\text{ns}$ .

General features of the time-resolved spectrum are: 1) the peak of backscattered light coincides with the peak of incident light, 2) the largest spectral shift was observed at the peak of incident light, 3) the peak spectral shift was always red (only the foot of the spectrum was slightly blue-shifted in some cases). It is important to note that the temporal modulation in the scattered light was not induced by the incident pulse, since our incident beam was temporally smooth (see section 4.1).

To illustrate the different behavior of SBS and specular reflectivity, fig.6.10 shows the intensity of incident light (solid line), backscattered light at laser wavelength  $\lambda_0$  (dotted line), and backscattered light with spectral shift ( $\lambda > \lambda_0$ , dashed line) as a function of time for Al target at  $0^\circ$ . The relative intensity has been normalized independently for a better view. At normal incidence, the backscattered light is a mix of specular reflection and spectrally shifted scattered light. It is clear, however, that 1) scattered light at  $\lambda_0$  is specular reflection, because it shows a slow rise of pulse similar to the incident pulse and decrease at the peak of incident pulse and beyond (see discussion of section 6.3.2), and 2) the

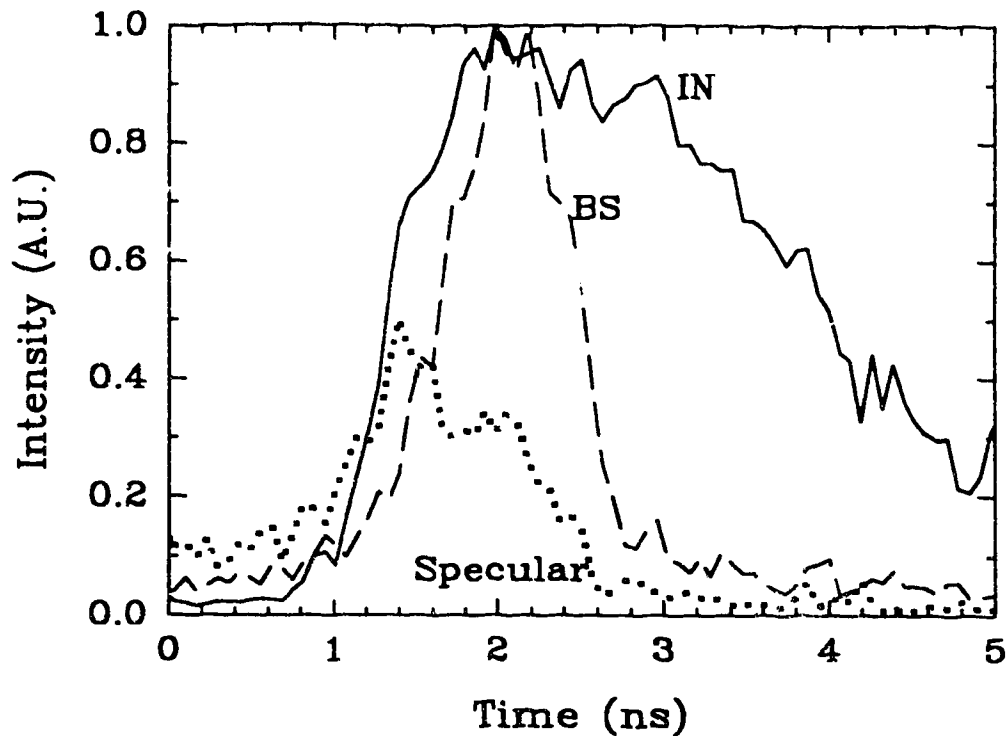


Fig.6.10. Intensity plot of incident light (solid line), scattered light at laser wavelength  $\lambda_0$  (dotted line), and spectrally shifted scattered light ( $\lambda > \lambda_0$ , dashed line).

spectrally shifted scattered light ( $\lambda > \lambda_0$ ) is evidently stimulated scattering, because it shows a sharp rise and fall of pulse with a peak at the peak of incident pulse. Although it is theoretically possible that SBS backscattered light could have a zero spectral shift (due to plasma flow), such features were experimentally not observed.

Figures 6.11 show interesting features of time-resolved spectra for Al targets. These individual shots are particular examples and their features were not always observed. Figure 6.11 (a) is an example of a spectrum whose bandwidth is as narrow as that of the incident pulse. This weak narrow spectral shift was observed only at a low intensity of  $2 \times 10^{13}$  W/cm<sup>2</sup>. Figure 6.11 (b) is an example of a

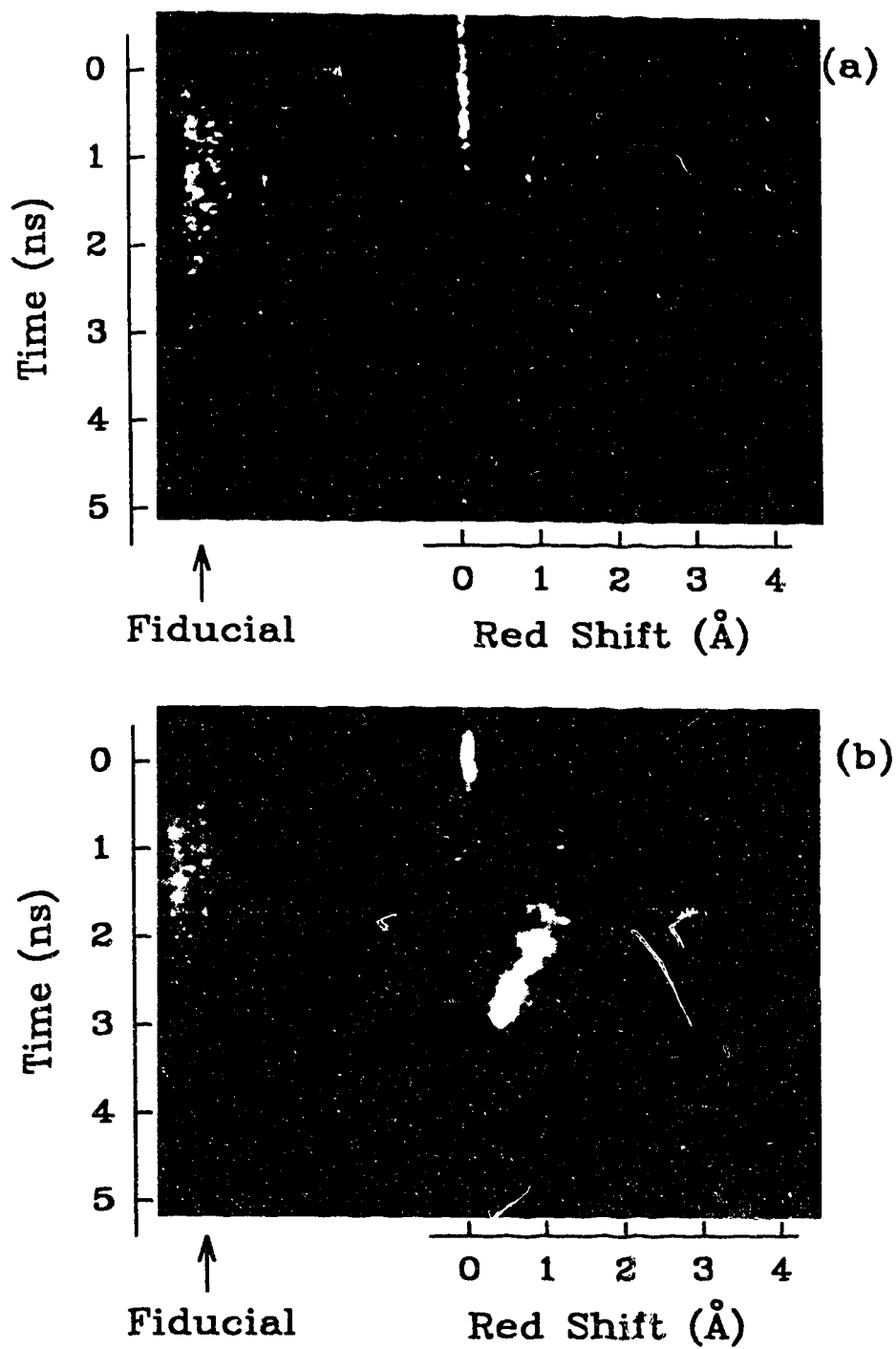


Fig. 6.11. Examples of time-resolved spectra for Al targets.  
 (a) Al target at  $0^\circ$ ,  $I_L = 2.1 \times 10^{13} \text{ W/cm}^2$ .  
 (b) Al target at  $0^\circ$ ,  $I_L = 1.4 \times 10^{14} \text{ W/cm}^2$ .

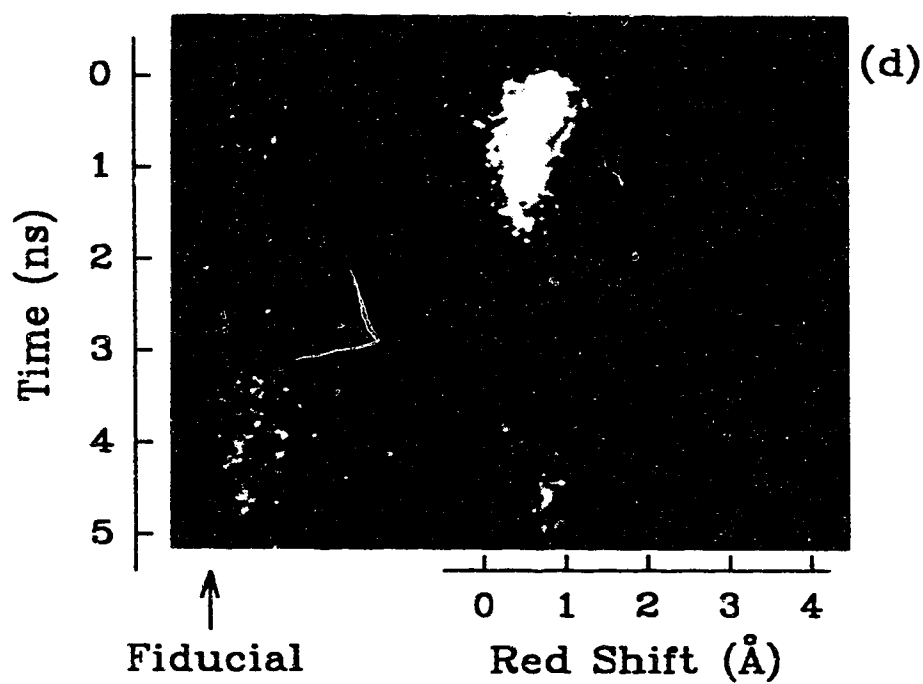
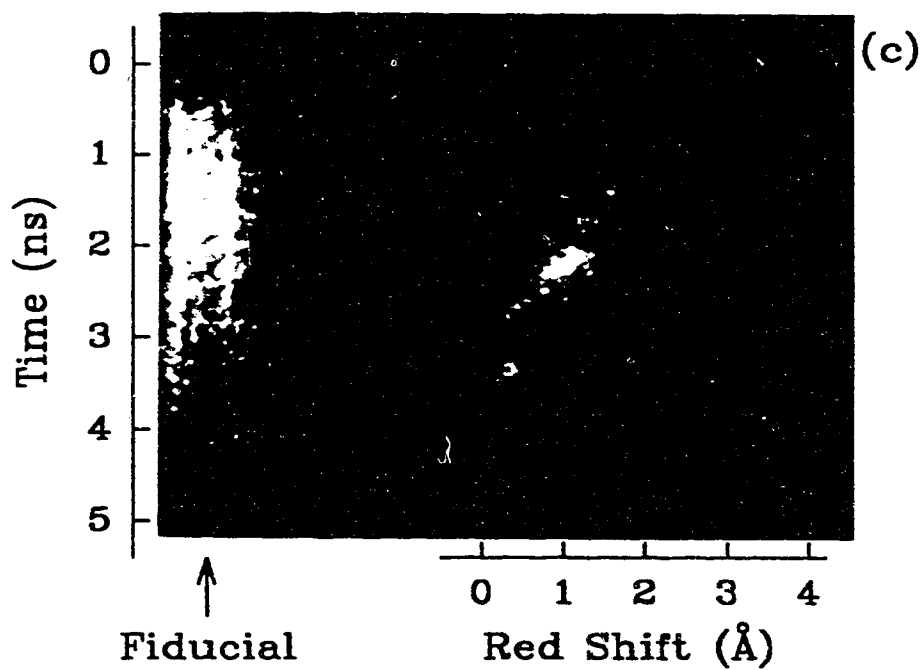


Fig.6.11. Examples of time-resolved spectra for Al targets (cont'd). (c) Al target at  $45^\circ$ ,  $I_L=1.2 \times 10^{14} \text{W/cm}^2$ . (d) Al target at  $60^\circ$ ,  $I_L=1.7 \times 10^{13} \text{W/cm}^2$ .

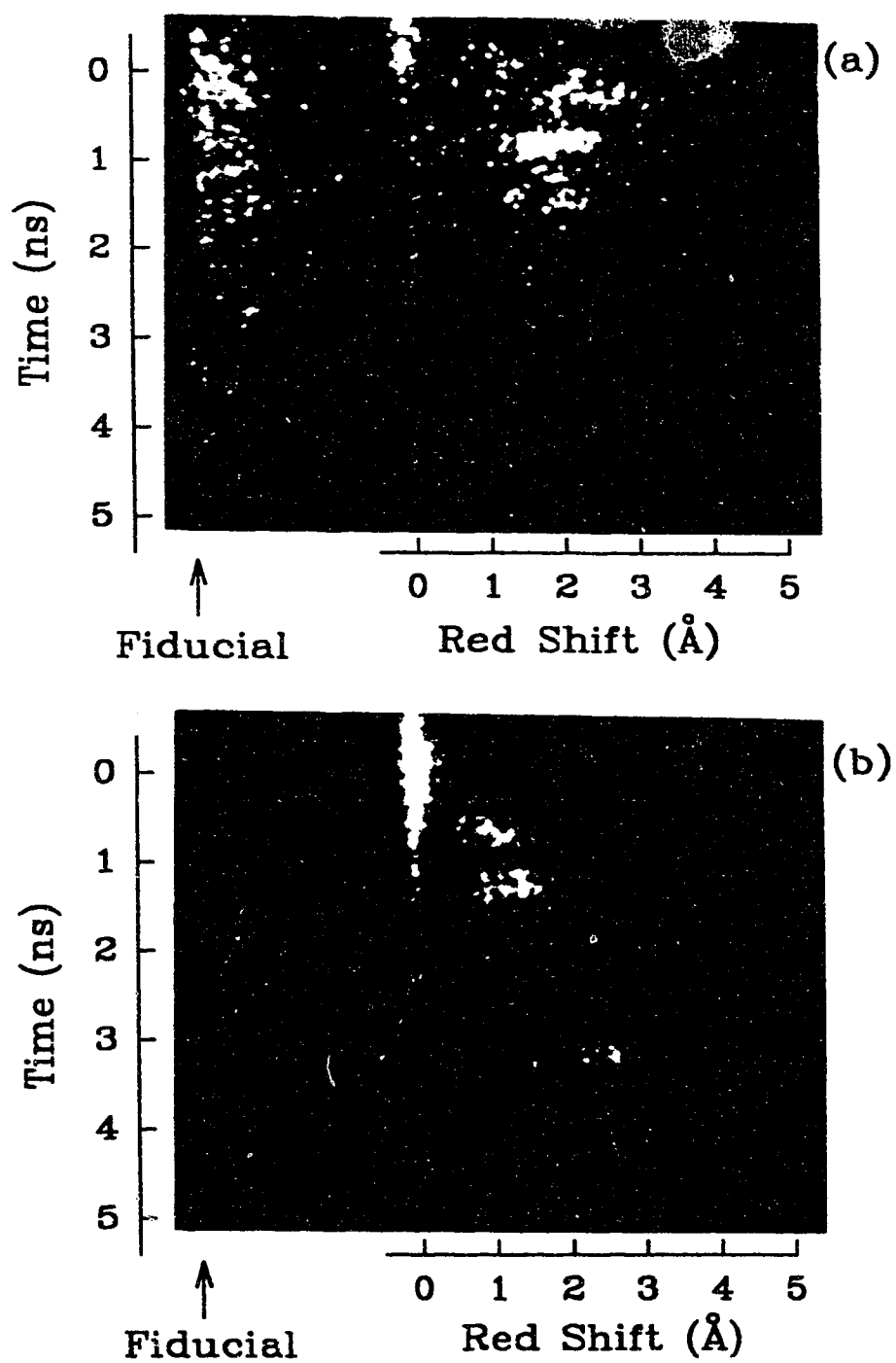


Fig.6.12. Examples of time-resolved spectra for Au targets.

(a) Au target at  $45^\circ$ ,  $I_L=9.5 \times 10^{13} \text{ W/cm}^2$ .

(d) Au target at  $45^\circ$ ,  $I_L=1.1 \times 10^{14} \text{ W/cm}^2$ .



spectrum which showed decreasing spectral shift in time following the peak of the incident pulse. Generally, the observed spectral shifts increased in time until the peak of the incident light and then decreased and diminished in intensity as the intensity of the incident light decreased. This particular shot, however, showed only a decreasing spectral shift in time. Figure 6.11 (c) is an example of a spectrum which showed rapid increase in spectral shift later in time. Fig.6.11 (d) is an interesting spectrum accompanying a double-humped incident pulse. Though the intensity of the second incident peak was higher than the first one, the backscattered light was stronger with the first peak.

Figure 6.12 is an example of a time-resolved spectrum for Au target at  $45^\circ$ . The strong signal at the laser wavelength was not specular reflection but scattered light from optics. Since the signal level was so low, stray light signals could not be eliminated. Features of the spectrum for Au target are; 1) the broad bandwidth ( $\approx 1\text{\AA}$ ), and 2) the short pulsation of scattered light ( $\approx 200\text{ps}$ ). The period of the pulsation varied shot to shot.

#### 6.4.2. Spectral Shift at Peak Backscattering

From the time-resolved spectra the spectral shift at the peak of backscattering was measured. Figure 6.13 shows spectral shift measured at the peak of backscattering as a function of laser intensity for Al (a) and C targets (b) at various angles of incidence. A modest increase in red shift was observed with increasing laser intensity, but no significant dependence on  $\theta$  was observed. Although the density profile is planar, plasma expansion is expected to be spherical as seen

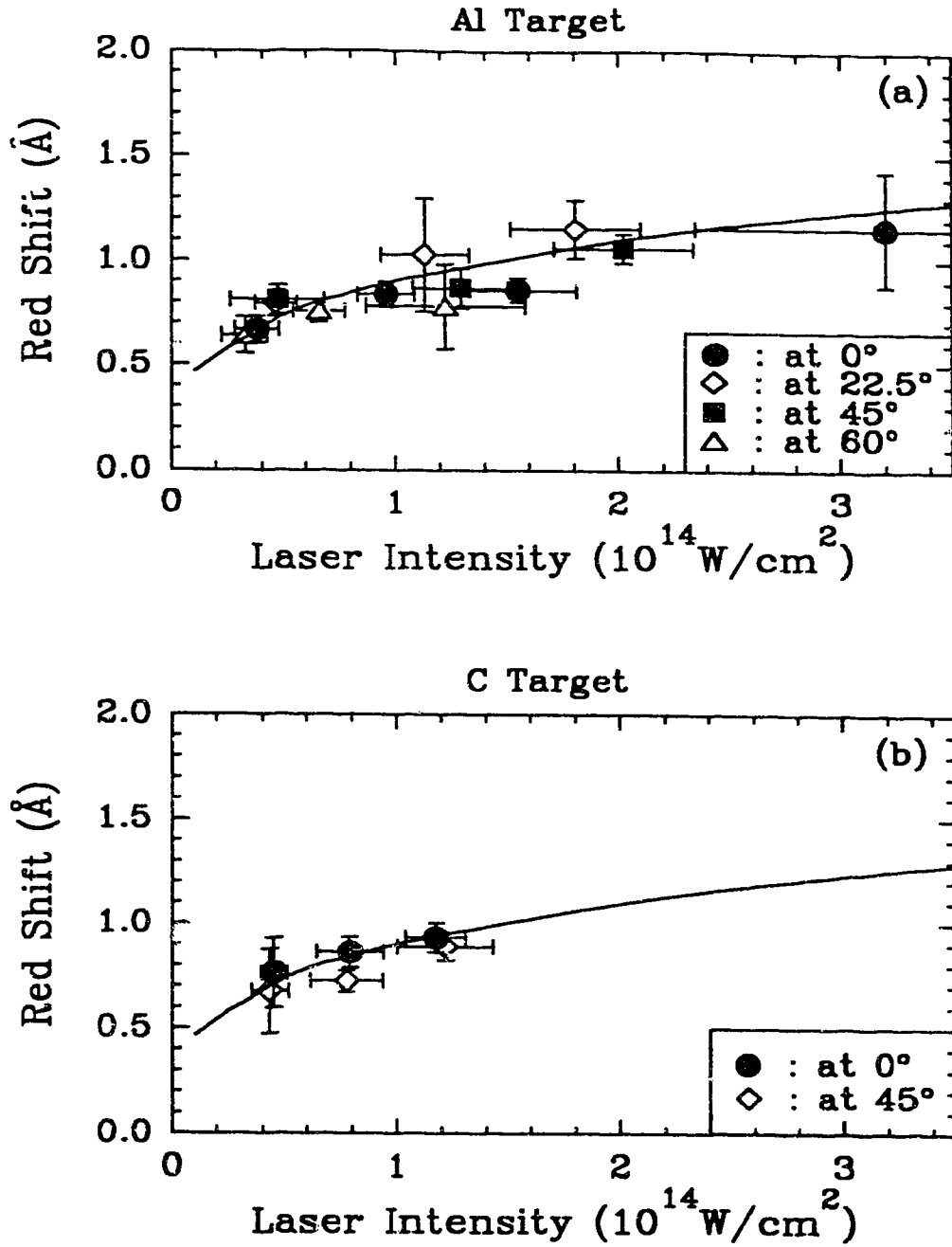


Fig.6.13. Spectral shift measured at peak backscattering for Al (a) and C (b) target. Solid line shows a relative wavelength scaling of  $I_L^{2/9}$ .

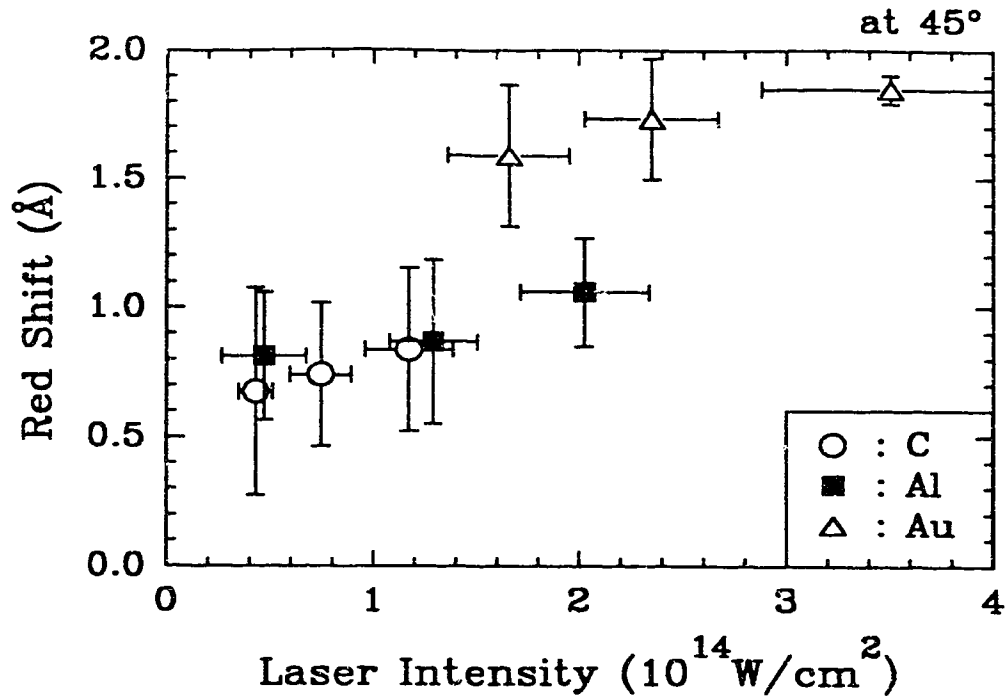


Fig.6.14. Spectral shift measured at peak backscattering for C, Al, and Au target at  $45^\circ$ .

In the hydrodynamic simulation results in chapter 4. The solid curve in both figures shows a relative wavelength scaling of  $I^{2/9}$  which would be expected from the scaling of temperature with intensity in the self-regulating model<sup>4)</sup>. The calculated red shift for scattering from stationary Al and C plasmas with the measured  $T_e$  of 600eV and 500eV is 2.5Å and 2.7Å, respectively (eq.2.23). Consequently, the measured red shift of  $1 \pm 0.5 \text{\AA}$  could be explained by taking into account a subsonic plasma flow (eq.2.24).

Figure 6.14 summarizes spectral shift data measured at peak backscattering as a function of laser intensity for C, Al, and Au target at  $45^\circ$ . The C and Al targets showed comparable red shift,

whereas the Au target showed much larger red shift. A slight increase in red shift with increasing laser intensity was again observed for Au targets. In order to explain the large shift of  $1.7\text{\AA}$  for Au target, relatively high values of  $T_e \approx 600\text{eV}$  and  $Z \approx 40$  would be required, even in stationary plasma. These values are higher than the measured values<sup>5)</sup> (extrapolated  $T_e \approx 360\text{eV}$  and  $\bar{Z} \approx 32$  at  $I_L \approx 10^{14}\text{W/cm}^2$ ) with assumption of a steady state coronal model. This model calculation and the pulsation in the time-resolved spectrum suggest that transient effects may play an important role in scattering from high Z plasma.

#### 6.4.3. Temporal Features of Spectra : $d\lambda/dt$

From time-resolved spectra, the rate of spectral shift change  $d\lambda/dt$  was calculated by manually fitting a straight line to the increasing and decreasing portions of the spectra. Figure 6.15 shows  $d\lambda/dt$  as a function of laser intensity for Al (a) and C (b) targets. Solid and open circles show positive slope (increasing red shift in time) and absolute value of negative slope (decreasing red shift in time). The steady spectral shift was regarded as zero slope and included in the data. Since the spectral shift at peak backscattering showed no significant dependence on  $\theta$ , the data at all angles were averaged. The negative slope data always showed smaller values than the positive slope. This correlates with our laser pulse shape which has a fast rise (0.8ns rise time from half maximum to maximum intensity) and slow fall (1.6ns fall time to half maximum intensity), giving more rapid change of plasma conditions at early time. The positive slope was generally observed on the leading part of the laser pulse. Al targets showed a relatively strong dependence of the

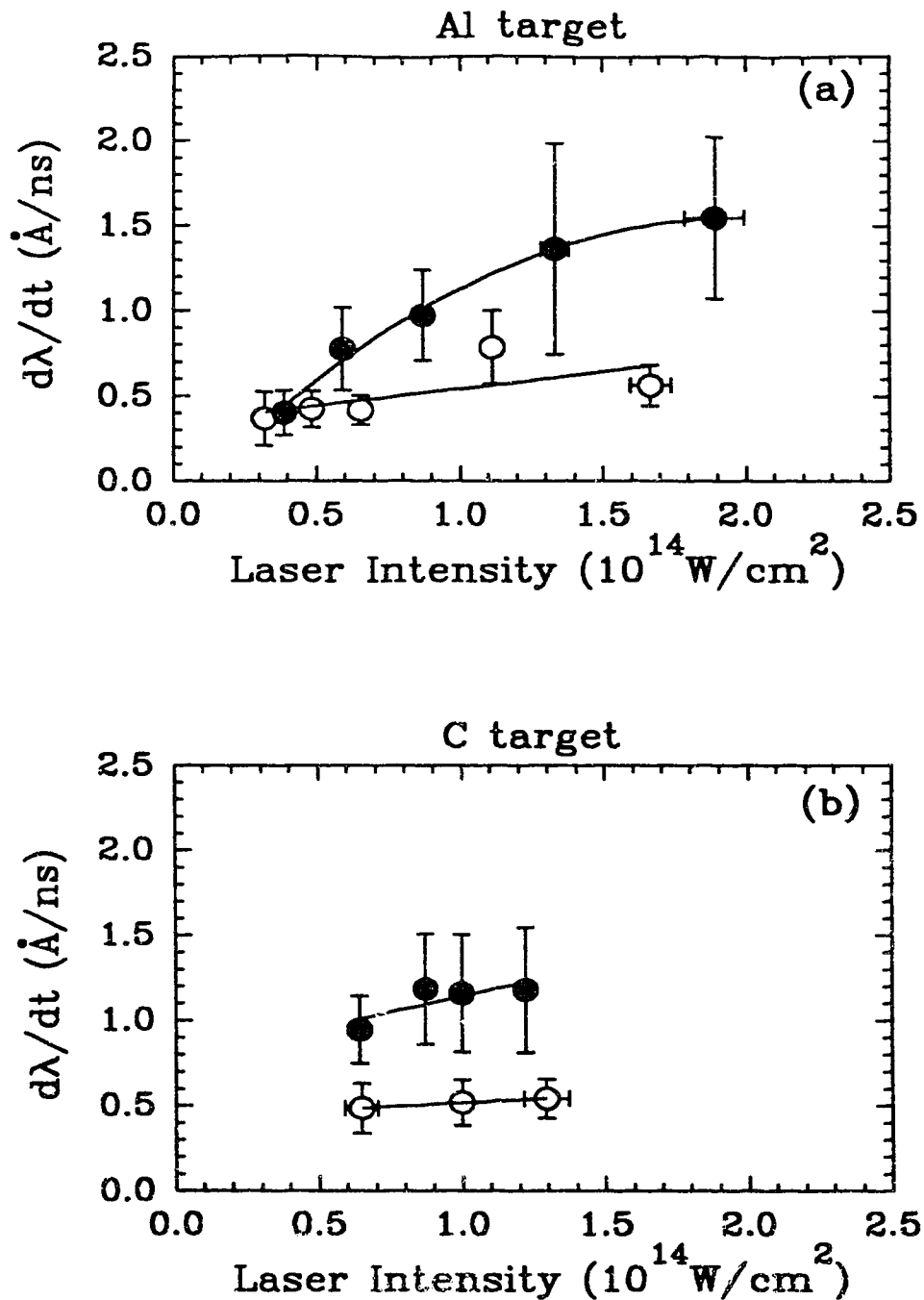


Fig.6.15. Temporal change of spectral shift  $d\lambda/dt$  as a function of laser intensity for Al (a) and C (b) target. Solid and open circles show positive slope (increasing red shift in time) and absolute value of negative slope (decreasing red shift in time)

positive slope on laser intensity. From eq.2.27, with assumption of  $T_e = T_i \approx 600\text{eV}$ ,  $n_e/n_c \approx 0.3$ ,  $M = 0.6$  and  $\cos\theta = 1$ ,  $d\lambda/dt$  of  $1\text{\AA}/\text{ns}$  would require  $\Delta T_e/\Delta t \approx 480\text{eV}/\text{ns}$ ,  $\Delta(n_e/n_c)/\Delta t \approx -1.4/\text{ns}$  (which is unrealistic), or  $\Delta M/\Delta t \approx -0.4/\text{ns}$  (which is less likely, since negative  $\Delta M/\Delta t$  means plasma flow slows down in time). The CASTOR results in section 4.4 shows  $\Delta T_e/\Delta t \approx 400\text{eV}/\text{ns}$  which is comparable to the above  $\Delta T_e/\Delta t$  calculations. Therefore, the increasing spectral shift in time could be explained by plasma heating.

### 6.5. Summary

The electron temperatures for Al and C plasmas were estimated to be  $600 \pm 150\text{eV}$  at  $I_L = 1.5 \times 10^{14}\text{W}/\text{cm}^2$  and  $500 \pm 100\text{eV}$  at  $1.1 \times 10^{14}\text{W}/\text{cm}^2$ , respectively. Backscatter reflectivity was measured to be 0.1 - 1.0% for Al and C plasma in the intensity range from  $3 \times 10^{13}$  to  $2 \times 10^{14}\text{W}/\text{cm}^2$  with higher reflectivity being observed for larger angle of incidence  $\theta$ , suggesting convective amplification in a longer interaction length for oblique incidence. Au plasma showed significantly lower reflectivity ( $\approx 0.005\%$ ). Specular reflectivity was measured to be 0.01-0.1% at  $I_L = 1 \pm 0.5 \times 10^{14}\text{W}/\text{cm}^2$  for Al target, with lower reflectivity being observed for larger  $\theta$ . These reflectivity measurements as well as the x-ray images support the planar density profile of the plasma seen in the hydrodynamic simulation. Spectrally resolved backscattered light always showed a red shift, typically  $1 \pm 0.5\text{\AA}$ , which can be explained by taking into account subsonic plasma flow. The bandwidth of the spectral shift was typically  $0.5\text{\AA}$ . The peak of backscattered light coincided with the peak of incident light. The largest spectral shift was observed at the peak of incident light.

The amount of red shift at peak backscattering increased with increasing laser intensity  $I_L$  and fitted well to the scaling  $I_L^{2/9}$ . No strong dependence on the angle of incidence was observed, consistent with the spherical plasma flow seen in the hydrodynamic simulations. Time-resolved spectra showed the rate of the spectral shift change increased with increasing laser intensity which could be explained by plasma heating rate.

#### Bibliography

- 1) R. Fedosejevs, Y. Y. Tsui, R. Popil, P. D. Gupta, J. Baker, and A. A. Offenberger, Proceedings of SPIE, **381**, 66 (1987).
- 2) P. D. Gupta, R. Popil, R. Fedosejevs, A. A. Offenberger, D. Salzmann, and C. E. Capjack, Appl. Phys. Lett., **48**, 103 (1986).
- 3) D. Salzmann and A. Krumbein, J. Appl. Phys., **49**, 3229 (1978).
- 4) P. Mora, Phys. Fluids, **25**, 1051 (1982).  
F. Dahmani and T. Kerdja, Phys. Fluids, **B3**, 1232 (1991).
- 5) P. D. Gupta, Y. Y. Tsui, R. Popil, R. Fedosejevs, and A. A. Offenberger, Phys. Rev. Lett., **34**, 4103 (1986).

## VII. Data Analysis I (Homogeneous Plasma)

In this chapter, the experimental data presented in chapter 6 is compared with theoretical calculations based on an analytical model for homogeneous plasma. Typical plasma conditions for C, Al, and Au plasma are determined both by experimental data and by optimum conditions for convective growth of SBS. Experimental threshold intensity and SBS gain for C and Al plasma are examined by taking into account the non-uniformity of the focal spot. Dependence of spectral shift and reflectivity on the plasma parameters ( $T_e$ ,  $n_e$ ,  $L$ ,  $M$ ) is investigated theoretically for Al plasma and compared with the experimental data to bracket the range of the plasma parameters. A model for treating hotspots in the focal spot is proposed. The possibility of double SBS occurring in our experiment is examined. Most of the model calculations are done for aluminum data.

### 7.1. Typical Plasma Conditions

Since it is difficult to precisely measure plasma parameters experimentally, it is important to estimate the plasma conditions ( $T_e$ ,  $n_e$ , etc.) for analytical calculation of SBS. Here, we summarize our estimation of plasma parameters used in the calculations for C, Al, and Au plasma.

#### 7.1.1. Al and C Plasma

Table 7.1 summarizes our estimated plasma parameters. These parameters are for an irradiation of  $1 \times 10^{14} \text{ W/cm}^2$  and will vary with laser intensity. Electron temperature  $T_e$  is obtained from a



Table 7.1. Estimated plasma conditions.

Element	L ( $\mu\text{m}$ )	$T_e$ (eV)	Z	$n_e$ ( $1/n_c$ )
C	20	500	6	0.4
Al	20	600	11	0.4

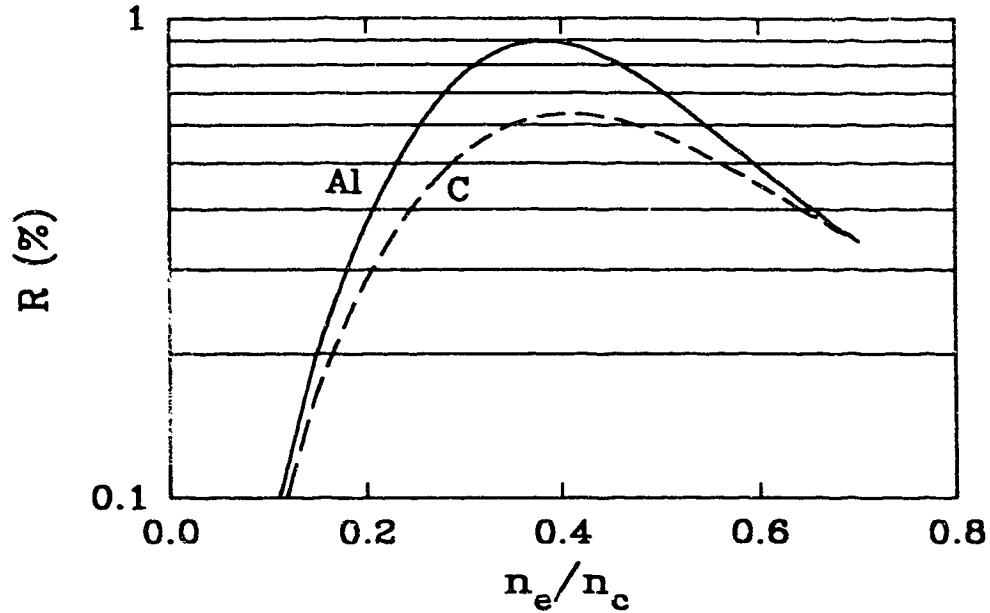


Fig.7.1. SBS reflectivity dependence on electron density for homogeneous C plasma (dashed line) and Al plasma (solid line).

temperature measurement procedure presented in section 6.2. The experimental value of  $T_e$  for Al plasma is consistent with the hydrodynamic simulation (CASTOR) results. The plasma scale length  $L$  is based on measurements of the focal spot size (90% energy radius) and density scale length  $L_n$  in the CASTOR results (see chapter 4). Since  $c_s \tau$  (= sound speed  $\times$  time scale of the laser pulse) for our plasma is estimated to be  $\approx 100\mu\text{m}$ , much larger than the focal spot radius ( $\approx 10\mu\text{m}$ ), the plasma scale length is expected to be determined by the

scale of the focal spot. Although the measured focal spot is  $10\mu\text{m}$  (90% energy radius), the x-ray images of plasma (with spatial resolution  $\approx 12\mu\text{m}$ ) in fig.6.1 show slightly larger emission region ( $\approx 20\text{-}50\mu\text{m}$ ) than the focal spot size, especially for oblique incidence. Moreover, the CASTOR results show refraction of the laser beam is significant for smaller focus. We therefore estimated the plasma scale length to be  $20\mu\text{m}$ , about twice the 90% energy radius. This value is smaller than the focal depth of the laser beam ( $\approx 60\mu\text{m}$ , experimentally). The effective electron density  $n_e$  is approximated by the optimum density for SBS amplification. The optimum density was estimated from the calculated SBS reflectivity dependence on electron density (similar to the results presented in chapter 3). Charge state  $Z$  was estimated from the measured electron temperature and calculations based on a collisional-radiative (CR) model.<sup>1,2)</sup>

Figure 7.1 shows the SBS reflectivity dependence on electron density calculated from eq.(2.38) for C and Al plasma. Both electromagnetic ( $\gamma_{\text{ib}}$ ) and ion wave ( $\gamma_s$ ) damping were included. The values for  $L$ ,  $T_e$ , and  $Z$  are listed in table 7.1. An initial density fluctuation level was assumed to be  $2 \times 10^{-3}$  to give reflectivity comparable to the experimental value. For both cases, the optimum electron density for SBS amplification was estimated to be  $0.4 \cdot n_c$ . Note that for longer scale length ( $L = 100\mu\text{m}$ ), the optimum density is lower ( $0.1\text{-}0.2 \cdot n_c$ ), (see chapter 3). This is a direct consequence of SBS in plasma with strong inverse bremsstrahlung absorption; the shorter plasma absorption length corresponds to a higher optimum density.

For varying laser intensity,  $L$  is unchanged, because it is based

on the focal spot scale length which was kept constant in the experiment.  $T_e$  is assumed to change in the manner described by the self-regulating model<sup>3)</sup>. We use the expression,

$$T_e = T_0 \cdot I_{14}^{0.44} \quad (7.1)$$

where  $T_0$  is measured electron temperature at laser intensity of  $1 \times 10^{14} \text{W/cm}^2$ , and  $I_{14}$  is the laser intensity normalized to  $10^{14} \text{W/cm}^2$ . The charge state  $Z$  for Al and C is essentially unchanged over the temperature range from 100eV to 1keV<sup>1,2)</sup>. For reference, ionization potentials<sup>4)</sup> for Al and C are listed in table 7.2. The electron density changes in a complex manner, since the optimum density for SBS is a function of  $\gamma_0$ ,  $\gamma_{1b}$ ,  $\gamma_s$ , and  $L$ . This will be discussed in section 6.4.2.

### 7.1.2. Au Plasma

Though it is difficult to estimate plasma conditions for Au plasma because of its complicated atomic shell structure and radiation effects, several sources of previous measurements are available for estimating  $T_e$ . P.D.Gupta et al.<sup>5)</sup> measured  $T_e$  of gold plasma irradiated by high intensity KrF laser. At a laser intensity of  $I_L = 1.6 \times 10^{13} \text{W/cm}^2$ ,  $T_e$  was calculated to be  $225 \pm 50 \text{eV}$  from x-ray continuum emission assuming a corona model. The experimental results also showed  $T_e$  scaled as  $T_e \propto I_L^{0.25}$ . Based on this scaling, we estimate  $T_e \approx 355 \text{eV}$  at  $I_L = 1 \times 10^{14} \text{W/cm}^2$ . P.Alaterre et al.<sup>6)</sup> measured x-ray spectra ( $0.1 < h\nu < 6 \text{keV}$ ) from gold plasma created by  $0.26 \mu\text{m}$  laser radiation at  $I_L = 2 \times 10^{14} \text{W/cm}^2$  and found that superposition of two temperature contributions ( $T_e = 150 \text{eV}$  and  $450 \text{eV}$ ) was required to fit the experimental data to CR model calculations. 2D LASNEX simulation

Table 7.2. Ionization potential for C, Al and Au.

Species	Ion	Ionization Potential (eV)
C	C <sup>+3</sup>	67.5
	C <sup>+4</sup>	374.2
	C <sup>+5</sup>	475.6
Al	Al <sup>+10</sup>	471.1
	Al <sup>+11</sup>	1671
	Al <sup>+12</sup>	2211
Au	Au <sup>+15</sup>	365.1
	Au <sup>+20</sup>	545.7
	Au <sup>+25</sup>	817.9
	Au <sup>+30</sup>	1097
	Au <sup>+35</sup>	1634

results<sup>7)</sup> showed  $T_e \approx 700\text{eV}$  for gold plasma irradiated by  $0.26\mu\text{m}$  laser at  $I_L = 1 \times 10^{14} \text{W/cm}^2$  (laser energy  $E_L = 1\text{kJ}$  and focal spot of  $1.4\text{mm}$ ), but this calculation is not directly applicable to our case of much smaller focal spot size and laser energy.

Scaling of average ion charge  $\bar{Z}$  has been proposed by several authors. R.Pakula et al.<sup>8)</sup> modelled the relation  $\bar{Z} = 60 \cdot T_{\text{keV}}^{1/2}$ . D.Colombant<sup>1)</sup> et al. derived  $\bar{Z} = (2/3) \cdot (AT_e)^{1/3}$  for high Z targets, where A is the atomic number of the element and  $T_e$  is in eV. W.Mróz et al.<sup>9)</sup> estimated  $\bar{Z} = Z_n \cdot T_e^{0.4} [(Z_n/34)^{1.5} + T_e]^{-0.4}$ , where  $T_e$  is given in keV, and  $Z_n$  is the nuclear charge of plasma ions. We consider two cases of electron temperature ( $T_e \approx 150$  and  $400\text{eV}$ ) for gold plasma. According to the above expressions,  $\bar{Z}$  is estimated to be  $22 (\pm 1)$  for  $150\text{eV}$  and  $33 (\pm 5)$  for  $400\text{eV}$ . The plasma scale length L is assumed to be  $20\mu\text{m}$ , since  $c_s \tau$  is still larger than the focal spot dimension. The optimum density can be estimated in the same way as for Al and C plasma, though the model of  $\gamma_s$  may not be valid. The

results showed the optimum density is  $\approx 0.15 \cdot n_c$  (150eV) and  $0.2 \cdot n_c$  (400eV). Note these numbers are estimates for comparison purposes only.

## 7.2. Instability Threshold and Gain

In this section, theoretical predictions of SBS intensity threshold and gain are calculated for both infinite and finite homogeneous plasmas. These results are compared with experimental data.

### 7.2.1. Infinite Homogeneous Plasma

In an infinite plasma, all three waves are confined and interact with each other in a closed system, resulting in absolute growth at a rate  $\gamma_0$ . The minimum intensity threshold for homogeneous infinite plasma with weak damping is given by eq.2.10. Equivalently, the SBS threshold can be defined by  $\Gamma = \gamma_0^2 / (\gamma_s \gamma_{ib}) > 1$ . Figure 7.2 shows the dependence of  $\Gamma$ ,  $\gamma_s$ ,  $\gamma_{ib}$ ,  $\gamma_0$ , and  $T$  ( $=T_e=T_i$ ) on laser intensity for Al plasma with  $n_e = 0.4 \cdot n_c$ .  $\gamma_s$  was calculated by the Casanova formula (see section 2.3.) and  $\gamma_{ib}$  was given by eq.3.6. Since wave damping is important and has a strong dependence on electron temperature, the intensity dependence of plasma temperature is implicitly included in the calculation. Note the gain curve in fig.7.2 shows saturation characteristics because the temperature dependence is included. At  $I_L = 10^{14} \text{ W/cm}^2$ ,  $\gamma_0$  was calculated to be  $2.0 \times 10^{12}$  (1/s) and the intensity threshold (where  $\Gamma = 1$ )  $I_{th}$  was found to be  $3.8 \times 10^{13} \text{ W/cm}^2$ . Similar calculations were made for C and Au plasma and the results are summarized in table 7.3. and 7.4. It is clear that the results for

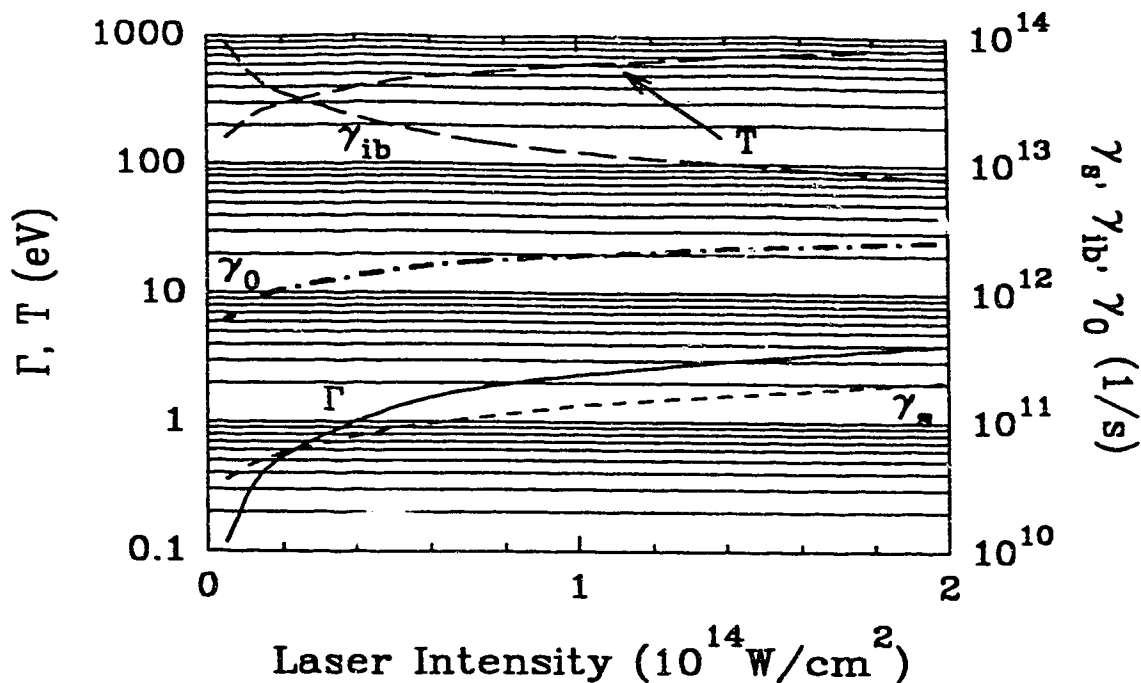


Fig.7.2. Dependence of  $\Gamma$ ,  $\gamma_s$ ,  $\gamma_{ib}$ ,  $\gamma_0$ , and temperature  $T$  on laser intensity for  $n_e/n_c=0.4$  (Al plasma).

Table 7.3. Threshold intensity  $I_{th}$  and growth rate  $\gamma_0$  at  $10^{14} \text{W/cm}^2$ .

Plasma	$T_e$ (eV)	$n_e/n_c$	$I_{th}$ ( $\text{W/cm}^2$ )	$\gamma_0$ (1/s)
C	500	0.4	$9.0 \times 10^{13}$	$2.1 \times 10^{12}$
Al	600	0.4	$3.8 \times 10^{13}$	$2.0 \times 10^{12}$
Au	150	0.15	$7.5 \times 10^{12}$	$1.4 \times 10^{12}$
	400	0.2	$1.8 \times 10^{13}$	$1.4 \times 10^{12}$

Table 7.4. Damping rates  $\gamma_s$ ,  $\gamma_{ib}$ , and SBS parameter  $\Gamma$  at  $10^{14} \text{W/cm}^2$ .

Plasma	$\gamma_s$ (1/s)	$\gamma_{ib}$ (1/s)	$\Gamma$
C	$4.1 \times 10^{11}$	$9.7 \times 10^{12}$	1.1
Al	$1.3 \times 10^{11}$	$1.2 \times 10^{13}$	2.3
Au (150eV)	$1.1 \times 10^{10}$	$8.3 \times 10^{12}$	21
Au (400eV)	$2.4 \times 10^{10}$	$9.7 \times 10^{12}$	8.1

the Au plasma (higher gain and lower threshold than Al plasma) are not in agreement with the experimental data.

### 7.2.2. Finite Homogeneous Plasma

In a finite plasma, waves can escape from the plasma, resulting in reduced absolute growth rate or convective growth. The effective size of the plasma is set by the finite gain length due to plasma inhomogeneity or by the physical size of the plasma. Here, we only consider the latter case and plasma inhomogeneity is discussed in the next chapter.

The criteria for absolute instability is given by eq.2.15 for weak damping.

$$L > \pi (v_g \cdot c_s)^{1/2} / 2\gamma_0 \quad (7.2)$$

which is to say that the length L must exceed a basic gain length determined by wave loss from the system. In our case, however, wave damping is so strong that the condition<sup>10)</sup>

$$\frac{\gamma_s}{\gamma_0} \cdot \left( \frac{v_g}{c_s} \right)^{1/2} > 2 \quad (7.3)$$

is satisfied for C and A. plasmas, whereby only convective growth can be expected. The convective growth parameter  $G_L$  is given by eq.2.19. For the plasma parameters listed in table 7.1,  $G_L$  for C and Al plasmas were calculated to be 0.88 and 2.0 with plasma parameters listed in table 7.1.

### 7.2.3. Comparison Between Theory and Experiment (Threshold and Gain)

Since the plasma in the experiment is inhomogeneous, the discussion above is not strictly applicable to the experimental data.

Table 7.5. Comparison between theoretical predictions and experimental data with three component intensity distribution.

Plasma	$I_{th}$ (W/cm <sup>2</sup> )		$G_L$		
	Theory ( $I_M$ )	Exp.	with $I_{av}$	with $I_M$	Exp.
C	$3.9 \times 10^{13}$	$5.5 \times 10^{13}$	0.88	1.4	1.1
Al	$1.6 \times 10^{13}$	$3.5 \times 10^{13}$	2.0	3.2	3.2

It is, however, still useful to compare the above theoretical calculations with the experimental data to gain qualitative information on the instability conditions.

From experiment, the threshold intensity was measured to be  $5.5 \times 10^{13}$  W/cm<sup>2</sup> and  $3.5 \times 10^{13}$  W/cm<sup>2</sup> for C and Al plasma, respectively. These values are slightly lower than the predictions for absolute instability in homogeneous infinite plasma. In the case of 45° incidence, experimentally estimated gain coefficients given by eq.6.1 were calculated to be 1.1 (C plasma) and 3.2 (Al plasma) in fig.6.5. These values are about 1.5 times higher than the predictions.

Since our laser beam is not uniform, however, we recalculated the threshold and gain to take into account the inhomogeneity of intensity distribution in the focal spot (three component model in chapter 4, discussed more fully later in this chapter). We assume that : 1) SBS is driven by the medium intensity region (area 2 in table 4.1) whose intensity  $I_M$  is 2.3 times higher than the average intensity  $I_{av}$ , and 2) plasma is characterized by  $I_M$  rather  $I_{av}$ , since the electron-ion mean free path is smaller than the scale length of the medium intensity region. To compare with experimental values of the threshold, the theoretical predictions of threshold should be evaluated 2.3 times



lower than the calculated intensity threshold. The results are summarized in table 7.5; the theoretical threshold and the convective gain  $G_L$  are calculated with the medium intensity  $I_M$ , resulting in closer agreement with experiment. In any event, it is necessary to take into account the inhomogeneity of the focal spot.

### 7.3. Spectral Shift

The SBS spectral shift  $\Delta\lambda$  in a flowing plasma is given by eq.2.24.  $\Delta\lambda$  is a simple function of  $T_e$ ,  $n_e$ ,  $M$ , and  $\theta$ . Since we did not observe any systematic dependence of the spectral shift on angle of incidence experimentally, we take  $\theta = 0^\circ$ . For Al plasma,  $T_e$  was estimated to be 600eV and the experimental data fits well to the scaling of temperature ( $T_e \propto I_L^{0.44}$ ), assuming constant  $n_e$  and Mach number. Figure 7.3 shows the calculated red shift (eq.2.24) for Al plasma as a function of Mach number (with several values of  $n_e/n_c$  as a parameter). The measured spectral shift was 0.9Å at  $I_L = 1 \times 10^{14} \text{W/cm}^2$ . From Fig.7.3, we estimate the Mach number of the Al plasma to be 0.60 at  $n_e/n_c = 0.4$ . For C plasma, the Mach number was estimated to be 0.63 with  $T_e=500\text{eV}$  and  $n_e/n_c=0.4$ . The effect of plasma inhomogeneity on the spectral shift and temporal features of the spectral shift will be discussed in the next chapter.

From the time-resolved spectrum (which included an instrumental width of 0.2Å), the linewidth of the SBS spectrum (FWHM) was measured to be typically 0.5Å. Assuming a Lorentzian profile, the net linewidth would be 0.3Å ( $\Delta\nu \approx 1.5 \times 10^{11} \text{ s}^{-1}$ ). Since the typical ion acoustic wave damping  $\gamma_s$  is about  $1.3 \times 10^{11} \text{ (1/s)}$  which is not much less than the observed bandwidth, it is necessary to calculate the detailed

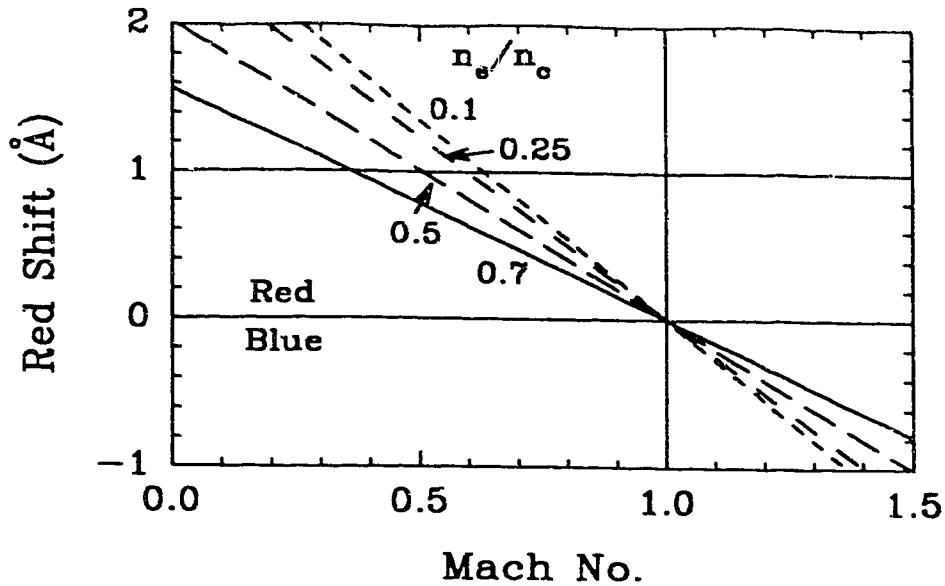


Fig.7.3. Calculated red shift (eq.2.24) as a function of the Mach number for Al plasma at various electron density.

SBS spectral shape by using the frequency dependent kinetic growth rate  $\gamma_k$  (see ref.11). Figure 7.4 shows a plot of the frequency-dependent part of  $\gamma_k(x)$  as a function of  $x \approx 2^{-3/2}(c/v_1)(\Delta\lambda/\lambda)$  for the case of broadening by Landau damping. The parameter  $\beta$  is given by  $(ZT_e/T_i)^{1/2}$  for  $k_s \lambda_D \ll 1$ . For C and Al plasma,  $\beta = 2.4$  and  $3.3$  which correspond to the Landau damping  $\gamma_s^L = 1.3 \times 10^{12}$  and  $2.2 \times 10^{11}$  (1/s), respectively. It is clear that Landau damping (which gives larger  $\gamma_s$  than the collisional damping in our case) would predict narrow spectral shapes (FWHM of the spectrum  $\ll$  peak of the spectral shift) for both cases. Experimentally, such spectral shapes were not observed. Clearly, other effects are important. For our case, these include collisions and plasma inhomogeneity (they will be discussed in the next chapter). In summary, simple homogeneous plasma cannot explain the observed bandwidth of the spectrum.

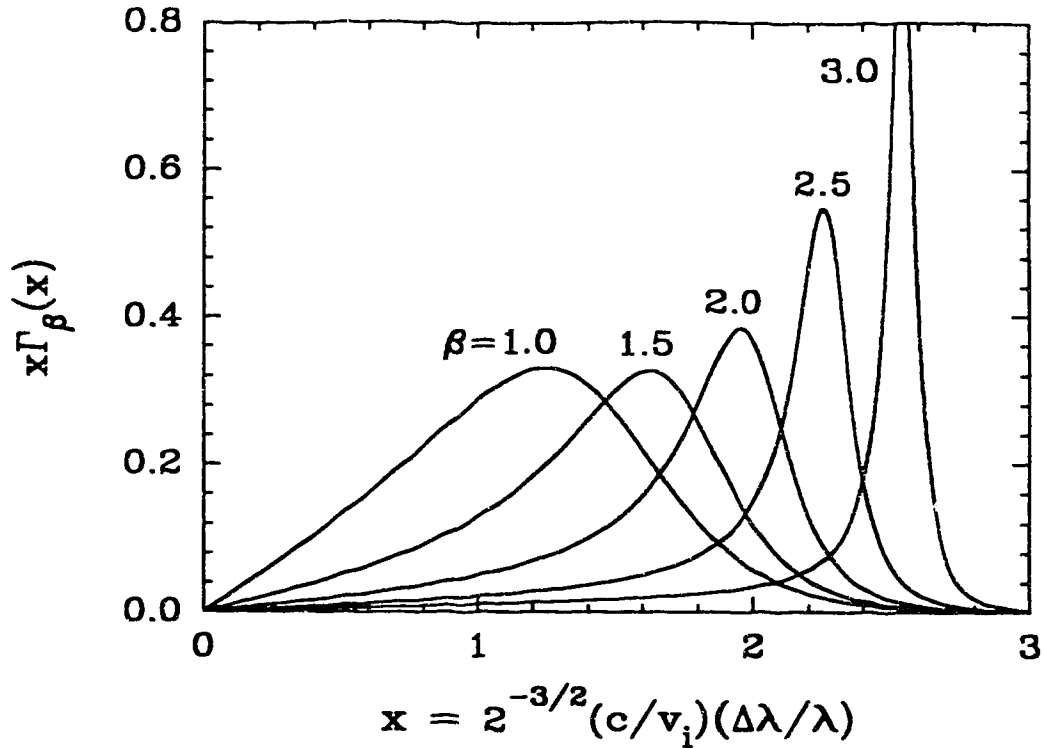


Fig.7.4. Frequency dependent part of the SBS growth rate  $\gamma_k$  calculated from random-phase theory for  $k_s \lambda_D \ll 1$ .  $\gamma_k$  is given in ref.11. The parameter  $\beta$  is given by  $2T_e / T_i$ . Note  $x$  is proportional to the SBS spectral shift  $\Delta\lambda$ .

#### 7.4. Reflectivity

SBS reflectivity is a complex function of plasma parameters ( $T_e$ ,  $n_e$ , etc.). In this section, we examine SBS reflectivity dependence on plasma scale length and electron density for convective amplification in homogeneous plasma (eq.2.38). These two parameters were not measured directly in the experiment. In the calculation of SBS reflectivity, we use eq.2.38 and take into account the inhomogeneity of the focal spot as discussed in section 7.2.3. Plasma conditions ( $T_e$ ,  $Z$ ,  $\gamma_{ib}$ ,  $\gamma_s$ , etc.) were taken to correspond to the medium intensity  $I_M$  ( $\approx 2I_{av}$ ) and the growth rate  $\gamma_0$  was calculated for  $I_M$  as well. We

assume that the medium intensity region is the main contributor to backscattering. Since the region contains 34% of the total energy, the calculated energy reflectivity was adjusted in order to compare to the experimental data; even if the region generates 100% backscattering, energy reflectivity of 34% will be measured outside the plasma.

#### 7.4.1. Dependence on Plasma Length

Figure 7.5 shows the calculated energy reflectivity (solid lines) as a function of average laser intensity for Al plasma (a) and C plasma (b) for various plasma lengths  $L$ . In all cases,  $n_e/n_c = 0.4$  was assumed. Experimental data at the angle of incidence of  $0^\circ$  (solid circles) and  $45^\circ$  (solid squares) are also plotted in order to show the range of measured reflectivity. The initial density fluctuation level was assumed to be  $2.0 \times 10^{-3}$  for Al and C plasmas to obtain comparable reflectivity to the experimental data. Note that the saturation effects are due to the incorporated temperature dependence on laser intensity ( $T_e \propto I_L^{4/9}$ ).

The results show that a range of plasma lengths from  $7\mu\text{m}$  to  $30\mu\text{m}$  are required to explain the experimental data. A single scale length is unable to account for the reflectivity data even for a single angle of incidence. The range of  $L$  required is larger than simply allowing for the change in length with oblique incidence ( $1/\cos(45^\circ) \approx 1.4$ ). Furthermore, the experimental data for Al at  $60^\circ$  showed lower reflectivity than that for Al at  $45^\circ$ . This cannot be explained simply by the effect of longer plasma length for larger angle of incidence.

On the other hand, plasma refraction effects of the laser beam may

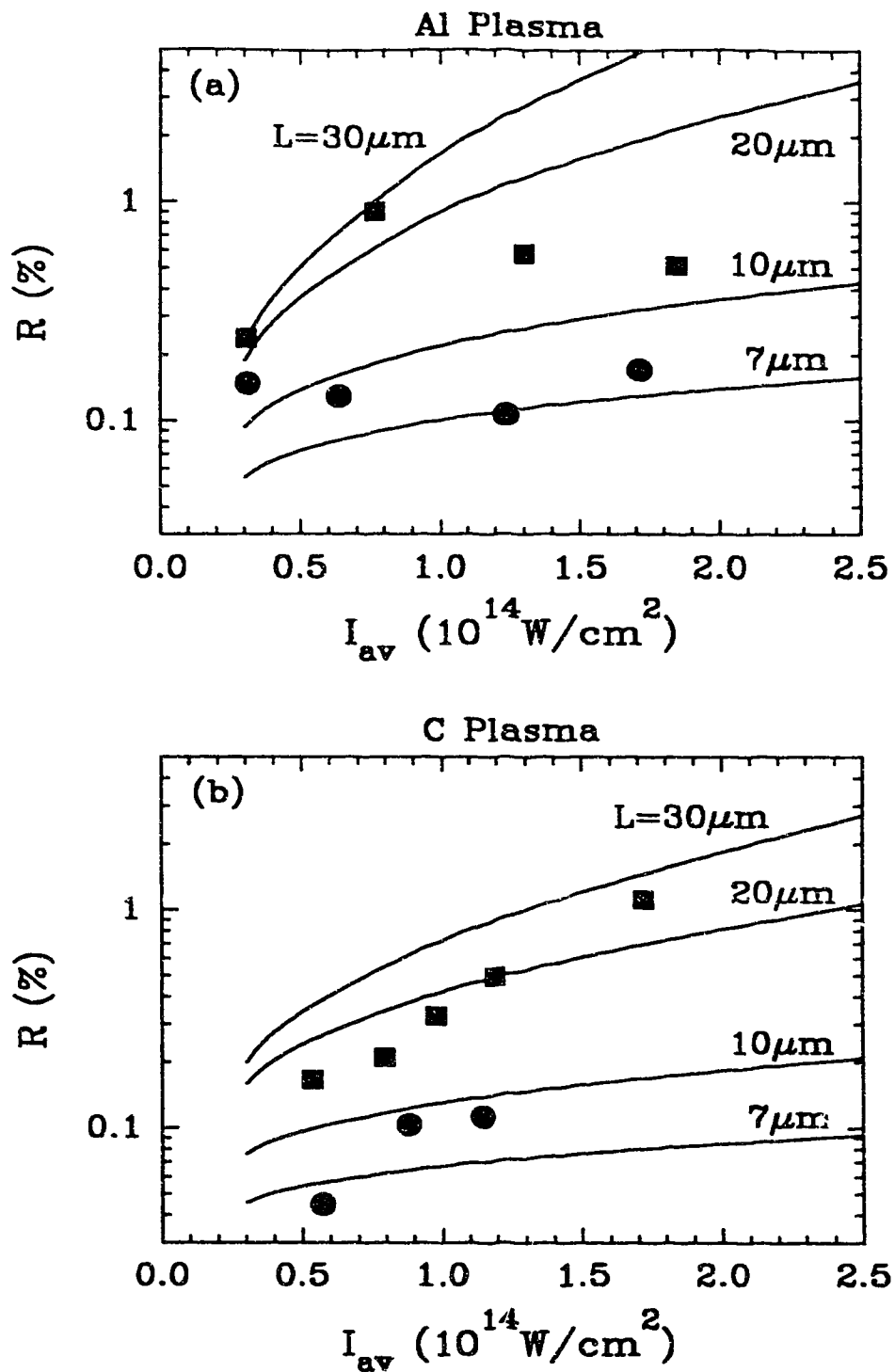


Fig. 7.5. Calculated SBS reflectivity as a function of average laser intensity (solid curves) for various plasma lengths  $L$ . The solid circles and squares are the experimental data at  $0^\circ$  and  $45^\circ$ , respectively.

explain the apparent wide range of the plasma lengths required to account for the data. The CASTOR simulation results (see chapter 4) show that: 1) a plasma larger than focal spot could be created by the laser beam refracted from the plasma, and 2) the effect of refraction is significant for smaller focus.

#### 7.4.2. Dependence on Electron Density

Figure 7.6 shows the calculated energy reflectivity as a function of average laser intensity for Al plasma with various electron density and plasma length  $L$ . The plasma length and initial density fluctuation level were assumed to be  $10\mu\text{m}$  and  $4.0 \times 10^{-3}$  (a),  $20\mu\text{m}$  and  $2.5 \times 10^{-3}$  (b), and  $30\mu\text{m}$  and  $2.0 \times 10^{-3}$  (c). In order to obtain reflectivity comparable to the experimental data, a larger initial density fluctuation level was required for shorter plasma because of the smaller convective gain. Experimental data for  $0^\circ$  angle of incidence (solid circles) and  $45^\circ$  (solid squares) are also plotted to show the range of measured reflectivity. The results show a complicated dependence of SBS reflectivity on electron density. For shorter plasma, the optimum density tends to be higher, because the growth rate  $\gamma_0$  is larger at higher density; hence the pump pulse can efficiently generate SBS scattering in a short distance. On the other hand, lower electron density requires longer gain length to make up for lower  $\gamma_0$ . At fixed plasma length, the optimum density is higher for higher laser intensity, since  $\gamma_{1b}$  is smaller for higher temperature and hence laser light can penetrate to higher density regions where  $\gamma_0$  is larger.

In a planar plasma, the densities of the turning point for  $45^\circ$  and

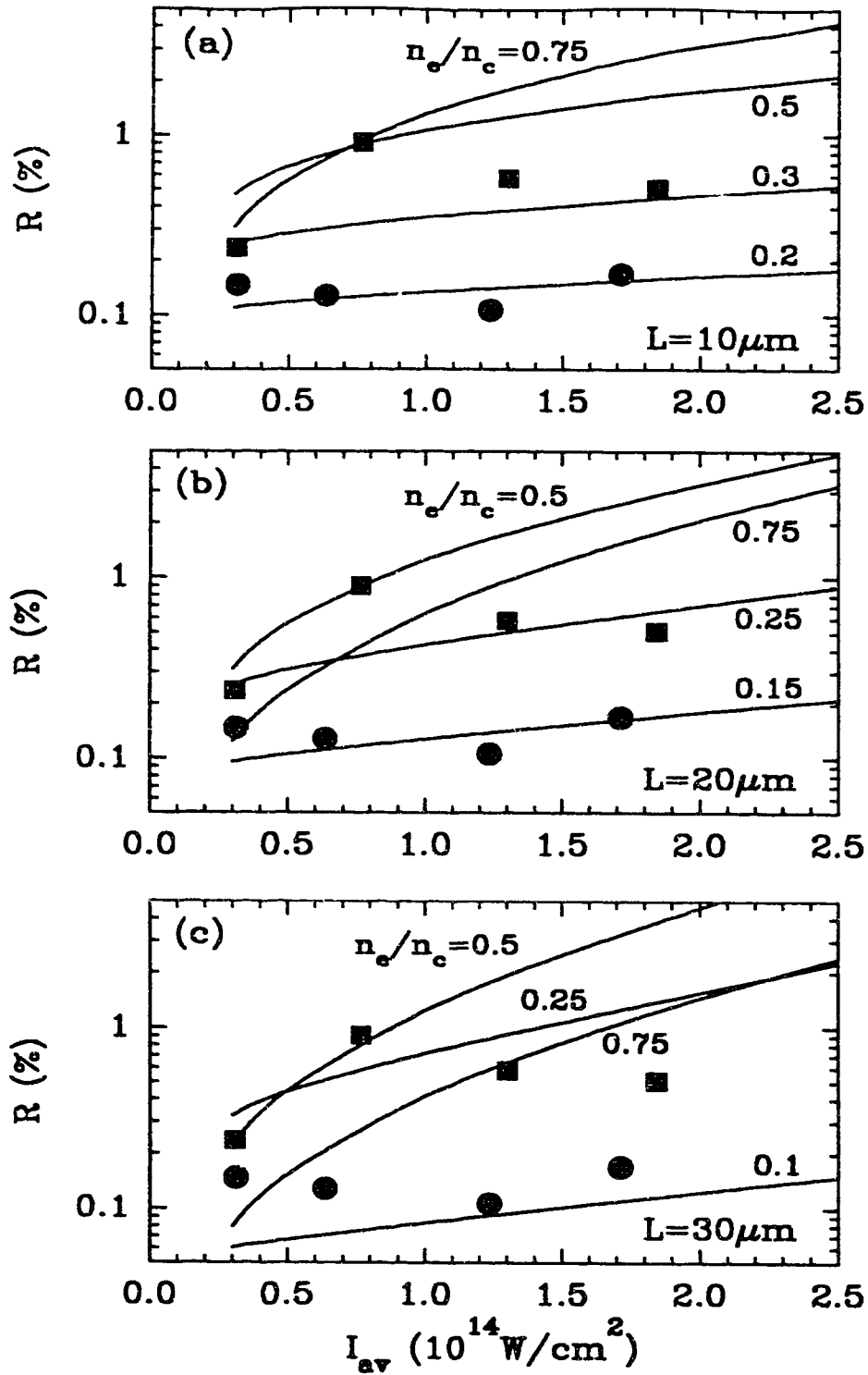


Fig.7.6. Calculated SBS reflectivity as a function of average laser intensity (solid curves) for various electron density  $n_e/n_c$  and plasma length  $L$ . The solid circles and squares are the experimental data at  $0^\circ$  and  $45^\circ$ , respectively.

60° angle of incidence are  $0.5 \cdot n_c$  and  $0.25 \cdot n_c$ . For fixed plasma length, the reflectivity for  $n_e = 0.25 \cdot n_c$  is always lower than that for  $n_e = 0.5 \cdot n_c$  in fig.7.6. By taking into account the turning point density, the lower reflectivity for 60° (compared to 45°) in the experimental data could be explained qualitatively. It is noted that curves for  $n_e/n_c \approx 0.1$  are not applicable to our experimental data, since plasma flow is generally supersonic at this low density which would be inconsistent with the measured red shift (effective Mach number  $\approx 0.6$ ). In any event, features such as saturation characteristics or decreasing reflectivity with increasing  $I_L$  cannot be explained by a single choice of density and plasma scale length. It may be necessary to incorporate laser intensity scaling not only of temperature but also of other plasma parameters such as density and scale length. In summary, the choice of optimum density assuming stationary homogeneous plasma cannot explain all features of the experimental data.

#### 7.4.3. Density Fluctuation Level

The density fluctuation level  $\delta n/n$  can be estimated from the measured reflectivity using eqs.2.33-2.37. Here, calculations for Al plasma (parameters listed in table 7.1) are presented. First, ignoring the phase mismatch, from the Bragg reflection coefficient (eq.2.33), assuming  $n_e/n_c=0.4$ ,  $L=20\mu\text{m}$ ,  $\delta n/n$  is calculated to be  $2.1 \times 10^{-3}$  for  $R=3\%$  (considering the hotspot adjustment for observed  $R=1\%$ ) and  $1.2 \times 10^{-3}$  for  $R=1\%$ . Compared with the calculations in section 7.4.2 (for  $L=20\mu\text{m}$ , and  $n_e/n_c \approx 0.4$ ), these numbers are lower than the assumed initial fluctuation level  $\approx 2.5 \times 10^{-3}$ , which implies



that eq.2.33 is not applicable to our case where damping ( $\gamma_{ib}$  and  $\gamma_s$ ) plays an important role.

From eq.2.36,  $\delta n/n$  is calculated to be  $9.7 \times 10^{-3}$  for  $R=3\%$  ( $\gamma_s/\omega_s = 0.025$ ,  $T_e = 814\text{eV}$ , and  $I_L = 2 \times 10^{14}\text{W/cm}^2$ ) and  $4.9 \times 10^{-3}$  for  $R=1\%$  ( $\gamma_s/\omega_s = 0.019$ ,  $T_e = 600\text{eV}$ , and  $I_L = 10^{14}\text{W/cm}^2$ ). These fluctuation levels are consistent with calculations in section 7.4.2 (small gain  $G_L$  and the initial  $\delta n/n \approx 2 \times 10^{-3}$ ), which implies that the fluctuations will not grow much beyond their initial value. The ion trapping limit calculated from the Water-Bag model<sup>12)</sup> (eq.2.39 gives  $\delta n/n > 0.18$  for  $ZT_e/T_i=11$ ) is well above the fluctuation level  $\approx 10^{-2}$ . It is noted that since eq.2.33 and 2.36 does not take into account the absorption of the scattered light, the results will give lower estimations for the absorbing plasma.

In the previous sections 7.4.1 and 7.4.2, the initial density fluctuation level ( $N_n$  in eqs.3.2 or  $[\delta n/n]_{ini}$  in eq.2.38) has been assumed to be  $\approx 10^{-3}$  in order to calculate reflectivity comparable to the experimental data. Equation 2.37 can be used to relate the initial density fluctuation level to the electromagnetic (EM) noise scattering level ( $R_{min}$  in eq.2.37). Assuming plasma conditions around threshold intensity ( $n_e/n_c=0.4$ ,  $T_e = T_i \approx 380\text{eV}$  for  $I_L \approx 3.5 \times 10^{13}\text{W/cm}^2$ ), the EM noise scattering levels are estimated to be  $3 \times 10^{-4}$  for  $N_n \approx 10^{-3}$  and  $1.4 \times 10^{-3}$  for  $N_n \approx 2 \times 10^{-3}$ . For an effective  $I_{th}$  ( $\approx 8 \times 10^{13}\text{W/cm}^2$ ) with hotspot enhancement of 2.3, the effective EM noise scattering level is  $8 \times 10^{-4}$  for  $N_n \approx 10^{-3}$ . Similar calculations with eq.2.36 give  $8 \times 10^{-4}$  and  $5 \times 10^{-4}$  for  $I_L \approx 3.5 \times 10^{13}\text{W/cm}^2$  and  $I_L \approx 8.0 \times 10^{13}\text{W/cm}^2$  ( $N_n \approx 10^{-3}$ ). In summary, the electromagnetic noise scattering level corresponding to the initial density fluctuation level  $\approx 10^{-3}$  is

estimated to be about  $10^{-3}$ - $5 \times 10^{-4}$ .

#### 7.4.4. Noise Source of Scattered Light

The electromagnetic noise scattering level was estimated to be roughly  $10^{-3}$ - $5 \times 10^{-4}$  for the convective amplification model in finite homogeneous plasma. This number can be compared with the scattering level calculated from the possible mechanisms listed in section 2.5. From eq.2.28, the incoherent Thomson scattered intensity can be calculated from

$$I_{TS} = \frac{dP_{TS}}{dS} \approx r_e^2 \sin^2 \phi I_0 n_e L d\Omega \quad (7.4)$$

where  $dS$  is the focal spot size of the laser beam ( $\approx 3.3 \times 10^{-6} \text{cm}^2$ ),  $r_e$  is the electron radius ( $= 2.8 \times 10^{-13} \text{cm}$ ),  $\sin \phi = 1$  for backscattering,  $n_e \approx 0.4 n_c$  ( $= 7.3 \times 10^{21} \text{cm}^{-3}$ ),  $L$  is the plasma length ( $\approx 20 \mu\text{m}$ ),  $d\Omega$  is the solid angle of the focusing cone ( $\approx 0.10$ ), and  $I_0$  is the threshold intensity ( $\approx 3 \times 10^{13} \text{W/cm}^2$ ).  $I_{TS}/I_0$  is calculated to be  $1.1 \times 10^{-7}$ , which is  $10^4$  times smaller than the estimated noise scattering level.

From eq.2.29, for  $T_e = 380 \text{eV}$ ,  $Z=11$ ,  $\nu = 1.2 \times 10^{15} \text{1/s}$  ( $0.248 \mu\text{m}$ ), and  $d\nu = 4.8 \times 10^{11} \text{1/s}$  ( $1 \text{\AA}$ ), the bremsstrahlung power density  $W_{BR}$  is calculated to be  $7 \times 10^6 \text{W/cm}^3$ . Assuming optically thin plasma of  $20 \mu\text{m}$ ,  $I_{BR}/I_0 \approx 4 \times 10^{-10}$ , which is much smaller than the Thomson scattering. From eq.2.30, the blackbody radiation flux was also calculated to be  $5 \times 10^3 \text{W/cm}^2$ , and  $I_{BB}/I_0 \approx 1 \times 10^{-10}$  which is the same order of magnitude as the bremsstrahlung radiation.

Thomson scattering of the laser beam by ion acoustic noise dominates the bremsstrahlung source by several orders of magnitude as pointed out by Berger et al.<sup>13,14</sup>. According to Berger, the backscattered flux per unit solid angle per unit wavelength of light

scattered from thermal ion fluctuations is given by

$$\frac{dF}{d\Omega d\lambda} = \frac{ck_B T_L}{\lambda_s^4} E'' \frac{\omega_1}{2\omega_s} \frac{1}{(1 - n_e/n_c)^{1/2}} (e^G - 1) \quad (7.5)$$

where  $k_B$  is the Boltzmann constant,  $\lambda_s$  is the wavelength of the scattered light,  $E''$  is the transmission coefficient for light from the interaction region to the vacuum,  $\omega_1$  ( $\approx \omega_0 =$  laser frequency) and  $\omega_s$  are frequencies of the scattered light and ion acoustic wave, and  $G$  is the SBS convective gain.  $T_L$  is given by

$$T_L = T_e \left\{ (1 + ZQ) / [1 + (ZT_e/T_i)Q] \right\} \quad (7.6)$$

where

$$Q = (v_e/v_i) \exp[ - (ZT_e + 3T_i) / 2T_i ] \quad (7.7)$$

In the case of  $T_e = T_i$ ,  $T_L \approx T_e$ . Assuming  $E'' \approx 1$ ,  $G \approx 3$ , and  $T_e = 600\text{eV}$  for  $I_L = 10^{14}\text{W/cm}^2$ , the flux is calculated to be  $1 \times 10^8\text{W/cm}^2$  or  $F/I_0 \approx 10^{-6}$ , which is three orders of magnitude smaller than the measured reflectivity. The experimental data cannot be explained by convective growth from thermal ion fluctuations.

Reflection from the critical surface could initiate the growth of SBS as pointed out in section 2.5. In our case, two kinds of experimental evidence refute this speculation. Firstly, from the time-resolved spectrum for  $\theta = 0^\circ$  (e.g. see fig.5.10, 5.11(a)), the narrowband, un-shifted reflected light was observed only at early time in the laser pulse. At later time the inverse bremsstrahlung absorption dominated whereby little light was reflected. Hence, it was unlikely that such reflection reasonably seeded the SBS scattered light which occurred later in the incident pulse. Secondly, almost the same reflectivity ( $\approx 0.1\%$ ) was observed at threshold for angles of incidence from  $0^\circ$  to  $45^\circ$ . Reflection from the critical surface should

be in the specular direction at early time in the laser pulse because of planar plasma expansion. In fact, we only observed such reflection (with zero frequency shift) in the time-resolved spectrum for normal incidence targets ( $\theta=0^\circ$ ). Hence reflection from the "critical" surface is less effective for oblique incidence (and cannot explain all the data taken at various angles of incidence).

Another possible mechanism for the relatively high noise source level is enhanced ion fluctuations produced by the two plasmon ( $2\omega_p$ ) decay instability (TPD)<sup>15)</sup>. Experiments in  $\text{CO}_2$ -laser-produced plasma by Meyer et al.<sup>16)</sup> and Baldis et al.<sup>17)</sup> have shown that TPD (or maybe mode coupling between TPD and SRS (stimulated Raman scattering)) can produce ion fluctuations with wavenumber  $k \approx 2k_0$ . We examine the possibility of such parametric instabilities in our plasma by calculating their threshold intensities. Threshold intensities for TPD and SRS in homogeneous infinite plasma are given by<sup>18)</sup>

$$\frac{v_0^2}{c^2} > \left( \frac{v_{ei}}{\omega_p} \right)^2 \quad \text{for TPD} \quad (7.8)$$

$$\frac{v_0^2}{c^2} > \left( \frac{\omega_p}{\omega_0} \right)^2 \cdot \left( \frac{v_{ei}}{\omega_0 \omega_p} \right)^2 \quad \text{for SRS} \quad (7.9)$$

where the dominant damping mechanism for the electron plasma waves is assumed to be electron-ion collisions. Using the plasma conditions expected at SBS threshold (measured  $I_{th} \approx 3.5 \times 10^{13} \text{W/cm}^2$ ,  $T_e = T_i = 380 \text{eV}$ ,  $n_e/n_c = 0.25$ ,  $Z=11$  for Al plasma), the threshold intensities for TPD,  $I_{th}^{TPD}$ , and SRS,  $I_{th}^{SRS}$ , are calculated to be  $6.8 \times 10^{15} \text{W/cm}^2$  and  $8.5 \times 10^{14} \text{W/cm}^2$ , respectively. These threshold intensities are higher than the laser intensity in the experiment. Moreover, the condition  $(v_{ei}/2\gamma_0)(v_0/v_e)^{1/2} > 2$  is satisfied whereby only convective SRS

instability is expected. Plasma inhomogeneity, however, dominates the instabilities and determines threshold intensity.  $I_{th}^{TPD}$  and  $I_{th}^{SRS}$  determined by plasma density gradient<sup>18)</sup> are calculated to be  $4.5 \times 10^{14} \text{ W/cm}^2$  and  $1.0 \times 10^{17} \text{ W/cm}^2$  (the former one is lower than the homogeneous threshold and hence not applicable), respectively. Even higher intensity hotspots in the focus would not satisfy the above threshold conditions. Therefore, both TPD and SRS are not expected in our experiment and, indeed, previous experiments found no evidence for their occurrence.

### 7.5. Hotspot Effects

In this section, a model for heating hotspots in the focal spot is presented and the effects of hotspots on SBS reflectivity is examined. We assume that : 1) the focal spot consists of three areas with different intensity levels as modelled in table 4.1., and 2) the measured total reflectivity is a linear sum of local reflectivities. Each area is characterized by three quantities; intensity  $I_n$ , area  $A_n$ , and contained energy  $E_n$  ( $n=1,2,3$ ) as shown in fig.7.7. The contained energy  $E_n$  is given by  $I_n \cdot A_n \cdot \tau_L$ , where  $\tau_L$  is the laser pulse width. Each intensity and area are related to the normalized intensity  $I_0$  and total area  $A_0$  as

$$I_1 : I_2 : I_3 = aI_0 : bI_0 : cI_0 \quad (7.10)$$

$$A_1 : A_2 : A_3 = xA_0 : yA_0 : zA_0 \quad (7.11)$$

Since we measured energy reflectivity in the experiment, we consider the SBS energy reflectivity  $R_e^{SBS} = E^{SBS} / E_0$ , where

$$E_0 = E_1 + E_2 + E_3 \quad (7.12)$$

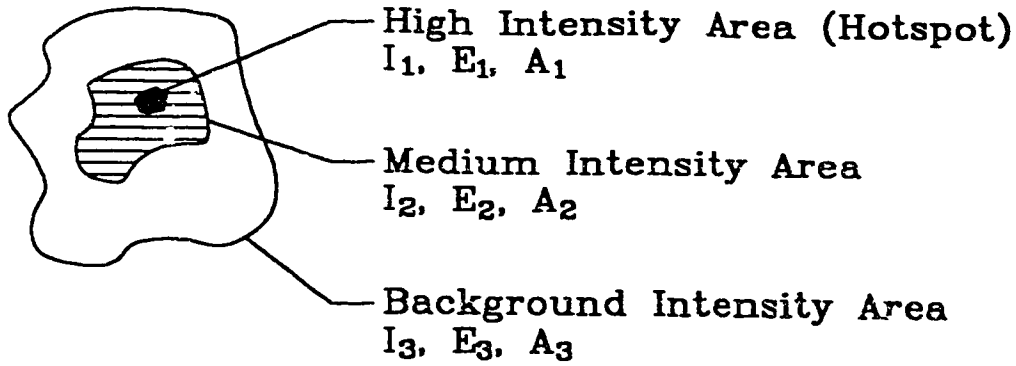


Fig.7.7. Model of focal spot for hotspot analysis.

$$\begin{aligned}
 E^{SBS} &= E_1^{SBS} + E_2^{SBS} + E_3^{SBS} \\
 &= I_1^{SBS} A_1 \tau_1 + I_2^{SBS} A_2 \tau_2 + I_3^{SBS} A_3 \tau_3
 \end{aligned}
 \quad (7.13)$$

$\tau_n$  is the backscattered pulse width,  $I_n^{SBS} = R_n^{SBS} \cdot I_n$ , and  $R_n^{SBS}$  is calculated by eq.2.38. Assuming  $\tau_1 \approx \tau_2 \approx \tau_3 \approx \tau_{SBS}$ ,

$$E^{SBS} = I_0 \tau_{SBS} A_0 ( axR_1^{SBS} + byR_2^{SBS} + czR_3^{SBS} ) \quad (7.14)$$

$$E_0 = I_0 \tau_L A_0 ( ax + by + cz ) \quad (7.15)$$

Hence,

$$R_c^{SBS} = \frac{\tau_{SBS}}{\tau_L} \cdot \frac{axR_1^{SBS} + byR_2^{SBS} + czR_3^{SBS}}{ax + by + cz} \quad (7.16)$$

In the experiment, we only know the average intensity  $I_{av} = E_0 / \tau_L A_0$ , which can be related to  $I_0$  as

$$I_{av} = I_0 ( ax + by + cz ) / ( x + y + z ) \quad (7.17)$$

Once we know the characteristics of the focal spot (coefficients a, b, c, x, y, and z), we can calculate  $I_0$  for each  $I_{av}$ , then using eq.2.38, we calculate  $E_n^{SBS}$ , and finally,  $R_c^{SBS}$  which can be compared with the experimental data. This model can be expanded to any number of different intensity areas.

We apply this hotspot model to two types of plasma. One is a

weakly collisional plasma in which  $\lambda_{ei} > (\text{focal spot size}) \gg \lambda_{HS}$ , where  $\lambda_{ei} = v_e / \nu_{ei}$  is electron ion collision mean free path and  $\lambda_{HS}$  is a scale length of the hotspot. In such a plasma, we expect that the thermal diffusion is so dominant that the plasma conditions over the entire focal spot are characterized by the average intensity and consequently the different intensity beams interact with the same plasma parameters. The other type is a strongly collisional plasma in which  $\lambda_{ei} \ll \lambda_{HS}$ . In such a plasma, we expect that local heating dominates thermal diffusion and each area has its own plasma conditions independently. In general,  $\lambda_{ei}$  can be any characteristic scale length of the dominant energy carrier, e.g. x-ray, hot electron, etc..

First, for simplicity, we consider two levels of intensity; a hotspot (HS) intensity  $I_{HS}$ , and a background (BG) intensity  $I_{BG}$ . We assume  $I_{HS} = 2.5 \cdot I_{BG}$  as an example. Then eq.7.15 becomes

$$I_{av} = I_0 ( 2.5r + (1-r) ) = I_{BG} ( 1 + 1.5r ) \quad (7.18)$$

where  $r$  ( $0 < r < 1$ ) is the hotspot area fraction. We also assume  $\tau_{SBS} / \tau_L \approx 0.5$ , and an initial fluctuation level  $\delta n / n \approx 10^{-3}$ .

Figure 7.8 shows the SBS energy reflectivity as a function of hotspot area fraction  $r$  for several average laser intensities. The solid and dashed lines show the results for collisionless and collisional Al plasma ( $n_e / n_c = 0.4$ ,  $L = 20 \mu\text{m}$ ). The dotted line is the contribution from the background area. It is important to note that for the same  $I_{av}$ ,  $I_{HS}$  and  $I_{BG}$  decrease with increasing  $r$  in order to conserve the energy contained in the focal spot (see eq.7.18). The reflectivity at  $r = 0$  represents the reflectivity for uniform focal spot with  $I_{av}$ .

The results show that the effect of hotspots is significant at

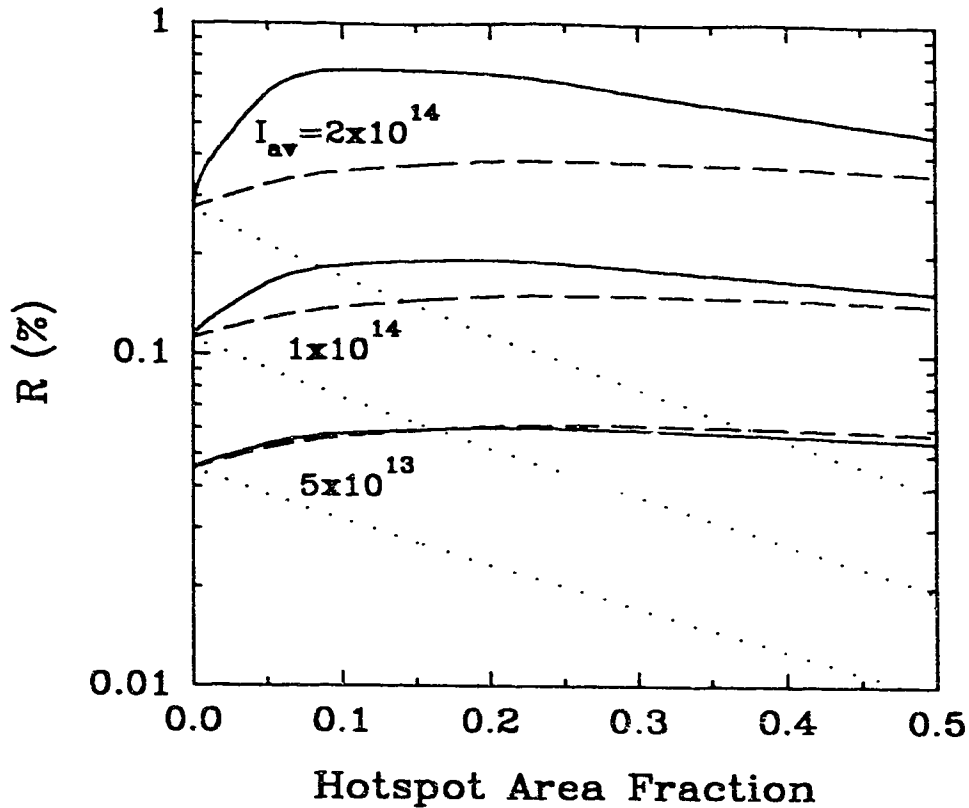


Fig.7.8. Two-level-intensity focal spot model. Calculated SBS energy reflectivity as a function of hotspot area fraction for Al plasma ( $n_e/n_c=0.4$ ,  $L=20\mu\text{m}$ ). The solid and dashed lines show the collisionless and the collisional model. The dotted lines show contributions from the BG intensity area.

higher intensity because of the nature of exponential growth. The reflectivity increases sharply with increasing  $r$  until  $r \approx 0.1$  and maximizes at  $r \approx 0.1-0.2$ . The smaller hotspot gives higher intensity and higher local reflectivity but contains less energy. For  $r < 0.1$ , the sharp rise in reflectivity is due to increasing hotspot area. On the other hand, a larger hotspot gives lower local reflectivity but contains more energy. For  $r > 0.1$ , the increased hotspot area is



compensated by decreased local reflectivity, resulting in the nearly saturated total reflectivity or even lower reflectivity for high intensity.

In fig.7.8, the collisionless plasma model (solid lines) shows more significant increase in reflectivity than the collisional plasma model (dashed lines). This is mainly due to the difference of temperature assumed in each model. Although the damping coefficients,  $\gamma_s$  and  $\gamma_{1b}$ , are functions of temperature, their scalings with temperature in this particular range of plasma parameters (Al plasma,  $n_e/n_c = 0.4$ ,  $T = 300\text{eV}-1\text{keV}$ ) work in a way to cancel each other in calculating gain ( $\propto \gamma_0^2/\gamma_s \gamma_{1b}$ ). As a consequence, SBS gain scales roughly as  $T^{-1/2}$ , resulting in higher gain for higher intensity beams into cold plasma.

Next, we apply the hotspot model to our focal spot which was modelled by three levels of intensity as described in section 5.1.2. The parameters of our focal spot are listed again in table 7.6. Using these parameters, we calculated SBS energy reflectivity as a function of average laser intensity for the two types of Al plasma; collisional and collisionless for  $n_e/n_c=0.4$ ,  $L=20\mu\text{m}$ , initial  $\delta n/n=10^{-3}$ . Figure 7.9 shows a comparison of reflectivities for collisionless (dashed line) and collisional (dotted line) plasma with a three-level-intensity

Table 7.6. Characteristics of focal spot

Area name	Intensity	Area	Energy contained
HS	3.8	0.01	0.06
Med.	2.3	0.09	0.34
BG	0.7	0.50	0.60
Average	1.0	1.00	1.00

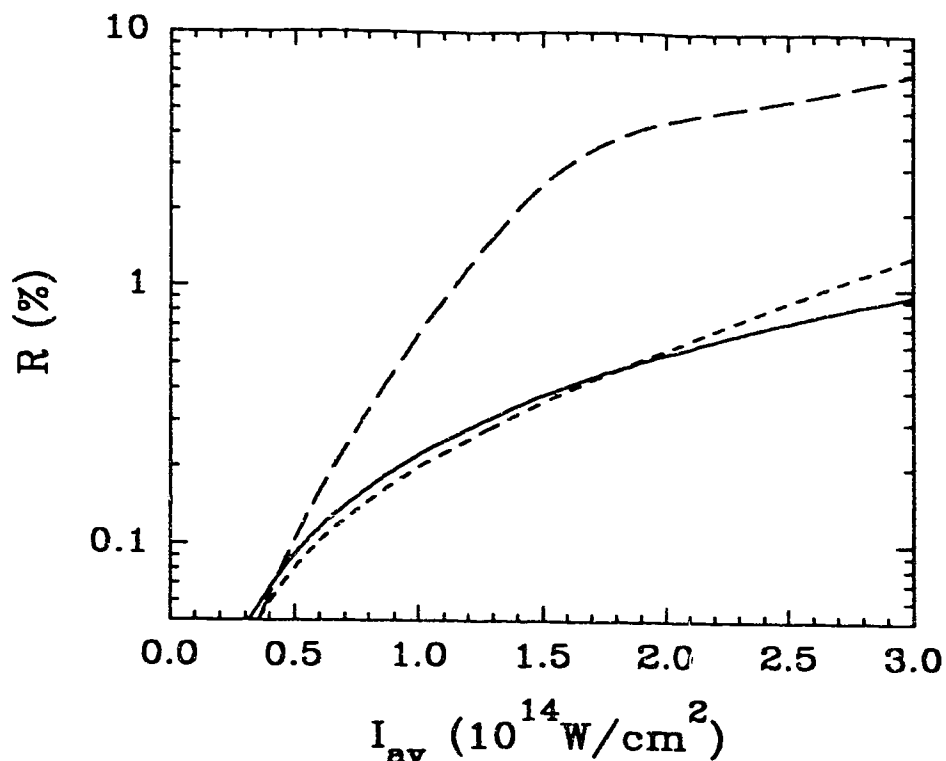


Fig.7.9. Three-level-intensity focal spot model. Calculated reflectivity as a function of average laser intensity for collisionless (long dashed line) and collisional (short dashed line) Al plasma ( $n_e/n_c=0.4$ ,  $L=20\mu\text{m}$ ). The solid line shows the reflectivity for uniform focal spot with  $I_{av}$ .

focal spot as well as the reflectivity for uniform focal spot with  $I_{av}$  (solid line). Figure 7.10 shows details of the reflectivity calculations for collisionless (a) and collisional (b) plasma. The solid lines show total reflectivity. The dashed, dotted and dash-dot lines show contributions of the hotspot (HS), medium intensity (Med.) and background (BG) areas. Note that the local reflectivities for  $R > 0.1\%$  ( $I_{av} > 0.7 \times 10^{14} \text{ W/cm}^2$ ) in the HS area and  $R > 0.5\%$  ( $I_{av} > 1.5 \times 10^{14} \text{ W/cm}^2$ ) in the Med. area are over-estimated and assumed to be saturated ( $R=100\%$ ) for HS area at  $I_{av} > 1.5 \times 10^{14} \text{ W/cm}^2$  in fig. 7.10 (a).

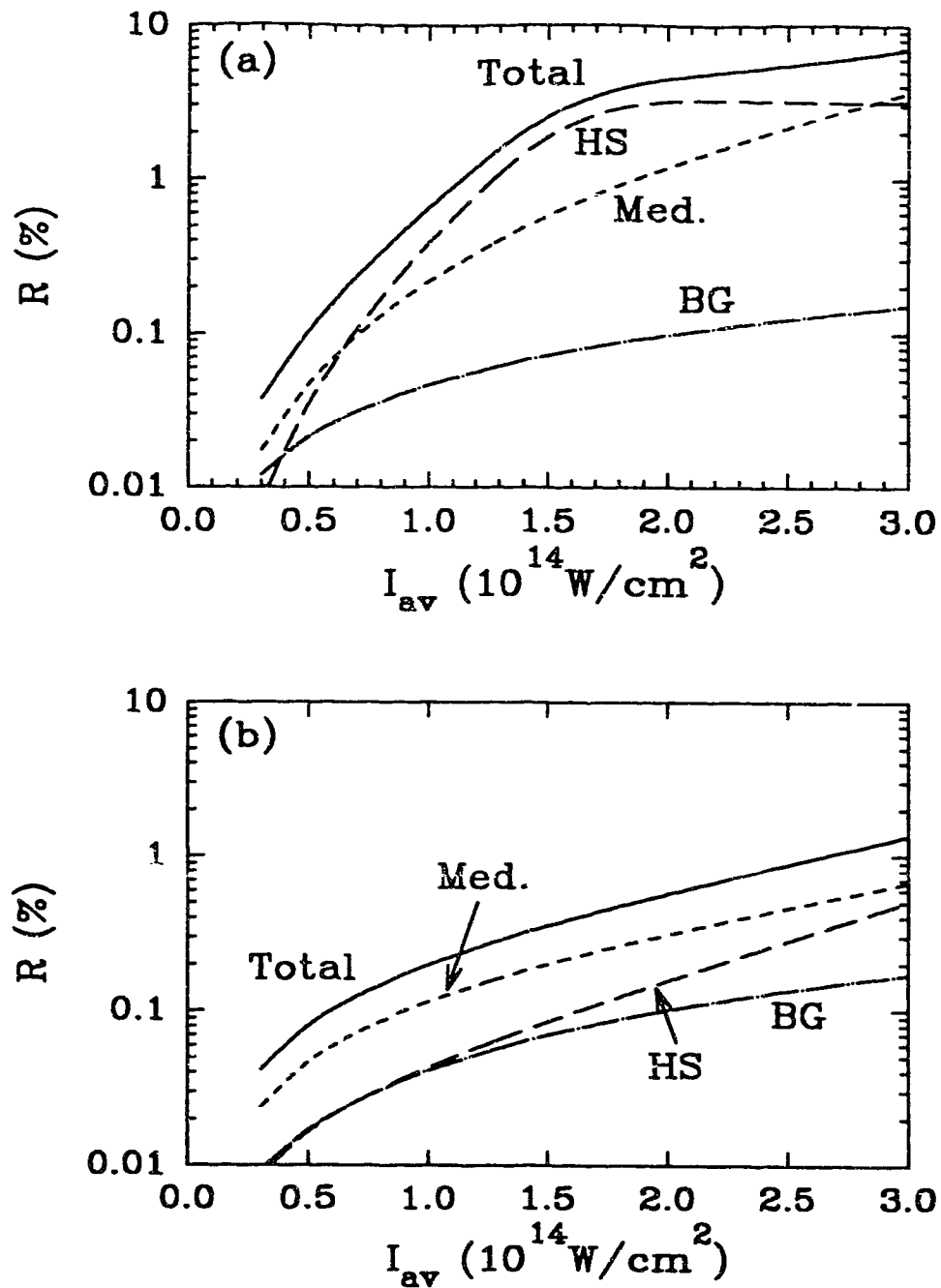


Fig. 7.10. Three-level-intensity focal spot model. Details of the total reflectivity (solid lines) as a function of average laser intensity are shown for collisionless (a) and collisional (b) Al plasma ( $n_e/n_c = 0.4$ ,  $L = 20\mu\text{m}$ ). The dashed, dotted and dash-dot lines show contributions of the hotspot (HS), medium intensity (Med.) and background (BG) areas.

Equation 2.38 is inaccurate for reflectivity higher than a few %, since pump depletion due to SBS interaction is neglected.

In fig.7.9, the collisionless plasma showed significant enhancement of reflectivity due to hotspots for the same reason as mentioned in fig.7.8. Since no saturation mechanism was included in the calculation, a local reflectivity  $R=100\%$  was assumed, resulting in a contribution of 3% to the total ( $=\tau_{\text{SBS}}/\tau_{\text{L}} \times$  energy contained in the area). If one assumes a saturation mechanism which restricts the maximum reflectivity to less than 100%, the effect of hotspots would be less. The reflectivity for the collisional plasma is comparable to that for the uniform focal spot. This is due to the limited energy contained in the Med. area. For higher intensity ( $I_{\text{av}} > 2 \times 10^{14} \text{W/cm}^2$ ), the hotspot model shows higher reflectivity than the uniform model.

In fig.7.10, both cases show that the Med. intensity region is dominant near the threshold intensity ( $I_{\text{th}} \approx 3 \times 10^{13} \text{W/cm}^2$ ), consistent with the results discussed in section 7.2.3. This domination holds in the case of collisional plasma (b) for  $I_{\text{av}} < 3 \times 10^{14} \text{W/cm}^2$ . In the case of collisionless plasma (a), depending on the saturation level of reflectivity, the HS and Med. areas compete with each other above the threshold intensity.

The electron-ion collision mean free path  $\lambda_{e1}$  in Al plasma is calculated to be  $0.2 \mu\text{m}$  for  $n_e/n_c = 0.4$ ,  $T=600\text{eV}$  and  $1.7 \mu\text{m}$  for  $n_e/n_c = 0.1$ ,  $T=1100\text{eV}$ . These values are smaller than or comparable to the scale length of the hotspot ( $L_{\text{HS}} < 5 \mu\text{m}$ ) and much smaller than the focal spot size. Therefore, we expect that the collisional plasma model is appropriate to our experiment; the medium intensity area (9% of the total area) is the principal contribution to the SBS interaction.

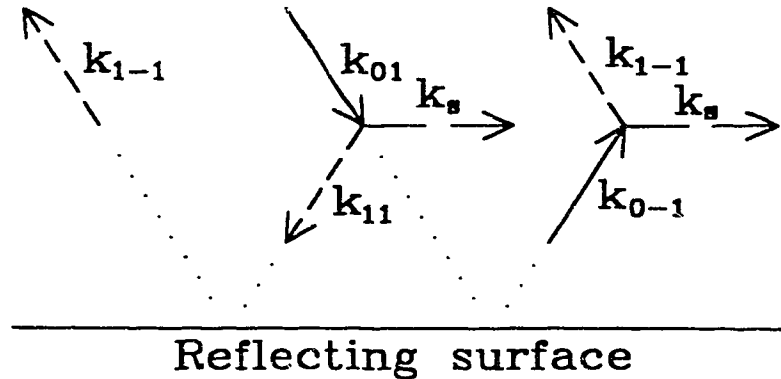


Fig.7.11. Schematics of interacting wavevectors of DSBS.

#### 7.6. Double Stimulated Brillouin Scattering (DSBS)

Figure 7.11 schematically shows the interacting wavevectors  $k_{nm}$  for DSBS,<sup>19)</sup> where  $n = 0, 1, s$  correspond to the incident, scattered and sound waves and  $m = 1, -1$  correspond to incoming and outgoing waves. The essential element of DSBS is not the backscattering but the specular forward scattering. The incident light  $k_{01}$  interacts with a sound wave  $k_s$  to generate forward scattered light  $k_{11}$  which is subsequently reflected back as  $k_{1-1}$ . In addition, reflected light  $k_{0-1}$  (reflection of  $k_{01}$ ), can interact with the same sound wave  $k_s$  to generate/amplify the scattered wave  $k_{1-1}$ . These two elementary processes provide positive distributed feedback. Both  $k_{11}$  and  $k_{1-1}$  are observed as backscattering from the external point of view. Note the direction of the sound wave is perpendicular to the density gradient. Thus phase matching conditions for this process do not depend on plasma density. Because of the positive feedback and the insensitivity to plasma inhomogeneity, DSBS can lead to increased reflectivity and lower intensity threshold. In this section, we

examine the possibility of DSBS in our experiment.

DSBS has three features to look for experimentally. The first is a  $\sin\theta$  dependence for wavelength shift where  $\theta$  is angle of incidence (eq.2.31), in contrast to a  $\cos\theta$  dependence for ordinary SBS. The second is the sum of the backscattered and the specular reflectivity is constant:

$$R_{BS} + R_{SP} = \bar{r} = r \cdot \exp(-2\tau) \quad (7.19)$$

where  $R_{BS}$  and  $R_{SP}$  are reflectivity of backward and forward specular reflection,  $\bar{r}$  is the "constant" reflectivity, and  $\tau$  is the optical depth of the plasma for the electromagnetic wave. The third feature is the high threshold intensity, given by eq.2.32. In this experiment, however, the first two features could not be clearly identified, since: 1) the spectral shift did not show a systematic dependence on angle of incidence (see fig.6.12), likely because of spherical expansion of the plasma, and 2) the specular reflectivity was an order of magnitude smaller than the backscatter reflectivity ( $R_{BS} \gg R_{SP}$ , see fig.6.6) thereby making it difficult to establish a relation between  $R_{BS}$  and  $R_{SP}$ .

The threshold intensity for DSBS depends on the optical depth  $\tau$ . In order to use the formulae given in reference 19, we assume a plasma density profile  $n_e(x) = n_0(x/L_n)^2$  with  $L_n \approx 20\mu\text{m}$ . Then  $\tau$  is given by

$$\tau = 0.6 \tau_0 \cos^4\theta_0 \quad (7.20)$$

where  $\tau_0 = \nu_{ei}(n_c) \cdot (L_n/c)$ ,  $\nu_{ei}(n_c)$  is the electron-ion collision frequency evaluated at critical density, and  $\theta_0$  is the angle of incidence. Assuming  $T_e = T_i \approx 400\text{eV}$ ,  $Z=11$ ,  $\ln\Lambda \approx 5$ , and  $L_n \approx 20\mu\text{m}$ ,  $\tau_0$  is calculated to be 37, whereby  $\tau \approx 22$  for  $\theta=0^\circ$  and  $\tau \approx 5.6$  for  $\theta=45^\circ$ . For this case of high absorption, the threshold intensity is given by

eq.2.32. Assuming  $\gamma_s/\omega_s \approx 0.02$ ,  $I_{th}$  was calculated to be  $8.6 \times 10^{15} \text{W/cm}^2$  for  $0^\circ$  and  $1.8 \times 10^{15} \text{W/cm}^2$  for  $45^\circ$ . These numbers are much higher than the observed threshold intensity ( $\approx 3.5 \times 10^{13} \text{W/cm}^2$ ), or even  $8 \times 10^{13} \text{W/cm}^2$  allowing for a hotspot enhancement of 2.3.

In contrast, for the case of weak absorption ( $\bar{r} \geq 10^{-4}$ ), the threshold intensity is given by<sup>19)</sup>

$$\frac{I_{th} \lambda_0^2}{10^{16} T} = 2 \frac{\gamma_s \lambda_0}{\omega_s L_n} \frac{e^\tau}{\cos^2 \theta_0} \ln^{-1} \left( \pi \frac{L_n}{\lambda_0} \cos^2 \theta_0 \right) \quad (7.21)$$

for  $T = T_e + 3T_i / Z$ ,  $I_{th}$  in  $\text{W/cm}^2$ ,  $\lambda_0$  in  $\mu\text{m}$ , and  $T$  in keV. For  $\theta=0^\circ$ , eq.7.21 gives a threshold intensity of  $1.2 \times 10^{15} \text{W/cm}^2$ . Consequently, to explain the measured threshold, we would have to assume  $\tau \approx 2.0$ . Such a short optical depth requires a turning point density  $n_t$  ( $\approx 0.09n_c$ ) or high temperature ( $\approx 2\text{keV}$ ) at the critical density, which are very unlikely. In either absorption model, and especially for the more realistic case of strong absorption, the threshold intensity seems to be too high. Hence we do not expect DSBS in our experiment.

### 7.7. Summary

We have compared the experimental data with analytical calculations for a homogeneous plasma. Convective growth of SBS is predicted for the expected plasma conditions. The experimental values of threshold and gain for SBS are higher than those expected for the average laser intensity conditions. These differences can be qualitatively (and quantitatively) accounted for by taking into account high intensity regions in the focal spot. The measured spectral shift can be accounted for by plasma flow with a Mach number  $\approx 0.6$ . The measured bandwidth of the SBS spectrum is larger than expected for

homogeneous plasma. Analytical calculations of the dependence of SBS reflectivity on plasma length and electron density were compared with the experimental data for Al targets. The measured reflectivity could only be fitted by assuming a wide range of plasma lengths from  $12\mu\text{m}$  to  $30\mu\text{m}$ . Calculations for longer plasma length compared satisfactorily with data for larger angle of incidence, suggesting increased laser light refraction and convective growth of SBS for larger  $\theta$ . The SBS dependence on electron density showed that a single value of electron density (homogeneous plasma) could not explain the experimental data over the full range of laser intensity; consequently, choosing the optimum density for SBS growth in homogeneous plasma is inadequate to explain the experiment. The ion density fluctuation level was estimated to be about  $10^{-3}$ , well below the trapping limit. Thomson scattering, the bremsstrahlung, SRS and/or TPD are not likely to be the noise source for seeding SBS. The mechanism for the relatively high level of scattered light required at the threshold intensity is still in question. We proposed a model of SBS reflectivity which includes hotspots in the focal spot. Results of model calculations showed that contributions to the reflectivity depend not only on the intensity level but also on the fraction of area in the hotspot. The effects of the hotspot appeared to be significant for collisionless plasma but less for collisional plasma. From the threshold analysis, DSBS was unlikely in our experiment because of the strong inverse bremsstrahlung absorption of the laser light.



Bibliography

- 1) D.Colombant and G.F.Tonon, J.Appl.Phys., **44**, 3524 (1973).
- 2) D.Duston and J.Davis, Phys.Rev.A, **21**, 1664 (1980).
- 3) P.Mora, Phys.Fluids, **25**, 1051 (1982).  
F.Dahmani and T.Kerdja, Phys.Fluids, **B3**, 1232 (1991).
- 4) T.A.Carlson, C.W.Nestor, Jr., N.Wasserman, and J.D.McDowell, Atomic Data, **2**, 63 (1970).
- 5) P.D.Gupta Y.Y.Tsui, R.Popil, R.Fedosejevs, and A.A.Offenberger, Phys.Rev.A, **36**, 4103 (1986).
- 6) P.Alaterre, H.Pepin, R.Fabbro, and B.Faral, Phys.Rev.A, **34**, 4184 (1986).
- 7) W.C.Mead, E.K.Stover, R.L.Kauffman, H.N.Kornblum, and B.F.Lasinski, Phys.Rev.A, **38**, 5275 (1988).
- 8) R.Pakula and R.Sigel, Phys.Fluids, **28**, 232 (1985).
- 9) W.Mróz. J.Farny, M.Kolanowski, and A.Nowak-Goroszczenko, IPPLM Rep. 1/91. (Institute of plasma Physics and Laser Microfusion, Warsaw, Poland)
- 10) D.W.Forslund, J.M.Kindel, and E.L.Lindman, Phys.Fluids, **18**, 1002 (1975).
- 11) A.A.Offenberger, M.R.Cervenak, A.M.Yam, and A.W.Pasternak, J.Appl.Phys., **47**, 1451 (1976).
- 12) J.W.Dawson, W.L.Kruer, and B.Rosen, "*Dynamics of Ionized Gas*", **47**, (John Wiley & Sons, 1971).
- 13) R.L.Berger, E.A.Williams, and A.Simon, Phys.Fluids **B3**, 414 (1989).
- 14) P.E.Young, H.A.Baldis, and K.G.Estabrook, Phys. Fluids **B3**, 1245 (1991).
- 15) A.Simon, R.W.Short, E.A.Williams, and T.Dewandre, Phys.Fluids **26**, 3107 (1983) and references therein.
- 16) J.Meyer and J.E.Bernard, Phys.Fluids **28**, 2618 (1985).  
J.Meyer and Y.Zhu, Phys.Rev.Lett., **64**, 2651 (1990).
- 17) H.A.Baldis and C.J.Walsh, Phys.Fluids **26**, 1364 (1983).
- 18) W.L.Kruer, "*The Physics of Laser Plasma Interactions*", (Addison-Wesley, 1988), p.83.
- 19) M.V.Chegotov, V.P.Silin, V.T.Tikhonchuk, and A.A.Zozulya, Plasma Phys. & Controlled Fusion, **28**, 413 (1986).

### VIII. Data Analysis II (Inhomogeneous Plasma)

In this chapter, inhomogeneity of plasma is taken into account to interpret the experimental data. As shown in chapter 7, an analytical model for homogeneous plasma cannot explain all features of data observed in the experiment. Threshold intensity and SBS gain are evaluated based on an analytical model for inhomogeneous plasma. The effect of flowing inhomogeneous plasma on spectral shift is examined. Linewidth of the spectral shift is explained mainly by inhomogeneity of flow velocity. Dynamics of the spectral shift show correlation with laser pulse shape. SRS reflectivity in inhomogeneous plasma is calculated by two models (coherent and incoherent SRS models). Incoherent model calculations give better fit to the experimental data, suggesting the importance of phase mismatch rate.

#### 8.1. Threshold and Gain (Inhomogeneous Plasma)

The first condition that has to be satisfied for absolute instability is eq.2.10, the threshold condition for infinite homogeneous plasma. For finite homogeneous plasma, on the other hand, threshold condition is given by eq.2.12 or equivalently, eq.7.3

$$\frac{\gamma_s}{\gamma_0} \cdot \left( \frac{v_1}{v_2} \right)^{1/2} < 2 \quad (8.1)$$

where  $v_1$  and  $v_2$  are group velocities of scattered EM and ion waves. In our case,  $v_1 = v_g = c \cdot (1 - n_e/n_c)^{1/2}$  and  $v_2 = c_s - v_p = c_s \cdot (1 - M)$ , where  $v_p$  is the plasma flow velocity (positive for outward flow). For typical Al plasma with  $I_L = 10^{14} \text{ W/cm}^2$ ,  $\gamma_0 \approx 2 \times 10^{12} \text{ (1/s)}$ ,  $\gamma_s/\omega_s \approx 0.02$ ,  $v_g \approx 2.3 \times 10^{10} \text{ (cm/s)}$  (for  $n_e/n_c = 0.4$ ),  $c_s \approx 1.7 \times 10^7 \text{ (cm/s)}$  (for  $T_e = T_i =$

600eV), and  $M=0.6$ , the left hand side of eq.8.1 is calculated to be 3.9, whereby eq.8.1 is not satisfied.

An even stricter criterion is set for inhomogeneous plasma. The condition to be satisfied for absolute instability in inhomogeneous plasma is given by eq.2.13;

$$\lambda \equiv \frac{\gamma_0^2}{|\kappa'| |v_1 v_2|} > \pi^{3/4} \quad (8.2)$$

If eq.8.2 is satisfied, the temporal growth rate is given by eq.2.14;

$$\gamma_{1h} = \left[ \frac{2\gamma_0}{(v_1 v_2)^{1/2}} \left( 1 - \frac{1}{\pi^{1/2} \lambda^{2/3}} \right) - \left( \frac{\gamma_{1b}}{v_1} + \frac{\gamma_s}{v_2} \right) \right] \cdot \left( \frac{v_1 v_2}{v_1 + v_2} \right) \quad (8.3)$$

For the same conditions discussed above,  $|\kappa'| < 2.5 \times 10^7 \text{ cm}^{-2}$  is required to fulfill eq.8.2. In chapter 5, however, a typical value for  $|\kappa'|$  is estimated to be  $10^9 \text{ cm}^{-2}$ . For  $|\kappa'| \approx 10^9 \text{ cm}^{-2}$ , eq.8.2 requires  $I_L \approx 1.2 \times 10^{16} \text{ W/cm}^2$ . Even hotspots in the focal spot cannot satisfy this high intensity requirement. Therefore, in general, we expect convective instability for our plasma.

### 8.1.1. Phase Mismatch Condition

As pointed out in chapter 5, there may be a singular point where  $\kappa' = 0$ . In this section, we examine possibilities of such a singular point and the absolute instability around the point. We model our inhomogeneous plasma (assumed to be stationary in time) with electron density profile  $n_e(x) = n_0 \cdot \exp[-(L-x)/L_n]$ , plasma flow velocity profile  $v_p = v_0 - x/L_v$ , and constant temperature ( $T_e = T_i = 600\text{eV}$ ) and charge state  $Z (= 11)$ . From the CASTOR results presented in chapter 5,  $L_n$  and  $L_v$  are assumed to be  $15\mu\text{m}$  and  $25\mu\text{m}$ , respectively. Although these

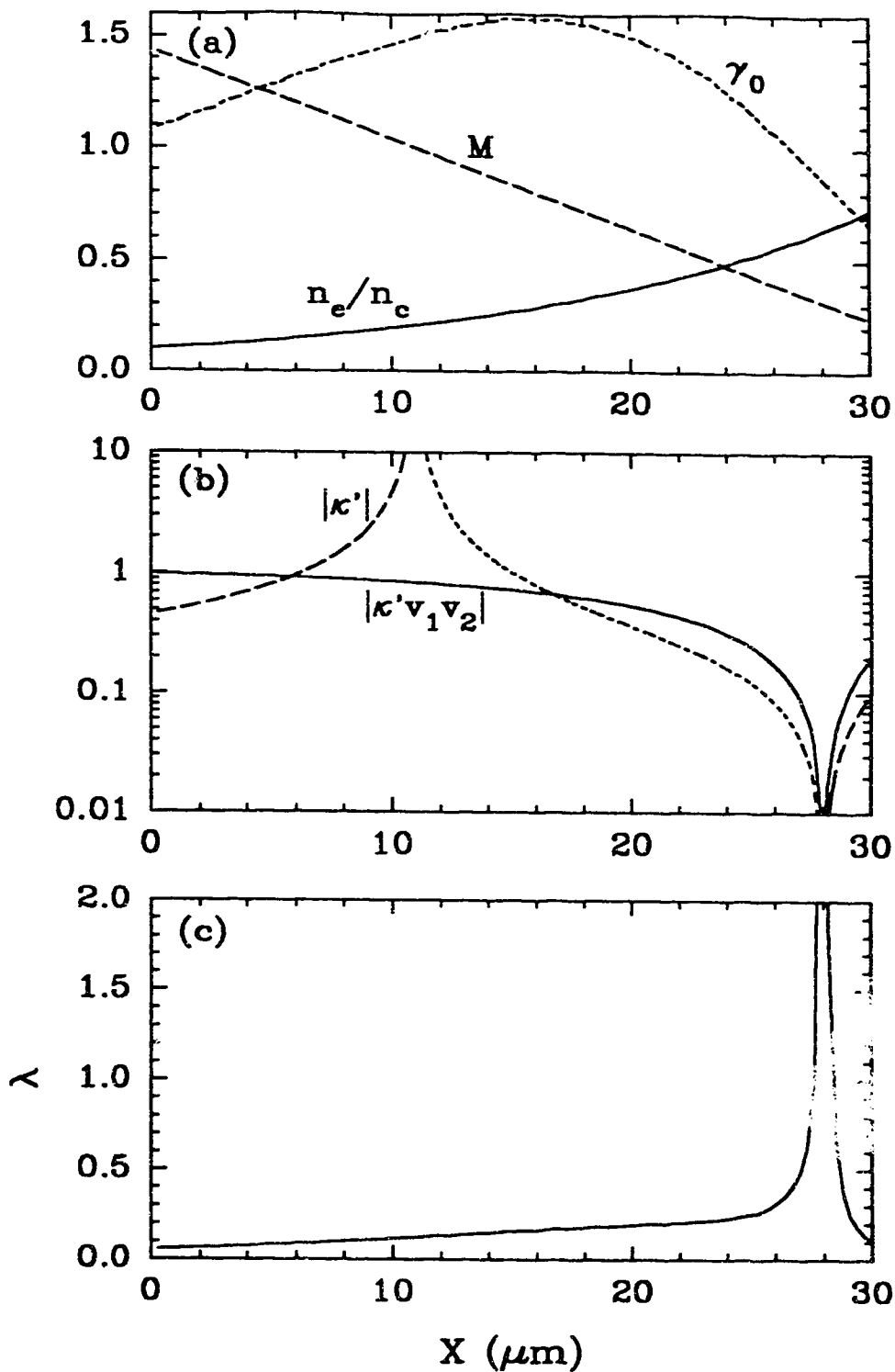


Fig.8.1. Gain profile for the modeled inhomogeneous plasma: (a) spatial profiles of density  $n_e/n_c$ , Mach number  $M$ , growth rate  $\gamma_0$ ; (b) phase mismatch rate  $\kappa'$ , parameter  $|\kappa' v_1 v_2|$ , and (c) inhomogeneous gain parameter  $\lambda$ .

scale lengths were calculated from the simulation data for small focus with  $r_{90\%} = 17\mu\text{m}$ , we assume the situation is applicable for our case of oblique incidence (focal spot size  $r_{90\%}$  for normal incidence is  $10\mu\text{m}$ ). Based on the simulation results in chapter 5,  $n_0$  and  $v_0$  are chosen so that conditions  $n_e/n_c = 0.4$  and  $M = 0.6$  are satisfied at some point in the plasma.

Spatial profiles of  $n_e/n_c$ , Mach number  $M$ , and the homogeneous growth rate  $\gamma_0$  are plotted in fig.8.1 (a). The growth rate  $\gamma_0(x)$  takes into account attenuated pump intensity  $I_L(x)$  due to inverse bremsstrahlung absorption and is normalized to  $1 \times 10^{12} \text{s}^{-1}$  for  $I_L = 10^{14} \text{W/cm}^2$ . Figure 8.2 (b) shows spatial profiles of the phase mismatch rate  $\kappa'$  and the denominator of eq.8.2,  $|\kappa' v_1 v_2|$ . As discussed in section 4.6,  $\kappa'$  has a singular point at  $M = 1$ , but  $|\kappa' v_1 v_2|$  is smooth at the same point. The point where  $\kappa' = 0$  exists at  $x \approx 28\mu\text{m}$  where  $n_e/n_c \approx 0.64$  and  $M \approx 0.32$  for the plasma shown in fig.8.1 (a). Figure 8.1 (c) shows the spatial profile of  $\lambda$  (eq.8.2) calculated for  $I_L = 4.6 \times 10^{14} \text{W/cm}^2$ , assuming hotspot enhancement of 2.3 for  $I_{av} = 2 \times 10^{14} \text{W/cm}^2$ . Although  $\lambda$  exceeds unity around the singular point ( $\kappa' = 0$ ), the width of such region is about  $1\mu\text{m}$  which is smaller than the basic gain length  $(v_1 v_2)^{1/2} / \gamma_0 \approx 3\mu\text{m}$  for  $I_L = 4.6 \times 10^{14} \text{W/cm}^2$ . Note the same temperature ( $= 600\text{eV}$ ) was assumed for both  $I_L = 10^{14}$  and  $4.6 \times 10^{14} \text{W/cm}^2$  in the above calculations. The results are applicable for plasmas with different temperatures, since the gain width is mainly determined by the density and velocity scale length. In order to satisfy both eqs.8.1 and 8.2 with enough gain length,  $I_L > 10^{15} \text{W/cm}^2$  would be necessary for our plasma. In summary, we do not expect absolute instability in the inhomogeneous plasma modeled for our

experimental conditions, even for  $\kappa'$  vanishing at some point in the plasma.

## 8.2. Spectral Shift

In this section, interpretation of the backscattered light spectra is presented, taking plasma inhomogeneity (temporal and spatial) in account. The effects of expanding inhomogeneous plasma on the spectral shift are examined. Our analysis shows that the broad bandwidth of the spectrum can be accounted for by spatial inhomogeneity of plasma. Temporal variations of the spectra show strong correlation with laser pulse shape, suggesting the importance of plasma dynamics.

### 8.2.1. Effects of Expanding Inhomogeneous Plasma on Spectral Shift

Apart from the SBS spectral shift, there are several mechanisms that can cause spectral shift of scattered light from plasma. T. Dewandre et al.<sup>1)</sup> has analyzed the frequency shift of light reflected from a planar expanding inhomogeneous plasma. It was found that the frequency shift consists of two components; one due to the motion of the reflecting surface (Doppler shift), the other due to plasma flow through that surface. The possibilities of these frequency shifts are discussed in this section.

The frequency shift due to the expanding inhomogeneous plasma is given by<sup>1)</sup>

$$\Delta\omega = -2 \frac{\omega_0}{c} \dot{x}_t + \int_{x_0}^{x_t} \frac{\partial\omega_p^2/\partial t}{c [\omega_0^2 - \omega_p^2]^{1/2}} dx \quad (8.4)$$

where  $x_t$  is the position of the reflecting surface. The first term represents the Doppler shift or "moving mirror" term. If the

reflecting surface is the critical density surface,  $\dot{x}_t \approx -5 \times 10^4 \text{ cm/s}$  from the CASTOR data, resulting in a predicted red shift of  $8 \times 10^{-3} \text{ \AA}$  (much smaller than the observed red shift  $\approx 1 \text{ \AA}$ ). Note the critical surface moves away from the laser in the case of short wavelength laser-produced plasma. In the case of oblique incidence, the reflecting surface is the turning density surface where  $\dot{x}_t$  is generally positive; this causes a blue shift which we did not observe in the experiment.

The second term in eq.8.4 is the "flow" term which can be seen to arise from the rate of change of the optical path length between the observer and the reflecting surface due to the time variation of the density of the moving plasma. If the density profile changes in time as  $n(x,t) = n_c \exp[(x-x_c)/c_s t]$ , where  $x_c$  is the position of the critical surface, eq.8.4 can be rewritten as

$$\Delta\omega = 2\omega_0 ( -\dot{x}_t/c + 0.613 \cdot c_s/c ) \quad (8.5)$$

for normal incidence. The second term in eq.8.5 gives a red shift comparable to the SBS spectral shift. However, we do not expect such a contribution in our experiment with small focal spot, since the density profile is steady for  $t > 1.0 \text{ ns}$  (CASTOR data in chapter 4). Moreover, the temporal features of the observed spectral shift cannot be explained by the reflection of light as discussed in section 6.4.1.

In summary, the effect of the expanding inhomogeneous plasma on spectral shift is not applicable to the highly absorbing plasma created by our tightly focused short wavelength laser.

### 8.2.2. Linewidth

From the experimental time-resolved spectra, a typical SBS

spectral linewidth was  $0.3\text{\AA}$  (see section 7.3). As discussed in section 7.3, line broadening due to ion wave damping is not enough to explain this linewidth. Spatial inhomogeneity of plasma can cause line broadening which is estimated by eq.2.27. For  $c_s/c=5.7\times 10^{-4}$ ,  $n_e/n_c=0.4$ ,  $M=0.6$ , and  $\cos\theta=1$ , the SBS spectral linewidth  $\lambda_w$  is given by

$$\lambda_w (\text{\AA}) = 1.1 \cdot \left( \frac{\Delta T}{T} - 0.67 \cdot \frac{\Delta n_e}{n_c} - 2 \cdot \Delta M \right) \quad (8.6)$$

where  $\Delta M = \Delta v_p/c_s$ . For each term individually account for  $\lambda_w = 0.3\text{\AA}$ , eq.8.6 would require  $\Delta T/T \approx 0.3$ ,  $\Delta n_e/n_c \approx 0.4$ , or  $\Delta M \approx 0.14$ . This implies if  $\Delta T$  is the main cause of the line broadening, SBS must be generated over a region where temperature changes from 500eV (or 400eV) to 700eV (600eV). This is unlikely, since 1) we expect high thermal conductivity in the coronal plasma and 2) the CASTOR results in chapter 4 show temperature variation of  $\sim 100\text{eV}$  over  $30\mu\text{m}$  in axial direction and  $15\mu\text{m}$  in lateral direction, which are larger than the SBS gain region. Similarly, if  $\Delta n_e$  dominates, SPS would have to arise from a region varying from  $n_e/n_c = 0.2$  to  $0.6$ . This is also unlikely, since the CASTOR results show Mach numbers for  $n_e/n_c = 0.2$  and  $0.6$  are  $1.3$  (supersonic) and  $0.4$  (subsonic) which should cause line broadening  $\approx 1.5\text{\AA}$  (much larger than  $0.3\text{\AA}$ ). Hence  $\Delta n_e/n_c$  alone cannot explain the broadening ( $\approx 0.3\text{\AA}$ ). Finally, if  $\Delta M$  dominates, the Mach number of the SBS region would have to range from  $0.53$  to  $0.67$ .

From the modeling calculations, the SBS region corresponds to the density region from  $0.5n_c$  to  $0.4n_c$  where SBS gain is the highest. Consequently, taking into account both  $\Delta n_e$  and  $\Delta M$ , the experimental linewidth  $0.3\text{\AA}$  can be explained by inhomogeneity of  $\Delta n_e \approx 0.1$  (from  $0.4n_c$  to  $0.5n_c$ ) and  $\Delta M \approx 0.1$  (from  $0.55$  to  $0.65$ ). Therefore, we conclude



the linewidth of the SBS spectral shift is mainly due to  $\Delta M$  and secondarily due to  $\Delta n_e/n_c$ .

### 8.2.3. Temporal Evolution of Spectral Shift

From the time-resolved spectra, the rate of spectral shift change  $d\lambda/dt$  was measured to be  $1 \pm 0.5 \text{ \AA/ns}$  (positive slope) for Al targets (see section 6.4.3). In this section, we analyze only the positive slope ( $+d\lambda/dt$ ), since CASTOR results are available for the leading part of the laser pulse ( $t \leq 2.2 \text{ ns}$ ). Equation 8.6 can be used to estimate the rate of spectral shift change. For temporal variation, eq.8.6 gives

$$\frac{\Delta\lambda}{\Delta t} (\text{\AA/ns}) = 1.1 \cdot \left( \frac{1}{T} \cdot \Delta T / \Delta t - 0.67 \cdot \frac{1}{n_c} \cdot \Delta n_e / \Delta t - 2 \cdot \Delta M / \Delta t \right) \quad (8.7)$$

where  $\Delta t$  is in ns. Since the plasma density profile is expected to be steady (for  $t > 1 \text{ ns}$  in CASTOR simulation), we ignore the second density term. Note the temperature and Mach number term have opposite signs and hence may cancel each other. In fact, if one assumes  $\Delta v_p$  is proportional to  $\Delta c_s$  ( $2 \cdot \Delta c_s / c_s = \Delta T / T$ ),  $2\Delta M / \Delta t$  ( $\equiv 2\Delta v_p / c_s$ ) is equal to  $\Delta T / \Delta t$  in the first order, resulting in  $\Delta\lambda / \Delta t \approx 0$ . Therefore, it is necessary to examine the hydrodynamic simulation data in detail.

Figure 8.2 shows SBS spectral shifts calculated from CASTOR data for case SF5 ( $I_L = 4 \times 10^{13} \text{ W/cm}^2$ ) (a) and case SF1 ( $I_L = 8 \times 10^{13} \text{ W/cm}^2$ ) (b) at various fixed densities. The simulation data are taken on laser axis ( $R=0$ ). The solid line shows SBS spectral shift without plasma flow effects ( $1 - M \cos\theta$ ) for density  $n_e/n_c = 0.3$ . It is noted that only a few cells represent high density plasma ( $n_e/n_c > 0.4$ ) in the simulation so that these results are approximate. The solid circles are actual

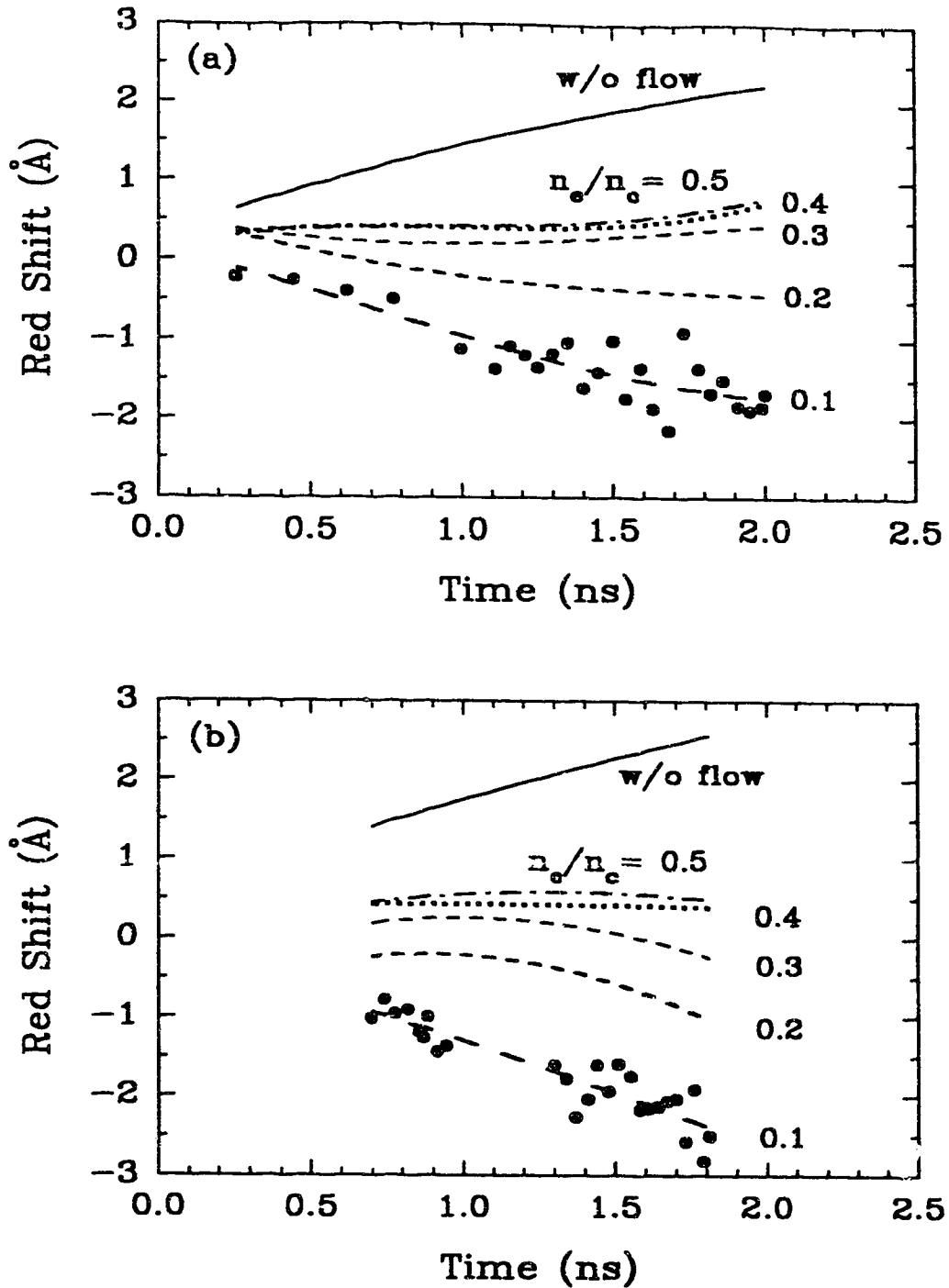


Fig.8.2. CASTOR predictions of SBS red shift at various fixed densities for case SF5 (a) and SF1 (b). The solid circles are actual simulation data for  $n_e/n_c=0.1$ . The solid lines show SBS spectral shift without the flow effects.

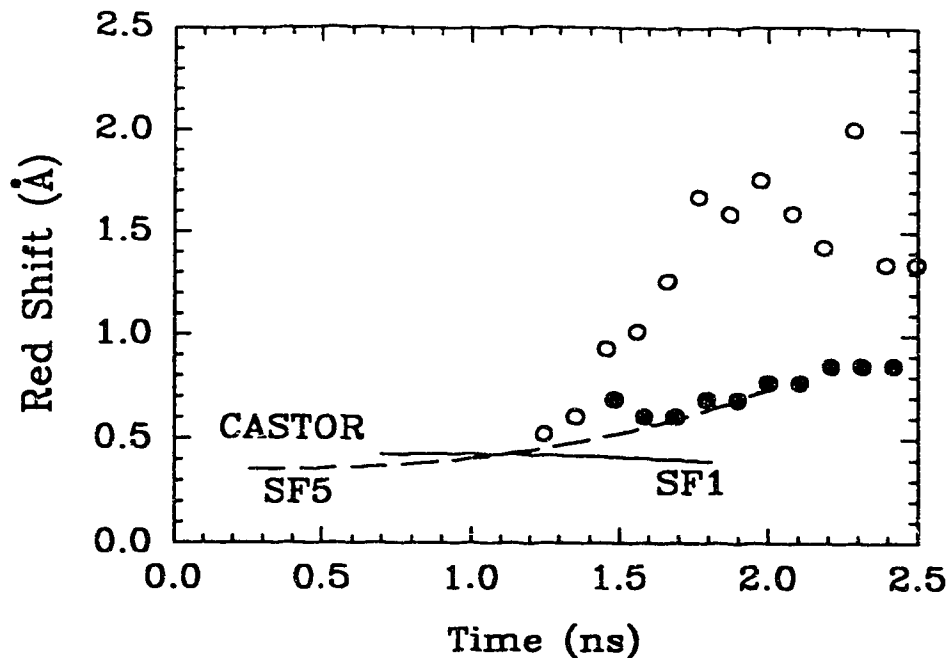


Fig.8.3. Comparison of dynamics of red shift between simulation and experimental data. The solid and dashed lines are CASTOR data at  $n_e/n_c = 0.4$ . The solid and open circles show two types of spectral shift observed at  $I_L = 3.8 \times 10^{13} \text{ W/cm}^2$  and  $1.3 \times 10^{14} \text{ W/cm}^2$  in the experiment, respectively.

simulation data for  $n_e/n_c = 0.1$  in order to show data variation of the simulation results. For  $n_e/n_c = 0.4$ , the red shift is almost constant (b) or slightly increases (a) in time at a rate of  $\approx 0.6 \text{ \AA/ns}$ , but not as much as  $1 \text{ \AA/ns}$ . At the peak of the laser pulse ( $t = 2.2 \text{ ns}$ ), it is expected that temperature is almost constant and hence red shift does not change very much (see fig.7.6).

Figure 8.3 shows a comparison of spectral shift dynamics between the experimental and simulation data. The solid and dashed lines are simulation data for case SF1 and SF5 at  $n_e/n_c = 0.4$ . The solid and open circles show two types of red shift (steady and time-varying) observed in the experiment. The steady and time-varying red shift

were observed for Al target at  $I_L = 3.8 \times 10^{13} \text{ W/cm}^2$  and  $1.3 \times 10^{14} \text{ W/cm}^2$ . The steady red shift ( $+d\lambda/dt \leq 0.5 \text{ \AA/ns}$ ) would fit well to the simulation data, whereas the time-varying red shift ( $+d\lambda/dt \approx 1.8 \text{ \AA/ns}$ ) cannot be explained by the hydrodynamic calculation results. We do not know the reason for the discrepancy which was generally seen in the experimental data with high intensity ( $I_L \geq 10^{14} \text{ W/cm}^2$ ) irradiation. It is, however, interesting to compare the temporal spectral shift with laser pulse shape, since the general trends of the positive and negative  $d\lambda/dt$  correlate with the fast rise and slow fall of the laser pulse as discussed in section 6.4.3.

Typical temporal evolutions of spectral shift are compared with relative laser intensity scaling in figs. 8.4 and 8.5. The open and solid circles are experimental data for low (a), medium (b), and high (c) laser intensity irradiations. The laser intensities and the rates of spectral shift change (positive slope) for both figures are  $4 \times 10^{13} \text{ W/cm}^2$  and  $0.5 \text{ \AA/ns}$  (a),  $(7 \pm 3) \times 10^{13} \text{ W/cm}^2$  and  $0.8 \text{ \AA/ns}$  (b), and  $(1.5 \pm 0.3) \times 10^{14} \text{ W/cm}^2$  and  $2.0 \text{ \AA/ns}$  (c). It is noted that these time-varying spectral shift data show slightly larger red shift than averaged data (fig. 6.13). The solid, dashed and dotted lines show the relative scaling with laser intensity,  $I_L^{0.22}$  (fig. 8.4) and  $I_L^{1.0}$  (fig. 8.5) and are normalized individually to fit to the data at the peak. The laser pulse shape  $I_L(t)$  is that described in section 5.1.2 (eq. 5.1). The experimental data fit better to the intensity scaling of  $I_L^{1.0}$  rather than  $I_L^{0.22}$ , especially, for high intensity data. Since CASTOR data show that temporal evolution of electron temperature fits well to the scaling of  $I_L(t)^{0.44}$  (fig. 7.6), the spectral shift is expected to follow the scaling of  $I_L(t)^{0.22}$  without flow effects.

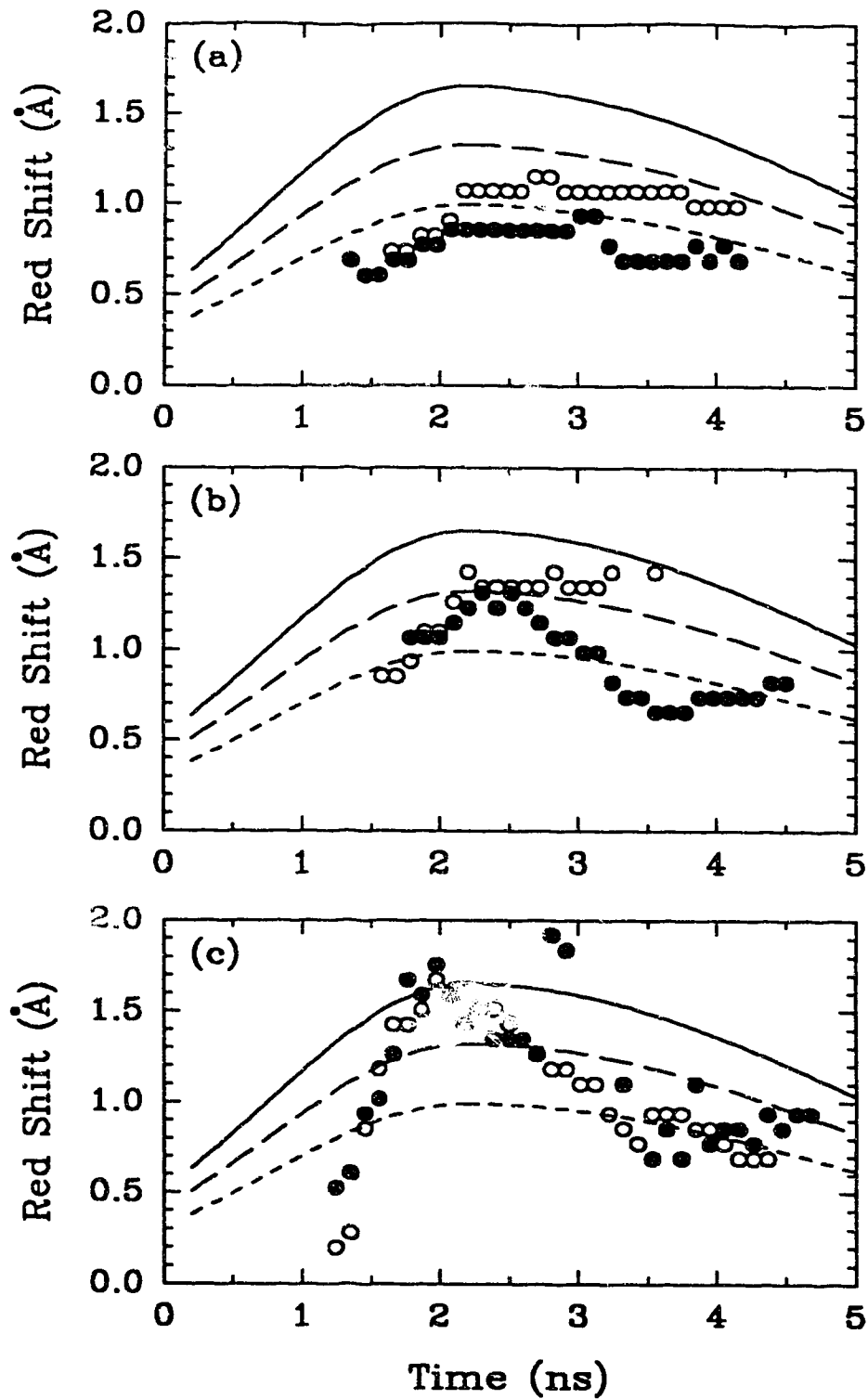


Fig.8.4. Typical red shift as a function of time observed in the experiment for low (a), medium (b), and high (c) laser intensity irradiations (solid and open circles). The lines show relative scaling with laser intensity  $I_L(t)^{0.22}$ .

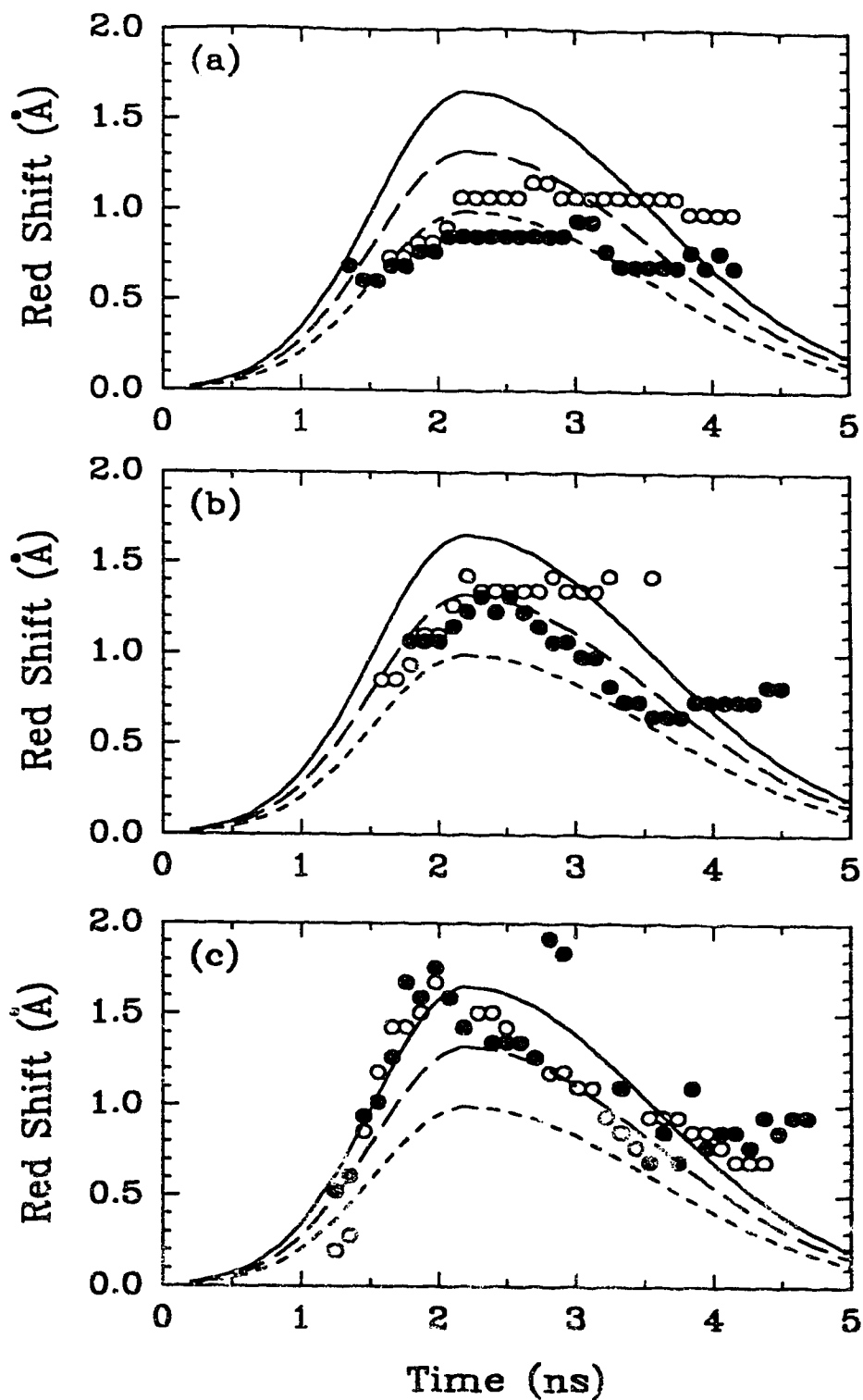


Fig. 8.5. Typical red shift as a function of time observed in the experiment for low (a), medium (b), and high (c) laser intensity irradiations (solid and open circles). The lines show relative scaling with laser intensity  $I_L(t)^{1.0}$ .

With flow effects, the dependence would be weaker, if one assumes  $\Delta M/\Delta t \propto \Delta c_s/\Delta t$ . In order to explain the strong dependence, one would have to assume: 1) Mach number of plasma flow decreases in time or no plasma flow ( $\Delta M/\Delta t \leq 0$ ), or 2) plasma heating is localized so that convective thermal transport is strongly inhibited. The first situation would be possible, since high intensity hotspots can penetrate into higher density plasma where the plasma flow is steady or negative. From CASTOR data (fig.7.6) and eq.8.6 with  $\Delta n_e/\Delta t = \Delta M/\Delta t = 0$ ,  $\Delta\lambda/\Delta t$  is calculated to be  $0.6\text{\AA}/\text{ns}$  for  $(\Delta T/\Delta t)/T = (300\text{eV}/\text{ns})/550\text{eV}$  at  $t = 1.5\text{--}2.0\text{ns}$ , which would be the case for fig.8.4 (a). The second situation can be inferred from the short electron-ion collision mean free path  $\lambda_{ei}$  in KrF laser-produced plasma, which is of the order of  $0.5\mu\text{m}$  and smaller than the scale of hotspots in our case. In the CASTOR simulation, the flux limiter  $f$  was assumed to be 0.08. It would be necessary to decrease  $f$  in order to explain the experimental data. Non-local electron heat transport is recognized to be an important issue, which suggests electron thermal conductivity decreases dramatically in a plasma where thermal effects dominate ponderomotive effects.<sup>2)</sup>

In summary, the effects of expanding inhomogeneous plasma on the spectral shift are not important in our case of tightly focused short wavelength laser-produced plasma. The broad bandwidth of the spectrum can be accounted for mainly by the spatial inhomogeneity of plasma flow (Mach number). Dynamics of the spectral shift shows strong correlation with laser pulse shape. More detailed hydrodynamic simulations with refined heat transport models are necessary to interpret the time-varying spectrum.

### 8.3. SBS Reflectivity from Inhomogeneous Plasma

In calculating SBS reflectivity for inhomogeneous plasma, it is necessary to take into account phase mismatch between waves which limits the effective gain length.<sup>3)</sup> In this section, we present and discuss two models of SBS coupling in inhomogeneous plasma: coherent and incoherent models. In the coherent coupling model, we ignore the phase mismatch and hence allow backscattered light to grow continuously over the full length of plasma. The effective gain length is limited by strong attenuation of the pump wave due to inverse bremsstrahlung absorption. The results of this model calculation are expected to give an upper limit of reflectivity. In the incoherent coupling model, on the other hand, the backscattered light grows only in a small region determined by phase mismatch. The net reflectivity is obtained by summing up the contribution from each region. This model gives substantially lower SBS gain than the coherent model for convective instability.

#### 8.3.1. Spatial Profile of SBS Gain

To determine the plasma conditions for SBS calculation in inhomogeneous plasma, it is useful to estimate the optimum density of SBS growth for non-uniform density profile. Since pump absorption is strong in KrF laser-produced plasma, the optimum density depends on electron temperature and density scale length. The optimum density is estimated from the spatial profile of growth rate  $\gamma_0(x)$  which is a function of plasma parameters and pump intensity. The spatial profile of pump intensity  $I_L(x)$  inside the plasma is calculated by the attenuation due to inverse bremsstrahlung absorption. Temperature and



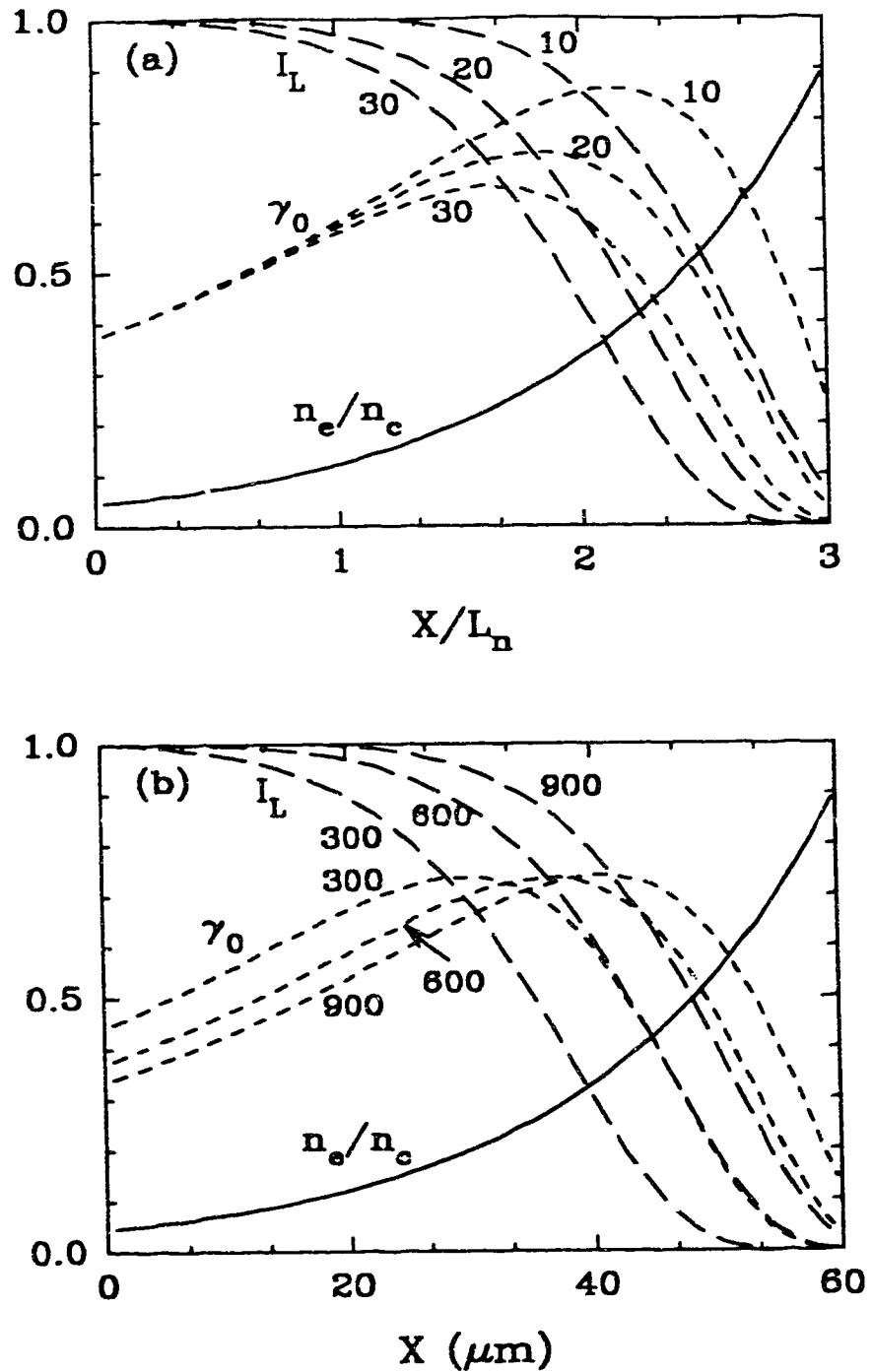


Fig. 8.6. Spatial profiles of density (solid line), pump intensity (dashed lines), and the homogeneous growth rate  $\gamma_0$  (dotted lines) for various density scale lengths with  $T=600\text{eV}$  (a) and temperatures with  $L_n = 20\mu\text{m}$  (b).

average ion charge state are assumed to be constant ( $T = T_e = T_i$ , and  $Z = 11$ ). The density profile is assumed to be exponential given by  $n_e(x) = n_c \cdot \exp(-x/L_n)$ , where  $L_n$  is the density scale length.

Figure 8.6 shows spatial profiles of density (solid line), pump intensity (dashed lines), and the homogeneous growth rate  $\gamma_0$  (dotted lines) for various density scale lengths with  $T=600\text{eV}$  (a) and temperatures with  $L_n = 20\mu\text{m}$  (b).  $\gamma_0$  is normalized to  $2 \times 10^{12}\text{s}^{-1}$  for  $I_L = 10^{14}\text{W/cm}^2$ . In fig.8.6 (a), the plasma length  $L$  is maintained at 3 times  $L_n$ . Numbers beside each line indicate  $L_n$  in  $\mu\text{m}$  (a), and temperature in eV (b). The results show  $\gamma_0$  has a peak around  $n_e/n_c = 0.3$ ; a direct consequence of competition between growth and damping of waves, consistent with results shown in fig.7.1 for the case of homogeneous plasma. Note the optimum density for SBS reflectivity will be slightly higher ( $n_e/n_c \approx 0.4$  in fig.7.1) than for the peak of  $\gamma_0$ , because ion wave damping  $\gamma_s$  is lower for higher density. The shorter scale length plasma allows the pump wave to penetrate to a higher density region, resulting in the peak of  $\gamma_0$  shifting toward higher density and therefore increasing gain. Calculations for higher temperature, which corresponds to higher laser intensity, give similar results.  $\gamma_0$ , however, does not increase as much as seen in fig.8.6 (a), since  $\gamma_0$  scales as  $T^{-1/4}$ . Since pump depletion due to SBS can be ignored in our experiment, these results should provide a good estimate of the interaction region.

### 8.3.2. Coherent Model

To calculate SBS reflectivity using the coherent model, the simulation code described in section 3.1.2 is used with boundary

conditions given by eqs.(3.3). A uniform mesh (50 cells) represent plasma of length  $L$  which is kept at 3 times the density scale length  $L_n$ . The density profile is assumed to be  $n_e = n_m \exp[-(L-x)/L_n]$ , where  $n_m$  is the maximum density and set to be  $0.9n_c$  for most of the calculations in order to avoid complicated physics around the critical density. From  $x=3L_n$  to  $2L_n$ , the density decreases exponentially, then decreases linearly from  $x=2L_n$  to 0, joining to vacuum boundary at  $x=0$ . Temperature and average charge state are assumed to be constant in space ( $T = T_e = T_i$ ,  $Z=11$ ). For different pump intensities, the temperature is changed as  $T(\text{eV}) = 600 \cdot I_{14}^{0.44}$ . The initial density fluctuation level is assumed to be  $10^{-3}$  which is required to obtain reflectivity comparable to the experimental data. For the electromagnetic waves, inverse bremsstrahlung absorption and swelling effects due to increasing density are taken into account. For the ion wave, semi-collisional damping (Casanova Formula)<sup>4)</sup> is used. Since the phase mismatch is ignored in this model and also  $c_s \gg v_p$  in the region where SBS growth is significant, plasma flow does not affect the results very much and hence is ignored.

Figure 8.7 shows an example of results in steady state for  $I_L = 10^{14} \text{ W/cm}^2$ ,  $L_n = 20 \mu\text{m}$ , and  $N_n = 10^{-3}$ . Temporal variation of reflectivity  $R (= a_1^2(0)/a_0^2(0))$  in fig.8.7 (a) shows the backscattered light grows exponentially and reaches steady state in 100ps. Figure 8.7 (b) shows spatial profiles of density ( $n_e/n_c$ ), pump wave amplitude  $a_0(\text{IN})$ , scattered wave amplitude  $a_1(\text{BS})$ , and density fluctuation  $a_2(\delta n/N)$ . Each quantity is normalized individually. The pump wave shows slight swelling effects at low density ( $n_e/n_c < 0.1$ ) and strong absorption above  $n_e/n_c > 0.3$ . Pump depletion due to SBS coupling is

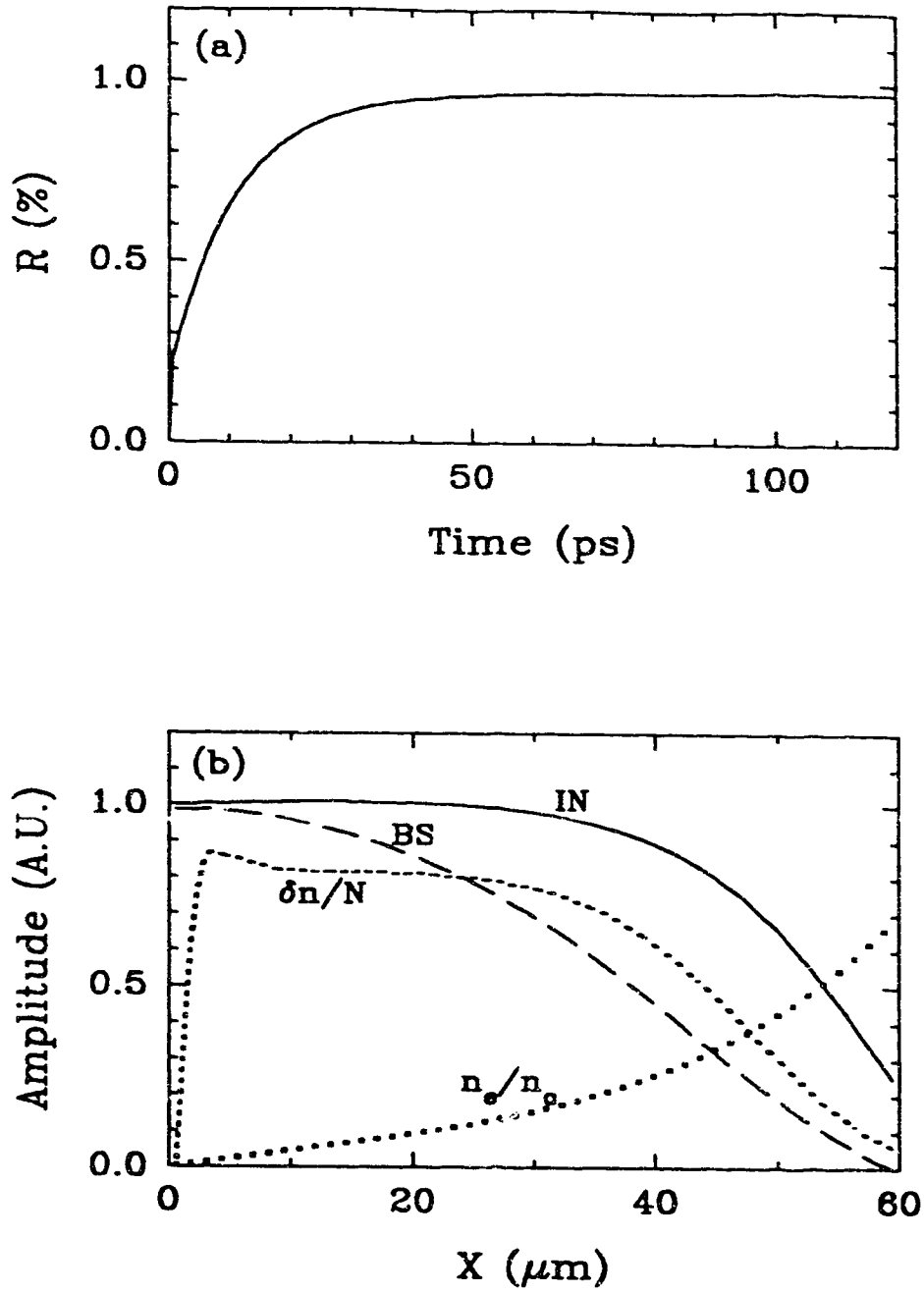


Fig. 8.7. An example of SBS simulation results (coherent model) for  $I_L=10^{14}\text{W/cm}^2$ ,  $L_n=20\mu\text{m}$ , and  $N_n=10^{-3}$ . Temporal evolution of reflectivity : (a). Spatial profiles of pump wave (IN) and scattered wave (BS) amplitude, density fluctuation ( $\delta n/N$ ) and electron density ( $n_e/n_c$ ) : (b).

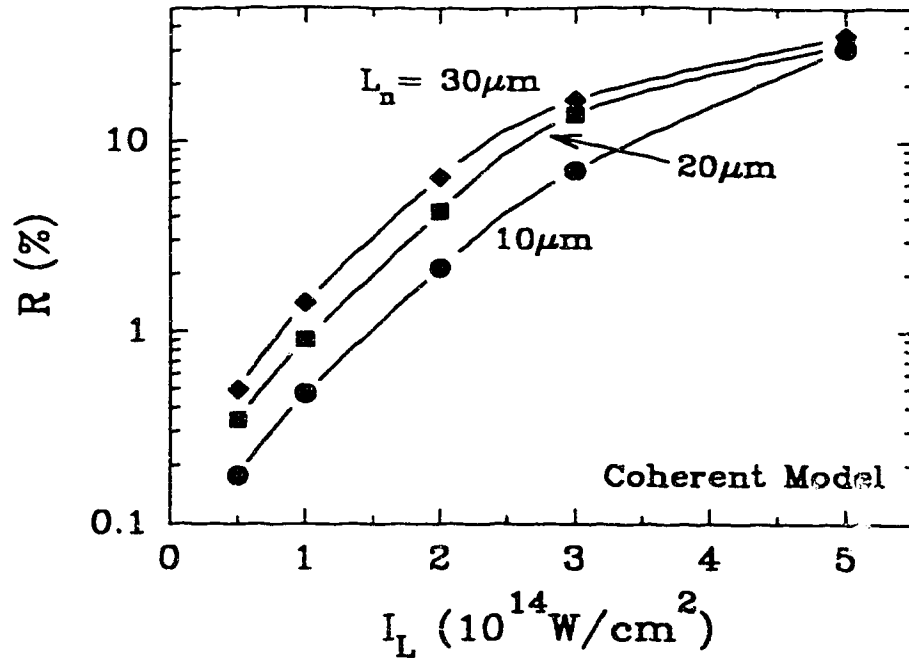


Fig.8.8. Coherent model calculation. SBS reflectivity as a function of pump intensity  $I_L$  for several density scale lengths  $L_n$ .

negligible in this case. Detailed spatial features of the backscattered wave are discussed later.

Figure 8.8 shows SBS reflectivities as a function of pump intensity  $I_L$  for several density scale lengths  $L_n$ . Each point shows simulation data. As expected for convective growth, longer scale lengths give larger gain and hence higher reflectivities. At high intensity, however, reflectivity above  $\approx 10\%$  tends to saturate as pump depletion becomes significant, causing the interaction region to shift toward lower density where SBS gain is lower.

In order to illustrate where SBS has the largest growth, it is informative to plot the spatial derivative of scattered light  $dBS/dx$  ( $\equiv d/dx(a_1(x))$ ). Figure 8.9 shows spatial profiles of  $dBS/dx$  for

$L_n = 10\mu\text{m}$  (a),  $20\mu\text{m}$  (b), and  $30\mu\text{m}$  (c). Each line in this figure corresponds to results shown in fig. 8.7 and is normalized to the same arbitrary number. Small numbers besides the lines denote pump intensity in  $10^{14}\text{W/cm}^2$ . The density profile is also plotted as a dash-dot line. Generally, SBS grows at lower density for longer scale length plasma because of two reasons: 1) strong inverse bremsstrahlung (IB) absorption limits the interaction region to lower density and 2) larger convective gain length compensates for lower growth rate. As pump intensity increases, SBS growth shows two different features depending on scale length. At higher intensity, the electron temperature is higher and hence IB absorption is lower, resulting in pump wave penetration to the higher density (higher gain) region. For the case of shorter scale length plasma (fig. 8.9 (a)), this causes SBS to grow at higher density (higher gain). For longer scale length plasma (fig. 8.9 (c)), on the contrary, SBS grows at lower density because of higher convective gain. As pump intensity increases, the pump wave is depleted before it reaches a potentially higher gain region. Even if IB absorption is lower for higher intensity, SBS growth is enhanced and limited to the lower density region.

The profile of  $dBS/dx$  is compared with pump wave amplitude ( $I_N$ ) and growth rate ( $\gamma_0$ ) profiles in fig. 8.10 for  $L_n = 10\mu\text{m}$  (a),  $20\mu\text{m}$  (b), and  $30\mu\text{m}$  (c) at  $I_L = 2 \times 10^{14}\text{W/cm}^2$ .  $\gamma_0$  is normalized to  $2 \times 10^{12}\text{ 1/s}$ . For longer scale length plasma, SBS grows downstream of the peak of  $\gamma_0$ , since the source of backscattered light comes from the higher density region. For shorter scale length plasma, on the contrary, the peak of SBS growth coincides with the peak of  $\gamma_0$ , because the effective convective gain length is shorter so that the supply of scattered light

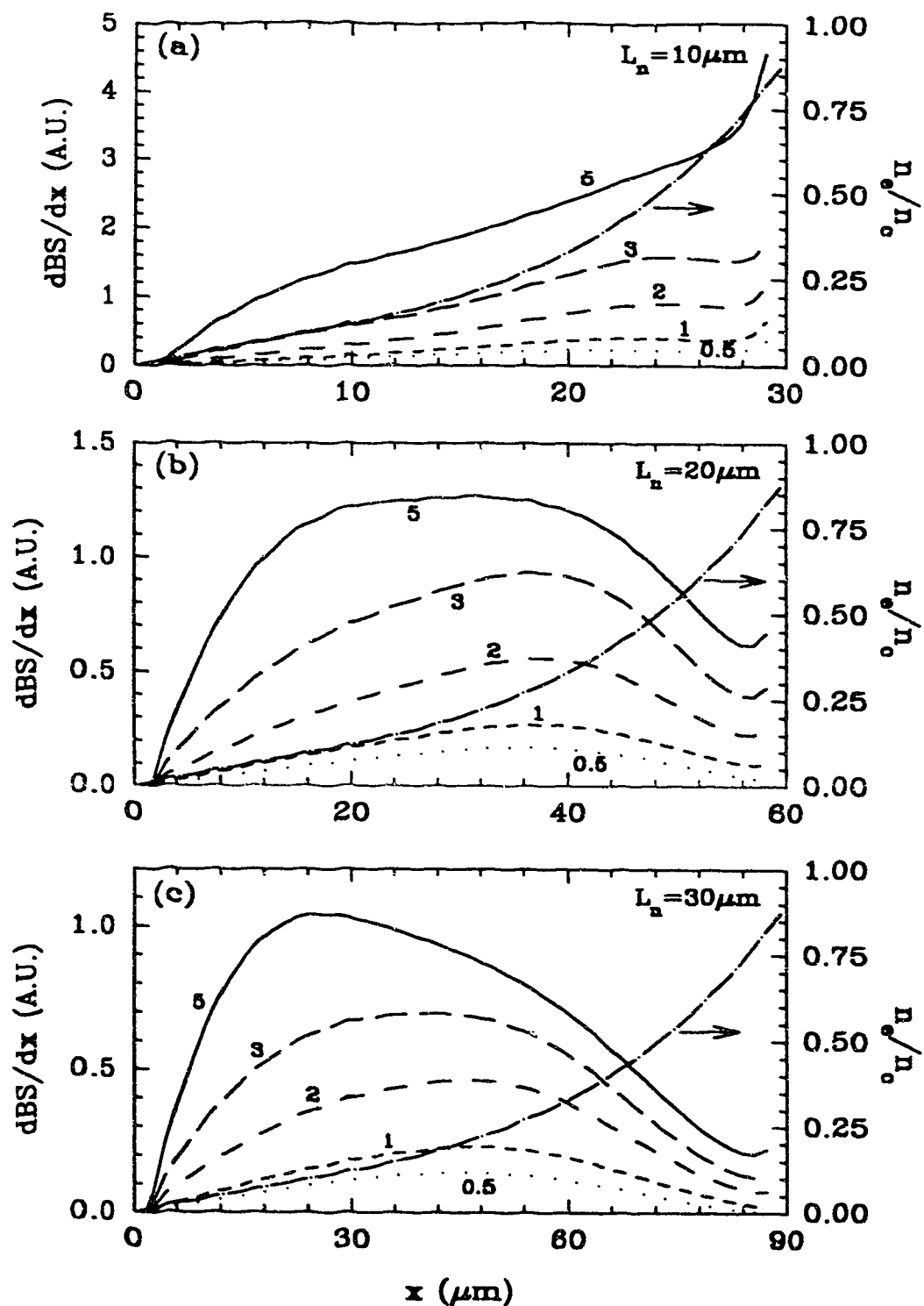


Fig. 8.9. Profiles of spatial derivative of scattered wave amplitude ( $dBS/dx$ ) for  $L_n = 10 \mu\text{m}$  (a),  $20 \mu\text{m}$  (b), and  $30 \mu\text{m}$  (c). Small numbers besides each line denote pump intensity in  $10^{14} \text{W/cm}^2$ . The dash-dot lines show density profile.

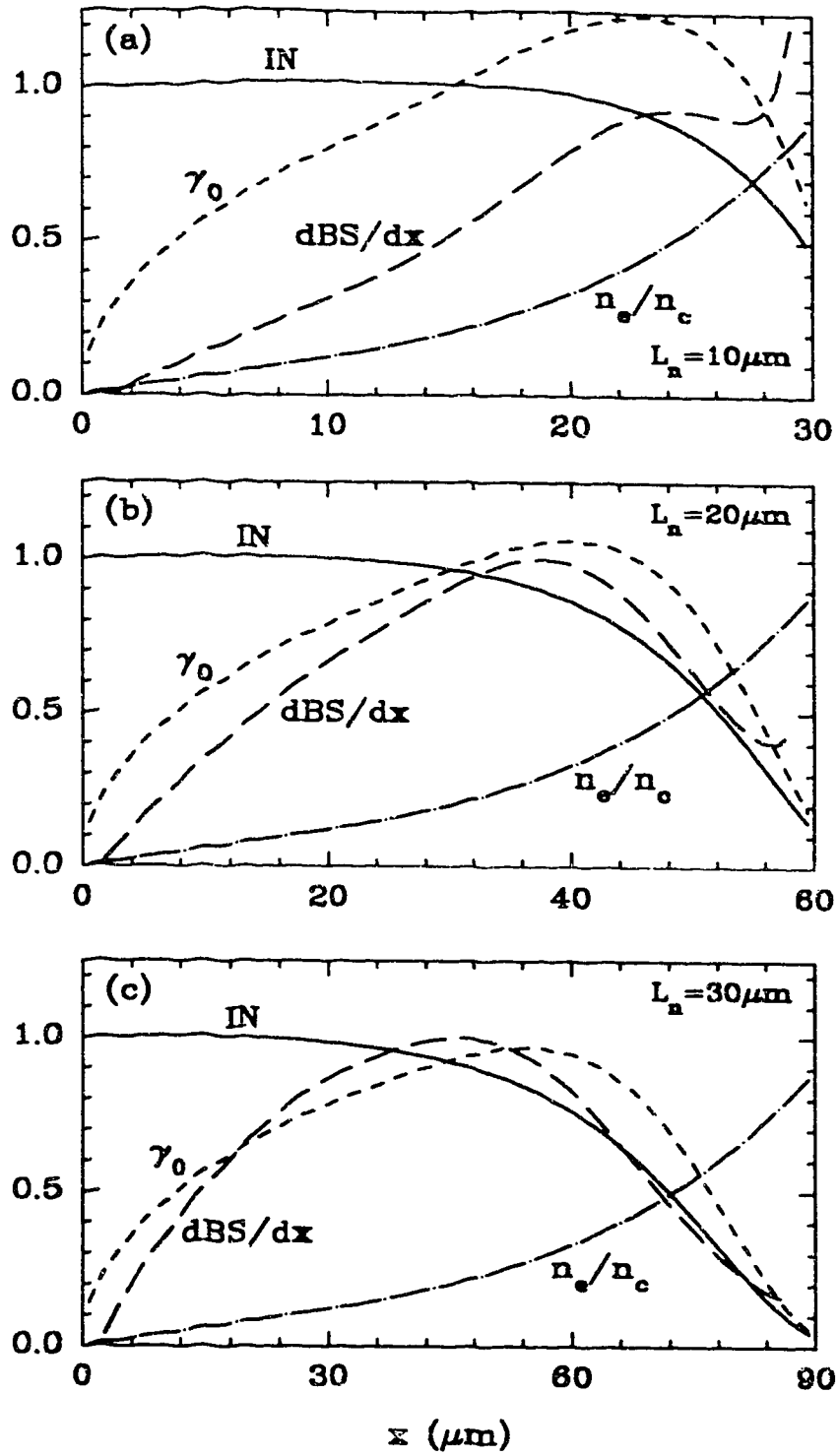


Fig.8.10. Spatial profiles of pump wave amplitude (IN), growth rate ( $\gamma_0$ ), and spatial derivative of scattered wave amplitude ( $dBS/dx$ ) for  $L_n = 10\mu\text{m}$  (a),  $20\mu\text{m}$  (b), and  $30\mu\text{m}$  (c) at  $I_L = 2 \times 10^{14} \text{W/cm}^2$ . The dash-dot lines show density profile.



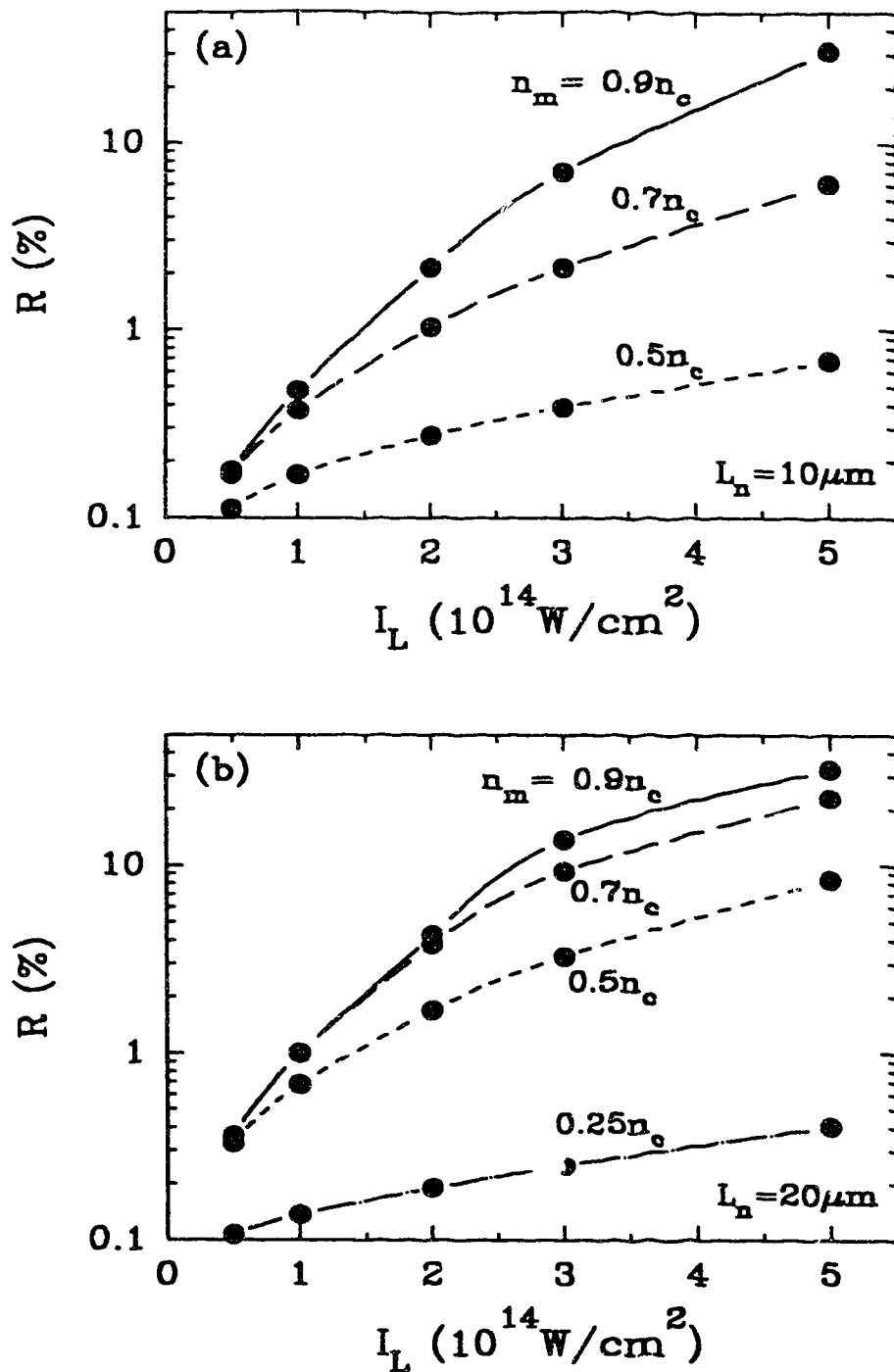


Fig.8.11. Effects of maximum density on reflectivity. Calculated reflectivity as a function of pump intensity  $I_L$  for several maximum densities  $n_m$  as a parameter. Density scale length  $L_n = 10 \mu\text{m}$  (a),  $20 \mu\text{m}$  (b). Coherent model.

from upstream (higher density) is not significant.

In a planar plasma, the turning point density  $n_t$  is given by  $n_c \cos^2 \theta$ . For  $\theta = 45^\circ$  and  $60^\circ$ ,  $n_t$  is  $0.5n_c$  and  $0.25n_c$ , respectively. In order to study the effects of turning point density, calculations were done with a truncated density profile; i.e., setting  $n_m = 0.5n_c$  (or  $0.25n_c$ ), instead of  $n_m = 0.9n_c$ . Figure 8.11 shows SBS reflectivity as a function of pump intensity  $I_L$  for several maximum densities  $n_m$  and two scale lengths  $L_n = 10\mu\text{m}$  (a) and  $20\mu\text{m}$  (b). Restricting the maximum density for SBS limits the interaction length, resulting in lower convective gain and hence lower reflectivity. The reduction of reflectivity is significant for shorter scale length plasma, because SBS prefers higher density for shorter scale length plasma as seen in fig.8.9. Lower  $n_m$  may be a cause of saturation of reflectivity for larger  $\theta$  seen in the experiment.

In summary, the coherent SBS model predicts higher reflectivity for longer scale length plasma. For longer scale length plasma, the SBS interaction is dominant at lower density. For higher pump intensity, SBS growth depends on the degree of inverse bremsstrahlung absorption and pump depletion. Applying a cutoff density to the SBS interaction leads to lower convective gain and reflectivity which is most significant for shorter scale length plasma.

### 8.3.3. Incoherent Model

In this section, the procedure for calculating SBS reflectivity using the incoherent model is briefly presented. Firstly, the plasma, of length  $L$ , is divided into small regions with length  $\Delta x$  in which SBS

reflectivity is calculated. It is assumed that SBS is amplified convectively in a limited length  $L_{\text{coh}}$  ("coherent length") which is determined by phase mismatch due to inhomogeneity of plasma parameters. We estimate  $L_{\text{coh}} \approx |\kappa'|^{-1/2}$ . In each  $L_{\text{coh}}$ , it is assumed that: 1) the frequency matching condition (eq.2.1) is satisfied and 2) the plasma is approximated to be homogeneous and hence the SBS reflectivity can be calculated analytically. It is noted that the frequency of scattered light from each  $\Delta x$  varies and has finite bandwidth  $\Delta\omega$ . Therefore, It is the power spectrum of scattered light  $\Delta I_{\text{BS}}/\Delta\omega$  that is equivalently calculated at each  $\Delta x$ . We modify eq.2.38 to calculate local SBS reflectivity  $R_{x(\omega)}$ ;

$$\begin{aligned}
 R_{x(\omega)} &= \frac{1}{I_{\text{IN}}} \frac{\Delta I_{\text{BS}}}{\Delta\omega} \\
 &= \left( \frac{1}{4} \frac{\omega_p^2}{\omega_0} \frac{\gamma_s}{\gamma_0^2} \right)^2 \cdot (N_n^\omega)^2 \cdot \\
 &\quad \cdot \left[ \exp \left( \frac{\gamma_0^2}{2\gamma_{\text{lb}} \gamma_s} \left( 1 - \exp \left( - \frac{2\gamma_{\text{lb}}}{v_g} L_{\text{coh}} \right) \right) \right) - 1 \right]^2 \quad (8.8)
 \end{aligned}$$

where  $N_n^\omega$  is the associated spectral noise density.  $R_{x(\omega)}$  is a function of  $\gamma_0(x)$ ,  $\gamma_{\text{lb}}(x)$ ,  $\gamma_s(x)$ , and  $n_e(x)$  as illustrated in fig.8.12 (a). The local growth of backscattered intensity  $\Delta I_{\text{BS}}$  is then calculated by

$$\begin{aligned}
 \Delta I_{\text{BS}}(x) &= \int_x^{x+\Delta x} \frac{dI_{\text{BS}}}{d\omega} d\omega \approx \frac{\Delta I_{\text{BS}}}{\Delta\omega} \Delta\omega \\
 &\approx R_{x(\omega)}(x) \cdot I_{\text{IN}}(x) \Delta\omega \quad (8.9)
 \end{aligned}$$

for each  $\Delta x$ , where  $I_{\text{IN}}(x)$  is the local pump intensity which is attenuated in space by inverse bremsstrahlung absorption (fig.8.12 (a)). It is noted that  $\Delta I_{\text{BS}}$  in the incoherent model corresponds to

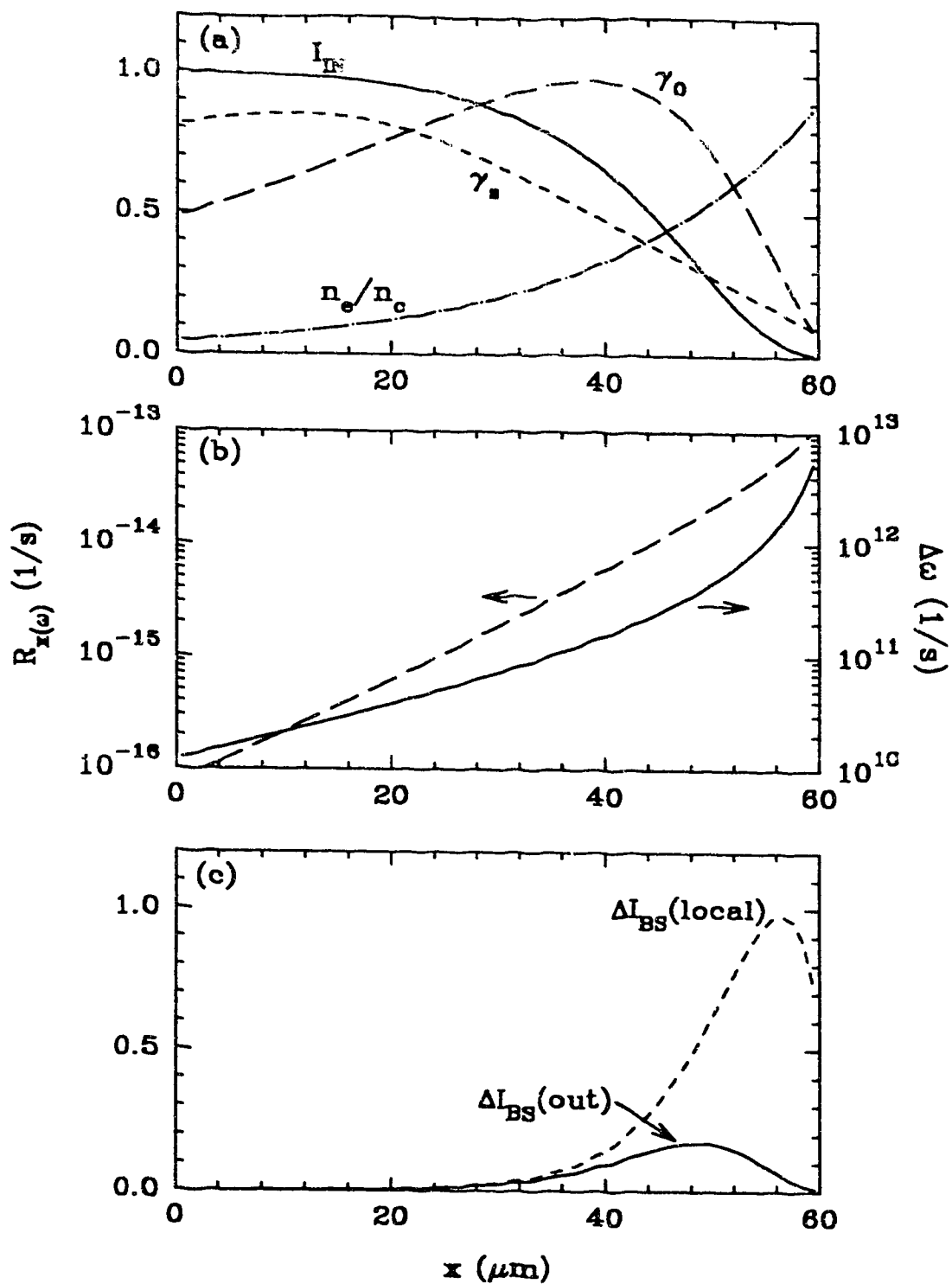


Fig.8.12. Spatial profiles of basic quantities used in model calculation for incoherent SRS (a). Calculated local reflectivity  $R_x$  and bandwidth  $\Delta\omega$  (b), and SRS growth in the plasma and observed outside the plasma (c).

$d/dx[a_1(x)^2]$  in the coherent model.

The finite bandwidth  $\Delta\omega$  for the spectra of backscattered light from each  $\Delta x$  is estimated in the following model. Assuming constant temperature in space and monochromatic scattered light, the scattered light from the region  $x = x_0$  to  $x_0 + \Delta x$  has bandwidth  $\Delta\omega$  given by

$$\Delta\omega = \omega_0 \frac{c_s}{c} \left(1 - \frac{n_e}{n_c}\right)^{-1/2} \cdot \frac{\Delta n_e}{n_c} \left(1 - \frac{n_e}{n_c}\right)^{-1} \quad (8.10)$$

where  $\omega_0$  is the laser frequency in vacuum, and  $\Delta n_e = n_e(x_0) - n_e(x_0 + \Delta x)$  which can be approximated by  $\Delta n_e / \Delta x = n_e / L_n$ . The bandwidth contribution from the flow velocity inhomogeneity is neglected, since these are calculated in the plasma frame. Then  $\Delta\omega$  for the scattered light from region  $\Delta x$  is given by

$$\Delta\omega = \omega_0 \frac{c_s}{c} \left(1 - \frac{n_e}{n_c}\right)^{-1/2} \cdot \frac{\Delta x}{L_n} \cdot \frac{n_e}{n_c} \left(1 - \frac{n_e}{n_c}\right)^{-1} \quad (8.11)$$

The choice of  $\Delta x$  is arbitrary and does not affect the results of the reflectivity calculation unless it is too large to violate the homogeneous approximation. One can estimate reasonable values of  $\Delta x$  by substituting the natural bandwidths of the SBS interaction (e.g. bandwidth due to ion damping  $\gamma_i$ , laser bandwidth, etc.) into eq.8.11. For simplicity, we typically use constant  $\Delta x \approx 1\mu\text{m}$  which corresponds to  $\Delta\omega \approx 10^{11}$  at  $n_e/n_c = 0.4$ . Profiles of  $R_{x(\omega)}(x)$  and  $\Delta\omega(x)$  calculated for  $\Delta x = 1\mu\text{m}$  are plotted in fig.8.12 (b).

Finally, in the laboratory frame at  $x=0$ , we observe attenuated backscattered light  $\Delta I_{BS}(\text{out}) = A_{1b} \times \Delta I_{BS}(\text{local})$ , where  $A_{1b}$  is an attenuation factor due to inverse bremsstrahlung absorption (fig.8.12 (c)). The total reflectivity  $R$  is given by summing up contributions from each  $\Delta x$ ;

$$R = \frac{1}{I_{IN}(x=0)} \sum A_{ib} \cdot \Delta I_{BS}(\text{local}) \quad (8.12)$$

We apply this incoherent SBS model to two situations. First, we assume constant  $L_{coh}(\kappa')$  in space to calculate SBS reflectivity. Since there is uncertainty in modeling  $\kappa'$  mainly due to the complex relationship between density and plasma flow, we treat  $L_{coh}$  as a parameter which reflects effects of both inhomogeneous density and plasma flow velocity. Second, we calculate  $L_{coh}(x)$  from  $\kappa'$  by taking into account only density inhomogeneity. This enables us to evaluate the spatial profile of  $\kappa'(x)$  analytically. Although inhomogeneity of plasma flow is ignored in this case, the main purpose of this calculation is to study the effects of space dependent  $L_{coh}$  on spatial characteristics of  $\Delta I_{BS}$ .

#### 8.3.4. Incoherent Model Results I : Constant $\kappa'$

Figure 8.13 shows SBS reflectivity as a function of pump intensity for several density scale lengths. The spectral noise density  $N_n^\omega$  is assumed to be  $3 \times 10^{-8} \text{ s}^{-1/2}$ . Since we do not have an appropriate model for spatial profile of phase mismatch rate, we assume  $L_{coh}(\propto |\kappa'|^{-1/2})$  is constant in space and treat it as a parameter. We roughly estimate  $L_{coh} = 0.5 \mu\text{m} - 2 \mu\text{m}$  for our plasma.  $L_{coh} = 0.5 \mu\text{m}$ ,  $1 \mu\text{m}$ , and  $2 \mu\text{m}$  correspond to phase mismatch rate  $\kappa' = 4 \times 10^8$ ,  $1 \times 10^8$ , and  $2.5 \times 10^7 \text{ cm}^{-2}$ . Typically,  $\kappa'$  is calculated to be  $3 \times 10^8 \text{ cm}^{-2}$  for  $n_e/n_c = 0.4$ ,  $M = 0.6$ ,  $L_v \approx 2 \cdot L_n \approx 30 \mu\text{m}$ . In fig. 8.13,  $L_{coh}$  is assumed to be  $0.5 \mu\text{m}$ ,  $1 \mu\text{m}$ , and  $2 \mu\text{m}$  for  $L_n = 10 \mu\text{m}$ ,  $20 \mu\text{m}$ , and  $30 \mu\text{m}$ , respectively. The results show that reflectivity is higher for larger  $L_{coh}/L_n$ . For the same  $L_{coh}/L_n$ , reflectivities are almost the same or slightly higher for shorter scale lengths.

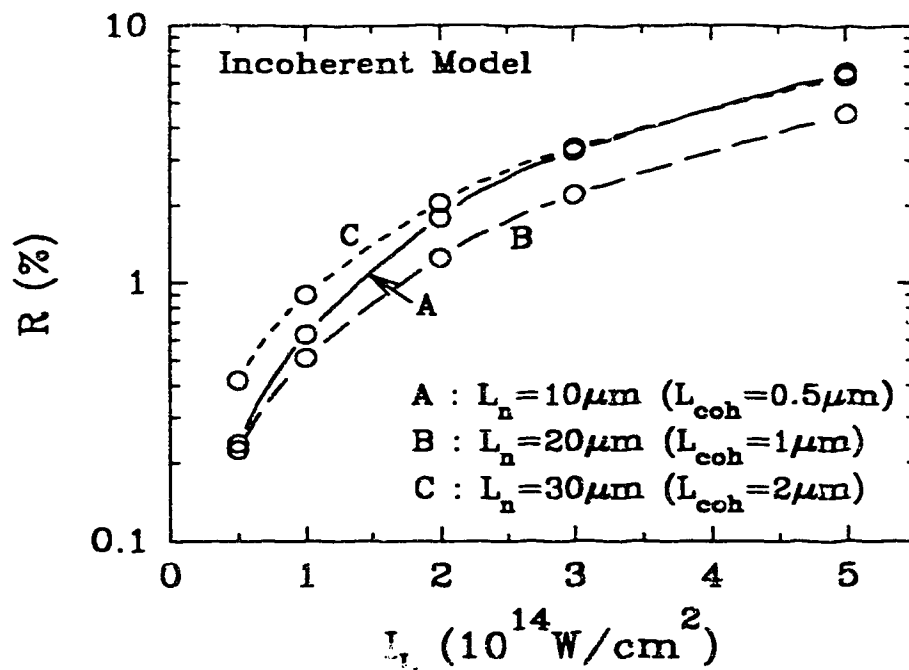


Fig.8.13. Incoherent model calculation with constant  $L_{\text{coh}}$ . SBS reflectivity as a function of pump intensity for several density scale lengths.

Figure 8.14 shows SBS reflectivity as a function of pump intensity for several  $L_{\text{coh}}$  (a) and  $L_n$  (b). For the same scale length ( $L_n = 20\mu\text{m}$ , fig.8.14 (a)), larger  $L_{\text{coh}}$  gives higher reflectivity and  $R$  roughly scales as  $L_{\text{coh}}^2$ . This is because  $R_x$  is proportional to  $L_{\text{coh}}^2$  for small  $L_{\text{coh}}$  and  $\gamma_0$  (eq.8.8); for small  $x \ll 1$ ,  $\exp(x) \approx 1 + x$ . On the other hand, for the same  $L_{\text{coh}}$  ( $=1\mu\text{m}$ , fig.8.14 (b)), smaller  $L_n$  gives higher reflectivities. It is rather surprising that shorter scale length plasma gives higher reflectivity in the incoherent model. This is because: 1) the pump wave can penetrate to a higher gain region for shorter scale length plasma and 2) the convective gain length is fixed by  $L_{\text{coh}}$  and independent of  $L_n$ . It is necessary to model an appropriate relationship between  $L_{\text{coh}}$  and  $L_n$ .

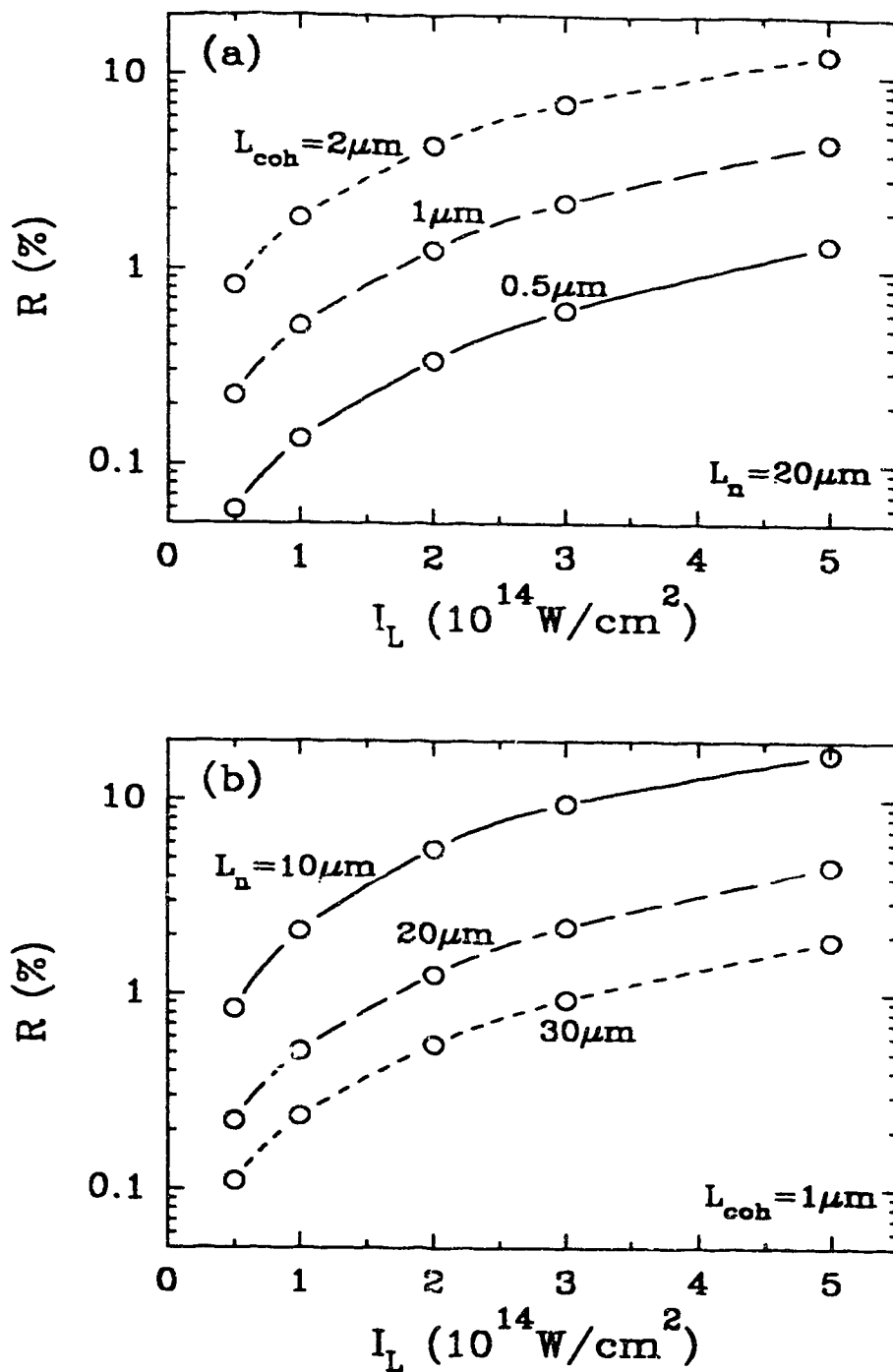


Fig.8.14. Calculated SBS reflectivity as a function of pump intensity for several  $L_{\text{coh}}$  (a) and  $L_n$  (b). Incoherent model with constant  $\kappa'$  in space.



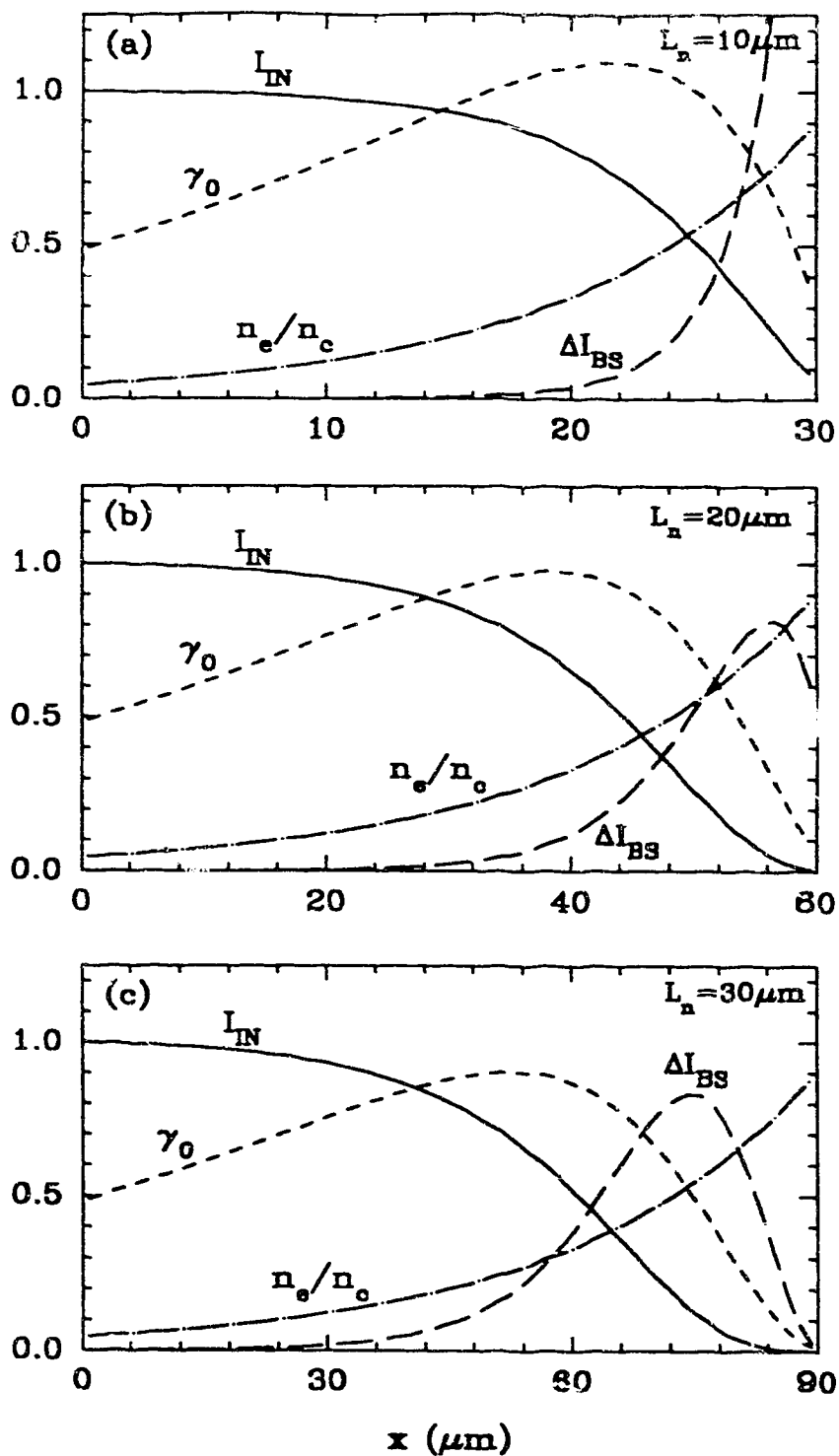


Fig. 8.15. Comparison of spatial profiles of pump intensity ( $I_{IN}$ ), growth rate ( $\gamma_0$ ), and local SBS growth  $\Delta I_{BS}$  for  $L_n = 10 \mu\text{m}$  (a),  $20 \mu\text{m}$  (b), and  $30 \mu\text{m}$  (c). Incoherent model with constant  $\kappa'$  in space.

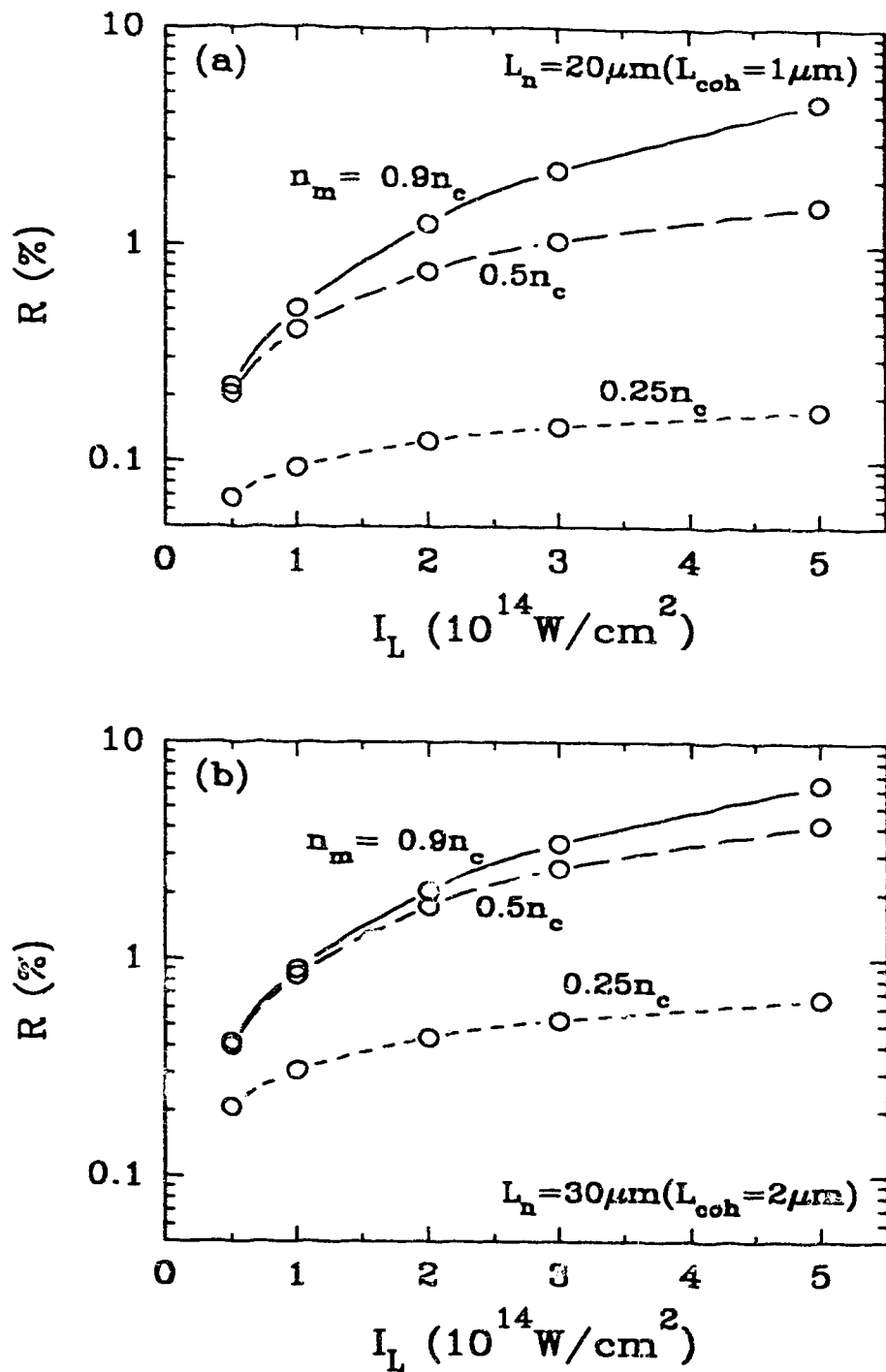


Fig. 8.16. Effects of maximum density on reflectivity. Calculated SBS reflectivity as a function of pump intensity for several maximum density and scale lengths  $L_n = 20 \mu\text{m}$  (a) and  $30 \mu\text{m}$  (b). Incoherent model with constant  $\kappa'$  in space.

Figure 8.15 shows spatial profiles of pump intensity ( $I_{IN}$ ), growth rate ( $\gamma_0$ ),  $\Delta I_{BS}$  (local), and electron density ( $n_e/n_c$ ).  $L_n$  and  $L_{coh}$  are  $10\mu\text{m}$  and  $0.5\mu\text{m}$  for (a),  $20\mu\text{m}$  and  $1\mu\text{m}$  for (b), and  $30\mu\text{m}$  and  $2\mu\text{m}$  for (c).  $I_{IN}$  and  $\gamma_0$  are normalized to  $2 \times 10^{14} \text{W/cm}^2$  and  $2 \times 10^{12} \text{s}^{-1}$ .  $\Delta I_{BS}$  is normalized to the same arbitrary number. Compared with the coherent model (fig.8.10), the peak of SBS growth is located at higher density than the peak of  $\gamma_0$ . This is because: 1) SBS growth in each small region is independent of the contribution from upstream (the higher density region) and 2) ion damping  $\gamma_s$  is lower at higher density (fig.8.12 (a)). It is also noticed that SBS growth is more localized than in the coherent model.

The effects of maximum density were also studied in the incoherent model. Figure 8.16 shows SBS reflectivity as a function of pump intensity for several maximum densities  $n_u$  and two scale lengths  $L_n = 20\mu\text{m}$  (a) and  $30\mu\text{m}$  (b).  $L_{coh}$  is assumed to be  $1\mu\text{m}$  (a) and  $2\mu\text{m}$  (b). The results show that the reduction of reflectivity is significant for shorter scale length plasma, consistent with results of the coherent model. The degree of reduction is, however, less for the incoherent model than coherent model. This is because each small part of plasma contributes to SBS generation independently in the incoherent model, whereas SBS in the coherent model depends on the supply of scattered light from upstream (the higher density region).

### 8.3.5. Incoherent Model Results II : $\kappa'(L_n)$

In this second application of the incoherent model, we evaluate  $L_{coh}$  as a function of space. By taking into account only inhomogeneity of density, we can reduce parameters to one quantity,  $L_n$ .

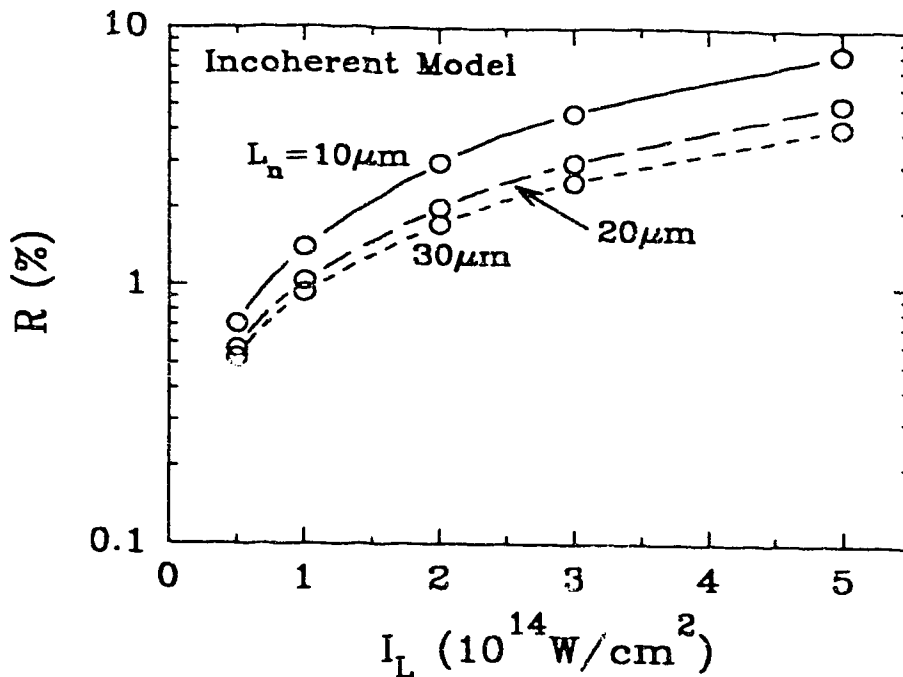


Fig. 8.17. Incoherent model calculation with space dependent  $L_{coh}$ . SBS reflectivity as a function of pump intensity for several  $L_n$ .

$L_{coh}$  is now a function of  $n_e(x)$  and is calculated at each plasma point, consistent with  $L_n$ . In this case,  $L_{coh}$  is given by

$$L_{coh} = \left[ \left( 1 - \frac{n_e}{n_c} \right) L_n / \left( k_0 \frac{n_e}{n_c} \right) \right]^{1/2} \tag{8.13}$$

where  $k_0$  is the wavenumber of the pump wave in the plasma.

Figure 8.17 summarizes SBS reflectivity as a function of pump wave intensity for several  $L_n$ . The results show no significant dependence on  $L_n$  and slightly higher reflectivity for shorter  $L_n$ . Similar features were seen in fig. 8.13 for the curves with the same  $L_{coh}/L_n$ . Compared with the results for constant  $L_{coh}$ , dependence on intensity is weaker, since  $L_{coh}$  at high density is smaller than in the case of constant  $L_{coh}$ , resulting in less contribution from the higher gain

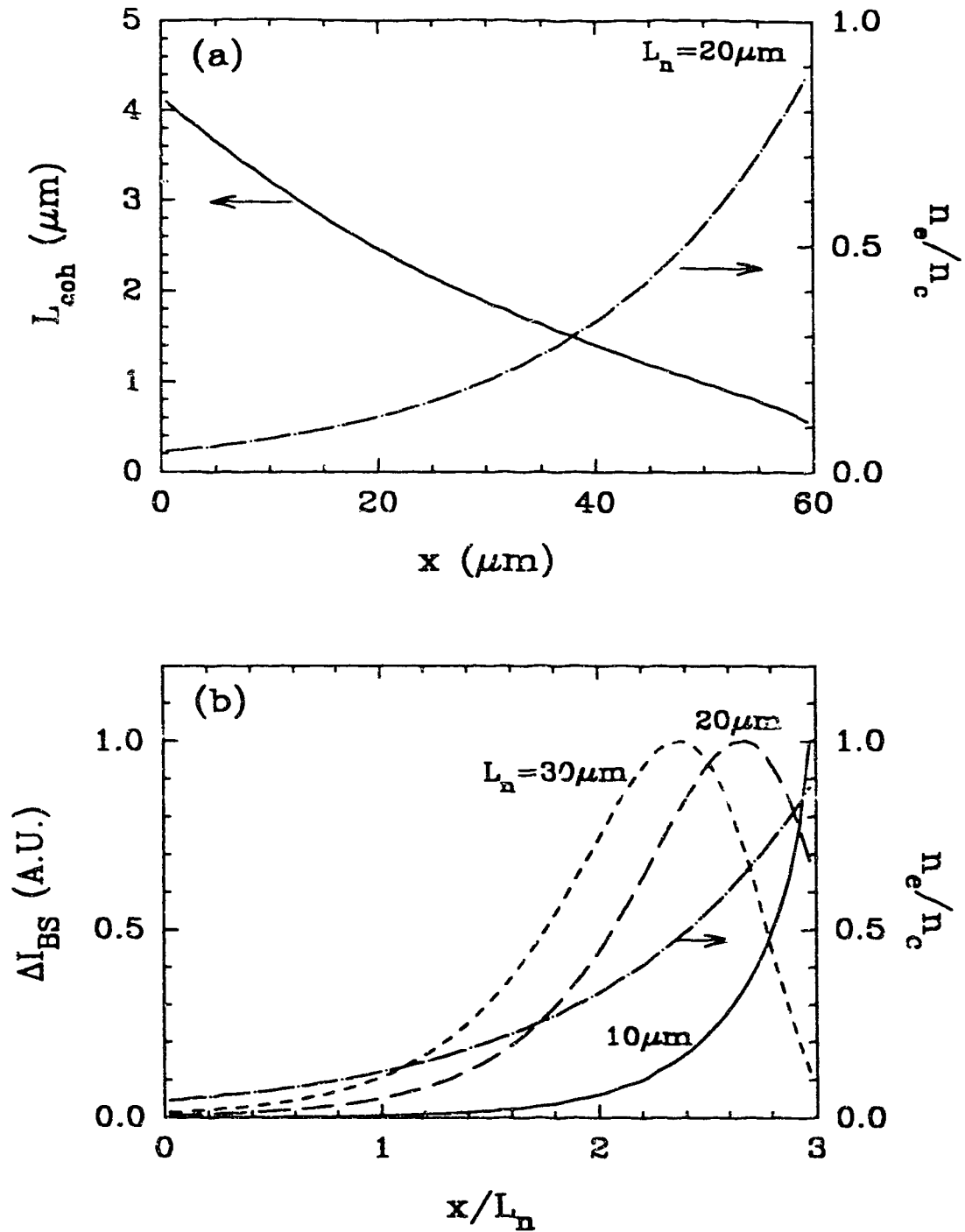


Fig. 8.18. Spatial profile of  $L_{coh}$  (solid line) (a). Spatial profiles of  $\Delta I_{BS}$  for  $L_n = 10 \mu\text{m}$  (solid line),  $20 \mu\text{m}$  (dashed line), and  $30 \mu\text{m}$  (dotted line) (b). The dash-dot lines show density profile.

region. This is illustrated in fig.8.18. Figure 8.18 (a) shows the spatial profile of  $L_{coh}$  for  $L_n = 20\mu\text{m}$  and  $I_L = 2 \times 10^{14} \text{W/cm}^2$ .  $L_{coh}$  varies from  $4\mu\text{m}$  to  $0.5\mu\text{m}$  in space, with shorter  $L_{coh}$  at higher density. Figure 8.18 (b) shows spatial profiles of normalized  $\Delta I_{BS}$  for several  $L_n$ , and electron density ( $n_e/n_c$ ) at  $I_L = 2 \times 10^{14} \text{W/cm}^2$ , which corresponds to fig.8.15 in the case of constant  $L_{coh}$ . Compared with fig.8.15, the peaks of  $\Delta I_{BS}$  locate at lower density.

It should be noted that the profile of  $\kappa'$  in fig.8.1 shows a lower value around the singular point ( $\kappa'=0$ ), which takes into account both density and plasma flow inhomogeneity. Existence of such point is expected to give large  $L_{coh}$  and localize SBS growth. It is, however, necessary to establish a model which can treat the singular point appropriately.

In summary, incoherent model predictions depend on the ratio  $L_{coh}/L_n$ . Compared with the coherent model, SBS growth is localized at higher density. Reducing the maximum density results in lower reflectivity as seen in the coherent model, which is significant for shorter scale length plasma. Because of the limited convective gain length, reflectivity is less sensitive to laser intensity than in the coherent model. Appropriate modeling of the spatial plasma conditions is essential in the incoherent model.

### 8.3.6. Comparison among SBS Models and Experimental Data

In the previous sections, two types of SBS model for inhomogeneous plasma have been discussed in detail and the mechanisms of SBS generation in each model were clarified. We will compare the

experimental data with the results from each model discussed above. In order to compare the analytical predictions with experimental data, we take into account non-uniform structure of our focal spot as discussed in section 7.2.3. We assume: 1) the laser intensity for analytical calculation is 2.3 times higher than the average intensity  $I_{av}$ , and 2) 34% of reflectivity from the analytical calculation corresponds to the reflectivity that would be observed.

Figure 8.19 shows comparison among three SBS models and the experimental data. Curves a, b, and c correspond to the results for coherent model (section 8.3.2), incoherent model with constant  $\kappa'$  (section 8.3.4), and incoherent model with  $\kappa'(L_n)$  (section 8.3.5), respectively. All calculations are for density scale length  $L_n = 20\mu\text{m}$ , and initial noise density level  $N_n = 10^{-3}$  for the coherent model and the spectral noise level  $N_n^\omega = 3 \times 10^{-8} \text{s}^{-1/2}$  for the incoherent model. Solid circles and diamonds shows experimental data for Al target at  $\theta = 0^\circ$  and  $45^\circ$ . Dependence of reflectivity on laser intensity is weaker for the incoherent model than the coherent model. This is mainly due to the limited convective gain length in the incoherent model. The similarity between the two models (coherent and incoherent) is that SBS growth is optimized at higher density for shorter  $L_n$ . The main differences are: 1) SBS growth is localized at higher density region for the incoherent model, and 2) the dependence of reflectivity on  $L_n$  and pump intensity is weaker for incoherent model. The first difference gives interesting results, if one assumes constant temperature for (or weak dependence on) different intensities. Since lower temperature and hence stronger IB absorption at higher intensity inhibits the pump wave from penetrating to higher density, the

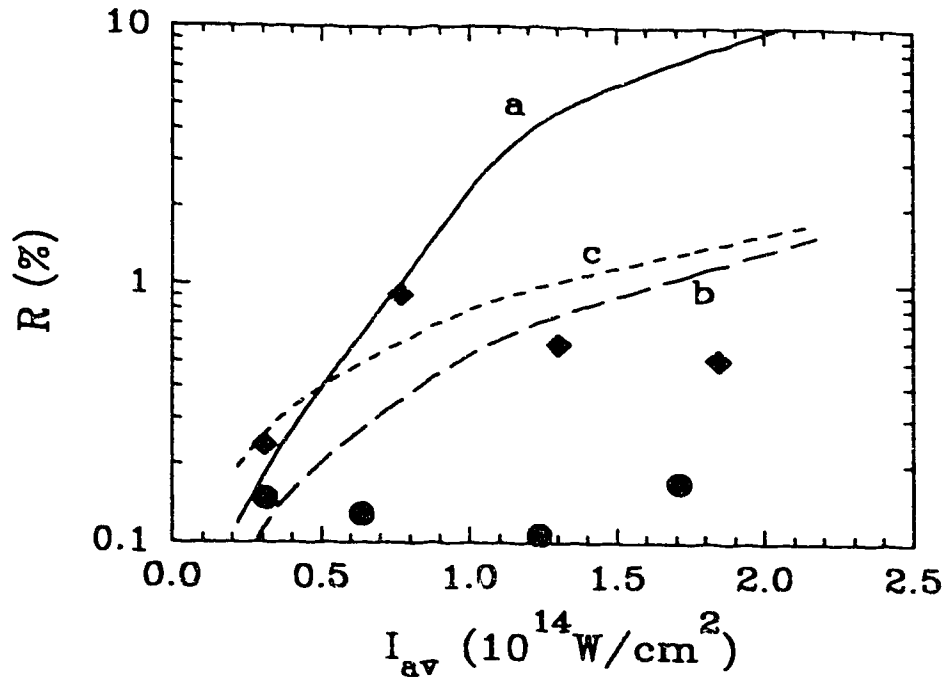


Fig. 8.19. Comparison among three SBS model calculations and experimental data. Coherent model: a, incoherent model with constant  $\kappa'$  : b, and incoherent model with  $\kappa'(L_n)$  : c. Solid circles and diamonds show experimental data for Al target at  $\theta = 0^\circ$  and  $45^\circ$ .

incoherent model gives lower reflectivity. In contrast to this, the coherent model gives higher reflectivity because lower temperature results in higher growth rate.

In order to compare the noise density level  $N_n$  for the coherent model with the spectral noise density  $N_n^\omega$  for the incoherent model, one has to assume a spectral width  $\Delta\omega$ . Assuming constant  $N_n^\omega$  for every frequency,  $N_n$  can be roughly related to  $N_n^\omega$  as

$$N_n \approx [ ( N_n^\omega )^2 \Delta\omega ]^{1/2} \quad (8.14)$$

If one estimates  $\Delta\omega$  from the observed linewidth ( $\Delta\lambda \approx 0.3\text{\AA}$ ,  $\Delta\omega \approx 10^{12} \text{ s}^{-1}$ ),  $N_n^\omega \approx 3 \times 10^{-8} \text{ s}^{-1/2}$  corresponds to  $N_n \approx 3 \times 10^{-2}$ . If one estimates  $\Delta\omega$



from the interaction region in the coherent model ( $n_e/n_c \approx 0.3 \pm 0.2$ ),  $\Delta\omega$  is roughly  $3 \times 10^{12} \text{ s}^{-1}$  for  $T = 800 \text{ eV}$ . On the other hand, the maximum limit for  $\Delta\omega$  is roughly given by  $\omega_{pi}$ , which is  $\approx 7 \times 10^{13} \text{ s}^{-1}$  for  $n_e/n_c = 0.4$  in our case. For any case, the incoherent model requires higher noise density level than the coherent model for the comparable reflectivity because of the shorter convective gain length.

In the coherent model, in order to explain the  $\theta$  dependence of reflectivity (increased reflectivity for larger  $\theta$  from  $0^\circ$  to  $45^\circ$ ), one would have to assume a wide range of density scale lengths - from less than  $10 \mu\text{m}$  to more than  $30 \mu\text{m}$ . If one applies the maximum density  $n_m (= n_c \cos^2 \theta)$  to the plasma,  $L_n = 40 \mu\text{m}$  is required for reflectivity comparable to experimental data for  $\theta = 60^\circ$ . It is noted that our SBS code cannot be applied to smaller scale length plasma, since most SBS generation occurs at high density ( $n_e/n_c > 0.8$ ), where treatment of the EM wave becomes complicated.

Figure 8.20 shows our best estimate using the coherent model. Curves a, b, and c are calculated reflectivities for  $L_n = 10 \mu\text{m}$  and  $n_m = 0.9$ ,  $L_n = 20 \mu\text{m}$  and  $n_m = 0.5$  ( $\theta = 45^\circ$ ), and  $L_n = 40 \mu\text{m}$  and  $n_m = 0.25$  ( $\theta = 60^\circ$ ), respectively. Solid circles and squares are experimental data for Al target at  $\theta = 0^\circ$  and  $45^\circ$ . It is clear that the coherent model overestimates the reflectivity because of neglect of phase mismatch. Furthermore, the coherent model results would show contradiction with spectral data. Since the scattered wave is allowed to grow continuously in an inhomogeneous plasma in the coherent model, SBS is generated over a wide range of density which is expected to result in a broad linewidth of scattered light spectrum. In section 8.2.2, the observed linewidth was explained by density inhomogeneity  $\Delta n_e/n_c = 0.1$

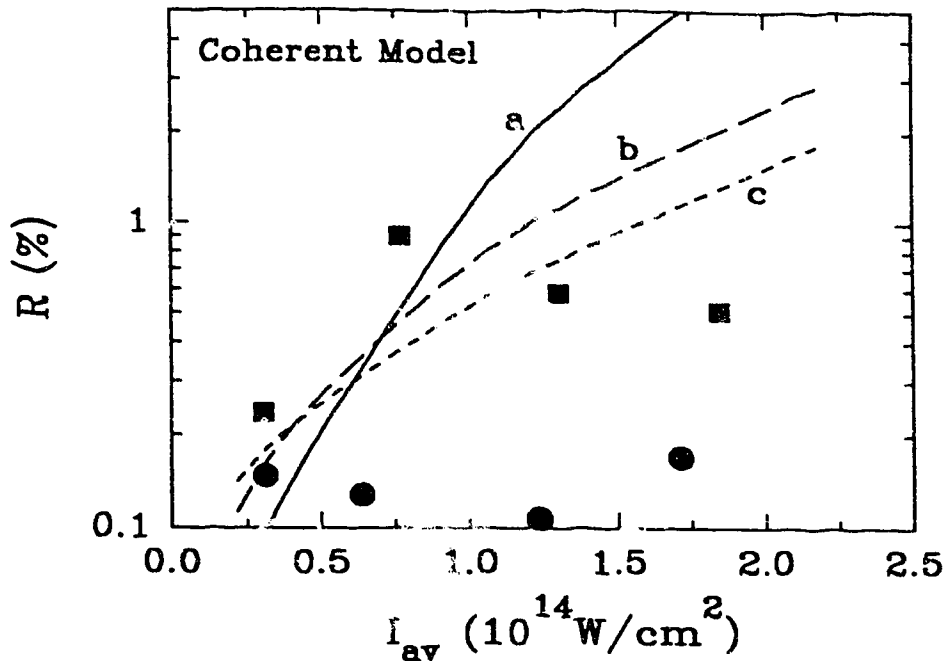


Fig.8.20. Fitting of coherent model calculations to the experimental data. Curves a, b, and c are calculated reflectivities for  $L_n=10\mu\text{m}$  and  $n_m=0.9$ ,  $L_n=20\mu\text{m}$  and  $n_m=0.5$ , and  $L_n=40\mu\text{m}$  and  $n_m=0.25$  ( $\theta=60^\circ$ ). Solid circles and squares are experimental data for Al target at  $\theta=0^\circ$  and  $45^\circ$ .

with assumption of flow velocity inhomogeneity  $\Delta M = 0.1$ . If inhomogeneity of plasma flow is negligible,  $\Delta n_e/n_c = 0.4$  could explain the observed linewidth. Therefore, in order to explain the experimental data - both reflectivity and spectrum - by the coherent model, it is required to assume that: 1) the density scale length varies substantially with angle of incidence, 2) some saturation mechanisms exist to limit reflectivity, and 3) plasma flow is homogeneous and subsonic in a density region from  $n_e/n_c \approx 0.2$  to  $0.6$ .

In the incoherent model, reflectivity depends on  $L_{\text{coh}}/L_n$ , rather than  $L_n$  itself. In order to explain the  $\theta$  dependence of reflectivity

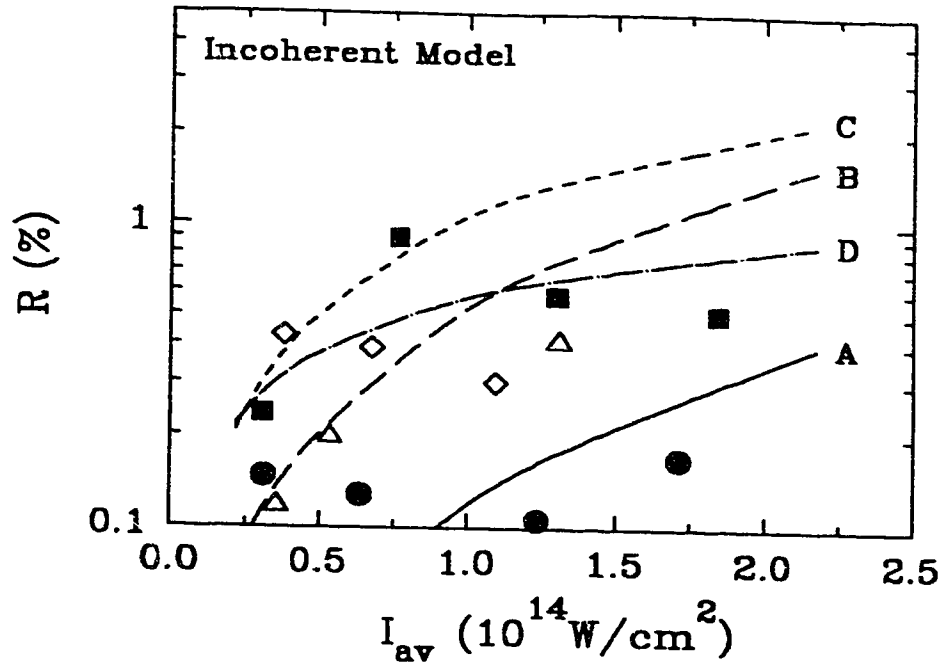


Fig.8.21. Fitting of incoherent model calculations to the experimental data. Curves A, B, C, and D are calculated reflectivities for  $L_{\text{coh}}/L_n=0.4/18$  with  $n_m=0.9$ ,  $L_{\text{coh}}/L_n=1/20$  with  $n_m=0.9$ ,  $L_{\text{coh}}/L_n=2.5/30$  with  $n_m=0.5$ ,  $L_{\text{coh}}/L_n=4.0/40$  with  $n_m=0.25$ . Solid circles, open triangles, solid squares, and open diamonds are experimental data for Al target at  $\theta=0^\circ$ ,  $22.5^\circ$ ,  $45^\circ$ , and  $60^\circ$ .

in the experiment, we estimate  $L_n$  from simple geometrical scaling  $1/\cos\theta$  and adjust  $L_{\text{coh}}/L_n$ . Figure 8.21 shows our best fit of incoherent model calculations with constant  $L_{\text{coh}}$  to the experimental data. Curves A, B, C, and D are calculated reflectivities for  $L_{\text{coh}}/L_n=0.4/18$  with  $n_m=0.9$ ,  $L_{\text{coh}}/L_n=1/20$  with  $n_m=0.9$ ,  $L_{\text{coh}}/L_n=2.5/30$  with  $n_m=0.5$  ( $\theta=45^\circ$ ),  $L_{\text{coh}}/L_n=4.0/40$  with  $n_m=0.25$  ( $\theta=60^\circ$ ), respectively. Solid circles and squares are experimental data for Al target at  $\theta=0^\circ$  and  $45^\circ$ . Except for the nearly constant reflectivity for  $\theta=0^\circ$  and decreasing feature of reflectivity at high intensity for  $\theta=45^\circ$ , the incoherent model fits

reasonably well to the experimental data. This fitting suggests that  $L_{\text{coh}} (\approx \kappa'^{-1/2})$  increases more than linearly with  $L_n$ ; that is,  $\kappa' \propto L_n^{-\alpha}$ , where  $\alpha > 2$ . To explain the spectral data simultaneously, it is also required that SBS generation is localized so that  $\Delta n_e/n_c \approx 0.1$ . We again emphasize that appropriate modeling of spatial profile of phase mismatch rate, especially due to plasma flow, is necessary and may explain the experimental data more thoroughly. The nonuniformity of the laser beam is also a possible cause of the the discrepancy between theory and experiment. The possibility of filamentation will be discussed briefly in the Appendix 4.

#### 8.4. Summary

Inhomogeneity of plasma was taken into account to interpret the experimental data. Analytical calculations of threshold intensity and SBS gain imply convective instability. The effects of flowing inhomogeneous plasma on the average SBS spectral shift were found to be negligible for the small focus laser irradiation. The linewidth of the SBS spectrum was explained mainly by inhomogeneity of plasma flow. Temporal features of the spectral shift showed strong correlation with laser pulse shape, suggesting the importance of plasma heating during the temporally varying laser pulse. SBS reflectivity was calculated by two models (coherent and incoherent) and compared with the experimental data. The incoherent model fitted the experimental data better than the coherent model, suggesting the importance of phase mismatch. Appropriate modeling of space-dependent phase mismatch rate would be necessary to completely explain the experimental data by the incoherent model.

Bibliography

- 1) T.Dewandre, J.R.Albritton, and E.A.Williams, Phys.Fluids, **24**, 528 (1981).
- 2) E.M.Epperlein, Phys.Rev.Lett., **65**, 2145(1990).
- 3) M.N.Rosenbluth, Phys.Rev.Lett., **29**, 565(1972).
- 4) M.Casanova, Laser and Particle Beams, **7**, 165(1989).

## IX. Conclusions

A comprehensive study of stimulated Brillouin scattering in nanosecond KrF laser-produced plasma at intensity  $I_L \approx 10^{14} \text{W/cm}^2$  has been performed. Measurements of reflectivity and time-resolved backscattered spectra were done for CH, Al, and Au targets at various angles of incidence. Numerical codes were developed to study SBS in homogeneous and inhomogeneous plasmas. Two-dimensional hydrodynamic simulations were performed to estimate the plasma conditions created by a tightly focused laser beam. These experimental and numerical results were compared with analytical calculations to identify the nature of SBS.

Numerical calculations of SBS in homogeneous plasma showed the existence of an optimum density as a consequence of competition between parametric wave growth and damping. The importance of inverse bremsstrahlung absorption in KrF laser-produced plasma was demonstrated. Similar results were seen in the calculations for inhomogeneous plasma.

The two-dimensional hydrodynamic simulation code CASTOR showed many important features of plasma created by a tightly focused laser beam. Refraction of laser radiation is important and can result in a plasma larger than the focal spot size. As a consequence of large mass ablation rate (for short wavelength lasers) and localized plasma heating due to short electron-ion mean free path, locally planar plasma is established with a spherical pressure profile.

Backscatter reflectivity was measured to be 0.1-1.0% for Al and C plasma, with higher reflectivity being observed for larger angle of

incidence  $\theta$ . Au plasma showed significantly lower reflectivity ( $\approx 0.005\%$ ). Time-resolved spectra of backscattered light always showed red shift, typically,  $1 \pm 0.5 \text{ \AA}$ . No strong dependence on  $\theta$  was observed. The rate of spectral shift change increased with increasing laser intensity. The observed  $\theta$  dependence of reflectivity and spectral shift is explained by convective growth of SBS in locally planar density and spherical pressure profiles seen in the CASTOR predictions.

Analytical and numerical calculations for homogeneous plasma established the convective nature of SBS for pulse duration  $\geq 100\text{ps}$ . Consideration of hotspots in laser focus is necessary to explain the experimental data. A model for calculating SBS reflectivity for non-uniform laser beams was proposed. It was found that the contribution of hotspots to reflectivity depended not only on the hotspot intensity level but also on their fraction of area in the focal spot. Threshold analysis showed that double SBS is not likely in our highly absorbing plasma.

Analytical and numerical calculations for inhomogeneous plasma also showed the convective nature of SBS. Linewidth of the spectral shift was explained mainly by inhomogeneity of plasma flow. Temporal features of the spectral shift showed strong correlation with laser pulse shape, suggesting the importance of plasma heating during temporally varying laser pulse. SBS reflectivity was calculated by two models (coherent and incoherent) and compared with the experimental data. The incoherent model fitted the experimental data better than the coherent model, suggesting the importance of phase mismatch.

A number of important questions remain to be solved. One of the outstanding issues is the need to resolve the mechanism which would

account for the relatively high level of scattered light required at threshold intensity. Density noise levels of  $10^{-2}$ - $10^{-3}$  required to explain the measured reflectivity ( $\approx 0.1$  - 1%) are far above the thermal level ( $\approx 10^{-5}$ - $10^{-6}$ ) estimated from the Thomson scattering and the blackbody radiation. A second issue is concerned with an appropriate model for plasma heating (thermal transport) which may be able to explain the correlation between spectral properties and laser pulse shape. This includes both spectral shift and width. The time-varying spectral shift observed at high intensity, which followed laser intensity scaling  $I_L(t)^{1.0}$ , could not be explained by the hydrodynamic simulation results or the self-regulating model. An appropriate modeling of the relationship between plasma flow and temperature ( $c_s$ ) in space and time is necessary to explain the peak spectral shift as well as the linewidth of the scattered light. A third problem is related to modeling of space-dependent phase mismatch rate  $\kappa'$  and a way to handle the singular point of  $\kappa'$ . The incoherent model for SBS reflectivity showed strong dependence on  $L_{coh}$  ( $\approx \kappa'^{-1/2}$ ) and requires detailed information of space-dependent  $\kappa'$ . More complete modeling of non-uniform laser beam and plasma conditions by 2D hydrodynamic simulations are also required to explain the experimental data in detail. Dependence of plasma conditions on laser intensity would necessarily have to be incorporated in the modeling.

In summary, an SBS database for KrF laser-produced plasma was successfully accumulated. Analytically and experimentally, we find the SBS instability to be convective. The importance of two-dimensional effects and strong inverse bremsstrahlung absorption was demonstrated by hydrodynamic simulations and SBS analysis. Models



for SBS in inhomogeneous plasma and non-uniform laser beams were proposed and used to explain the experimental data.

Appendix 1

**A1. Derivation of Steady State Convective SBS in Finite Homogeneous Plasma**

The coupling equations of SBS are given by eqs. (2.6) and eq. (3.1).

Ignoring  $\partial k/\partial x$ , these equations are simplified to

$$\left( \frac{\partial}{\partial t} + v_g \frac{\partial}{\partial x} + \gamma_{ib} \right) a_0 = - A \cdot a_1 \cdot n \quad (\text{A1.1a})$$

$$\left( \frac{\partial}{\partial t} - v_g \frac{\partial}{\partial x} + \gamma_{ib} \right) a_1 = A \cdot n \cdot a_0 \quad (\text{A1.1b})$$

$$\left( \frac{\partial}{\partial t} + c_s \frac{\partial}{\partial x} + \gamma_s \right) n = B \cdot a_1 \cdot a_0 + \gamma_s N_n \quad (\text{A1.1c})$$

where  $A = \frac{1}{4} \frac{\omega_p^2}{\omega_0}$ ,  $B = \frac{1}{4} \frac{Z m_e k_s^2 v_0^2}{M_1 \omega_s}$ .

For a steady state solution, we put  $\partial/\partial t = 0$ . Assuming small growth of SBS ( $a_0 \approx \text{constant}$ : small  $a_1, n$ ), and  $v_g \gg c_s$  (ion motion negligible compared with EM wave velocity), these equations can be simplified to

$$\left( v_g \frac{\partial}{\partial x} + \gamma_{ib} \right) a_0 = 0 \quad (\text{A1.2a})$$

$$\left( -v_g \frac{\partial}{\partial x} + \gamma_{ib} \right) a_1 = A \cdot n \cdot a_0 \quad (\text{A1.2b})$$

$$\gamma_s \cdot n = B \cdot a_1 \cdot a_0 + \gamma_s N_n \quad (\text{A1.2c})$$

From eq. (A.2a),

$$a_0(x) = a_0(0) \cdot \exp(-\gamma_{ib} x/v_g) \quad (\text{A1.3})$$

From eq. (A.2c),

$$n = (B/\gamma_s) \cdot a_0 \cdot a_1 + N_n \quad (\text{A1.4})$$

Substituting eqs. (A.3) and (A.4) into eq. (A.2b) yields

$$\frac{\partial}{\partial x} \cdot a_1 + \left( -\frac{\gamma_{ib}}{v_g} + \frac{AB}{\gamma_s v_g} \cdot a_0(x)^2 \right) a_1 = -A \cdot N_n \cdot a_0(x)/v_g \quad (\text{A1.5})$$

To get a solution of eq. (A.5), we first solve

$$\frac{\partial}{\partial x} \cdot a_1 + \left( -\frac{\gamma_{1b}}{v_g} + \frac{AB}{\gamma_s v_g} \cdot a_0(x)^2 \right) a_1 = 0 \quad (\text{A1.6})$$

to obtain

$$a_1 = \alpha \cdot \exp \left( -\frac{\gamma_{1b}}{v_g} x + \frac{\gamma_0^2}{2\gamma_s \gamma_{1b}} \cdot \exp(-2\gamma_{1b} x/v_g) \right) \quad (\text{A1.7})$$

where  $\alpha$  is a constant,  $\gamma_0^2 = AB \cdot a_0(0)^2$ .

Next, let  $\alpha = \alpha(x)$  and substitute eq. (A.7) into eq. (A.5)

$$\frac{\partial a_1}{\partial x} + f(x) \cdot a_1 = g(x) \quad (\text{A1.5})'$$

$$a_1 = \alpha(x) \exp \left( -\int f(x) dx \right) \quad (\text{A1.7})'$$

where

$$f(x) = -\frac{\gamma_{1b}}{v_g} + \frac{AB}{\gamma_s v_g} \cdot a_0(x)^2 \quad (\text{A1.8})$$

$$g(x) = -A \cdot N_n \cdot a_0(x) / v_g \quad (\text{A1.9})$$

Taking the derivative of eq. (A.7)' gives

$$\frac{\partial a_1}{\partial x} = \frac{\partial \alpha}{\partial x} \exp \left( -\int f(x) dx \right) - f(x) \cdot a_1 \quad (\text{A1.10})$$

From eqs. (A.5)' and (A.10), we find

$$\frac{\partial \alpha}{\partial x} \exp \left( -\int f(x) dx \right) = g(x) \quad (\text{A1.11})$$

or

$$\frac{d\alpha(x)}{dx} = g(x) \cdot \exp \left( \int f(x) dx \right) \quad (\text{A1.12})$$

which can be written as

$$\frac{d\alpha}{dx} = -\frac{A N_n a_0(0)}{v_g} \exp \left[ -Cx - \frac{\Gamma}{2} \cdot \exp(-Cx) \right] \quad (\text{A1.13})$$

where  $C = 2\gamma_{1b}/v_g$ ,  $\Gamma = \gamma_0^2 / \gamma_{1b} \gamma_s$ .

For infinite plasma, integrating eq. (A.13) from  $x = x$  to  $\infty$  gives  
(by transforming variables as  $z = \exp(-Cx)$ )

$$\alpha(x) = \frac{1}{4} \frac{\omega_p^2}{\omega_0} \frac{\gamma_s}{\gamma_0^2} N_n a_0(0) \cdot \left[ 1 - \exp \left( -\frac{\Gamma}{2} \cdot e^{-Cx} \right) \right] \quad (\text{A1.14})$$

From eq. (A7).

$$a_1(x) = \frac{1}{4} \frac{\omega_p^2}{\omega_0} \frac{\gamma_s}{\gamma_0^2} N_n a_0(0) \cdot [ \exp(\frac{\Gamma}{2} e^{-Cx} - 1) - 1 ] \exp(-\frac{C}{2}x) \quad (\text{A1.15})$$

The reflectivity R can be immediately calculated. At  $x=0$ , R is defined as

$$\begin{aligned} R^{1/2} &= a_1(0) / a_0(0) \\ &= \frac{1}{4} \frac{\omega_p^2}{\omega_0} \frac{\gamma_s}{\gamma_0^2} N_n \cdot ( \exp \frac{\Gamma}{2} - 1 ) \end{aligned} \quad (\text{A1.16})$$

which for  $\gamma_0^2 \ll \gamma_s \gamma_{ib}$ , reduces to

$$R^{1/2} = \frac{1}{8} \frac{\omega_p^2}{\omega_0 \gamma_{ib}} N_n \quad (\text{A1.17})$$

and for  $\gamma_0^2 \gg \gamma_s \gamma_{ib}$ ,

$$R^{1/2} = \frac{1}{4} \frac{\omega_p^2}{\omega_0} \frac{\gamma_s}{\gamma_0^2} N_n \cdot \exp \frac{\Gamma}{2} \quad (\text{A1.18})$$

Defining  $R_{\min}$  as

$$R_{\min} = \left( \frac{1}{8} \frac{\omega_p^2}{\omega_0 \gamma_{ib}} N_n \right)^2 \quad (\text{A1.19})$$

gives

$$R = R_{\min} \left( \frac{e^A - 1}{A} \right)^2 \quad (\text{A1.20})$$

where  $A = \Gamma/2 = \gamma_0^2 / 2\gamma_s \gamma_{ib}$ .

For finite plasma of length L, on the other hand, eq. (A.13) should be integrated from  $x = x$  to L.

$$\begin{aligned} a_1(x) &= \frac{1}{4} \frac{\omega_p^2}{\omega_0} \frac{\gamma_s}{\gamma_0^2} N_n a_0(0) \cdot [ \exp(-\frac{\Gamma}{2} e^{-CL}) - \exp(-\frac{\Gamma}{2} e^{-Cx}) ] \cdot \\ &\quad \cdot \exp(\frac{C}{2}x) \cdot \exp(\frac{\Gamma}{2} e^{-Cx}) \end{aligned} \quad (\text{A1.21})$$

Then at  $x=0$ ,

$$R^{1/2} = \frac{1}{4} \frac{\omega_p^2}{\omega_0} \frac{\gamma_s}{\gamma_0^2} N_n \cdot \left\{ \exp\left[ \frac{\Gamma}{2} (1 - e^{-G_L}) \right] - 1 \right\} \quad (\text{A1.22})$$

which for  $2\gamma_{1b}L/v_g \ll 1$ , becomes

$$\frac{\Gamma}{2} (1 - e^{-G_L}) \approx \frac{\gamma_0^2 L}{\gamma_s v_g} \equiv \frac{G_L}{2} \quad (\text{A1.23})$$

(  $e^x \approx 1 + x$  for  $x \ll 1$  )

and assuming  $G_L \gg 1$ ,

$$R = D \exp G_L \quad (\text{A1.24})$$

where

$$D = \left( \frac{1}{4} \frac{\omega_p^2}{\omega_0} \frac{\gamma_s}{\gamma_0^2} N_n \right)^2 \quad (\text{A1.25})$$

## Appendix 2

### A2. Conversion of Focal Length

In using commercially available UV lens, most manufacturers give specification in a wavelength other than 248nm which is our interest for KrF laser-plasma experiments. Here, we summarize formulae to convert focal length from one wavelength to another and physical constants necessary to use the formulae.

The formulae to convert focal length is given by

$$F_2 = \frac{n_1 - 1}{n_2 - 1} \cdot F_1 \quad (\text{A2.1})$$

where  $F_m$  and  $n_m$  are focal length and refractive index of the lens for wavelength  $\lambda_m$ , ( $m = 1, 2$ ). For example, for  $F_1 = 50\text{mm}$  Lens ( supplied by Melles Griot ) and  $n_1 = 1.46008$  at  $546.1\text{nm}$ , eq.(B.1) gives  $F_2 = 0.46008 / 0.5084 \times 50\text{mm} = 45.25\text{mm}$  for  $n_2 = 1.5084$  at  $248\text{nm}$ .

Table 1 summarizes specification of design wavelength for plano-covex fused silica lens and refractive index of fused silica at the design wavelength for several manufacturers.

Table A2.1. Specification provided by manufacturers

Manufacturer	Design wavelength	Refractive index
Melles Griot	546.1nm	1.46008
Oriel	589nm	1.458
Ealing	0.59 $\mu\text{m}$	1.458

Table 2 summarizes refractive index of fused silica and fused quartz at several important wavelengths.

Table A2.2. Refractive index of fused silica and fused quartz

$\lambda$ (Å)	refractive index n	
	fused silica	fused quartz
2482.72 ( $\approx$ KrF laser)	1.5084*	1.508398 (1.508383:calc.) <sup>1)</sup>
2538 (Hg line)		1.505468 ( calc. ) <sup>1)</sup>
5461 (Melles Griot design $\lambda$ )	1.46008*	1.460078 (1.460077:calc.) <sup>1)</sup>
5890 (Oriel & Ealing design $\lambda$ )	1.458*	
6328.2 (He-Ne laser)		1.456655 ( calculated ) <sup>2)</sup>

\* : from manufacturer's catalogues ( Melles Griot & Oriel )  
 calc. : calculated by empirical formulae in reference listed  
 below

Listed below are empirical formulae for refractive index of fused quartz and several references for the refractive index. Note each formulae has its applicable region.

- 1) I.H.Malitson, J. Opt. Soc. Am. 55, 1205 (1965).  
 ( from 2138.56Å to 37067Å )

$$n^2 = 1 + \frac{a_1 \lambda^2}{\lambda^2 - b_1^2} + \frac{a_2 \lambda^2}{\lambda^2 - b_2^2} + \frac{a_3 \lambda^2}{\lambda^2 - b_3^2} \quad ( \lambda \text{ in } \mu\text{m} )$$

(A2.2)

where

$a_1 = 0.6961663$	$b_1 = 0.0684043$
$a_2 = 0.4079426$	$b_2 = 0.1162414$
$a_3 = 0.8974794$	$b_3 = 9.896161$

- 2) W.S.Rodney and R.J.Spindler, J. Opt. Soc. Am. 44, 677 (1954).  
 ( from 0.34 $\mu\text{m}$  to 3.50 $\mu\text{m}$  )

$$n^2 = 2.978645 + \frac{0.008777808}{\lambda^2 - 0.010609} - \frac{84.06224}{96.00000 - \lambda^2} \quad (\lambda \text{ in } \mu\text{m})$$

(A2.3)

## Other references

- 3) VUV region ( 537Å - 10140Å )
  - T.Sasaki, H.Fukutani, K.Ishiguro, and T.Izumutani,  
Jpn.J.Appl.Phys., 4, (suppl.1), 527 (1965).
  - K.Platzöder and W.Steinmann, J.Opt.Soc.Am., 58, 588 (1968).
- 4) UV region ( 1999.6Å - 2961.16Å )
  - H.G.Jerrard and J.Turpin, J.Opt.Soc.Am., 55, 453 (1965).
  - B.Brixner, J.Opt.Soc.Am., 44, 674 (1967).
- 5) Visible ( 0.5μm - 4.3μm )
  - M.Hertzberger and C.D.Salzberg, J.Opt.Soc.Am., 52, 420(1962).



Appendix 3**A3. Formulae for Plasma Parameters in Practical Units**

In this section, formulae in practical units used for laser-plasma interaction are summarized. Units are CGS unless otherwise noted.

**Unit Conversion**

$$\text{erg} = \text{cm}^2 \cdot \text{g}/\text{s}^2 = \text{dyn} \cdot \text{cm}$$

$$\text{dyn} = \text{statcoul}^2/\text{cm}^2$$

$$W = 10^7 \text{ erg/s}$$

$$W/\text{cm}^2 = 10^7 \text{ g/s}^3$$

**Basic Parameters for KrF laser**

$$\lambda_0 = 0.248 \text{ } (\mu\text{m})$$

$$\omega_0 = 7.5861 \times 10^{15} \text{ (1/s)}$$

$$k_0 = 2.5305 \times 10^5 \text{ (1/cm)}$$

$$n_c = 1.8082 \times 10^{22} \text{ (1/cm}^3\text{)}$$

**Laser intensity ( $W/\text{cm}^2$ )**

$$\begin{aligned} I &= \frac{E_0^2}{8\pi} c && \text{for linear polarization} && \text{(A3.1)} \\ &= 10^{-7} \frac{c \text{ (cm/s)}}{8\pi} E_0^2 \text{ (statV/cm)} \\ &= 119.28 E_0^2 \text{ (statV/cm)} \end{aligned}$$

**EM wave wavenumber ( $\text{cm}^{-1}$ ) in plasma**

$$k_0 = \frac{\omega_0}{c} \sqrt{1 - n_e/n_c} \quad \text{(A3.2)}$$

**Debye length (cm)**

$$\begin{aligned} \lambda_D &= \sqrt{\frac{T_e}{4\pi n_e e^2}} = 7.4340 \times 10^2 \sqrt{\frac{T_e \text{ (eV)}}{n_e}} && \text{(A3.3)} \\ &= 5.5283 \times 10^{-9} \sqrt{\frac{T_e \text{ (eV)}}{n_e/n_c}} && \text{for KrF laser} \end{aligned}$$

Electron and ion thermal velocity (cm/s)

$$v_e = \sqrt{T_e / m_e} = 4.1939 \times 10^7 \sqrt{T_e \text{ (eV)}} \quad (\text{A3.4})$$

$$v_i = \sqrt{T_i / M_i} = 9.7873 \times 10^5 \sqrt{T_i \text{ (eV)} / A} \quad (\text{A3.5})$$

Group velocity of EM wave (cm/s)

$$v_g = c \sqrt{1 - n_e / n_c} \quad (\text{A3.6})$$

Sound velocity (cm/s)

$$c_s = \sqrt{\frac{ZT_e + 3T_i}{M_i}} = 9.7873 \times 10^5 \sqrt{\frac{ZT_e \text{ (eV)} + 3T_i \text{ (eV)}}{A}} \quad (\text{A3.7})$$

, where A is an atomic mass number

Electron oscillatory velocity (cm/s)

$$V_{os} = \frac{e E_0}{m_e \omega_0} = \frac{e}{m_e} \frac{10^{-4} \lambda (\mu\text{m})}{2\pi c} \sqrt{\frac{8\pi}{c} 10^7 I \text{ (W/cm}^2\text{)}} \quad (\text{A3.8})$$

$$= 25.630 \sqrt{I \text{ (W/cm}^2\text{)} \cdot \lambda^2 (\mu\text{m})} \quad (\text{for linear polarization})$$

$$= 6.356 \sqrt{I \text{ (W/cm}^2\text{)}} \quad \text{for KrF laser}$$

$$V_{os}^2 = 656.92 I \lambda_{\mu\text{m}}^2$$

$$= 40.403 I \quad \text{for KrF laser}$$

Electron and ion plasma frequency (rad/s)

$$\omega_{pe} = \sqrt{\frac{4 \pi n_e e^2}{m_e}} = 5.6414 \times 10^4 \sqrt{n_e} \quad (\text{A3.9})$$

$$= 7.5860 \times 10^{15} \sqrt{n_e / n_c} \quad \text{for KrF laser}$$

$$\begin{aligned}\omega_{pi} &= \sqrt{\frac{4 \pi n_i Z^2 e^2}{M_i}} = 1.3166 \times 10^3 Z \sqrt{\frac{n_i}{A}} & (A3.10) \\ &= 1.7704 \times 10^{14} \sqrt{Z \frac{n_e}{n_c} \frac{1}{A}} & \text{for KrF laser}\end{aligned}$$

if  $n_e = Zn_i$ ,

$$\omega_{pi} = \omega_{pe} \sqrt{\frac{Z m_e}{M_i}} = 0.02334 \omega_{pe} \sqrt{\frac{Z}{A}}$$

**Electron-ion collision frequency ( $s^{-1}$ )**

$$\begin{aligned}\nu_{ei} &= 1/\tau_{ei} = \frac{4 \sqrt{2\pi} e^4 Z n_e \ln\Lambda}{3 m_e^{1/2} T_e^{3/2}} & (A3.11) \\ &= 2.9062 \times 10^{-6} Z n_e \ln\Lambda / T_e^{3/2} (\text{eV}) \\ &= 5.2551 \times 10^{16} Z \frac{n_e}{n_c} \ln\Lambda / T_e^{3/2} (\text{eV}) & \text{for KrF laser}\end{aligned}$$

**Ion-ion collision frequency ( $s^{-1}$ )**

$$\begin{aligned}\nu_i &= 1/\tau_{ii} = \frac{4 \sqrt{\pi} e^4 Z^4 n_i \ln\Lambda}{3 M_i^{1/2} T_i^{3/2}} & (A3.12) \\ &= 4.7958 \times 10^{-8} Z^3 n_e \ln\Lambda / (A^{1/2} T_i^{3/2} (\text{eV})) \\ &= 8.6718 \times 10^{14} Z^3 \frac{n_e}{n_c} \ln\Lambda / (A^{1/2} T_i^{3/2} (\text{eV})) & \text{for KrF laser}\end{aligned}$$

**Electron-ion collision mean free path ( $cm^{-1}$ )**

$$\lambda_{ei} = \nu_e \tau_{ei} = 7.9806 \times 10^{-10} T_e^2 (\text{eV}) / \left( Z \frac{n_e}{n_c} \ln\Lambda \right) \quad (A3.13)$$

**Damping**

o Inverse Bremsstrahlung Absorption Coefficient  $\kappa_{ib}$  ( $\text{cm}^{-1}$ )

$$\kappa_{ib} = (2\pi)^{1/2} \left( \frac{16\pi}{3} \right) \frac{Z n_e^2 e^6 \ln\Lambda}{c (m_e T_e)^{3/2} \omega_0^2 \left( 1 - \frac{n_e}{n_c} \right)^{1/2}} \quad (\text{A3.14})$$

$$\Lambda \equiv \frac{V_e}{\omega_0 P_{\min}}, \quad P_{\min} \equiv \max \left[ \frac{Ze^2}{T_e}, \frac{\hbar}{(m_e T_e)^{1/2}} \right] \quad (\text{cm})$$

$$= 3.0853 \times 10^{-7} Z n_e^2 \ln\Lambda T_e^{-3/2} (\text{eV}) \omega_0^{-2} \left( 1 - n_e/n_c \right)^{-1/2}$$

$$= 1.7529 \times 10^6 Z \left( \frac{n_e}{n_c} \right)^2 \ln\Lambda / \left( T_e^{3/2} (\text{eV}) \left( 1 - n_e/n_c \right)^{1/2} \right)$$

for KrF laser

$$\frac{Ze^2}{T_e} = 1.4399 \times 10^{-7} \frac{Z}{T_e} (\text{eV}) \quad \frac{\hbar}{(m_e T_e)^{1/2}} = 2.760 \times 10^{-8} T_e^{1/2} (\text{eV})$$

$$\gamma_{ib} = \kappa_{ib} \cdot v_g \quad (1/\text{s}) \quad (\text{A3.15})$$

$$= 9.2494 \times 10^3 Z n_e^2 \ln\Lambda T_e^{-3/2} (\text{eV}) \omega_0^{-2}$$

$$= 5.2550 \times 10^{16} Z \left( \frac{n_e}{n_c} \right)^2 \ln\Lambda T_e^{-3/2} (\text{eV}) \quad \text{for KrF laser}$$

o Ion Landau Damping rate

$$\gamma_s = \omega_s \sqrt{\frac{\pi}{8}} \left\{ \frac{\omega_{pi}}{\omega_{pe}} + \frac{Z T_e}{T_i} \frac{k_s c_s}{k_s V_i} \cdot \exp \left[ - \frac{Z T_e}{2 T_i} - \frac{3}{2} \right] \right\} \quad (\text{A3.16})$$

$$= \omega_s \sqrt{\frac{\pi}{8}} \left\{ \sqrt{\frac{Z m_e}{A m_p}} + \beta^2 \sqrt{\beta^2 + 3} \cdot \exp \left[ - \frac{1}{2} (\beta^2 + 3) \right] \right\}$$

$$\beta^2 = \frac{Z T_e}{T_i} \quad \sqrt{\frac{\pi}{8}} = 0.62666 \quad \sqrt{\frac{Z m_e}{A m_p}} = 0.023337 (Z A)^{-1/2}$$

### SBS in infinite homogeneous plasma

Growth rate

$$\begin{aligned}
 \gamma_0 &= \frac{1}{2} \cdot \frac{v_0}{c} \cdot \left( \frac{\omega_0}{\omega_s} \right)^{1/2} \cdot \omega_{pi} \cdot \sqrt{1 - n_e/n_c} & (A3.17) \\
 &= 3.9796 \times 10^{-7} \lambda_{\mu m} Z \sqrt{\frac{n_1 v_g}{c_s A}} \cdot \sqrt{I \text{ (W/cm}^2\text{)}} \\
 &= 1.3271 \times 10^{11} \sqrt{\frac{Z v_g n_e}{A c_s n_c}} \cdot \sqrt{I_{14}} & \text{for KrF laser}
 \end{aligned}$$

Intensity threshold

$$\begin{aligned}
 \frac{v_{os}^2}{v_e^2} &= 8 \frac{\gamma_s}{\omega_s} \frac{\gamma_{lb}}{\omega_0} \frac{n_c}{n_e} & (A3.18) \\
 I_{th} \text{ (W/cm}^2\text{)} &= \frac{v_e^2}{328.44 \cdot \lambda^2 (\mu m)} \cdot \left[ 8 \frac{\gamma_s}{\omega_s} \frac{\gamma_{lb}}{\omega_0} \frac{n_c}{n_e} \right]
 \end{aligned}$$

## Appendix 4

### **A.4. Target Burnthrough Experiment**

In this appendix, preliminary results of target burnthrough experiments are briefly reported. It is found that transmitted light through a thin foil target shows strong spatial and temporal modulations. This experiment provides supportive information to our SBS analysis and CASTOR 2D hydrodynamic simulation results. The possibility of filamentation is examined by taking into account nonlocal thermal transport.

#### **A4.1. Experimental Setup**

The experimental setup was basically the same as for the SBS experiment except that the streak camera was placed behind the target without a time fiducial. Thin foil targets were irradiated by the KrF laser at normal incidence and the rear surface of the target was imaged on the streak camera. Two kinds of material were used for targets; Al and plastic. The Al foil used was a commercial product from Goodfellow Inc. (Cambridge, England); the thickness of the foil was varied from  $3\mu\text{m}$  to  $9\mu\text{m}$ . As it is easily available, we used the commercial product "Saran Wrap" ( $-\text{CH}_2\text{CCl}_2-$ ) for the plastic thin foil target whose specific gravity and thickness are  $\approx 1.7$  and  $12\mu\text{m}$ , according to the manufacturer. The transmission of the Saran Wrap foil was measured to be 65% at 248nm. These target foil thicknesses were thin enough to burn through during laser pulse.

The rear surface of the targets was imaged on the streak camera by a 12.5cm aspheric triplet lens ( $f=2.5$ ) with magnification  $M \approx 50$ . The

spatial resolution of the lens was measured to be about  $2\mu\text{m}$ . To avoid damage by target debris, KODAK Wratten gelatin filters (ND 0, 0.5, or 0.6) were placed in front of the lens, which also worked as an appropriate attenuator of the intense laser beam. Distortion of the image by the filter was visibly confirmed to be negligible. To discriminate the transmitted laser light from the self-emission of the target, an interference bandpass filter (Oriel, 11.8nm bandwidth at 250nm, transmission = 22%) was used.

#### A4.2. Experimental Results

A slice of the target image ( $\approx 1\mu\text{m}$  width) was streaked in time. Since there was no time fiducial, timing of the incident pulse was measured every few shots. The timing jitter was estimated to be about  $\pm 1$  ns. Relative timing between the transmitted light and the incident pulse can be correlated in  $\pm 1$  ns.

Figure A4.1 shows a streaked image of the original laser pulse (taken without target). The spatial modulation period of the original pulse was about  $2\mu\text{m}$ . Although the nominal spatial resolution of this experiment is about  $2\mu\text{m}$ , we also measured our focal spot with better resolution ( $< 2\mu\text{m}$ ) and found the typical hotspot size is  $\approx 2\mu\text{m}$  (see section 5.1.2). The image also shows slight temporal modulation ( $\approx 10\%$ ) with a period of 200ps.

Figures A4.2 and A4.3 show streaked images of the transmitted light through Saran Wrap targets with low laser energy  $E_L = 386\text{mJ}$  (fig.A4.2) and high laser energy 820mJ (fig.A4.3). Although Saran Wrap is transparent to 0.248nm light, we did not observe strong transmitted light signal at the beginning of the laser pulse. We

therefore expect that plasma was quickly formed by the weak leading foot of the laser pulse. The transmitted light signals show  $12\mu\text{m}$  of plastic target was burned through at relatively early time of the laser pulse: the peak of the laser pulse is at 2-3ns in the vertical axis of the figure. The spatial modulation period is about  $2-4\mu\text{m}$  - almost the same scale as that of the original pulse. The temporal modulation period depended on the laser energy. Stronger temporal modulations ( $\approx 90\%$ ) were observed for higher energy shots with a period as short as 200ps (limited by time resolution of the streak camera). Even in the fastest sweep mode with time resolution of 40ps, we only observed temporal modulation periods  $\geq 150\text{ps}$ .

Figures A4.4 and A4.5 show streaked images of the transmitted light through Al targets with thickness of  $3\mu\text{m}$  (fig.A4.4) and  $9\mu\text{m}$  (fig.A4.5). Laser energies for these shots were 790mJ (fig.A4.4) and 708mJ (fig.A4.5). The  $3\mu\text{m}$  target was burned through about 2ns earlier than the  $9\mu\text{m}$  target. Even  $9\mu\text{m}$  Al target was burned through by the peak of the laser pulse. Similar temporal and spatial modulation features were observed for these comparable energy shots. It is noted that generally, in spite of the strong spatial modulation, the intense and weak parts of the transmitted laser light appeared simultaneously over a region comparable to the focal spot size.

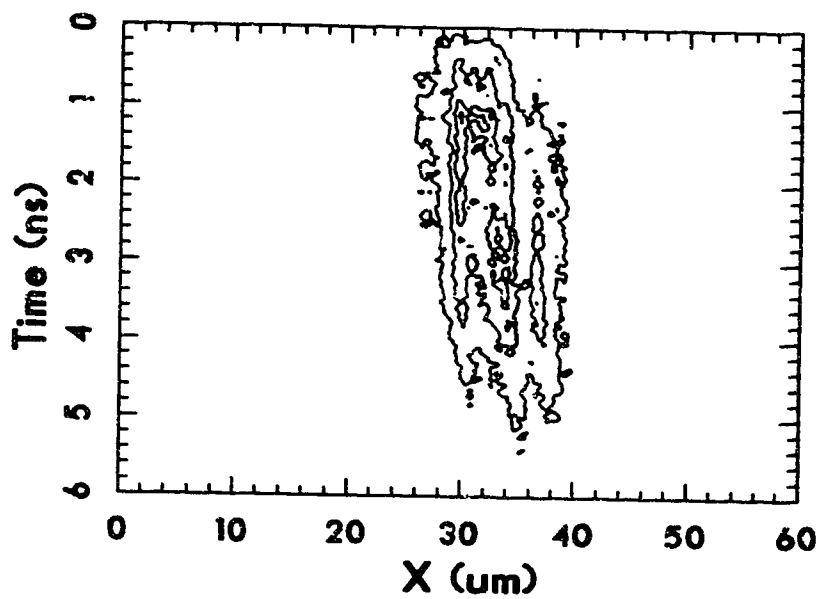
Partial burnthrough was only observed for a few individual shots. Figure A4.6 shows an example of early partial burnthrough observed for  $9\mu\text{m}$  Al target with  $E_L = 575\text{mJ}$ . Intense laser light with a spatial scale of  $2\mu\text{m}$  appeared early in the laser pulse. It is noted that such an early partial burnthrough was observed in this particular shot and was not usually observed.



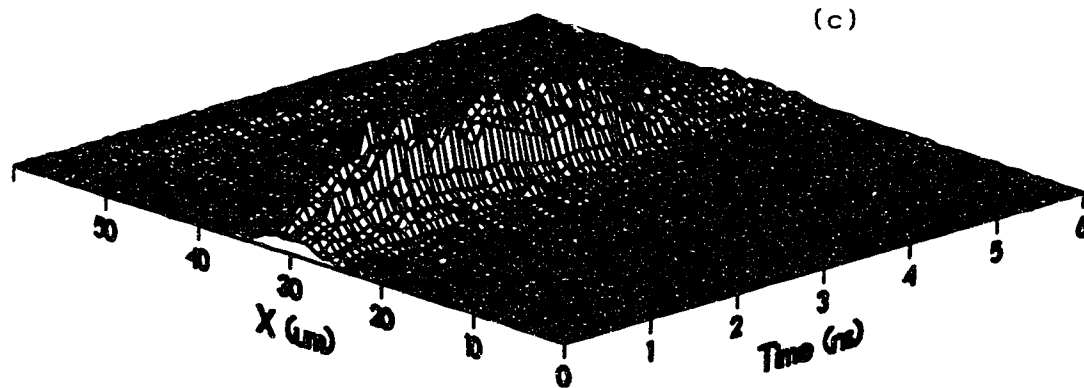


(a)

Fig.A4.1. Streaked image of the original laser light (a), its contour (b), and 3D intensity map (c). Laser energy was 650mJ.



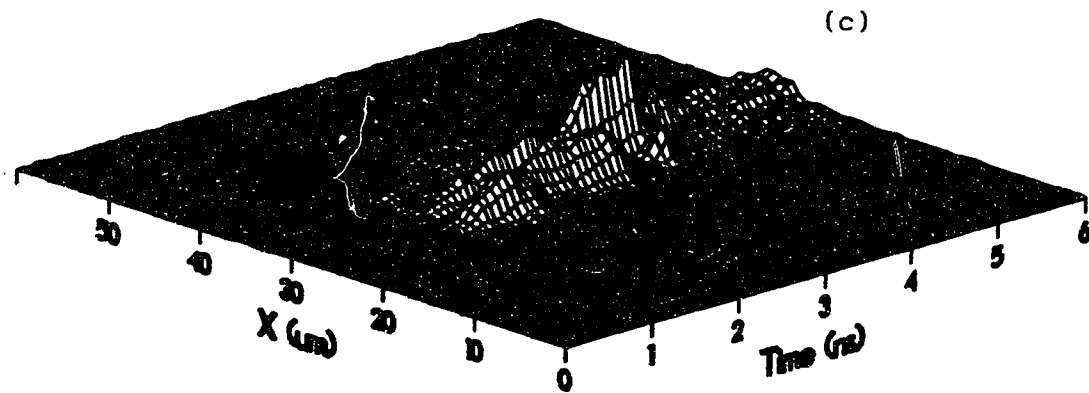
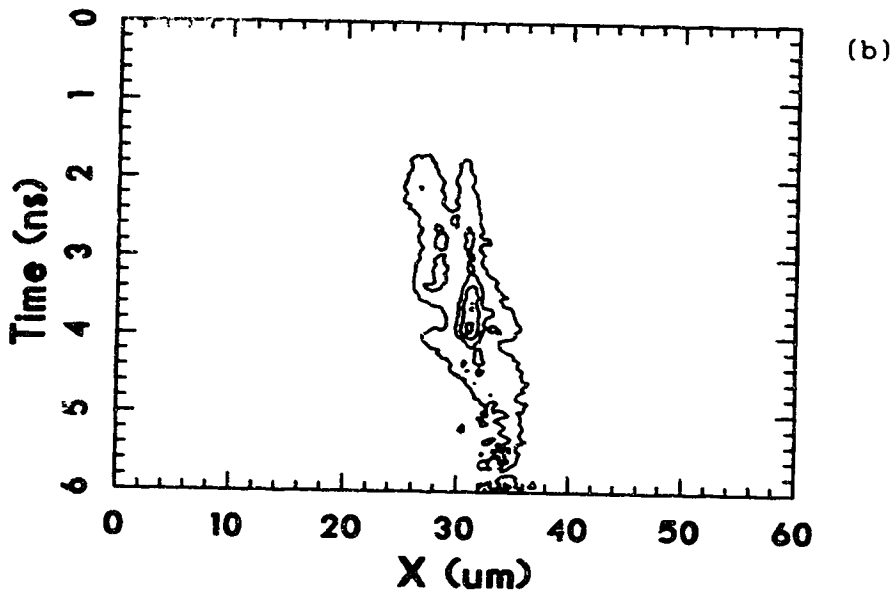
(b)

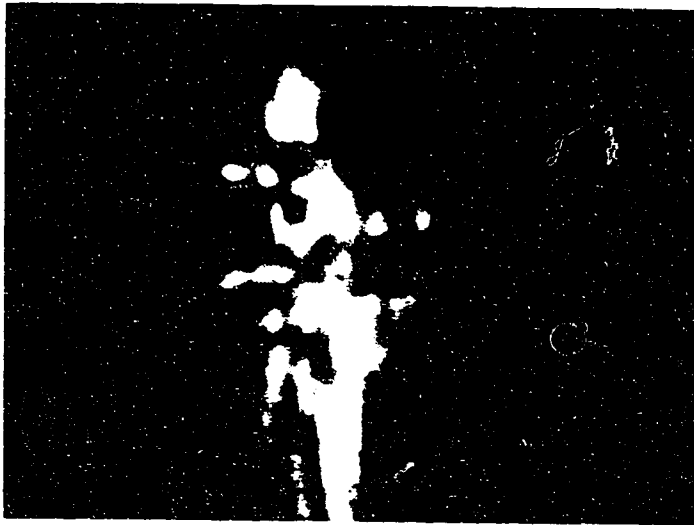


(c)



Fig.A4.2. Streaked image of the transmitted light through Saran Wrap target (a), its contour (b), and 3D intensity map (c). Laser energy was 386mJ.

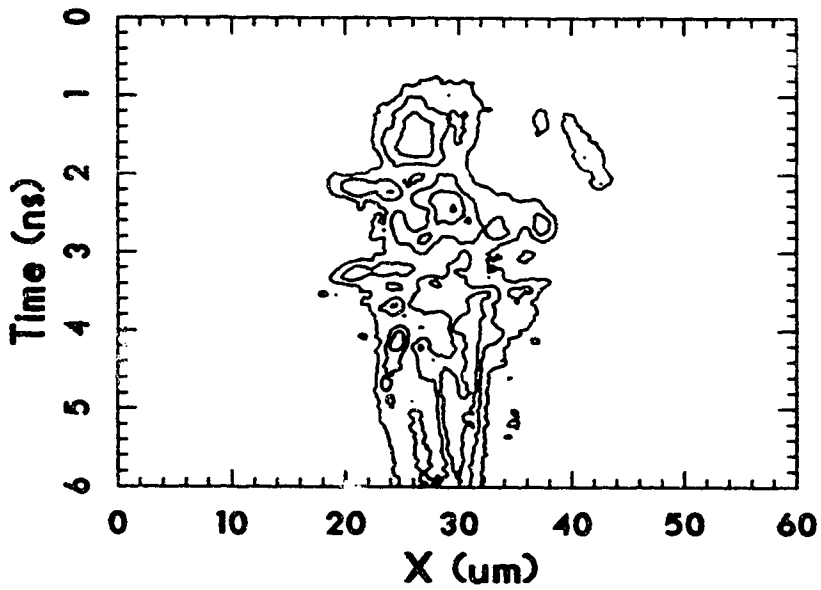




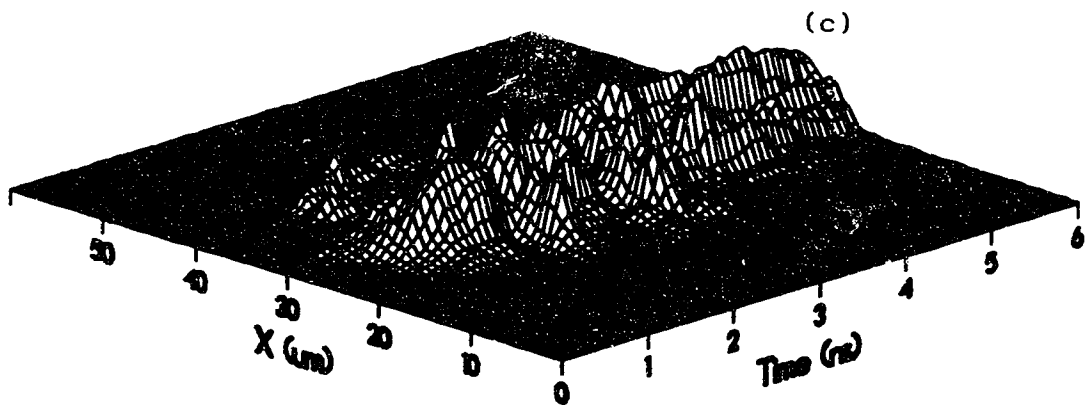
(a)

Fig.A4.3. Streaked image of the transmitted light through Saran Wrap target (a), its contour (b), and 3D intensity map (c).

Laser energy was 820mJ.



(b)

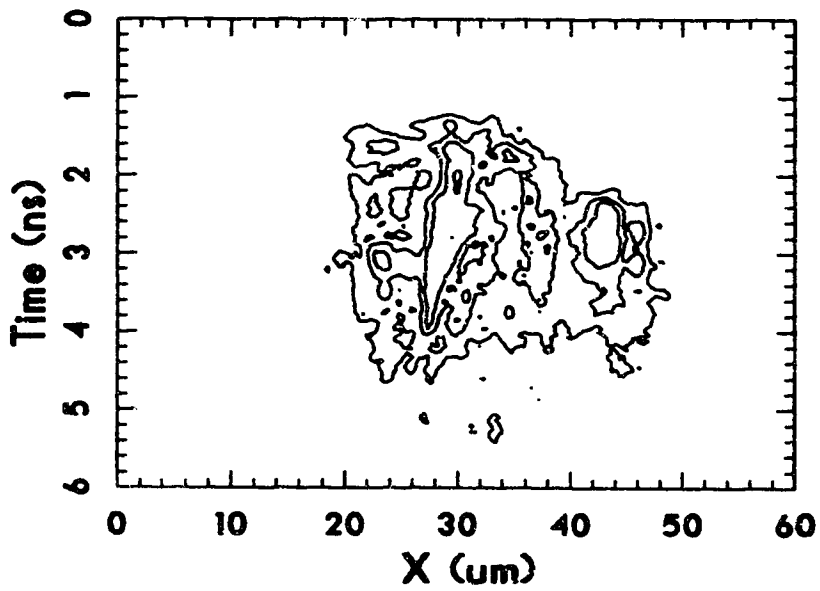


(c)

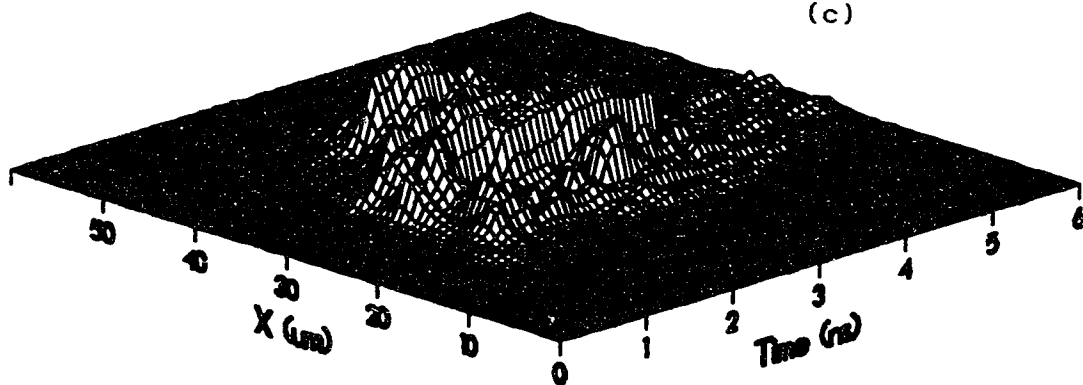


(a)

Fig.A4.4. Streaked image of the transmitted light through Al 3 $\mu$ m target (a), its contour (b), and 3D intensity map (c). Laser energy was 790mJ.



(b)

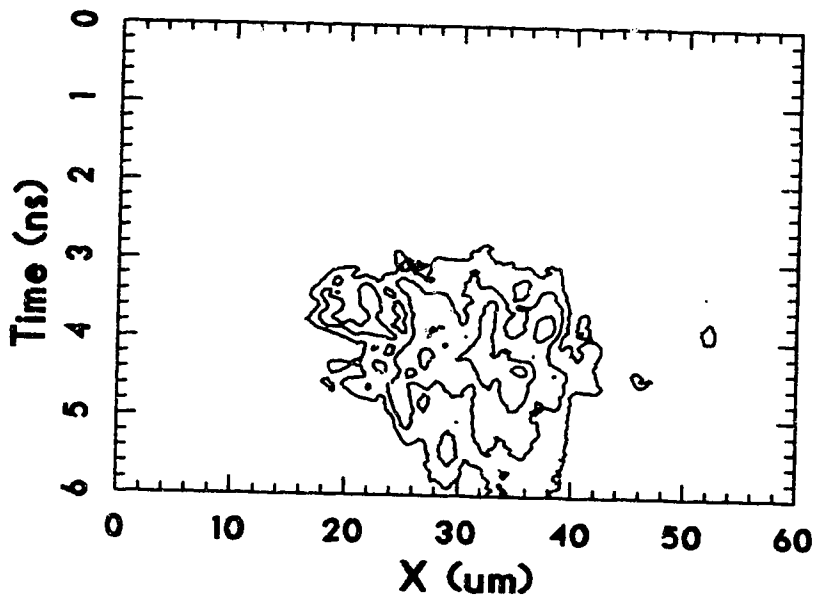


(c)

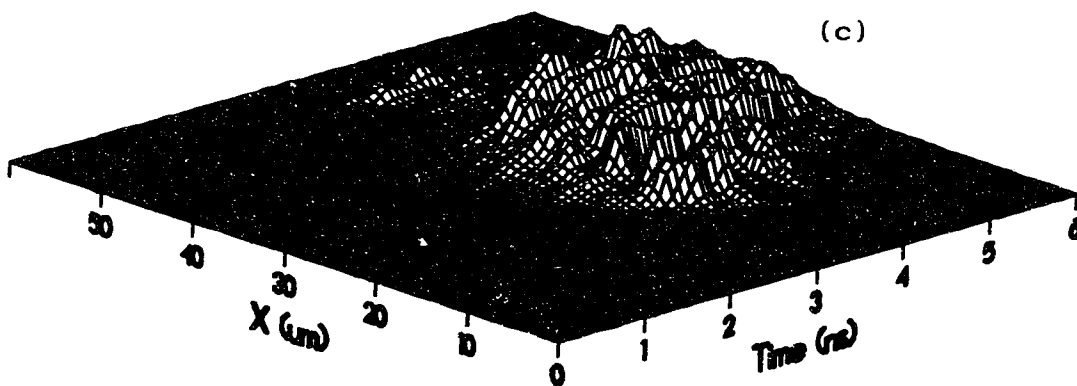


(a)

Fig. A4.5. Streaked image of the transmitted light through Al 9 μm target (a), its contour (b), and 3D intensity map (c). Laser energy was 708mJ.



(b)



(c)

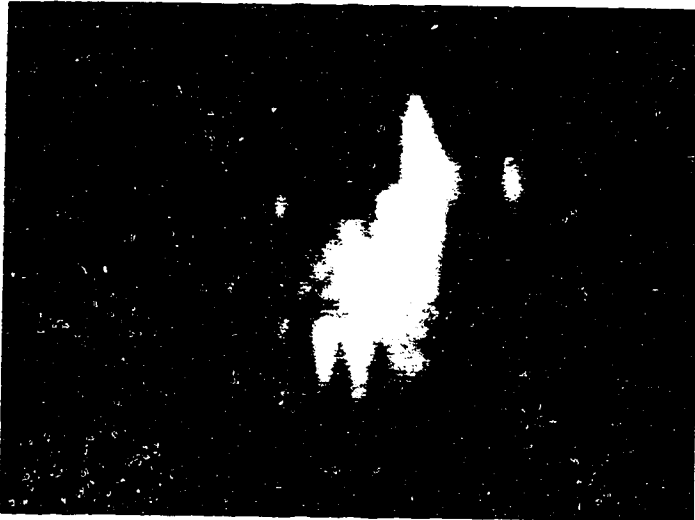
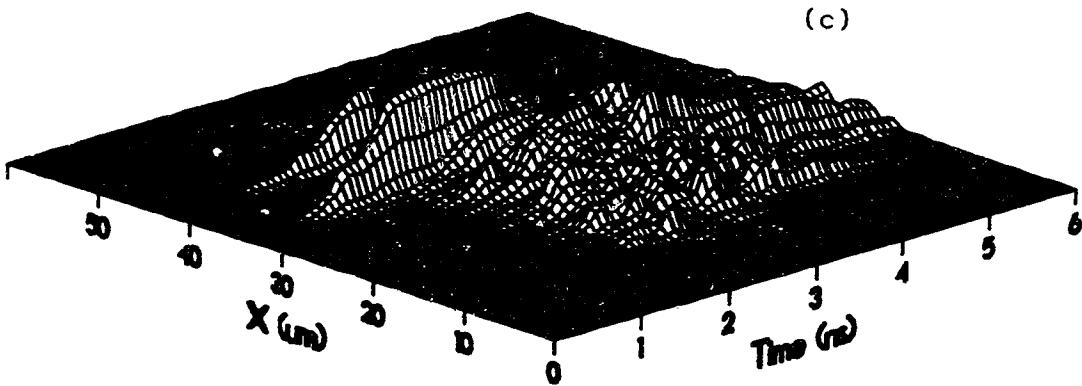
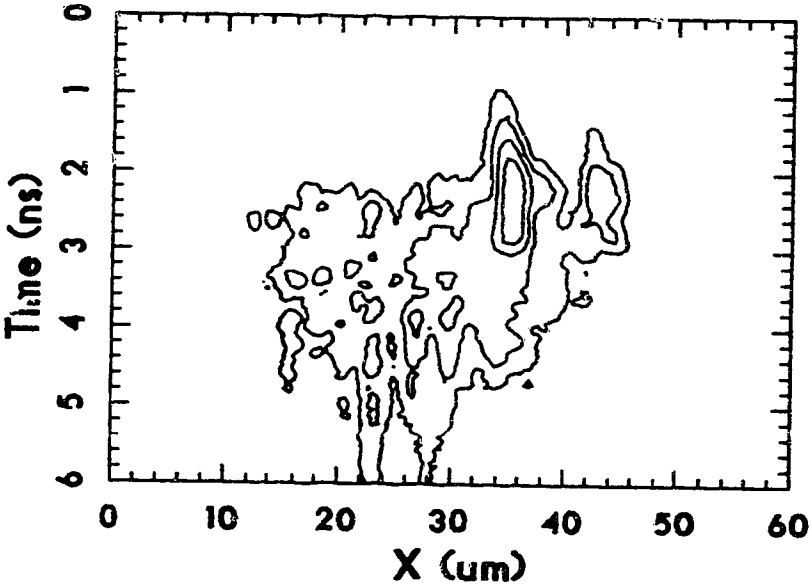


Fig.A4.6. Streaked image of the transmitted light through Al 9µm target (a), its contour (b), and 3D intensity map (c). Laser energy was 575mJ.



### A4.3 Discussion

By just looking at the transmitted light through plasma, it is difficult to conclude the existence of filamentation because of the effects of refraction by plasma. We can, however, determine several experimental observations from the burnthrough experiments. First of all, the  $10\mu\text{m}$  Al target was burned through around the laser peak. If one assumes that the burnthrough was due to the target ablation, a mass ablation rate  $\dot{m}$  is estimated to be  $3 \times 10^6 \text{ g/cm}^2\text{s}$ . This value is significantly higher than  $\dot{m} \approx 4 \times 10^5 \text{ g/cm}^2\text{s}$  which is derived from the scaling law obtained in a previous KrF laser-plasma experiment with lower intensity ( $\approx 10^{13} \text{ W/cm}^2$ ) and larger focal spot size ( $74\mu\text{m}$  diameter for 90% energy contour)<sup>1)</sup>. This implies that the shock wave, rarefaction, and resulting target disassembly are playing an important role in the target burnthrough. The 2D hydrodynamic simulation results in chapter 4 show the critical surface is located  $10\mu\text{m}$  inside the initial target surface at  $t=1.8\text{ns}$  ( $0.6\text{ns}$  before laser peak).

Secondly, if one assumes that the modulation seen in the image was caused by refraction of the transmitted light by the plasma (temporal misalignment of the image to the streak camera slit), the time scale of change in the refractive index is roughly estimated as fast as  $150\text{ps}$ . Such a fast change in density variation was observed in the CASTOR results; indeed, at early time in the laser pulse, CASTOR predicted a density variation time scale of  $\approx 20\text{ps}$ . The interesting point here is that this experimental evidence supports the density variation seen in CASTOR (see chapter 4.3), which is caused by a complex interplay of laser beam refraction and local mass ablation.

Thirdly, despite the strong temporal modulations in the

transmitted light, the signals appeared at almost the same spatial position throughout the pulse. One can see vertical stripes of light signal in most of the images except for fig.A4.3 with high laser energy. As seen in fig.A4.1, our beam has spatial structure which is constant in time. Similar structure is observed in the transmitted light, especially at late time in the laser pulse. This means that the structure was not smoothed out by the plasma but remained so throughout the laser pulse. Although more details of the target behavior have to be examined by experiment and 2D simulations, this experimental observation may suggest the imprint of the laser beam<sup>2)</sup>. In addition, this observation confirms that our hotspot analysis in which the focal spot structure was implicitly assumed to be steady in time is appropriate for our case.

Finally, in spite of the strong modulations in space and time in the transmitted light, the intense and weak parts appeared at almost the same time (clearly seen in the 3D maps), except for the particular data in fig.A4.6. This experimental evidence excludes the possibility of filamentation. If the modulation was caused by filamentation, one would expect the intense part to burn through faster than the weak part, since the mass ablation rate is larger for high intensity. We conclude that generally global burnthrough is observed, not a partial burnthrough due to filamentation. In the next section, the possibility of filamentation are discussed in detail.

#### **A4.4 Possibility of Filamentation**

Filamentation<sup>3)</sup> is an important process by which spatial modulations in the laser pulse intensity profile can be amplified due



to changes in the plasma refractive index. The resultant enhancement in intensity can modify other instabilities such as SBS. Filamentation can be classified as ponderomotive<sup>3,4)</sup> or thermal<sup>5)</sup>. At high intensity, the ponderomotive force of the laser beam can drive plasma out of the beam, thereby increasing the refractive index and leading to stronger focusing of the beam. At low intensity, if the beam size is larger than the electron mean free path, inverse bremsstrahlung heating increases the plasma pressure inside the beam, resulting in lower density of plasma and increased refractive index inside the beam.

The instability thresholds for filamentation are summarized in reference 6. If we define the threshold condition by one  $e$ -fold increase of the laser intensity and amplification distance by an inverse bremsstrahlung absorption length  $L_{abs}$ , the intensity thresholds for ponderomotive filamentation ( $I_p$ ) and thermal filamentation ( $I_T$ ) are given by<sup>6)</sup>

$$I_p \text{ (W/cm}^2\text{)} \approx 3 \times 10^{12} \frac{1}{\lambda^3} \frac{Z}{T^{1/2}} \frac{n_e}{n_c} \quad (\text{A4.1})$$

$$I_T \text{ (W/cm}^2\text{)} \approx 6 \times 10^{13} \frac{1}{\lambda^2} T^2 \frac{n_e}{n_c} \quad (\text{A4.2})$$

where  $\lambda$  and  $T$  are laser wavelength in  $\mu\text{m}$  and electron temperature in keV. Figure A4.6 (a) shows the dependence of intensity thresholds on incident laser intensity for  $\lambda = 0.25\mu\text{m}$  and  $n_e/n_c = 0.5$ . It is noted that the temperature dependence for threshold was converted to intensity dependence via a relationship  $T_{eV} = 600 \cdot I_{14}^{0.44}$ , where  $I_{14}$  is laser intensity in  $10^{14}\text{W/cm}^2$ . At low intensities (low temperature),  $I_p$  is substantially higher than  $I_T$ . As intensity (temperature) increases,  $I_T$  increases because of longer electron mean free path.

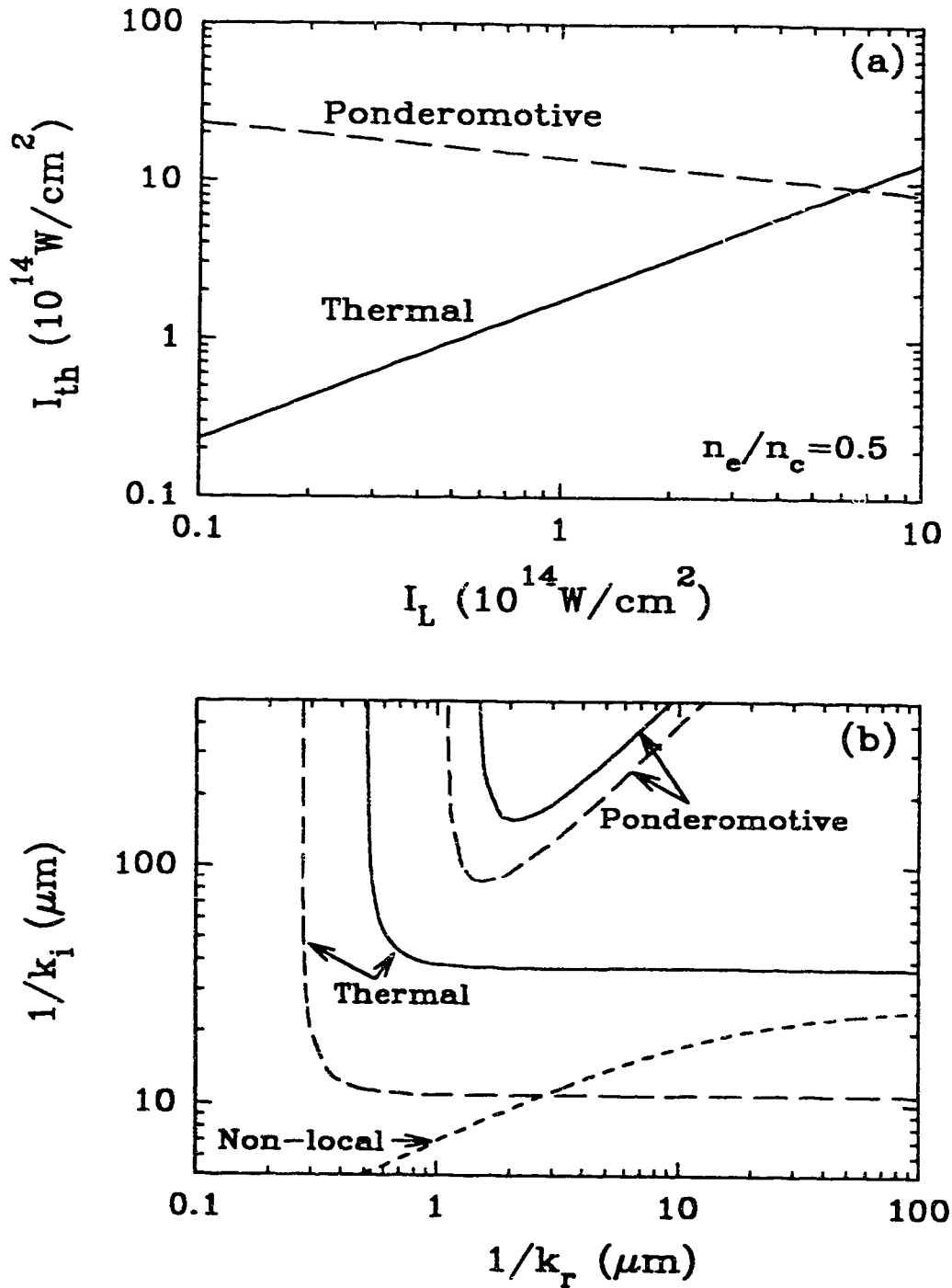


Fig.A4.6. Intensity threshold for ponderomotive (dashed line) and thermal filamentation (solid line) as a function of laser intensity (a). Relationship between perturbation wavenumber ( $k_r$ ) and filamentation growth length ( $k_i$ ) (b).

For the assumed conditions ( $n_e/n_c=0.5$ ,  $L_{abs} \approx 5\mu\text{m}$ ), both intensity thresholds are higher than the corresponding laser intensity, hence we do not expect amplification of intensity by filamentation. This is mainly due to strong inverse bremsstrahlung absorption restricting the amplification distance. On the other hand, if one assumes  $n_e/n_c=0.1$  ( $L_{abs} \approx 180\mu\text{m}$ ), the intensity threshold for thermal filamentation is actually lower than the corresponding laser intensity. However, such a long scale length of plasma in our experiment is not expected.

The above discussion is based on a simple homogeneous plasma theory, where the average laser intensity and plasma temperature are related by a simple scaling law expected from the self-regulating model. Next, we examine the dependence of filamentation growth rate by taking into account laser beam inhomogeneity and also non-local thermal transport<sup>7)</sup>. The dispersion relations for ponderomotive and thermal filamentation are given by<sup>6)</sup>

$$4 k_1^2 k_0^2 + k_r^4 - k_r^2 \frac{\omega_{pe}^2}{c^2} \frac{v_o^2}{2\nu_{ei}^2} = 0 \quad (\text{ponderomotive}) \quad (\text{A4.3})$$

$$4 k_1^2 k_0^2 + k_r^4 - \frac{v_o^2}{14\nu_{ei}^2} \frac{\omega_{pe}^2}{c^2 \lambda_{ei}^2} = 0 \quad (\text{thermal}) \quad (\text{A4.4})$$

where the wavenumber of the perturbation is defined by  $\underline{k} = \underline{k}_r + i\underline{k}_1$ ,  $\underline{k}_r \cdot \underline{k}_0 = 0$ , and  $\underline{k}_1$  is parallel to  $\underline{k}_0$ .  $\nu_{ei}$  and  $\lambda_{ei}$  are electron-ion collision frequency and mean free path. The solid lines in fig.A4.6 (b) show the relationship between instability wavenumber ( $k_1$ ) and intensity perturbation wavenumber ( $k_r$ ) calculated from eqs.(A4.3) and (A4.4) for  $I_L = 2 \times 10^{14} \text{W/cm}^2$ ,  $T=814\text{eV}$ , and  $n_e/n_c=0.5$ . Ponderomotive filamentation shows an optimum perturbation scale length ( $1/k_r$ )  $\approx 1\mu\text{m}$  but requires a growth length of  $100\mu\text{m}$  (defined by  $2k_1 L = 1$ ). Thermal

filamentation requires less growth length ( $\approx 20\mu\text{m}$ ) than ponderomotive filamentation, but it is still larger than the absorption length.

If one assumes that a beam with hotspots of intensity  $I_{\text{hs}}$  interacts with background plasma whose temperature is decided by the average intensity  $I_{\text{av}}$  ( $I_{\text{hs}} \approx 2.3 \cdot I_{\text{av}}$ ), the required growth length becomes shorter. This is shown by dashed lines in fig.A4.6 (b) which are calculated for  $I_L = 2.3 \times 10^{14} \text{W/cm}^2$ ,  $T=600\text{eV}$ , and  $n_e/n_c=0.5$  ( $I_{\text{av}}=10^{14} \text{W/cm}^2$ ). Thermal filamentation shows substantial reduction of growth length for these conditions.

Recently, the classical theory of laser filamentation in a homogeneous plasma has been extended to include the effects of nonlocal electron heat transport<sup>7)</sup>. It has been shown that the classical thermal conductivity  $\kappa_{\text{SH}}$  given by Spitzer-Härm<sup>8)</sup> is not adequate under conditions where the temperature scale length is shorter than some appropriate electron mean free path. The new theory suggests that the thermal conductivity  $\kappa$  should be modified to account for kinetic transport effects. By solving the Fokker-Planck equation numerically<sup>9)</sup>, Epperlein derived an empirical relationship<sup>7)</sup>

$$\kappa/\kappa_{\text{SH}} = [ 1 + ( 30k\lambda_e )^2 ]^{-1} \quad (\text{A4.5})$$

where  $\lambda_e$  is defined by

$$\lambda_e = \frac{T^2}{4\pi n e^2} (Z+1)^{1/2} \ln \Lambda \quad (\text{A4.6})$$

and  $k$  is the perturbation wavenumber for filamentation. For large  $k$ , eq.(A4.5) gives  $\kappa/\kappa_{\text{SH}} < 1$ , which is commonly known as flux inhibition.

By taking into account eq.(A4.5), eq.(A4.4) is modified as

$$4 k_i^2 k_o^2 + k_r^4 - \frac{v_o^2}{14\nu_{ei}^2} \frac{\omega_{pe}^2}{c^2 \lambda_{ei}^2} \frac{\kappa_{\text{SH}}}{\kappa} = 0 \quad (\text{A4.7})$$

The dotted line in fig.A4.6 (b) shows the solution of eq.(A4.7) for the same conditions as before. Evidently, for shorter perturbation wavelength, the growth length can be reduced substantially.

For the focused laser beam conditions in our experiment, we roughly estimate  $1/k_r \approx 2\mu\text{m}$ , which then requires a growth length  $\approx 5\mu\text{m}$ . This condition may or may not be satisfied in our plasma. It might be satisfied in the particular case of fig.A4.6 where the intense transmitted light signal (saturated in the image) appeared  $\approx 1\text{ns}$  earlier than the rest of the signal. If perturbations smaller than  $2\mu\text{m}$  exist in our laser beam, we should expect growth of thermal filamentation. However, since spatial resolution in our focal spot measurement was  $\approx 2\mu\text{m}$ , we cannot conclude the existence of filamentation due to such a small perturbation in our experiment. It should be noted that we do not expect such small perturbations, since generally we did not observe evidence for filamentation.

#### A4.5 Summary

Images of the transmitted light through Al and plastic targets of various thickness showed strong temporal and spatial modulations. Relatively thick  $10\mu\text{m}$  Al target was burned through by the irradiation of tightly focused KrF laser beam. Temporal modulation in the transmitted light is expected due to temporal density variations seen in the CASTOR simulation results. It was found that the laser beam non-uniformity is not smoothed out by the plasma but remains throughout the laser pulse, which may suggest the importance of "imprint". For our laser-plasma conditions, thermal filamentation dominates ponderomotive filamentation. Taking into account non-local heat

transport, thermal filamentation shows significant decrease of the growth length for short scale perturbations. Because of the short scale axial length of our plasma, we generally do not expect and did not observe filamentation in our experiment.

#### Bibliography

- 1) P.D.Gupta, Y.Y.Tsui, R.Popil, R.Fedosejevs, and A.A.Offenberger, *Phys.Fluids*, **30**, 179 (1987).
- 2) M.H.Emery, J.H.Gardner, R.H.Lehmberg, and S.P.Obenschain, *Phys.Fluids*, **B3**, 2640 (1991).
- 3) P.Kaw, G.Schmit, and T.Wilcox, *Phys.Fluids*, **16**, 1522 (1973).
- 4) B. I. Cohen and C. E. Max, *Phys.Fluids*, **22**, 1115 (1979).
- 5) M.S.Sodha, A.K.Ghatak, and V.K.Tripathi, in *Progress in Optics*, vol.13, edited by E.Wolf (North Holland, Amsterdam, 1976).
- 6) W.L.Kruer, *Comments Plasma Phys. Controlled Fusion*, **9**, 63 (1985).
- 7) E.M.Epperlein, *Phys.Rev.Lett.*, **65**, 2145 (1990).
- 8) L.Spitzer, Jr., and R.Härm, *Phys.Rev.*, **89**, 977 (1953).
- 9) E.M.Epperlein, G.J.Rickard, and A.R.Bell, *Phys.Rev.Lett.*, **61**, 2453 (1988).

## VITA

Name : Masayuki Fujita  
 Place of Birth : Kumamoto, Japan  
 Year of Birth : 1961

### Post-Secondary Education

1979-1983	Department of Electrical Engineering Osaka University, Osaka, Japan Bachelor of Science, 1983
1983-1985	Department of Electromagnetic Energy Engineering Osaka University, Osaka, Japan Master of Engineering, 1985
1985-1987	Department of Electromagnetic Energy Engineering Osaka University, Osaka, Japan
1987-1992	Department of Electrical Engineering University of Alberta, Alberta, Canada PhD, 1992

### Research Topics

1982-1987	Experimental research on CO <sub>2</sub> laser driven implosion at ILE, Osaka; topics included hot electron production, magnetic field effects, cavity plasma.
1987-1992	Experimental research on SBS in KrF Laser-produced plasma, Univ. of Alberta; topics include measurements of temporally resolved SBS spectrum, modelling of SBS from inhomogeneous plasma.

### Honors and Awards

Andrew Stewart Graduate Prize, Univ. of Alberta, 1989  
 Killam Doctoral Scholarship, Univ. of Alberta, 1990-1992

### Conference Presentations

- 1) "Stimulated Brillouin Scattering from KrF Laser-Produced Plasmas"  
**M.Fujita**, J.Santiago, R.Fedosejevs, and A.A.Offenberger  
 Canadian Association of Physicists Annual Congress  
 Univ. of Guelph, 1989
  
- 2) "Stimulated Brillouin Scattering from KrF Laser-Produced Plasmas"  
**M.Fujita**, J.Santiago, R.Fedosejevs, and A.A.Offenberger  
 The 21st Annual Anomalous Absorption Conference  
 The Banff Centre, 1991

### Contributor to Other Conference Presentations

- a) "Stimulated Brillouin Scattering from Laser-Produced Plasmas"  
 J.Santiago, **M.Fujita**, R.Fedosejevs, and A.A.Offenberger  
 the 30th Annual Meeting of the Division of Plasma Physics,  
 American Physical Society, Hollywood, Florida, 1988
  
- b) " Stimulated Scattering from Laser Produced Plasma "  
 A.A.Offenberger, J.Santiago, **M.Fujita**, R.Fedosejevs, and W.Rozmus.  
 the 19th European Conference on Laser Interaction with Matter, 1988
  
- c) " KrF Laser/Plasma Interaction Experiments with ns and ps Pulses"  
 A.A.Offenberger, R.Fedosejevs, **M.Fujita**, , Y.-Y.Tsui and J.N.Broughton  
 the 22th European Conference on Laser Interaction with Matter, 1991

### Contributor to Other Publications

- i) " Stimulated Scattering from Laser Produced Plasma "  
 A.A.Offenberger, J.Santiago, **M.Fujita**, R.Fedosejevs, and  
 W.Rozmus.  
 Laser and Particle Beams, vol.8, No.1-2, pp.153-171, (1990).
  
- ii) " KrF Laser/Plasma Interaction Experiments with ns and ps Pulses"  
 A.A.Offenberger, R.Fedosejevs, **M.Fujita**, , Y.-Y.Tsui and J.N.Broughton  
 Laser and Particle Beams, (to be published).